

**Magnetic mineralogy and fabrics of small-scale glacial flutes, Múlajökull and
Breiðamerkurjökull, Iceland**

by

Libby Rosa Woodford Ives

A thesis submitted to the graduate faculty

in partial fulfillment of the requirements for the degree of

MASTER OF SCIENCE

Major: Geology

Program of Study Committee:

Neal R. Iverson, Major Professor

Alan D. Wanamaker

Peter L. Moore

Iowa State University

Ames, Iowa

2016

TABLE OF CONTENTS

LIST OF FIGURES	iv
LIST OF TABLES	viii
LIST OF TERMS AND ABBREVIATIONS	ix
ACKNOWLEDGEMENTS	xiii
ABSTRACT	xv
CHAPTER 1. INTRODUCTION	1
1.1 Glacial flutes	1
1.2 Anisotropy of magnetic susceptibility	15
1.3 Motivation and objective	26
CHAPTER 2. FIELD SETTINGS	28
2.1 Múlajökull	28
2.2 Breiðamerkurjökull	33
CHAPTER 3. METHODS	39
3.1 Introduction	39
3.2 Field methods	39
3.3 Field site descriptions	42
3.4 Magnetic mineralogy	54
3.5 Fabric analyses	75
3.6 Physical analyses	92
3.7 Resampling and reanalyzing clast fabrics from the literature	94
CHAPTER 4. RESULTS	96
4.1 Magnetic mineralogy	96
4.2 Anisotropy of magnetic susceptibility	105
4.3 Relative density	135
4.4 Grain size distribution	142
4.5 Analysis of pebble fabrics from the literature	142
CHAPTER 5. DISCUSSION	150
5.1 Magnetic Characteristics	150
5.2 Till density and estimated effective stress distribution	151
5.3 Fabrics	153
5.4 Flute Formation	156

5.5	Implications.....	164
CHAPTER 6. CONCLUSIONS		166
6.1	Flute Formation.....	166
6.2	Magnetic Mineralogy	167
REFERENCES		169
APPENDIX A. MATLAB SCRIPT FOR DETERMINING LOCATIONS OF AMS SAMPLES.....		181
APPENDIX B. MATLAB SCRIPT FOR CALCULATING PRINCIPAL VECTORS OF AND ORIENTATION TENSOR		184
APPENDIX C. TEST FOR SYMMETRICAL DISTRIBUTION OF ORIENTATIONS ABOUT A POLE.....		190
APPENDIX D. MAGNETIC MINERALOGY DISCUSSION		192
D.1	Múlajökull	192
D.2	Breiðamerkurjökull till.....	194
D.3	B14-F1, Site A Black Sand	196

LIST OF FIGURES

Figure 1-1. Examples of glacial flutes.	2
Figure 1-2. Examples of methods used to analyze and display flute clast fabrics.	7
Figure 1-3. (A) A plan-view illustration of the orientation of a “parallel” fabric pattern in a flute. (B) A plan –view illustration of “herringbone” fabric pattern in a flute.	8
Figure 1-4. Illustration of the cavity infilling by till proposed as part of both the cavity propagation and freeze-on hypotheses.	10
Figure 1-5. An illustration of the freeze-on hypothesis	11
Figure 1-6. An illustration of the cavity propagation hypothesis.	14
Figure 1-7. The relationships between first, Magnetization, M , and magnetic field magnitude, H , and second, magnetic susceptibility, χ , and temperature, T ,	18
Figure 1-8. An illustration of the alignment of electron spins and the associated magnetization of different classes of magnetic materials	19
Figure 1-9. Domain size of magnetite as a function to grain shape.	24
Figure 1-10. Figure from Boulton (1976) showing the distribution, orientation, and magnitude of individual AMS ellipsoids of till samples from a flute	26
Figure 2-1. Maps of the Hofsjökull ice cap	29
Figure 2-2. (A) Map of Iceland with the location of Múlajökull marked by a red dot. (B) Graph of the distance of the Múlajökull margin from a datum over time, with surge events indicated. (C) Oblique aerial photograph of Múlajökull looking northwest with major geographical landmarks noted....	30
Figure 2-3. Landform map of the Múlajökull forefield	31
Figure 2-4. Generalized geological maps of	32
Figure 2-5. Map of the Vatnajökull ice cap with ice flow basins of outlet glaciers delineated.....	33
Figure 2-6. Map of Breiðamerkurjökull,.....	34
Figure 2-7. Smaller scale reproduction of the 1:30,000 map of Breiðamerkurjökull and part of Fjallsjökull forefields.....	36
Figure 2-8. Landform map of the western Breiðamerkurjökull forefield	37
Figure 3-1. Photographs depicting the collection of AMS samples	42
Figure 3-2. View of flute M13-F1 looking downglacier.	43
Figure 3-3. Plan view sketch of flute M13-F1, with sampling area indicated.	44
Figure 3-4. View of the boulder at the head of flute M14-F1 looking southwest.	45
Figure 3-5. View of flute M14-F1 looking upglacier.	46

Figure 3-6. Plan view sketch of flute M14-F1, with sampling sites indicated.	46
Figure 3-7. View of flute M14-F2 looking to the south.....	48
Figure 3-8. View of flute M14-F2 looking downglacier.	48
Figure 3-9. (A) View looking downglacier of M14-F2 and other flutes in the same “swarm.” (photo credit: Lucas Zoet). (B)View looking upglacier of several flutes emerging from beneath Múlajökull near M14-F2. Meltwater flows in the depressed areas on either side of the flutes and is carrying sediment in suspension.	49
Figure 3-10. Plan view sketch of flute M14-F2, with sampling sites indicated.	49
Figure 3-11. View of flute B14-F1 looking downglacier.	51
Figure 3-12. View looking northeast of the boulder at the head of flute B14-F1.....	52
Figure 3-13. Deformed sand body in flute B14-F1 immediately downglacier of the flute’s stoss-end boulder.....	52
Figure 3-14. Plan view sketch of flute B14-F1, with sampling sites indicated.	52
Figure 3-15. View of flute B14-F2’s stoss-end boulder looking northeast.	53
Figure 3-16. View of flute B14-F2 looking downglacier. This flute is located on a densely fluted surface.....	54
Figure 3-17. Plan view sketch of flute B14-F2, with sampling sites indicated.	54
Figure 3-18. Volume normalized susceptibility (SI) vs. weight percent of mineral.....	57
Figure 3-19. Normalized in-phase susceptibility curves of synthetic titanomagnetites during warming from 15 K to 300 K.....	60
Figure 3-20. Behavior of idealized ferrimagnetic grains and associated magnetic hysteresis curve.	64
Figure 3-21. Day plots from Dunlop (2002) showing how hysteresis parameters can be a function of not only magnetic domain type but also of the degree of mixing between magnetic domain type and of magnetic grain size.....	65
Figure 3-22. Idealized hysteresis loops of end-member behaviors:.....	66
Figure 3-23. An uncorrected hysteresis curve (solid line) with a substantial high-field susceptibility (χ_{hf}).....	68
Figure 3-24. How a FORC is measured.	69
Figure 3-25. FORC diagrams.....	70
Figure 3-26. FORC diagrams have different contours depending on the magnetic grain sizes (domain states).....	71
Figure 3-27. Visualizations of AMS measurements	72
Figure 3-28. Bivariate Flinn plot of the lineation (P_1) vs. foliation (P_3) of an AMS ellipsoid.	75

Figure 3-29. (A) Plan view and (B) cross sectional view of a “standard” flute with the orientation and magnitudes of the normalized, three-dimensional flute coordinate system used in this study.	77
Figure 3-30. A Benn ternary diagram.	80
Figure 3-31. Woodcock biaxial logarithmic plot.	81
Figure 3-32. Examples of typical k_1 , k_2 , and k_3 AMS axial orientations displayed on lower hemisphere, equal area stereonet.	83
Figure 3-33. The decision tree used to determine the best analysis AMS orientation data.	89
Figure 3-34. Visualizations of AMS fabric end-member shapes.	90
Figure 4-1. Normalized susceptibility vs. temperature heating curves	97
Figure 4-2. In-phase susceptibility vs. low temperature curves.	99
Figure 4-3. Normalized SIRM on cooling from 300 to 20 k (Room Temperature Remanence on Cooling) and Normalized SIRM on warming from 20 to 300 k (Zero Field Remanence on Warming) curves	101
Figure 4-4. Magnetic hysteresis curves of bulk sediment samples.	103
Figure 4-5. Day plots displaying magnetic hysteresis parameters.	107
Figure 4-6. First Order Reversal Curves.	108
Figure 4-7. (A) Plan and longitudinal views of flute M13-F1, with the approximate mean location of samples used in each fabric indicated. (B) AMS fabrics and fabric analysis results from flute M13-F1.	110
Figure 4-8. (A) Plan and longitudinal views of flute M14-F1, with the approximate mean location of samples used in each fabric indicated. (B) AMS fabrics and fabric analysis results from flute M14-F1. (C) Corrected shear plane attitudes and pole-to-plane confidence intervals derived from AMS fabrics of flute M14-F1.	113
Figure 4-9. (A) Plan and longitudinal views of flute M14-F2, with the approximate mean location of samples used in each fabric indicated. (B) AMS fabrics and fabric analysis results from flute M14-F2. (C) Corrected shear plane attitudes and pole-to-plane confidence intervals derived from AMS fabrics of flute M14-F2.	117
Figure 4-10. (A) Plan and longitudinal views of flute B14-F1, with the approximate mean location of samples used in each fabric indicated. (B) AMS fabrics and fabric analysis results from flute B14-F1. (C) Corrected shear plane attitudes and pole-to-plane confidence intervals derived from AMS fabrics of flute B14-F1.	122
Figure 4-11. (A) Plan and longitudinal views of flute B14-F2, with the approximate mean location of samples used in each fabric indicated. (B) AMS fabrics	

and fabric analysis results from flute B14-F2. (C) Corrected shear plane attitudes and pole-to-plane confidence intervals derived from AMS fabrics of flute B14-F2.	126
Figure 4-12. AMS fabrics from B14-F1, site A, immediately downglacier from the headward boulder.	130
Figure 4-13. Fabric analysis of AMS principal susceptibilities from flutes M14-F1, M14-F2, B14-F1 (excluding site A), and B14-F2, referenced to flute axes	133
Figure 4-14. Uncorrected shear orientations derived from AMS fabrics referenced to the flute axes, grouped by their position in flutes, and plotted on rose diagrams	135
Figure 4-15. Variations in dry bulk density of AMS samples along the x, y, and z axes of flutes.....	136
Figure 4-16. Mean densities and standard deviations (error bars, ± 1 S.D.) of individual AMS fabrics grouped by fabric shape.....	140
Figure 4-17. (A) Cumulative grain size distributions for bulk sediment sample fractions of < 4 mm, from locations in flute M14-F1 shown in (B).....	143
Figure 4-18. (A) Cumulative grain size distributions for bulk sediment sample fractions of < 4 mm, from locations in flute M14-F2 shown in (B).....	144
Figure 4-19. Cumulative grain size distributions for bulk sediment sample fractions of < 4 mm from B14-F1, site A.	145
Figure 4-20. Fabrics regrouped by flute position (A, center, and B) and referenced to a common flute orientation, based on 2594 pebble orientations compiled from 83 fabrics measured in five different glacier forefields.....	147
Figure 4-21. Uncorrected shear orientations derived from pebble fabrics in flutes and referenced to a common flute orientation from five different glacier forefields.....	149
Figure 5-1. Transverse cross-section of a flute in the forefield of Isfallsglaciären, Sweden.	156
Figure 5-2. Illustration of the flute formation model outlined in the text	157
Figure 5-3. Examples of headward boulders of flutes with extensive quarrying	162
Figure A-1. (A) AMS sampling platform in a flute at Múlajökull. (B) The same photograph imported into the Matlab program described in this appendix, with all of the boxes marked by open, red circles.	181
Figure D-1. Absolute difference in normalized susceptibility of heating and cooling curves vs. temperature	197

LIST OF TABLES

Table 3-1. Some generalized properties of ferromagnetic minerals	56
Table 3-2. AMS fabric data from tills sheared in ring-shear experiments	86
Table 4-1. Hysteresis parameters for sediment samples from Múlajökull and Breiðamerkurjökull.	102
Table 4-2. AMS fabric results from flute M13-F1	112
Table 4-3. AMS fabric results from flute M14-F1	116
Table 4-4. AMS fabric results from flute M14-F2	120
Table 4-5. AMS fabric results from flute B14-F1	125
Table 4-6. AMS fabric results from flute B14-F2	129
Table 4-7. AMS fabric results from flute B14-F2, site A	131
Table 4-8. AMS fabric results from flute fabrics displayed in Figure 4-13	134
Table 4-9. Mean and standard deviation of sediment dry bulk density by fabric shape.	141
Table 4-10. Grain size data for sediment in and adjacent to flutes. Size fraction is reported in mass percent.	146
Table 4-11. Flute pebble fabrics displayed in Figure 4-20	148

LIST OF TERMS AND ABBREVIATIONS

AMS	anisotropy of magnetic susceptibility
B	applied magnetic field [T]
B_c	coercive field [T]
B_{cr}	coercivity of remanence [T]
B_u	Bias Field [T], y-axis of FORC diagram, function of H_A and H_B
C	$= \ln(S_1/S_3)$ (Woodcock, 1977)
C^*	Curie constant, material specific [K or °C]
CGI	cluster-girdle index (Benn, 1994a)
D	height of the flute's stoss-side boulder
D^*	declination of orientation vector
E	Elongation index (Benn, 1994a)
FORC	first-order reversal curve
F	F statistic to test for total significance anisotropy in a single AMS ellipsoid
F_{12}	F statistic to test for significance between the principal and intermediate susceptibility axes in a single AMS ellipsoid
F_{23}	F statistic to test for significance between the minimum and intermediate susceptibility axes in a single AMS ellipsoid
F_W	Watson probability density function
GSD	grain-size distribution
H	applied magnetic field [T]
H_{SAT}	saturating magnetic field [T]
H_A	FORC measurement, some magnetic field less-than and opposite H_{SAT}
H_B	FORC measurement, some magnetic field less-than H_{SAT} in the same direction
H_c	x-axis of FORC diagram, function of H_A and H_B
H_u	y-axis of FORC diagram, function of H_A and H_B
I	Isotropy index (Benn, 1994a)
I^*	inclination of orientation vector
I_n	3 x 3 identity matrix
K	$= (r_2/r_1)$ (Woodcock, 1977)
L	length of the flute

LIA	Little Ice Age
M	magnetization [T]
M_{rs}	saturation remanence [T]
MD	multi-domain
MPMS	Magnetic Property Measurement System
M_s	saturation magnetization [T]
N	number of samples
P	cute angle bisection k_1 and k_2 girdle planes
P_j	corrected degree of anisotropy of an AMS ellipsoid
P_w	pore water pressure [kPa]
P_1	lineation of AMS ellipsoid
P_3	foliation of AMS ellipsoid
PDF	probability density function
PSD	pseudo-single-domain
\mathbf{T}	second-rank, symmetric orientation tensor
T	shape parameter of an AMS ellipsoid
T	temperature [K or °C]
T_C	Curie temperature [K or °C]
T_N	Néel temperature [K or °C]
T_v	Verwey transition [~120 K in magnetite]
T_i	magnetic isotropic point [~130 K in magnetite]
Ti	Titanium
R	resultant vector length
SD	single-domain
SIRM	saturation isothermal remanence magnetization
S_x	where $x = 1, 2$, or 3 ; normalized eigenvalues (λ_x) of \mathbf{T}
S_o	residual sum of squares
SP	superparamagnetic
V_x	where $x = 1, 2$, or 3 ; eigenvectors of \mathbf{T}
VSM	vibrating sample magnetometer
W	width of the flute

a1	sample axis parallel to sampling surface (AMS)
a2	sample axis perpendicular to a1 and a3 (AMS)
a3	sample axis perpendicular to sampling surface (AMS)
a.s.l	above sea level
c	cohesion [kPa]
\mathbf{k}_{ij}	symmetric, second rank magnetic susceptibility tensor
k	magnetic susceptibility [SI]
k_x	where $x = 1, 2$, or 3 ; principal susceptibilities of \mathbf{k}_{ij}
k'	in-phase magnetic susceptibility [SI]
k_m	volume-normalized bulk susceptibility [SI]
k_{para}	paramagnetic susceptibility
m.y.a.	million years ago
n	porosity
n_f	degrees of freedom
r_1	$= \ln(S_2/S_3)$ (Woodcock, 1977)
r_2	$= \ln(S_1/S_2)$ (Woodcock, 1977)
<i>s.l.</i>	<i>senu lato</i>
<i>s.s.</i>	<i>sensu strictu</i>
x	real measurement of AMS sample position along the flute's long axis
x'	corrected measurement of AMS sample position along the flute's long axis
x_i	where $i = 1, 2$, or 3 ; directional cosines of vector orientations
y	real measurement of AMS sample position across the flute's width
y'	corrected measurement of AMS sample position across the flute's width
z	real measurement of AMS sample depth
z'	corrected measurement of AMS sample depth
α	difference between a given direction and axis of symmetry (Bingham PDF)
β	angle of high-field hysteresis slope from the horizontal
λ_x	where $x = 1, 2$, or 3 ; eigenvalue of orientation tensor \mathbf{T}
θ	angular difference from the axis of symmetry (Watson PDF)
θ_b	angular difference from axis of symmetry in V_1 - V_2 plane (Bingham PDF)

κ	shape parameter for a probability density function
κ'	$\cong \frac{N-1}{N-R}$; estimate for shape parameter
κ_1	concentration parameter 1 for Bingham PDF
π	pi
$\overline{\rho_b}$	average bulk dry density [kg m^{-3}]
σ_v	estimate variance
σ'	past maximum effective stress [kPa]
σ	total normal stress [kPa]
τ_s	shear strength
τ_x	where $x = 1, 2$, or 3 ; eigenvalues of \mathbf{k}_{ij}
ϕ	angular difference from axis of symmetry in V_2 - V_3 plane (Bingham PDF)
φ	angle of internal friction
χ	magnetic susceptibility (alternative) [SI]
$\chi_{antiferro}$	antiferromagnetic susceptibility
χ_{dia}	diamagnetic susceptibility
χ_{FD}	frequency dependence of magnetic susceptibility
χ_{ferri}	ferrimagnetic susceptibility
χ_{HF}	high- frequency field magnetic susceptibility
χ_{hf}	high-magnitude field magnetic susceptibility
χ_{LF}	low-frequency field magnetic susceptibility
χ_m	mass-normalized bulk susceptibility [m^3kg^{-1}]
χ_{para}	paramagnetic susceptibility

ACKNOWLEDGEMENTS

There are many people to who I owe thanks, because without them this thesis and my graduate school experience would not have been the same. My gratitude goes out:

To the institutions that supported this research: The Geological Society of America, for granting me means to have a second field site at Breiðamerkurjökull; Mike Jackson and the other faculty, scientists, and students at the University of Minnesota Institute for Rock Magnetism for allowing me to use their machines, software, and knowledge; and Vatnajökull National Park, for allowing me to dig up a couple of their flutes.

To Tom, for giving me opportunities to learn, travel, and grow.

To the graduate students, faculty, and staff at UW-Milwaukee, especially Julie Bowles and John Isbell, for your camaraderie and mentorship.

To the field crews of Múlajökull and Breiðamerkurjökull, without whom this work would have been impossible.

To Neal, for taking me on under unfortunate circumstances and giving me the time and guidance to do the best science I possibly could.

To Al and Pete, whose feedback and thoughts have much improved this thesis.

To the many friends I have made in Ames - I never thought I would ever live in the middle of Iowa, but, because of you, I'm glad I got the chance.

To Reba and Geoff for, well, you know, everything.

To my parents for the means, support, and love that have given me priceless experiences and allowed me to pursue my goals.

And, finally, to Patrick, my dear husband, without whom I'd be making my exit from graduate school much more the worse for wear. Thank you for keeping my feet on the ground and head screwed on, often through brute force of will; for always seeing the best in people and situations so that I might look a little closer; and for your unwavering support. I'm excited for our next adventure!

Thank you.

ABSTRACT

Flutes are low-relief, elongate landforms that form subglacially and parallel to the glacier flow direction. They usually consist of till and have boulders at their heads. Flutes can be pervasive in the forefields of glaciers and contain information about the role of bed deformation in basal slip. There are two leading hypotheses for their formation that involve cavity formation in the presence of a deformable bed: the freeze-on hypothesis, in which till that flowed into a cavity downstream from a boulder is frozen into the glacier sole, transported downstream in ice, and then redeposited at the downstream end of the flute, and the cavity–propagation hypothesis, in which till flows into a cavity that begins in the lee of a boulder but propagates downstream in the lee of the flute as it builds downstream with time.

Five flutes were studied at two temperate, surge-type outlet glaciers in Iceland, Múlajökull and Breiðamerkurjökull, by measuring fabrics based on anisotropy of magnetic susceptibility (AMS) and till matrix densities to infer past strain patterns. To increase the robustness of AMS measurements, a new method for characterizing AMS ellipsoids, calibrated to laboratory ring-shear fabrics, was used, and the magnetic mineralogy of the till was determined with a series of geomagnetic tests, many of which have not before been applied to tills. Flute pebble fabrics from the literature were also re-analyzed.

The magnetic susceptibility of the Múlajökull and Breiðamerkurjökull tills is dominated by pseudo-single-domain titanomaghemite and magnetite, respectively, allowing for a straight-forward interpretation of AMS fabrics. When referenced to a

single flute orientation, both AMS fabrics from this study and pebbles fabrics from the literature show that convergent fabrics dominate flutes. Locally, however, AMS fabric orientations are highly variable and had shapes that indicate low-to-moderate shear strains (less than, or not much in excess of, ~ 7). More importantly, till matrix densities, which are a proxy for past maximum effective stress, are significantly higher in the middle of flutes than at their sides. The difference in densities across the width of flutes was much larger in a parallel-sided flute than in a tapered one.

Together, these data indicate that flutes form by cavity propagation (e.g., [Benn \(1994b\)](#)) that requires unsteady, subglacial water pressures and sliding speeds for fluted till to strengthen sufficiently to propagate a cavity downstream. Flutes are initiated and grow through flow of weak till into cavities during periods of high subglacial water pressure and sliding speed. Newly accreted till at a flute's end is then compacted and hence strengthened during a subsequent period of lower subglacial water pressure and sliding speed when water pressure in the leeward cavity falls and the stress that ice exerts downward on the till increases. This effect accounts for high till density near the middle of flutes where cavities were longest and stress increases largest when water pressure fell, and also accounts, through strengthening of till, for the preservation of transverse fabric components in an environment dominated by flow-parallel shear. The strengthened till provides the rigid take-off point for a cavity during subsequent glacier acceleration and thereby allows the flute to grow downstream. Long, parallel-sided flutes and short, tapered flutes are likely end-members of a continuum and represent a high and low degree of till strengthening, respectively, during periods of low water pressure. Flute formation and growth may be influenced by the hydraulic diffusivity of till, and therefore

by its texture, which controls the rate and magnitude of effective stress increases during decreases in basal water pressure.

CHAPTER 1. INTRODUCTION

1.1 Glacial flutes

1.1.1 Definition and description

Flutes are low-relief elongate, landforms that form subglacially and are streamlined in the direction of glacier flow ([Fig. 1-1](#)) ([Dyson, 1952](#); [Hoppe and Schytt, 1953](#); [Boulton, 1976](#); [Morris and Morland, 1976](#); [Benn, 1994b](#); [Benn and Evans, 2010](#)). Their sedimentary composition is typically similar to that of adjacent material. They are most often composed of unsorted diamicton ([Dyson, 1952](#); [Hoppe and Schytt, 1953](#); [Boulton, 1976](#); [Åmark, 1980](#); [Karlén, 1981](#); [Benn, 1994b, 1995](#); [Glasser and Hambrey, 2001](#); [Roberson et al., 2011](#); [Eyles et al., 2015](#)) but can also include sorted material ([Boulton, 1971](#); [Paul and Evans, 1974](#); [Eklund and Hart, 1996](#)). With few exceptions, flutes form on the lee side of lodged boulders with widths and heights proportional to those of the flute ([Dyson, 1952](#); [Boulton, 1976](#); [Åmark, 1980](#); [Benn and Evans, 2010](#)). Flutes are bordered on either side by shallow, cm-scale troughs ([Dyson, 1952](#); [Boulton, 1976](#); [Rose, 1989](#); [Benn, 1994b](#)). Flutes can range from one meter to one kilometer in length ([Boulton, 1976](#); [Åmark, 1980](#); [Gordon et al., 1992](#); [Benn and Evans, 2010](#)) and can either be parallel-sided, meaning their height and width are constant throughout its length, or tapered, meaning that its height and width gradually decrease downglacier ([Benn and Evans, 2010](#)).

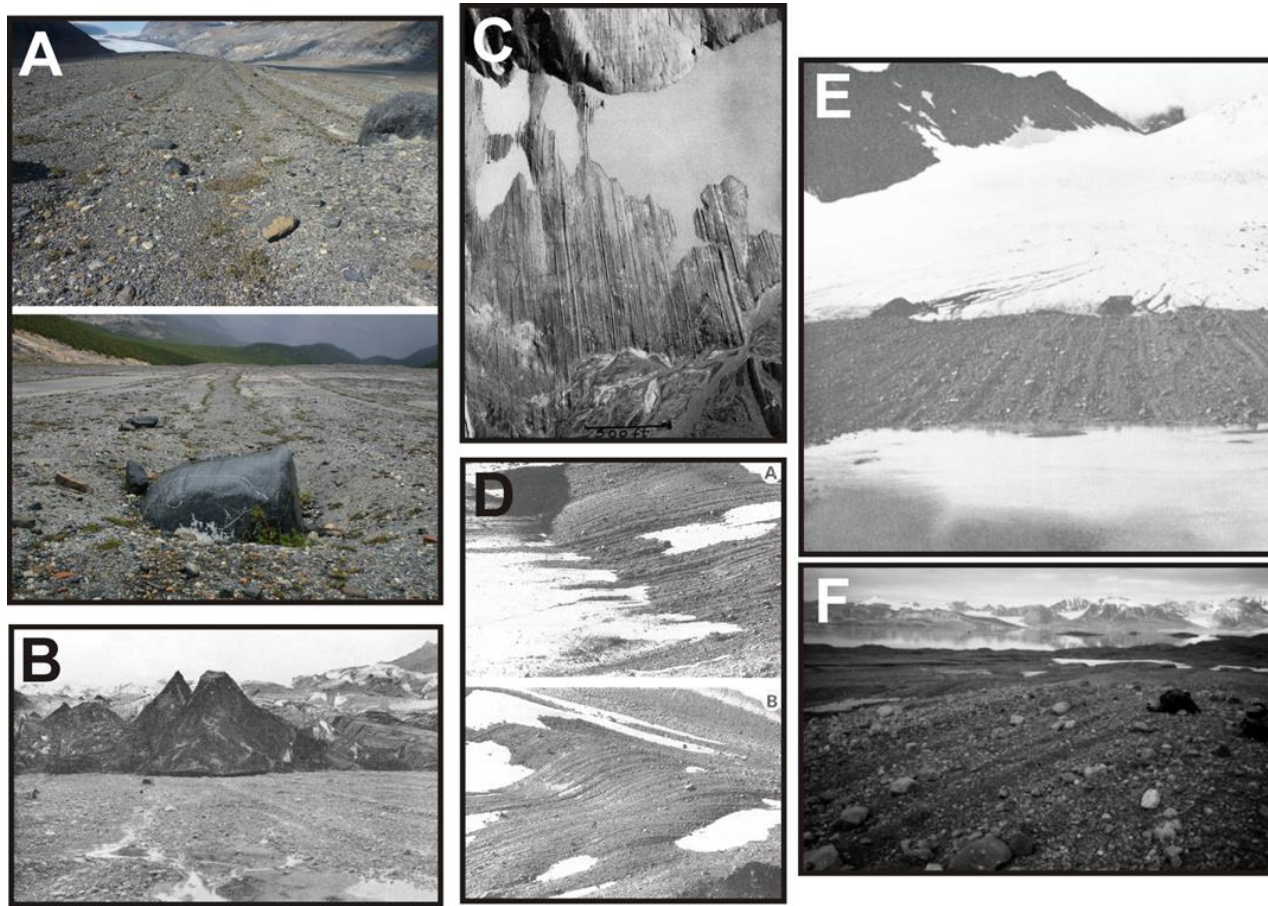


Figure 1-1. Examples of glacial flutes. (A) The fluted forefield of Saskatchewan Glacier, Canada ([Eyles et al., 2015](#)). (B) Small flutes (left side of picture) in front of Fláajökull, Iceland ([Hoppe and Schytt, 1953](#)). (C) Flutes dominating the forefield of Woodworth Glacier, Alaska ([Dyson, 1952](#)). (D) (A) Ice-proximal and (B) ice-distal portions of the “Flutes Glacier” forefield, Lyngsdalen, Norway ([Gordon et al., 1992](#)). (E) Flutes in front of Isfallsglaciären, Sweden ([Schytt, 1959](#)). (F) Flutes in the forefield of Midtre Lovénbreen, Svalbard ([Glasser and Hambrey, 2001](#))

Flutes are ubiquitous landforms in the forefields of valley glaciers. They are prevalent in recently deglaciated areas of alpine regions in Iceland ([Boulton, 1976](#); [Evans et al., 2010](#)), Canada ([Eyles et al., 2015](#)), Alaska ([Hart and Smith, 1997](#)), the conterminous United States ([Dyson, 1952](#)), Sweden ([Hoppe and Schytt, 1953](#)), mainland Norway ([Rose, 1989](#); [Gordon et al., 1992](#)), Svalbard ([Paul and Evans, 1974](#)), Switzerland ([Van der Meer, 1997](#)), New Zealand ([Kirkbride, 2000](#)), and Argentina ([Nichols and Miller, 1952](#)). Flutes tend to occur in groups that can occupy large areas of glacier forefields, from tens to hundreds of square kilometers ([Boulton, 1976](#)). Within a group, or “swarm,” flutes tend to have similar heights, widths, shapes, and compositions, and may be separated by up to 10 meters ([Dyson, 1952](#); [Hoppe and Schytt, 1953](#); [Boulton, 1976](#)). Both soft- and hard-bedded glaciers and both warm-based and polythermal glaciers have given rise to flutes ([Schytt, 1959](#); [Glasser and Hambrey, 2001](#); [Roberson et al., 2011](#)). Flutes can be superimposed on moraines, drumlins, outwash gravels, glaciofluvial sediment, and bedrock surfaces ([Boulton, 1976](#); [Karlén, 1981](#); [Rose, 1989](#); [Gordon et al., 1992](#)).

[Rose \(1987\)](#) suggested that small-scale flutes are part of a continuum of streamlined, subglacial landforms whose sizes are a function of ice thickness and velocity, with a similar mechanism of formation at all scales. This continuum is also proposed to include drumlins and mega-scale lineations. In contrast, several studies of flutes have suggested that for such a continuum, the dominant mechanism for the formation of these landforms is likely scale dependent ([Gordon et al., 1992](#); [Schoof and Clarke, 2008](#); [Roberson et al., 2011](#)). Owing to the lack of a conclusive formation mechanism for flutes, either small or large, both claims are conjectures ([Schoof and Clarke, 2008](#)). The small-scale flutes

addressed in this study were considered independently of a continuum because many of the processes invoked in their formation cannot be feasibly scaled up for large flutes.

1.1.2 Sediment fabrics of tills

The interaction between a glacier and its bed is recorded in a till's composite strain history. For subglacial sediments with no primary structures, such as massive diamictos, strain history can be inferred only through proxies that characterize that sediment's anisotropy ([Benn and Evans, 1996](#)). As sediments deform, sedimentary particles rotate and move to accommodate stress. At sufficient strains, particles become oriented in ways that reflect strain type and orientation. Thus, the preferred orientation of particles in sediment, called a sediment fabric, can be used to infer past strain conditions. For example, when sediment experiences simple shear, which is predominant in subglacial environments, most prolate particles rotate until their long axes are parallel to flow and plunge slightly upglacier ([Thomason and Iverson, 2006](#)). The strain experienced by tills can, therefore, be inferred by measuring the orientation of elongate sedimentary particles.

Sediment fabrics can be measured through the preferred orientation of the material's matrix (*microfabric*) or by the orientation of the material's coarse fraction (*macrofabric*). Sediment microfabrics can be characterized by either directly measuring grain orientations in thin section optically ([Menzies and Maltman, 1992](#); [Van der Meer, 1993](#); [Van der Wateren, 1999](#); [Thomason and Iverson, 2006](#)) or with a scanning electron microscope ([Derbyshire et al., 1976](#)), or indirectly by measuring the sediment's anisotropy of magnetic susceptibility (AMS) ([Fuller, 1962](#); [Boulton, 1976](#); [Eyles et al., 1987](#); [Hooyer et al., 2008](#); [Iverson et al., 2008](#)). Sedimentary macrofabrics, which are

also called “clast fabrics” or “pebble fabrics,” are characterized by measuring the *in situ* orientations of elongate pebble-sized clasts ([Evans and Benn, 2004](#)).

Till macrofabrics have long been used to identify glacier flow direction ([Holmes, 1941](#)). More recently they have been used to distinguish till from other diamictos and differentiate among various subglacial landforms and depositional processes ([Mark, 1974](#); [Dowdeswell and Sharp, 1986](#); [Benn, 1995](#); [Hicock et al., 1996](#); [Van der Meer et al., 2003](#)), and infer magnitudes of subglacial shear strain ([Hooyer and Iverson, 2002](#)). At the scale of a glacier’s forefield, macrofabrics of till tend to align in the direction of paleo ice flow ([Holmes, 1941](#)). Variability in a glacier’s basal depositional processes can lead to differences in fabric shape and orientation in discrete till units and landforms ([Benn and Evans, 1996](#); [Van der Meer et al., 2003](#)). In glacial sediments, the information provided by microfabrics agrees closely with macrofabrics collected from the same location ([Fuller, 1962](#); [Gentoso et al., 2012](#)). Fabric data are also consistent among microfabric techniques ([Thomason and Iverson, 2006](#); [Shumway and Iverson, 2009](#)).

The clast-fabric method has long been the most popular for characterizing till fabrics, as it is inexpensive, requires little equipment, and is well accepted. However, fabrics measured in this way, as well measured from thin sections, are subject to human error and bias when selecting particles. AMS measurements remove most of that subjectivity and also supply data that can be used to interpret strain type and magnitude ([Hooyer et al., 2008](#)). The three principal directions of magnetic susceptibility provide AMS fabrics that contain more information of about strain type and orientation than only the long axes of particles ([Shumway and Iverson, 2009](#); [Ankerstjerne et al., 2015](#); [Vreeland et al., 2015](#)). Variability in AMS fabrics is minimized because each AMS measurement of a

small sample cube ($\sim 5.1 \text{ cm}^3$) characterizes the volume-averaged orientation of potentially thousands of magnetic particles as opposed to individual sediment particles. AMS also allows for a large number of samples to be measured quickly and inexpensively in the laboratory, provided a susceptibility bridge is available ([Hooyer et al., 2008](#); [Iverson et al., 2008](#)). There are also limitations to using AMS to characterize till fabrics. For example, the magnetic mineralogy of the till may limit the usefulness of susceptibility measurements. AMS sampling density and ease depend on grain-size distribution and are reduced in stony tills.

An objective of this study was to use AMS fabrics to characterize strain orientation and type in small-scale flutes and compare the results to previously published clast-fabric data from flutes.

1.1.2.1 Clast fabric studies of flutes

Many studies of flutes have used pebble fabrics to characterize their strain history and thereby infer a mechanism for flute formation ([Boulton, 1976](#); [Lawson, 1979](#); [Åmark, 1980](#); [Rose, 1989](#); [Gordon et al., 1992](#); [Benn, 1994b](#); [Eklund and Hart, 1996](#); [Evans et al., 2010](#); [Eyles et al., 2015](#)). In these studies fabrics were measured in flutes of variable sizes, ages, morphologies, landscape positions, and glacier thermal regimes, with numbers and positions of fabrics varying widely. Additionally, in each study, fabric data were reported and analyzed in different ways ([Fig. 1-2](#)). Unsurprisingly, these studies of flute macrofabrics have not converged on an answer to the problem of flute formation, undoubtedly in part due to the diversity of flutes studied and analytical techniques used.

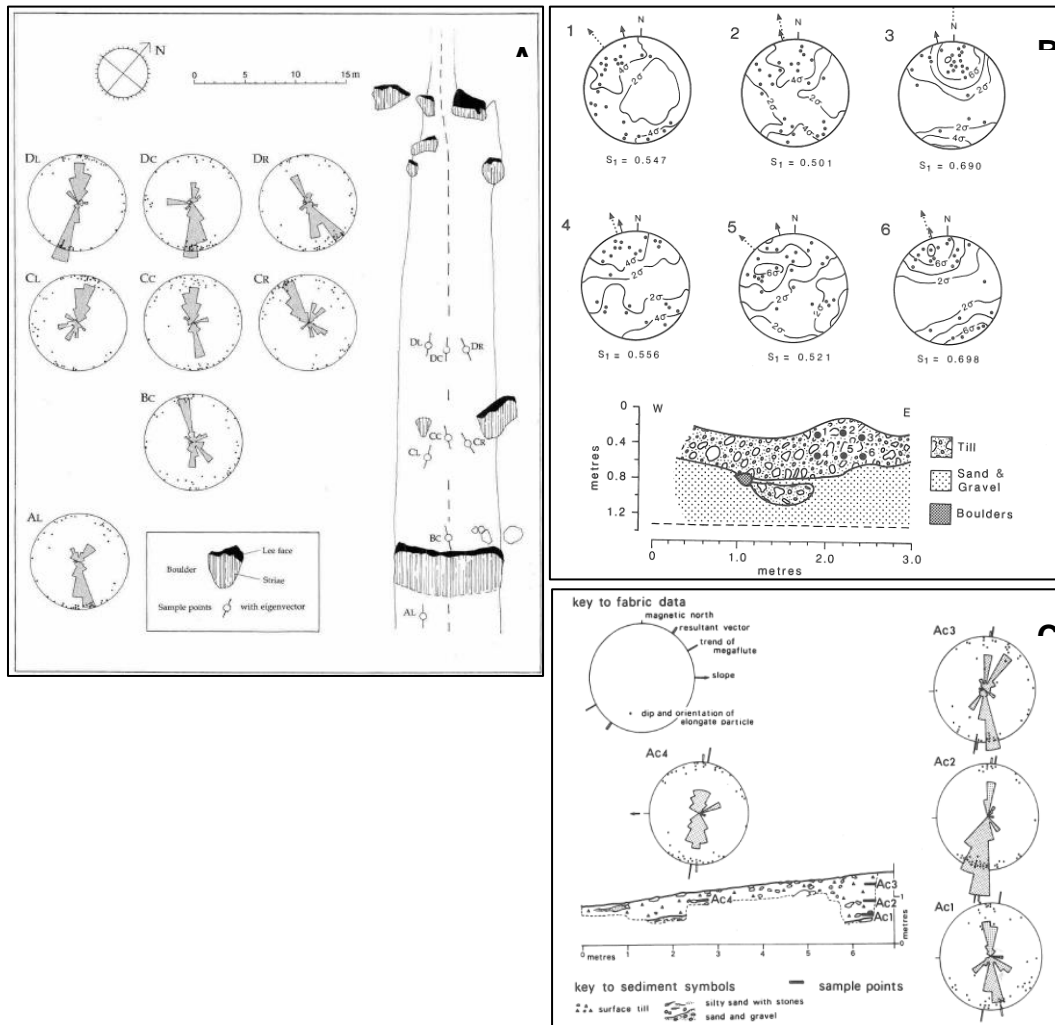


Figure 1-2. Examples of methods used to analyze and display flute clast fabrics. (A) [Benn \(1994b\)](#) represented the trend of each fabric with its eigenvector. Eigenvectors are found using a principal orientation tensor analysis. To show the variation in clast orientations within each fabric, rose diagrams and orientation measurements were plotted on lower-hemisphere stereonets. (B) [Gordon et al. \(1992\)](#) also used principal orientation tensor analysis to determine the primary trend of each fabric (dashed arrow). The solid arrows indicate the former ice movement direction. To characterize the spread of clast orientations in each fabric, [Gordon et al. \(1992\)](#) used [Kamb \(1959\)](#) contours and orientation measurements on lower hemisphere stereonets as well as S_1 eigenvalues found using the principal orientation analysis. (C) [Rose \(1989\)](#) calculated the resultant vector of the clast orientations in each fabric and used the resultant vector's azimuth to characterize the fabric's orientation. To show the variation of clast orientations in each fabric, rose diagrams and orientation measurements were plotted on lower-hemisphere stereonets.

A number of analytical techniques have been used to characterize flute pebble fabrics. Pebble orientations have typically been plotted on lower hemisphere, equal-area (Schmidt) stereonet. These stereonet have been almost always accompanied by rose diagrams and/or contour intervals, which allow the reader to qualitatively examine fabric orientation and strength. By far the most common quantitative method of describing pebble fabric orientation is the principal orientation tensor analysis, or “eigenvalue” method ([Mark, 1973](#); [Woodcock, 1977](#); [Lawson, 1979](#); [Gordon et al., 1992](#); [Benn, 1994a, b](#); [Eklund and Hart, 1996](#); [Evans et al., 2010](#); [Eyles et al., 2015](#)). Other numeric orientation analyses of flute macrofabrics exist in the literature (e.g., ([Rose, 1989](#)) ([Fig. 1-2c](#))). Thus, directly comparing reported fabric orientations from flute studies is difficult.

Despite the incongruity of the flute literature, the fabrics of most flutes can be classified as either “herringbone” or “parallel” ([Fig. 1-3](#)). A herringbone pattern has flute-parallel fabrics at its center and fabrics near its sides that converge on the flute’s central axis ([Fig. 1-3A](#)) ([Boulton, 1976](#); [Rose, 1989](#); [Benn, 1994b](#)). Parallel-flute fabrics are oriented parallel to the flute’s central axis everywhere ([Fig. 1-3B](#)) ([Gordon et al., 1992](#); [Hubbard and Reid, 2006](#)). No matter the trend of the pebble fabrics measured in flutes, the plunge of the fabric is usually near zero.

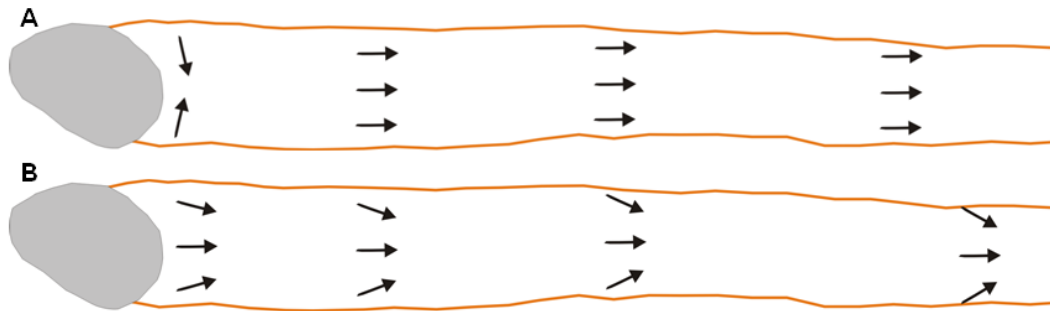


Figure 1-3. (A) A plan-view illustration of the orientation of a “parallel” fabric pattern in a flute. (B) A plan-view illustration of “herringbone” fabric pattern in a flute.

1.1.3 Hypotheses for flute formation

The mechanism of flute formation is poorly understood because subglacial processes are difficult to observe directly. Hypotheses for flute formation are, therefore, based on clast fabric data and the modeling of subglacial processes. Although numerous hypotheses have been suggested to explain flute formation, two are commonly invoked: the freeze-on ([Schytt, 1963](#); [Roberson et al., 2011](#)) and cavity propagation ([Åmark, 1980](#); [Benn, 1994b](#)) hypotheses. These hypotheses share two points: (1) that cavities in basal ice caused by the presence of lodged boulders are necessary to initiate flute formation ([Fig. 1-4](#)) and (2) that flutes do not form instantaneously along their entire length but instead have sediment added to them incrementally ([Fig. 1-5](#) and [1-6](#)). Other hypotheses for flute formation include the streamlining of debris-rich basal ice ([Gordon et al., 1992](#)) and a combination of unspecified sediment transport mechanisms and melt-out of basal debris ([Rose, 1989](#)). Authors often note that none of these mechanisms likely acts exclusively and that many flutes cannot be explained by a particular hypothesis ([Åmark, 1980](#); [Gordon et al., 1992](#); [Benn, 1994b](#); [Roberson et al., 2011](#)).

Flute Initiation

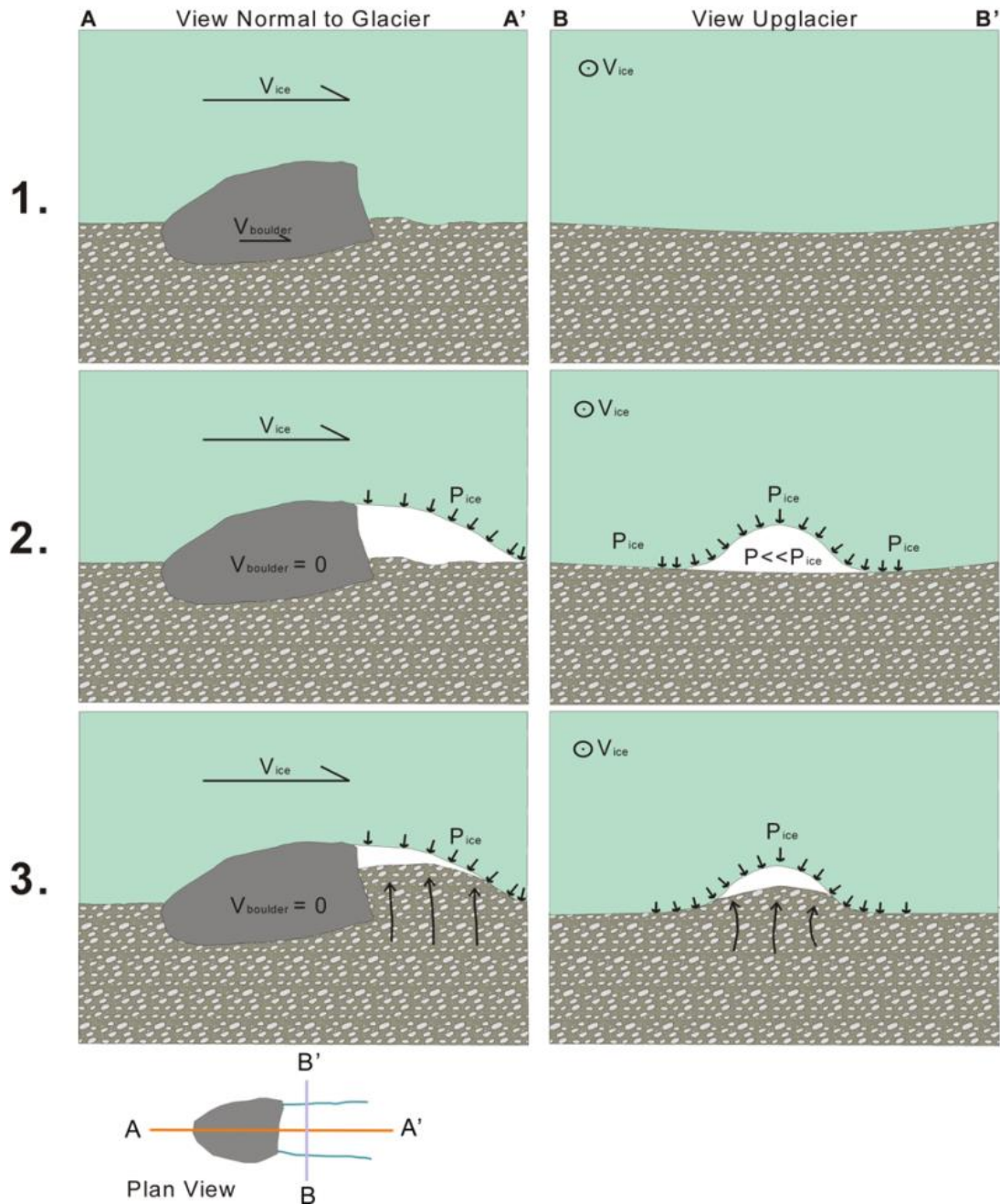


Figure 1-4. Illustration of the cavity infilling by till proposed as part of both the cavity propagation and freeze-on hypotheses. (1) Once a boulder becomes lodged in the subglacial sediment, it becomes an obstruction of the flow of basal ice. (2) A cavity in the ice will then form in the lee of an obstruction at the base of a glacier, so long as the sliding velocity of the ice is greater than the rate of ice creep downward toward the lee side of the boulder. (3) If the effective stress on sediment beneath the ice exceeds the pressure the sediment can support, then the till will flow and fill the cavity. Steps (2) and (3) are probably not discrete events, but happen simultaneously.

1.1.3.1 Freeze-on hypothesis

The freeze-on hypothesis proposes that flutes form by till squeezing into a cavity in the lee of a lodged boulder where the till is incorporated into the basal ice by freezing and subsequently transported downglacier and redeposited ([Fig. 1-5](#)) ([Schytt, 1959, 1963](#); [Roberson et al., 2011](#)). Sediment evacuation from the cavity by entrainment in ice is balanced by flow into the cavity, thereby providing a source of till for freeze-on and transport downglacier. [Roberson et al. \(2011\)](#) suggested two potential mechanisms for the re-freezing of sediment squeezed into the cavity of a lee-side boulder: (1) a [Robin \(1976\)](#)-type heat pump mechanism caused by the ice pressure variation across the boulder or (2) regelation infiltration associated with unsteady sliding. The re-deposition of ice-entrained debris was not addressed by [Roberson et al. \(2011\)](#) but could occur by basal melting once ice is sufficiently distant from the boulder.

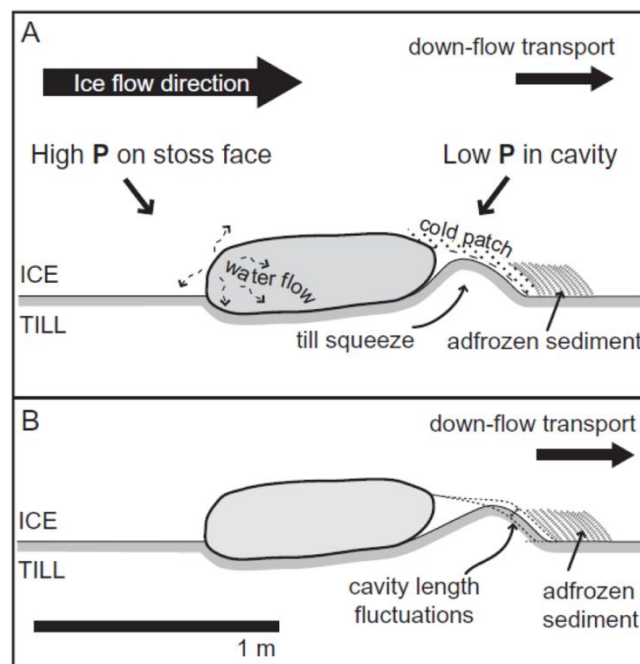


Figure 1-5. An illustration of the freeze-on hypothesis as proposed by [Roberson et al. \(2011\)](#).

The principal strength of this hypothesis is that it can explain fluted till frozen into the basal ice of polythermal glacier margins. Unsurprisingly, flute formation hypotheses that incorporate the freezing of till are generally suggested by those who have studied flutes at polythermal glaciers ([Hoppe and Schytt, 1953](#); [Schytt, 1959, 1962, 1963](#); [Gordon et al., 1992](#); [Roberson et al., 2011](#)). This hypothesis is also supported by observations and stable isotope measurements that suggest ice lenses within frozen flutes at polythermal glaciers were sourced from meltwater, not basal ice ([Schytt, 1959](#); [Roberson et al., 2011](#)). Although this hypothesis is able to explain parallel-sided flutes of a constant height, it does not directly account for the geometry of tapering flutes.

The deposition of flutes formed by the freeze-on process would likely differ depending on glacier thermal regime. Since “squeezing” till into a cavity requires temperate conditions, [Schytt \(1959\)](#) suggested that flute initiation and formation under polythermal glaciers would primarily occur upglacier of the frozen margin. Once the fluted, debris-rich ice was transported to the portion of the glacier where underlying sediment was frozen, it would preferentially couple to the frozen bed and become resistant to glacier motion ([Schytt, 1959](#)).

No depositional process has been suggested in the literature for flutes formed by the freeze-on mechanism at temperate glaciers. Therefore, details of the freeze-on hypothesis and properties of temperate basal ice were used to inform the following model for fabrics in flutes formed by a freeze-on process. The freeze-on hypothesis would likely result in strongly convergent fabrics in the lee of the boulder and flow parallel fabrics throughout the rest of the flute ([Fig. 1-3A](#)) ([Lawson, 1979](#); [Gordon et al., 1992](#)). Fabrics and internal sediment structures of some flutes have shown that till deformation in the lee

of boulders is transverse to glacier flow ([Paul and Evans, 1974](#); [Rose, 1989](#); [Eklund and Hart, 1996](#)). Parallel fabrics are the most likely to occur in accordance with the freeze-on mechanism because fabrics from debris in basal ice tend to align with glacier flow ([Lawson, 1979](#); [Hart, 1998](#)) and re-deposition of till from ice (i.e., lodgment) will result in strains in till near the glacier sole that align particles downglacier. Herringbone fabrics, although they could be inherited from deformation of till into the cavity ([Roberson et al., 2011](#)), are unlikely away from boulders at flute heads because strains sufficient to re-orient till particles are not large ([Iverson et al., 2008](#)).

The density of fluted till emplaced by a freeze-on mechanism would likely differ depending on how the sediment was redeposited. If the fluted till is only deposited on the glacier forefield as melt-out once the glacier ice has retreated from a frozen margin, as per [Schytt \(1959\)](#), the till density in the flute would likely be uniformly and significantly less than the surrounding, unfluted till. If the fluted till were re-deposited through a lodgement process, as it would likely be beneath a temperate glacier, the till density in the flute would likely be very uniform and similar to adjacent, unfluted tills.

1.1.3.2 Cavity propagation hypothesis

The cavity propagation hypothesis proposes that flutes form when till is squeezed into a cavity in the lee of a lodged boulder where the till becomes rigid enough to halt the downward creep of ice into the cavity, thereby moving the cavity's take-off point (i.e. propagating the cavity) farther downglacier ([Fig. 1-6](#)) ([Dyson, 1952](#); [Paul and Evans, 1974](#); [Boulton, 1976](#); [Åmark, 1980](#); [Benn, 1994b](#)). As the cavity extends downglacier, till will be deformed into it and thus add to the flute's length. This cycle of

till deformation leading to cavity propagation would allow flutes to build to great lengths while maintaining a uniform geometry.

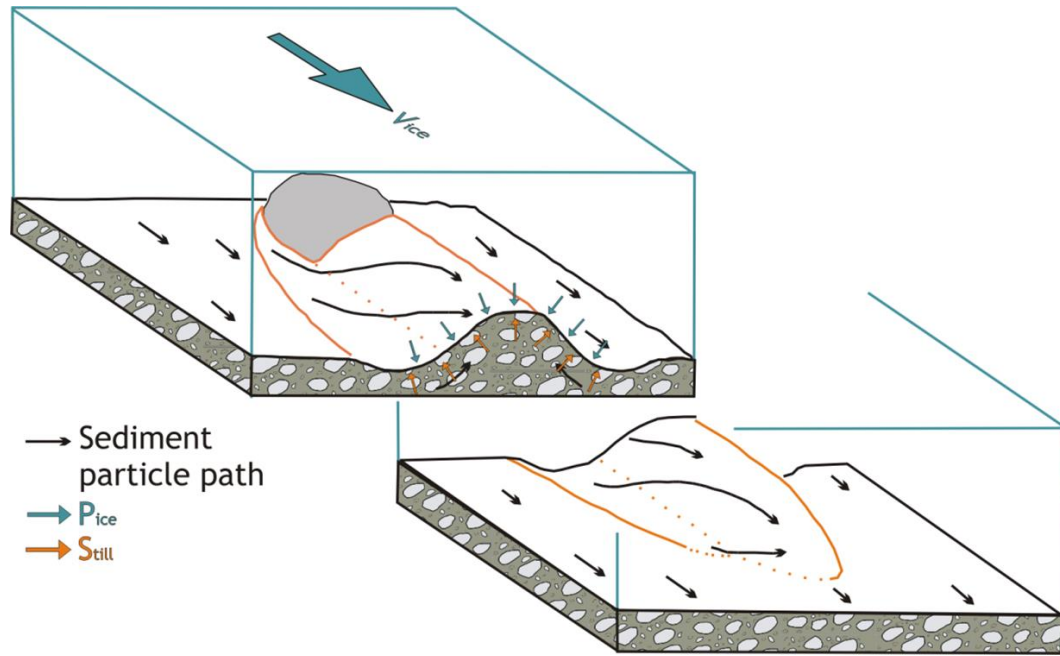


Figure 1-6. An illustration of the cavity propagation hypothesis. P_{ice} is the ice pressure and S_{till} denotes upward pressure exerted by the till, proportional to the till strength. Figure modified from [Benn \(1994b\)](#).

This hypothesis is the most widely accepted because it is able to more easily account for a wider variety of flute morphologies than other proposed mechanisms. For example, the cavity propagation hypothesis can explain the downglacier decrease in flute width and height as simply an outcome of the ice creeping into a cavity from above at a faster rate than till intrusion from below. Differences between rates of till deformation and basal ice creep into a cavity can also be used to explain why flutes can be either tapered or parallel sided and why flutes within a swarm have similar morphologies ([Benn and Evans, 2010](#)). This mechanism is most often suggested in studies with field sites at temperate glaciers, where fluted till extends beneath, but does not extend into, the basal ice (e.g. [Boulton, 1976](#)). The principal weakness of the cavity propagation hypothesis

is its failure to adequately explain how till that is weak enough to flow into a cavity then increases in strength sufficiently to resist ice stresses ([Gordon et al., 1992](#); [Schoof and Clarke, 2008](#)).

The cavity propagation hypothesis would likely result in strongly convergent fabrics in the lee of the boulder and herringbone fabrics throughout the rest of the flute ([Fig. 1-3B](#); [Fig. 1-6](#)) ([Boulton, 1976](#); [Benn, 1994b](#); [Benn and Evans, 2010](#)). Strong convergence in the lee of the boulder is frequently observed in flute fabrics and sediment structures. Herringbone fabrics, which are sometimes measured in flutes, are thought to be the result of additive strain from two strain events ([Benn, 1994b](#)). First, deformation of till into the cavity would impart a flow-transverse fabric, and then the downglacier flow of basal ice would impart a flow-parallel fabric component.

The density of till in flutes that form by the cavity propagation hypothesis would likely be smaller than in adjacent, unfluted till because the sediment would be emplaced beneath a pressure shadow in the ice.

1.2 Anisotropy of magnetic susceptibility

Measuring the anisotropy of magnetic susceptibility (AMS) of rocks is a technique that was developed to characterize the type, history, and orientation of strain in deformed rocks, particularly those lacking visible strain indicators ([Graham, 1954](#); [Borradaile, 1988](#); [Tarling and Hrouda, 1993](#); [Hrouda, 2007](#)). AMS fabrics have also been successfully used to characterize fabrics in unlithified sediments, including subglacial till.

There has been renewed interest recently in using AMS to characterize till fabrics. This interest is partly due to laboratory “ring-shear” experiments that showed that

orientations of greatest principal magnetic susceptibility align in the direction glacier flow in tills that have experienced shear strains of sufficient magnitude ($> \sim 10$) ([Hooyer et al., 2008](#); [Iverson et al., 2008](#); [McCracken et al., 2014](#)). Magnetic minerals have a variety of magnetic susceptibility characteristics; identifying the magnetic characteristics of a till is imperative to correctly interpreting its fabric. For example, the presence of certain minerals can cause AMS axes to be offset or inverted. While all of the magnetic methods used in this thesis are standard in the geomagnetic community, they have not been widely utilized in the context of glacial AMS fabrics. This section discusses fundamental concepts in magnetic mineralogy, how those concepts relate to AMS measurements, and how AMS fabrics have been applied to till.

1.2.1 Introduction of magnetic concepts and magnetic properties of minerals

1.2.1.1 Magnetic susceptibility

Magnetic susceptibility is the nature and intensity of the response of a material to an external magnetic field ([Petrovsky, 2007](#)). All materials, including those that do not carry permanent magnetizations, have a magnetic susceptibility. Magnetic susceptibility (k) describes the relationship between the magnitude of an applied field (H , [T]) and the magnetization (M , [T]) induced in materials subjected to that field. Magnetic susceptibility is often treated as a scalar quantity so that $M = k H$.

1.2.1.2 Classes of magnetic materials

All materials develop a magnetization in the presence of an applied field. Thus, all materials have a magnetic susceptibility. The magnitude of magnetization induced by an applied field predominately reflects the effect an applied field has on a material's

electrons ([Moskowitz, 1991](#); [Petrovsky, 2007](#)). Materials can be classified based on how they respond to an applied field: diamagnetic, paramagnetic, ferromagnetic, ferrimagnetic, and antiferromagnetic.

Both diamagnetic and paramagnetic materials have no magnetization in the absence of an applied field. Diamagnetic materials have no unpaired electrons ([Moskowitz, 1991](#); [Petrovsky, 2007](#); [Tauxe et al., 2015](#)). A magnetic field applied to a diamagnetic material induces a small magnitude magnetization in the opposite direction of the field.

Diamagnetic materials, therefore, have small and negative magnetic susceptibilities (-10^{-8} [m³/kg]) ([Fig. 1-7A](#), [Fig. 1-8a](#)) ([Moskowitz, 1991](#)). Most organic compounds are diamagnetic, as are quartz, plagioclase, calcite, and apatite ([Petrovsky, 2007](#)).

Paramagnetic materials have unpaired electrons that are randomly oriented, so these minerals do not have a net magnetization in the absence of an applied field ([Moskowitz, 1991](#)). Unpaired electrons of paramagnetic materials tend to align in the direction of an applied field and align more readily the stronger an applied field is. The susceptibility of paramagnetic materials, therefore, has a positive, linear relationship to an applied field and thus a positive susceptibility with magnitudes between $10-100 \times 10^{-8}$ [m³/kg] ([Fig. 1-7B](#), [Fig. 1-8b](#)) ([Moskowitz, 1991](#); [Petrovsky, 2007](#); [Tauxe et al., 2015](#)). Paramagnetic materials (at room temperature) include phyllosilicates, iron and magnesium carbonates, and ferromagnesian silicates ([Moskowitz, 1991](#); [Petrovsky, 2007](#)). Paramagnetic susceptibility is also a function of temperature. That relationship can be defined by the Curie-Weiss Law:

$$k_{para} = C^*/(T - T_c),$$

where C^* is the Curie constant, T is temperature, and T_C is the Curie temperature (see [Section 3.4.2](#)) ([Fig. 1-7B](#)) ([Richter and van der Pluijm, 1994](#)).

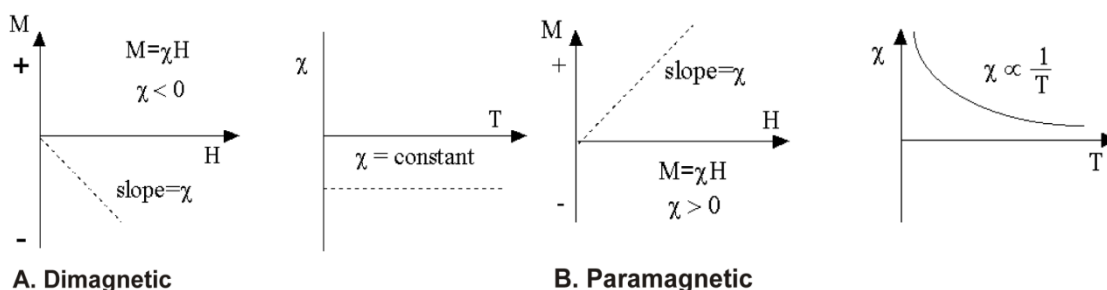


Figure 1-7. The relationships between first, Magnetization, M , and magnetic field magnitude, H , and second, magnetic susceptibility, χ , and temperature, T , for (A) diamagnetic and (B) paramagnetic materials. Figures from ([Moskowitz, 1991](#)).

Ferromagnetic and ferrimagnetic materials have a magnetization in the absence of an applied field, or remanent magnetization, because their electron spins tend to spontaneously couple and align ([Tarling and Hrouda, 1993](#); [Tauxe et al., 2015](#)).

Spontaneous coupling links the spins of unpaired electrons in the $3d$ orbitals of transition metals – in particular, iron, nickel, and cobalt ([Tarling and Hrouda, 1993](#); [Tauxe et al., 2015](#)). In metallic compounds, the $3d$ orbitals of cations directly couple to adjacent compounds so that all of their electron spins align ([Fig. 1-8c](#)) ([Tarling and Hrouda, 1993](#); [Tauxe et al., 2015](#)). Materials with these properties are known as ferromagnetic (*sensu strictu*) and have susceptibility values of $1000\text{-}10000 \times 10^{-8} \text{ [m}^3/\text{kg]}$ ([Moskowitz, 1991](#)).

Truly ferromagnetic (*s.s.*) materials do not occur naturally. In more chemically complex compounds, like oxides, unpaired $3d$ electrons in transition metal cations are coupled through an intermediary anion, like oxygen ([Tarling and Hrouda, 1993](#)). These links are formed in such a way that the electron spins of adjacent cations are antiparallel. If one cation (A) has a stronger magnetization than another (B), then the material produces a net magnetization in the direction of A and is called ferrimagnetic ([Fig. 1-8e](#)) ([Moskowitz,](#)

1991; Tarling and Hrouda, 1993; Tauxe et al., 2015). Ferrimagnetic susceptibility values are similar to those of ferromagnetic (s.s.) materials. Antiferromagnetic materials are magnetized in a similar way to ferrimagnetic materials, except their antiparallel spins have equivalent magnetization magnitudes and therefore produce little-to-no remanent magnetization (Fig. 1-8d). Together, ferromagnetic, ferrimagnetic, and antiferromagnetic materials are referred to as ferromagnetic (*sensu lato*).

All materials have a magnetic susceptibility value, so all components of a rock or sediment sample will contribute to an AMS signal or fabric. Because ferrimagnetic materials have such large magnetic susceptibilities, very little ferrimagnetic material is needed for it to control the susceptibility anisotropy of a sample (Tarling and Hrouda, 1993).

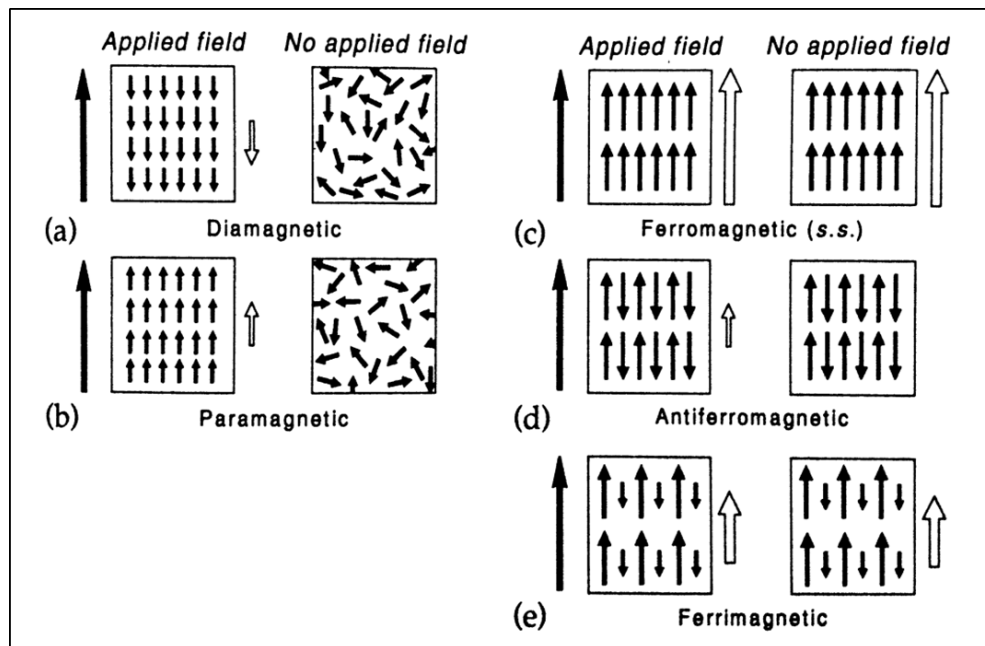


Figure 1-8. An illustration of the alignment of electron spins and the associated magnetization of different classes of magnetic materials (a-e), both in the presence and absence of an applied field. Black arrows to the left of boxes show the orientation of the applied field, and white arrows to the right of boxes show the orientation of the resulting magnetization. Figure adapted from Tarling and Hrouda (1993).

1.2.1.3 Magnetic anisotropy and domain states

The AMS of a rock or sediment sample is not solely a function of the bulk susceptibility magnitudes of its constituent minerals, but is also dependent on those minerals' susceptibility anisotropies. Both ferromagnetic (*s.l.*) and paramagnetic (predominately phyllosilicate) minerals preferentially magnetize – have larger susceptibility values – in discrete directions depending ultimately on their crystallographic structure. The characteristics of ferromagnetic (*s.l.*) minerals that can control their susceptibility anisotropy can also include both shape and domain state.

A material will always seek the most efficient (lowest energy) distribution of its electron spins ([Tauxe et al., 2015](#)). For a ferromagnetic (*s.l.*) material this means that within its crystalline structure there are certain directions that require less energy than others to stay magnetized. The direction in which a mineral is most efficiently, and therefore preferentially, magnetized is called its “easy direction.” When a mineral's magnetization aligns with its crystalline easy direction, it is said to have magnetocrystalline anisotropy.

When a magnetic mineral has a high saturation magnetization (in natural settings these are typically ferrimagnetic minerals), its shape can control the easy direction orientation instead of its crystal structure. For any magnetic mineral, the permanent field it produces is identical to a field produced by a set of “free poles” distributed over the crystal's surface ([Tauxe et al., 2015](#)). The distribution of these free poles on the surface of the mineral produces an internal “demagnetization” field in the opposite direction of the external field. For some physically anisotropic minerals, the internal demagnetization field is minimized parallel to that mineral's long axis. The minimization of the mineral's

demagnetization field therefore produces an easy direction of magnetization along the mineral's long axis. When the easy direction of a magnetic mineral is controlled by its shape, it is said to have "shape anisotropy." The magnetic susceptibility of ferromagnetic (*s.l.*) minerals is most often shape anisotropic.

The volume and shape of ferromagnetic (*s.l.*) particles strongly affects how they can most efficiently organize their electron spins ([Fig. 1-9](#)). In the simplest case, when magnetic particles are relatively small, their electron spins align parallel (or antiparallel) to one another and consequently develop a uniform magnetization ([Tarling and Hrouda, 1993](#); [Tauxe et al., 2015](#)). Such particles are called single-domain (SD). The most energy efficient way for larger magnetic particles to distribute their magnetization is for the electron spins to organize themselves into regions within the particle that have quasi-uniform magnetizations. These regions are known as magnetic domains, and particles with more than one domain are referred to as multi-domain (MD). For particles between SD and MD sizes, the energy needed to stay magnetized can be minimized by allowing some spins to diverge from strict (anti-) parallelism but not form true domains ([Tauxe et al., 2015](#)). Particles with these characteristics are called pseudo-single-domain (PSD). Finally, magnetic mineral grains may be so small that the energy needed to overcome their anisotropy energy (the energy keeping its spins aligned along the easy axis) is relatively small. This critical energy can be reached either by thermal energy from ambient earth surface temperatures or by small applied fields. Because these particles have characteristics similar to paramagnetic materials (they tend to adopt randomly oriented remanent magnetizations on laboratory timescales and align readily with an applied field) they are known as superparamagnetic (SP) ([Tauxe et al., 2015](#)). Unlike

paramagnetic materials, SP grains have large susceptibility magnitudes and become magnetically saturated in applied fields much less than 1 T ([Tauxe et al., 2015](#)).

Magnetic materials with different domain states, even of the same mineral composition, behave differently in an applied magnetic field and therefore have different properties of magnetic susceptibility anisotropy ([Tarling and Hrouda, 1993](#)). An MD particle will produce a maximum magnetic susceptibility parallel to its easy axis. For elongate, MD magnetite grains this means their maximum susceptibility orientation is parallel to their physical long axes ([Tarling and Hrouda, 1993](#); [Hrouda, 2007](#)). Conversely, the long axes of SD ferrimagnetic grains are normal to their maximum susceptibility and parallel to their minimum susceptibility in low-strength fields ([Rochette et al., 1992](#); [Tarling and Hrouda, 1993](#)). The AMS fabrics produced by MD grains are referred to as “normal fabrics,” and the AMS fabrics produced by SD grains are called “inverse fabrics” ([Potter and Stephenson, 1988](#); [Tarling and Hrouda, 1993](#); [Rochette et al., 1999](#); [Ferré, 2002](#)). The susceptibility anisotropy of PSD grains has not been thoroughly explored. Nevertheless, rocks with PSD magnetite as the primary magnetic susceptibility carrier have most often been observed to produce normal AMS fabrics ([Raposo, 1997](#); [Rochette et al., 1999](#)). Since SP particles readily align in the direction of an applied magnetic field, a collection of SP particles in a sample will likely produce a large bulk susceptibility but show no net susceptibility anisotropy ([Tauxe, 2015](#)).

Any natural rock or sediment sample should be expected to consist of a combination of magnetic material classes and domain states. Identifying the materials contributing to an AMS fabric is, therefore, necessary to correctly interpret it.

1.2.2 AMS fabrics of tills

AMS fabrics have been measured in a variety of unlithified sediments including varves ([Granar, 1958](#)), unstratified glaciolacustrine and glaciomarine diamicts ([Gravenor, 1984](#); [Eyles et al., 1987](#)), loess ([Lagroix and Banerjee, 2002](#); [Zhu et al., 2004](#)), submarine fans ([Rees et al., 1968](#)), deep-sea sediments ([Flood et al., 1985](#)), laboratory experiments ([Hamilton and Rees, 1970](#); [Hooyer et al., 2008](#); [Iverson et al., 2008](#)), and till ([Fuller, 1962](#); [Stupavsky et al., 1974b](#); [Stewart et al., 1988](#); [Shumway and Iverson, 2009](#); [Gentoso et al., 2012](#); [Fleming et al., 2013](#); [Ankerstjerne et al., 2015](#); [Vreeland et al., 2015](#)). AMS fabrics of sediments typically have low anisotropy values, are foliated parallel to the sediment's bedding plane (if applicable), and have lineation orientations that generally agree with clast fabrics and microfabrics ([Fuller, 1962](#); [Hamilton and Rees, 1970](#); [Tarling and Hrouda, 1993](#); [Gentoso et al., 2012](#)).

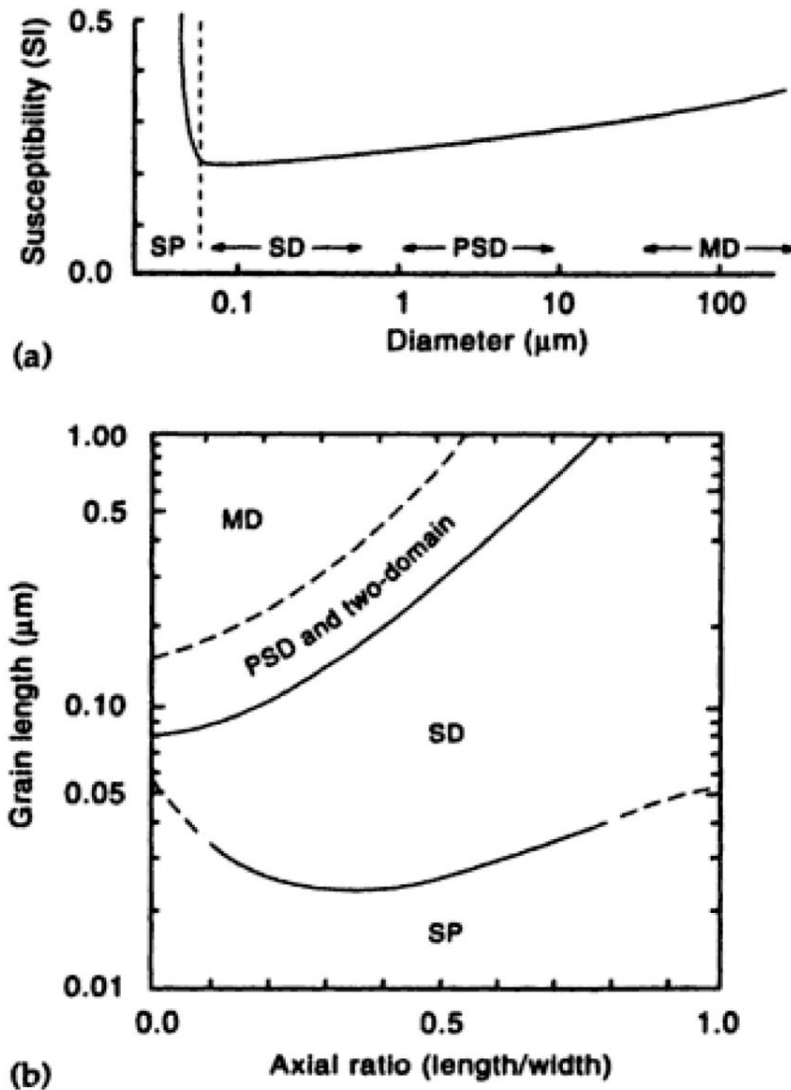


Figure 1-9. Domain size of magnetite as a function to grain shape. (A) Susceptibility of equidimensional magnetite as a function of domain state. (B) The relationship between elongation and domain state. Figure adapted from [Tarling and Hrouda \(1993\)](#).

AMS fabrics most often develop due to the alignment of either non-equidimensional, shape anisotropic grains or crystals of minerals with magnetocrystalline anisotropy ([Tarling and Hrouda, 1993](#); [Hrouda, 2007](#)). Owing to crystalline alignment being unlikely in unlithified, granular materials, the “working rule” for studying AMS fabrics in sediments is that the easy direction of magnetization corresponds with the long axes of grains ([Fuller, 1962](#); [Hamilton and Rees, 1970](#); [Hooyer et al., 2008](#)). The

dominant magnetic minerals in most tills studied using AMS has either been magnetite, titanomagnetite, or maghemite ([Fuller, 1962](#); [Eyles et al., 1987](#); [Hooyer et al., 2008](#)). Magnetite, titanomagnetite, and maghemite are ferrimagnetic and shape anisotropic, and therefore comply with the assumptions of this working rule. AMS fabrics have also been successfully characterized in till where the dominant magnetic mineralogy is chlorite clays, and the AMS signal therefore primarily reflects the alignment of paramagnetic clay minerals ([Fleming et al., 2013](#)).

Numerous attempts to apply AMS fabric techniques to tills were made after [Fuller \(1962\)](#) observed that AMS fabrics agreed with clast fabric orientations. Until the publication of results from ring-shear experiments, AMS fabrics of tills were primarily explored simply as a substitute for clast fabrics ([Gravenor et al., 1973](#); [Stupavsky et al., 1974a](#); [Stupavsky et al., 1974b](#); [Boulton, 1976](#); [Stewart et al., 1988](#)). Ring-shear experiments, where tills were sheared at constant rates showed a clear relationship between the strength, shape, and orientation AMS fabrics and the magnitude and orientation of strain experienced by till ([Hooyer et al., 2008](#); [Iverson et al., 2008](#)). Informed by ring-shear results, AMS fabrics of tills can and have been used to infer past subglacial strain conditions ([Shumway and Iverson, 2009](#); [Gentoso et al., 2012](#); [Fleming et al., 2013](#); [Ankerstjerne et al., 2015](#); [Hopkins et al., 2015](#); [McCracken, 2015](#)).

Prior to this study a single attempt had been made to measure AMS in fluted till ([Boulton, 1976](#)). That paper reported only the shape and orientation of individual AMS ellipsoids (*not* fabrics) throughout a single cross-section of a flute at Breiðamerkurjökull ([Fig. 1-10](#)).

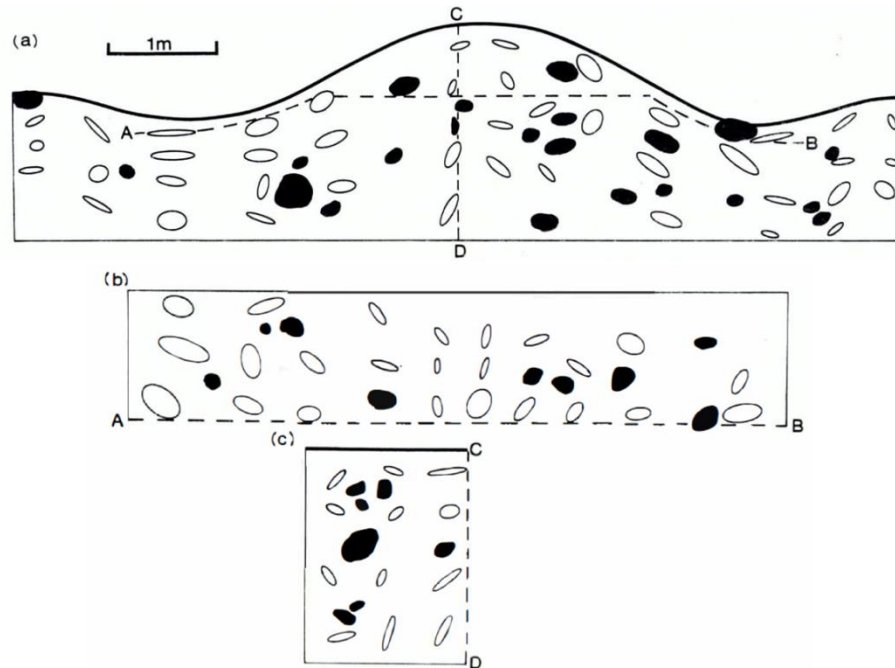


Figure 1-10. Figure from [Boulton \(1976\)](#) showing the distribution, orientation, and magnitude of individual AMS ellipsoids of till samples from a flute (hollow ellipsoids). Pebbles 10 cm or larger were also included in the sketch (opaque ellipsoids). (a) A transverse cross section across the flute, (b) a horizontal plane through the flute, and (c) a vertical section parallel to the flute crest. The position of the trenches within the flute and the orientation of the sketches relative to the glacier margin were not noted.

1.3 Motivation and objectives

The question of flute formation remains unresolved after more than six decades of study. Flutes occupy large areas of glacier forefields, so they clearly once occupied the same areas subglacially. The processes that contribute to flute formation must therefore reflect subglacial conditions and their relationship to the basal slip of glaciers. A better understanding of flute formation would also improve knowledge of subglacial sediment transport and inform the longstanding, unresolved debate regarding the importance of bed deformation in that transport (e.g., see contrasting reviews by [Piotrowski et al. \(2001\)](#) and [Boulton et al. \(2001\)](#)). The overall goal of this study was to determine what insight into

flute formation mechanisms could be obtained from patterns of strain inferred from AMS, sediment grain-size, and sediment bulk density data.

In this study mechanisms of flute formation were evaluated by measuring AMS fabrics of flutes at two glaciers in Iceland: Múlajökull and Breiðamerkurjökull. AMS fabrics were used to infer the character of strain in fluted till. In order to accomplish this objective, the following questions were addressed:

- What were the magnetic properties of the Múlajökull and Breiðamerkurjökull tills?
- How did the strain patterns of till vary within flutes?
- How did the density and grain size distribution of till vary both within flutes and relative to till adjacent to flutes?
- How do the AMS fabrics of this study compare to previously published macrofabrics

This study was the first to apply AMS fabrics to small-scale glacial flutes.

CHAPTER 2. FIELD SETTINGS

2.1 Múlajökull

Múlajökull is a surge-type, piedmont outlet glacier of the Hofsjökull ice cap in the central highlands of Iceland ([Johnson et al., 2010](#); [Jónsson et al., 2014](#)). Hofsjökull ice cap is a single, warm-based ice dome that overlies on an active central volcano of the same name ([Gourmelen et al., 2011](#)). The Múlajökull ice flow basin lies on the southern flank of the steep-sided Hofsjökull caldera ([Fig. 2-1](#)) ([Björnsson, 1986](#); [Jóhannesson et al., 2006](#)). Before it spills onto the relatively flat Þjósárver wetlands, Múlajökull passes through a 2 km gap between two rhyolitic peaks, Hjartafell to the southwest and Kerfjall to the northeast ([Fig. 2-2C](#)) ([Jónasson, 2007](#); [Jónsson et al., 2014](#)). Additionally, Múlajökull overlies an overdeepening in the bedrock between Hjartafell and Kerfjall that has a minimum elevation below 500 m a.s.l. ([Fig 2-1B](#)) ([Björnsson, 1986](#)). The ice margin in 2008 had an elevation of ~620 m a.s.l. ([Jónsson et al., 2014](#)). The position of the glacier margin in 2008 was ~2 km inside Múlajökull's outermost Little Ice Age (LIA) moraine ([Fig. 2-3](#)) ([Jónsson et al., 2014](#); [Benediktsson et al., 2015](#)).

Since records began in 1924, Múlajökull has surged at fairly regular ~10 year intervals ([Fig. 2-2B](#)) ([Björnsson et al., 2003](#); [Johnson et al., 2010](#)). The last major surge was in 1992, with smaller surge advances occurring in 2002 and 2008 ([Björnsson et al., 2003](#); [Jónsson et al., 2014](#)). Since 1992, the Múlajökull margin has retreated at an average rate of ~45 m/yr ([Johnson et al., 2010](#)).

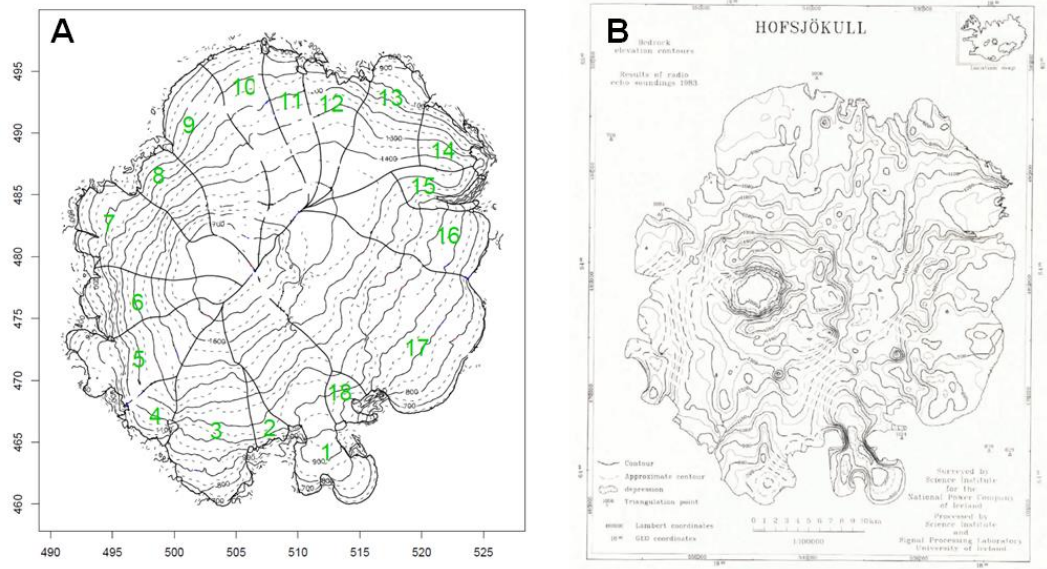


Figure 2-1. Maps of the Hofsjökull ice cap (A) with elevation contours and delineated ice flow basins. Ice flow basin 1 feeds both Múlajökull (eastern piedmont lobe) and neighboring Nauthagajökull (western lobe). Figure is modified from [Jóhannesson et al. \(2006\)](#). (B) Subglacial bedrock contours inferred from radio echo-sounding measurements. Figure is from [Björnsson \(1986\)](#).

The Múlajökull forefield is largely dominated by subglacial till with some outwash and lacustrine deposits ([Fig. 2-3](#)) ([Jónsson et al., 2014](#)). Múlajökull is the location of the only known actively forming modern drumlin field in the world ([Johnson et al., 2010](#)). The distribution of drumlins has controlled the routing of glacial meltwater and has limited the dispersal of proglacial discharge and outwash ([Jónsson et al., 2014](#)). The routing of outwash through low areas between drumlins has preserved large areas dominated by subglacial landforms, including not only drumlins but crevasse-fill ridges and flutes ([Jónsson et al., 2014](#)).

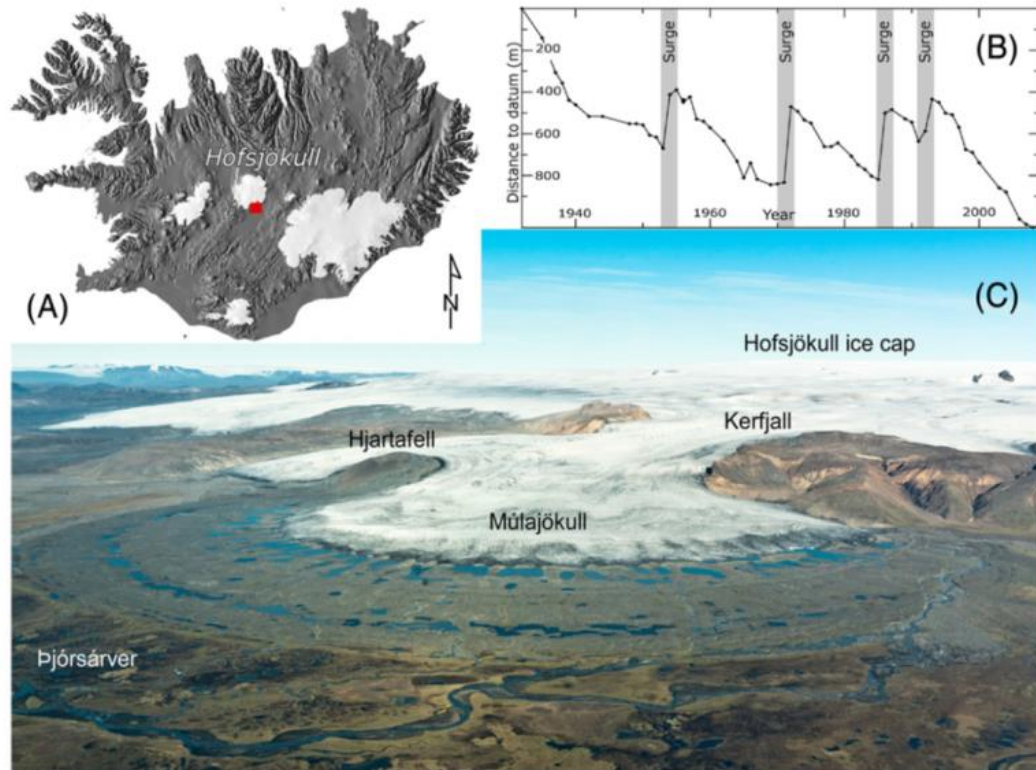


Figure 2-2. (A) Map of Iceland with the location of Múlajökull marked by a red dot. (B) Graph of the distance of the Múlajökull margin from a datum over time, with surge events indicated. (C) Oblique aerial photograph of Múlajökull looking northwest with major geographical landmarks noted. Figure is from [Jónsson et al. \(2014\)](#).

Although much of the Múlajökull forefield is dominated by a subglacial till plain, the distribution of flutes is limited ([Fig. 2-3](#)). Two swarms with large, parallel-sided flutes occur at the far north and south ends of the glacier margin. Throughout the rest of the forefield, flutes are almost always small and tapered, and isolated flutes not within a swarm or part of a small group (two to four flutes) are not uncommon.

The geology of the Hofsjökull volcano is poorly understood because it is largely covered by ice. It is located along Iceland's active central rift zone, and the dominant bedrock is mapped broadly as young (<0.8 m.y.a.) hyaloclastites and pillow lavas ([Fig. 2-4](#)) ([Jóhannesson, 2014](#)). This interpretation is supported by the lithologies of sediments in

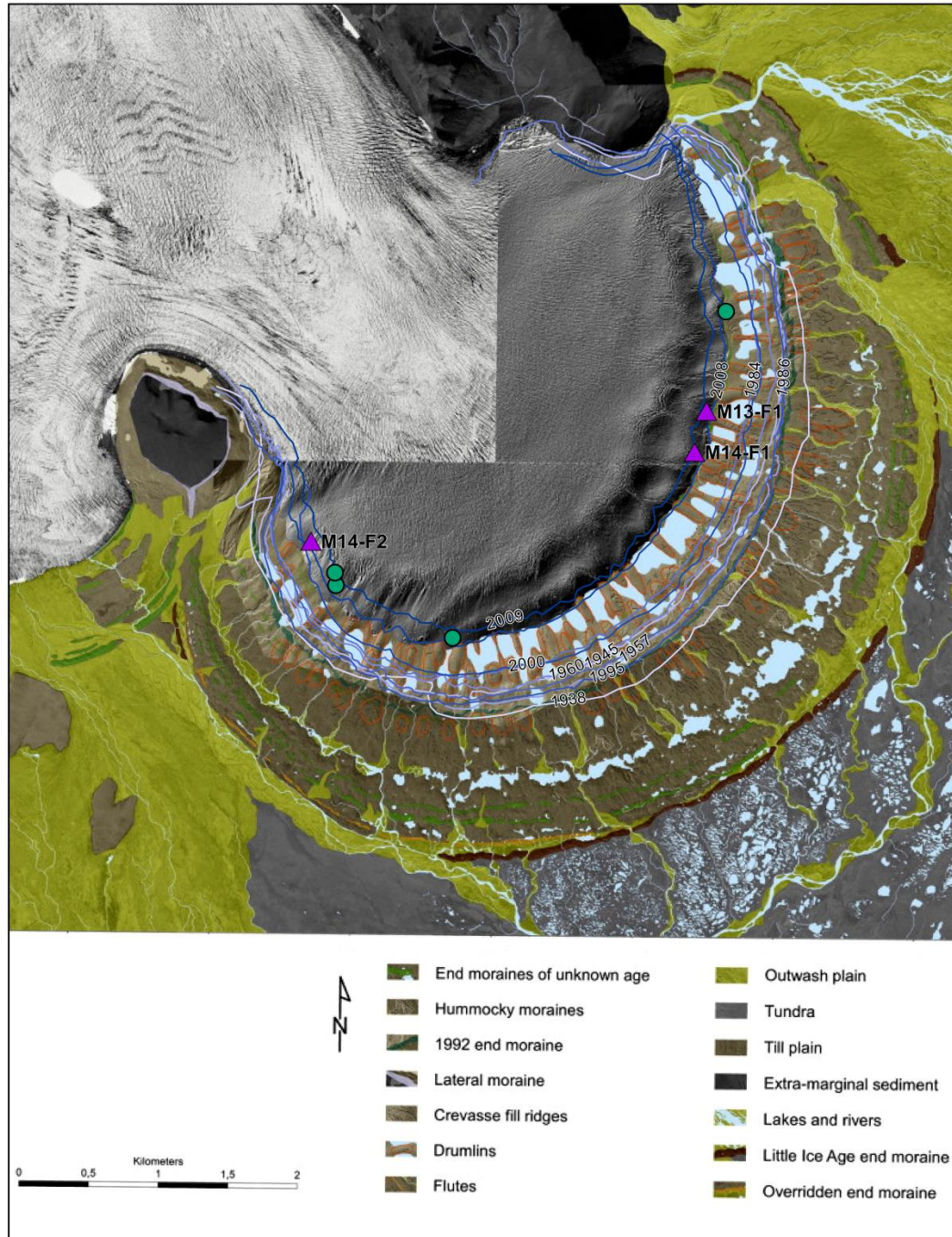


Figure 2-3. Landform map of the Múlajökull forefield, with locations of the flutes sampled for this study (M13-F1, M14-F1, and M14-F2) marked. Locations of other flutes surveyed during this study are indicated by circles. Base map and landform classifications from [Jónsson et al. \(2014\)](#). Glacier margins, indicated by their year, were mapped using georeferenced aerial photographs and topographic maps available from the National Land Survey of Iceland, ESRI satellite imagery, and the [Jónsson et al. \(2014\)](#) base map.

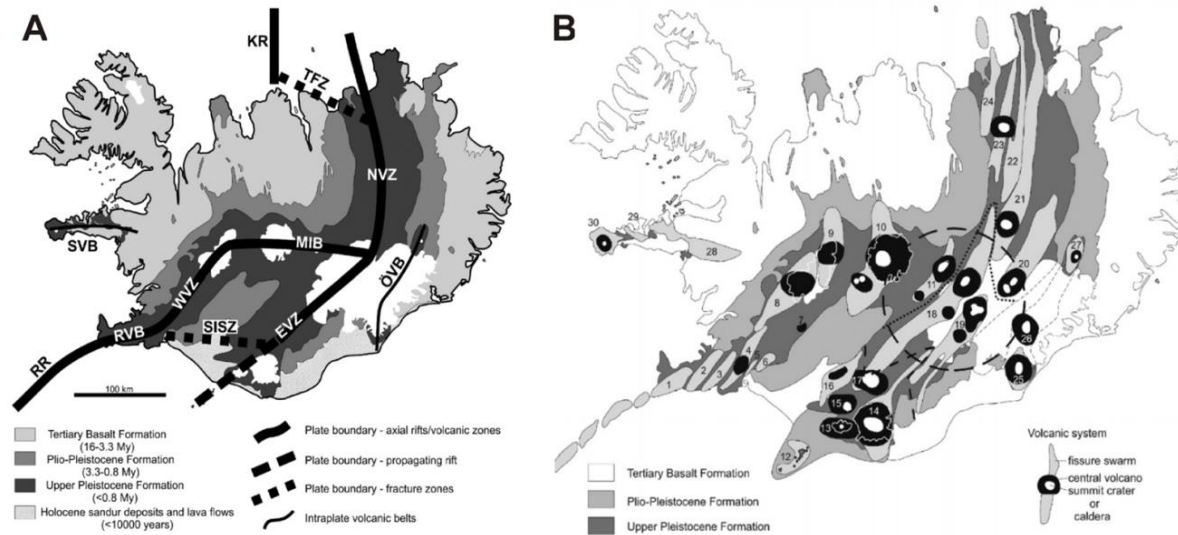


Figure 2-4. Generalized geological maps of Iceland outlining (A) principal geological elements including the main fault structures and volcanic zones and belts: RR, Reykjanes Ridge; RVB, Reykjanes Volcanic Belt; SISZ, South Iceland Seismic Zone; WVZ, West Volcanic Zone; **MIB, Mid-Iceland Belt**; EVZ, East Volcanic Zone; NVZ, North Volcanic Zone; TFZ, Tjörnes Fracture Zone; KR, Kolbeinsey Ridge; **ÖVB, Öraefi Volcanic Belt**; SVB, Snæfellsnes Volcanic Belt. (B) distribution of active volcanic systems among volcanic zones and belts in Iceland Reykjanes Volcanic Zone: (1) Reykjanes–Svartsengi, (2) Krýsuvík, (3) Brennisteinsfjöll; **West Volcanic Zone:** (4) Hengill, (5) Hrómundartindur, (6) Grímsnes, (7) Geysir, (8) Prestahnjúkur, (9) Langjökull; **Mid-Iceland Belt:** (10) Hofsjökull, (11) Tungnafellsjökull; East Volcanic Zone: (12) Vestmannaeyjar, (13) Eyjafjallajökull, (14) Katla, (15) Tindfjöll, (16) Hekla–Vatnafjöll, (17) Torfajökull, (18) Bárðarbunga–Veiðivötn, (19) Grímsvötn; North Volcanic Zone: (20) Kverkfjöll, (21) Askja, (22) Fremrinámur, (23) Krafla, (24) Þeistareykir; **Öraefajökul Volcanic Belt:** (25) Öraefajökull, (26) Esjufjöll, (27) Snæfell; Snæfellsnes Volcanic Belt: (28) Ljósufjöll, (29) Helgrindur, (30) Snæfellsjökull. The large dashed circle indicates the approximate center of the Iceland mantle plume/anomaly. Dotted line shows the northern limits of the East Volcanic Zone, whereas the hachured line indicates the boundary between the active and propagating rift segments of the zone. Figures and captions are from [Thordarson and Larsen \(2007\)](#).

the Múlajökull forefield that are almost exclusively basalt, vesicular basalt, and porphyritic basalt with glassy phenocrysts. Rhyolitic units have been observed on the north margin of Hofsjökull, in Hjartafell and Kerfjall, and in nunataks closer to the Hofsjökull caldera ([Jónasson, 2007](#)).

2.2 Breiðamerkurjökull

Breiðamerkurjökull is the second largest outlet glacier draining the southern portion of the Vatnajökull icecap in southeast Iceland ([Fig. 2-5](#)) ([Björnsson and Pálsson, 2008](#); [Hannesdóttir et al., 2010](#)). Vatnajökull is the largest non-polar ice cap in Europe at ~8,000 km² and is wholly temperate ([Hannesdóttir et al., 2010](#); [Schomacker, 2010](#)). This ice cap has some of the country's highest annual precipitation rates, owing to its location near Iceland's southeast coast ([Björnsson and Pálsson, 2008](#)). Breiðamerkurjökull is bounded by Örfajökull to the west, the nunataks Mávabyggðir and Esjufjöll to the north, and Veðurárdalsfjöll to the east ([Fig. 2-6](#)). Breiðamerkurjökull has an eastern

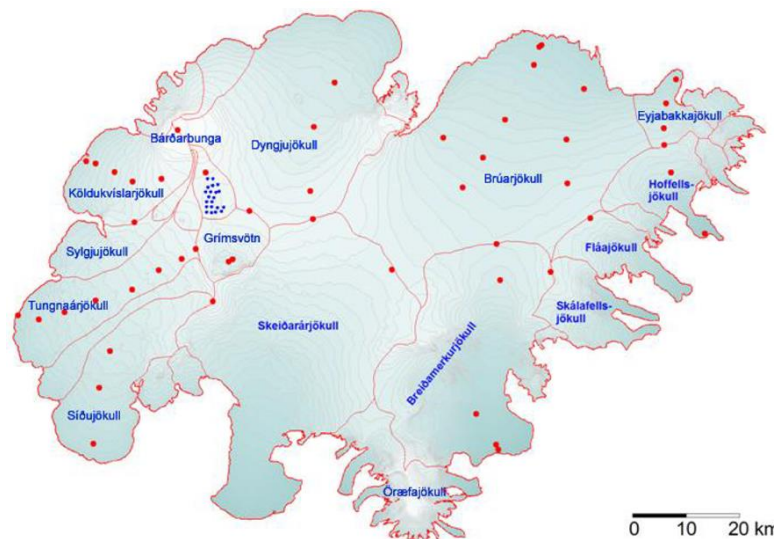


Figure 2-5. Map of the Vatnajökull ice cap with ice flow basins of outlet glaciers delineated. Figure is from [Hannesdóttir et al. \(2010\)](#).

(Norðlingalægðarjökull), central (Esjufjallajökull), and western (Máfabyggðajökull) branch ([Fig. 2-6](#)) ([Björnsson, 1996](#); [Sigurðsson, 1998](#)). The western ice stream overlies Öraefajökull, Iceland's largest (by height) active central volcano, and one of seven volcanoes underlying Vatnajökull ice cap ([Fig. 2-5](#); [Fig. 2-6](#)) ([Sigurðsson, 1998](#); [Stevenson et al., 2006](#)). The eastern and central ice streams begin farther towards the interior of the ice cap ([Fig. 2-5](#); [Fig. 2-6](#)) ([Sigurðsson, 1998](#)). Near the glacier's margin, both the eastern and western ice streams overlie bedrock valleys that were likely carved by Breiðamerkurjökull during the Little Ice Age (LIA) ([Björnsson, 1996](#)).

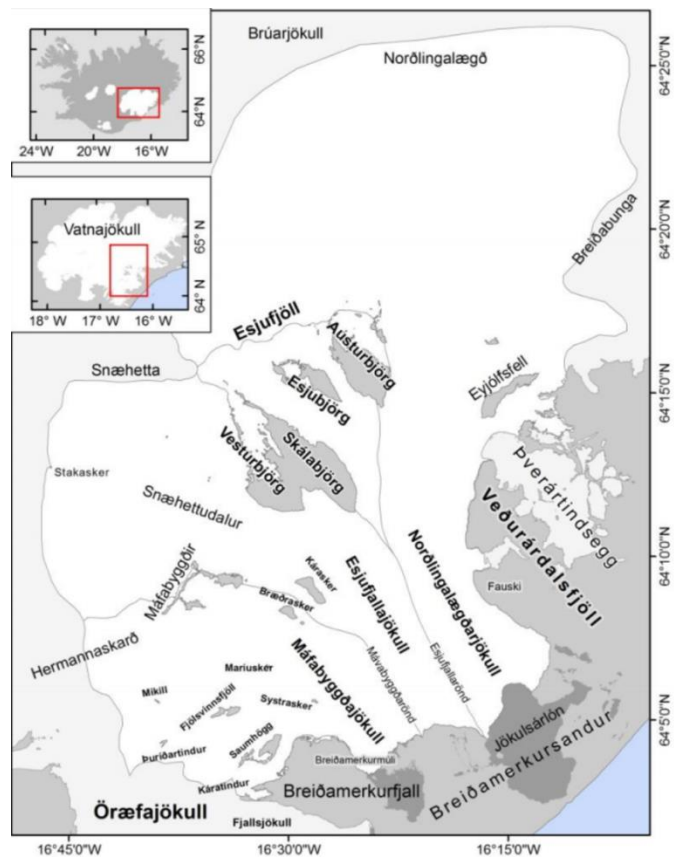


Figure 2-6. Map of Breiðamerkurjökull, southeast Iceland, and its adjoining mountain ranges. Ice divides (solid lines) of Breiðamerkurjökull's three ice streams. Figure is from [Guðmundsson \(2014\)](#).

The eastern Breiðamerkurjökull ice stream has surged 11 times since 1794 at irregular intervals ranging from six to 38 years, the last event being in 1969 ([Sigurðsson, 1998](#); [Björnsson et al., 2003](#)). The central and western ice streams have been far less likely than the eastern one to experience large-scale surging but have experienced some small-scale surge activity ([Sigurðsson, 1998](#)). Breiðamerkurjökull's central and western ice streams have also been observed to experience “gagnur” events in which an increase in glacier slope results in the propagation of a bulge down the ice stream but with no subsequent advance of the glacier terminus ([Björnsson et al., 2003](#)). Besides intermittent surging and minor late winter advances of the eastern and central ice streams, the Breiðamerkurjökull margin has been retreating from its LIA maximum since 1894 ([Evans and Twigg, 2002](#)).

The Breiðamerkurjökull forefield consists of a large sandur, subglacial bedforms, and two large glacially-fed lakes that occupy the aforementioned bedrock valleys ([Fig. 2-7](#)) ([Björnsson, 1996](#); [Evans and Twigg, 2002](#)). Heavily fluted regions are present throughout the Breiðamerkurjökull forefield ([Evans and Twigg, 2002](#)). The flutes considered in this study and in past studies are those that occupy an island in the western-most portion of the forefield and were formed beneath the western ice stream ([Fig. 2-7](#); [Fig. 2-8](#)) ([Boulton, 1976](#); [Benn, 1995](#)). Flutes at Breiðamerkurjökull are generally long and parallel-sided.

Breiðamerkurjökull is likely underlain by a wide variety of volcanic lithologies, ranging in age from the Miocene to the recent Holocene ([Jóhannesson, 2014](#)). Veðurárdalsfjöll is mapped as being dominantly Miocene and lower Pliocene extrusive lavas of intermediate to basaltic composition ([Jóhannesson, 2014](#)). The two active

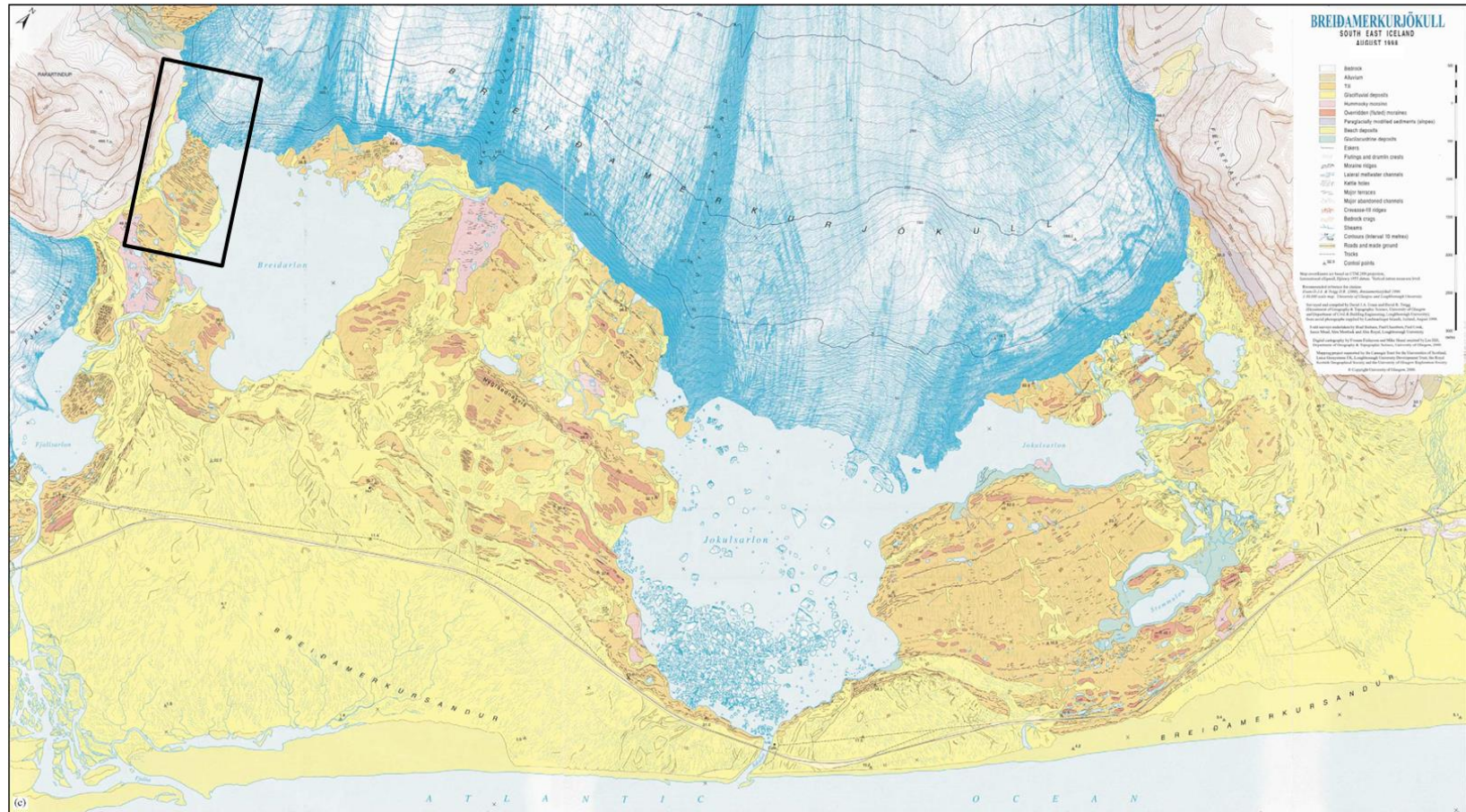


Figure 2-7. Smaller scale reproduction of the 1:30,000 map of Breiðamerkurjökull and part of Fjallsjökull forefields by [Evans and Twigg \(2000\)](#), as published in [Evans and Twigg \(2002\)](#). Outlined section is the map area shown in [Fig. 2-8](#).

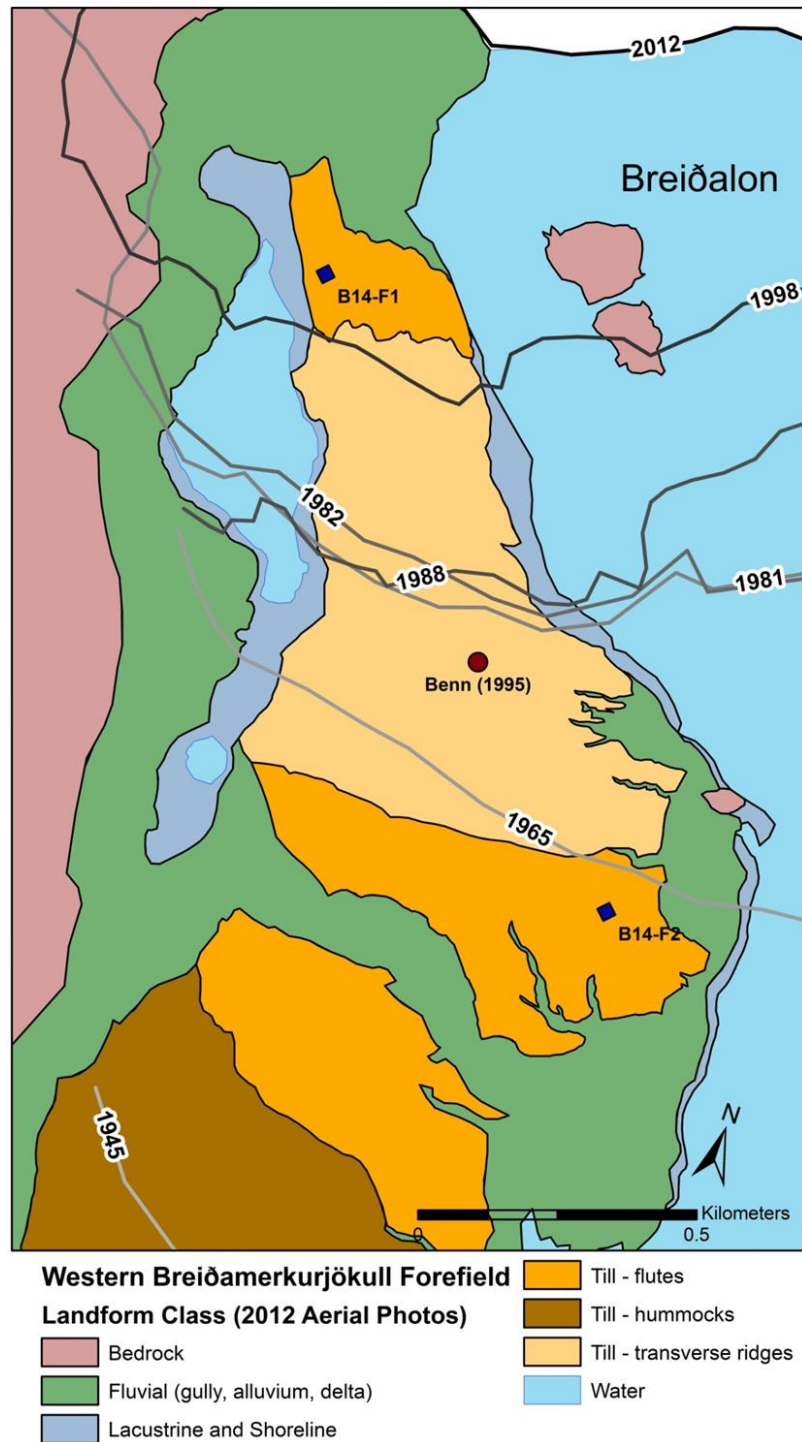


Figure 2-8. Landform map of the western Breiðamerkurjökull forefield, with sampling sites for this study (B14-F1 and B14-F2) and a past flute fabrics study ([Benn, 1995](#)) indicated. Landform regions were mapped using 2012 satellite imagery from ESRI. Glacier margins, indicated by their year, were mapped using georeferenced aerial photographs and topographic maps available from the National Land Survey of Iceland.

volcanoes underlying Breiðamerkurjökull, Öräfajökull and Esjufjöll, are part of the eastern flank (or off-rift) Icelandic volcanic zone, which is also called the Öräfi Volcanic Belt ([Fig. 2-4](#)) ([Jónasson, 2007](#); [Thordarson and Larsen, 2007](#)). Volcanic deposits associated with Öräfajökull include subaerially, subglacially, and intrusively deposited units with both basaltic and silicic compositions ([Stevenson et al., 2006](#)). Rhyolite and obsidian have been found in the Esjufjöll nunataks ([Jónasson, 2007](#)).

CHAPTER 3. METHODS

3.1 Introduction

This study focused on correctly interpreting AMS fabrics of fluted till in order to infer patterns of subglacial strain associated with flute formation. Intact till samples were collected for AMS analysis from flutes in the forefields of Múlajökull and Breiðamerkurjökull. The magnetic characteristics, including AMS, of the till samples were measured. AMS orientation data were statistically analyzed to determine patterns of strain in the till. The grain-size distribution and densities of fluted and adjacent, unfluted till were measured to determine the extent of sedimentary sorting and consolidation, respectively, associated with flutes. Additionally, pebble fabrics of flutes from the peer-reviewed literature were reanalyzed so that comparisons could more easily be made between those pebble fabrics and the AMS fabrics measured in this study.

3.2 Field methods

3.2.1 Flute selection

As this study is the first that has used AMS to characterize fabrics in small-scale flutes, a concerted effort was made to collect samples from only well-developed flutes. A well-developed flute has the following characteristics:

1. It is continuous, elongate, streamlined in the direction of glacier flow, and composed primarily of diamicton ([Ámark, 1980](#); [Gordon et al., 1992](#)). The width and height of the flute can either be either uniform along its length or decrease gradually in the downglacier direction.

2. It has a boulder lodged at its head, at least during its formation. Flutes that do not have boulders at their stoss end may have formed through processes dissimilar to those that do or have had their boulder eroded after flute formation ([Gordon et al., 1992](#); [Eyles et al., 2015](#)). The freeze-on and cavity propagation hypotheses for flute formation both require a boulder at the upglacier end of a flute ([Dyson, 1952](#); [Boulton, 1976](#); [Benn, 1994b](#); [Roberson et al., 2011](#)). Thus, testing these hypotheses requires study of flutes with boulders at their heads.
3. It is less than 5 m tall ([Rose, 1987](#)). If the flute is taller than this, the landform sampled may not have formed by the same processes as other small scale flutes ([Schoof and Clarke, 2008](#)).
4. It should be recently deglaciated to assure that effects of sub-aerial erosion and deposition are minimized. [Boulton \(1976\)](#) recognized that flutes at Breiðamerkurjökull had been greatly reduced in relief after only four years. Similarly, [Glasser and Hambrey \(2001\)](#) observed that flutes at Midtre and Austre Lovénbreen, Svalbard, degraded rapidly with distance from the glacier margin. Sampling flutes as close to the glacier margin as possible is, therefore, desirable.

Extensive reconnaissance of the forefields of Múlajökull and Breiðamerkurjökull resulted in the identification of five flutes that closely matched these criteria.

3.2.2 Collection of AMS samples

Sets of AMS samples were collected from each of the five flutes. Each set of AMS samples consisted of 25 or more AMS samples, and 4-20 sets were collected from each flute. AMS samples were collected from horizontal platforms made by excavating

till to expose an approximately flat, horizontal surface. Horizontal platforms were dug using shovels. When the appropriate depth was reached, hand spades, trowels, and coarse brooms were used to level and clear the platform. Individual AMS samples were collected by pushing 18x18x15 mm plastic boxes with 1 mm wall thickness into these platforms, then carefully removing the boxes from the platforms, and capping each box with the intact till sample inside ([Fig. 3-1](#)). AMS samples were collected from as small an area as possible on each platform. The sampling area for each fabric was less than or equal to 1 m² at both Múlajökull and Breiðamerkurjökull. The orientation and location of each box were measured before it was removed from the till. AMS samples are meant to reflect the *in situ* state of the sediment.

For each of the five flutes, several sites were selected along their lengths for AMS sampling. This was done to compile as complete a picture as possible of sediment deformation kinematics in each flute. If the flute was sufficiently tall, samples were gathered from platforms at multiple depths at the same site. At all five flutes, AMS samples were collected from sites immediately upglacier of the boulder, immediately downglacier of the boulder, and in the middle of the flute. The tail ends of three of the five flutes had been eroded. Samples were collected from the tail of only the one flute that had its downstream end intact, e.g., was not truncated by fluvial erosion or obstructed by another subglacial landform. The location of each fabric was measured relative to the central, uppermost, and farthest downglacier point of the flute's boulder. Where sampling conditions were favorable, samples for AMS fabrics were also collected from the unfluted till adjacent to the flute.



Figure 3-1. Photographs depicting the collection of AMS samples . (A) Plastic sample boxes are pressed into a horizontal platform using as little force as possible, and stopping once the box is full (photo credit: Reba McCracken). (B) A sampling platform with many boxes in place. The orientation and location of each box are noted before they are removed from the sediment. (C) Sample boxes are carefully removed from the sediment by inserting a flat tool beneath the sample and lifting up. Excess sediment is then trimmed using a wire saw. (D) A collection of AMS samples after they have been capped and are ready to be taken back to the lab.

3.3 Field site descriptions

3.3.1 Múlajökull

AMS samples were collected from three flutes in the Múlajökull forefield during July and August of 2013 (M13-F1) and 2014 (M14-F1 and M14-F2). Flutes M13-F1 and M14-F1 are both tapered and 100 m and 5 m long, respectively. Flute M14-F2 is ~250 m long and parallel-sided. All flutes are located upglacier of the 2008 glacier margin, composed of diamicton, less than 1.0 m tall, streamlined in the direction of glacier motion, and have boulders lodged at their heads.

3.3.1.1 M13-F1

Flute M13-F1 is located in the north-central portion of the Múlajökull forefield (UTM 27 W 611480 E 7172424 N). This flute is positioned 75 m from the 2013 glacier margin and ~100 m upglacier of the 2008 moraine. The flute “swarm” that includes M13-F1 is on top of a drumlin. The flute has three boulders at its head, all aligned with the flute’s long axis ([Fig. 3-2](#)). The farthest upglacier boulder is ~0.37 m tall. This flute is 20 m long, 0.21 m high and 0.86 m wide nearest its boulders. The height and width of the flute progressively tapers downglacier ([Fig. 3-2](#)), and its long axis trends 44°.



Figure 3-2. *View of flute M13-F1 looking downglacier.*

Samples for five AMS fabrics were collected from three horizontal platforms in M13-F1 ([Fig. 3-3](#)). The three platforms were located 0.21 m, 0.26 m, and 0.37 m below

the top of the flute's most upglacier boulder. The platforms at depths of 0.21 m and 0.26 m extended about 1 m downglacier from the lee of the farthest downglacier boulder. Two AMS fabrics were collected from each of the 0.21 and 0.26 m platforms, on either side of the flute's long axis. The 0.37 m platform was located from ~ 0.75 m to 1.00 m downglacier of the flute's boulders. Samples for a single fabric that straddled the flute's central axis were collected from the 0.37 m platform.

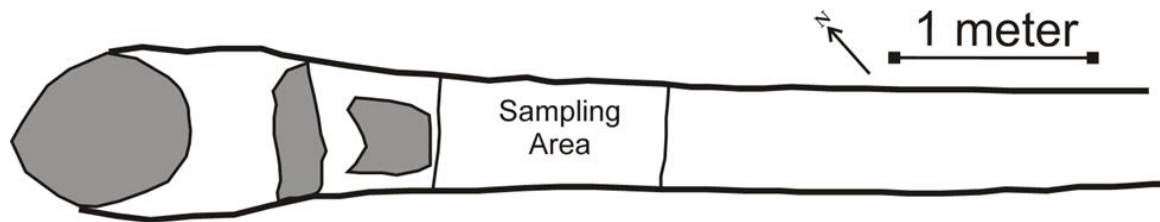


Figure 3-3. Plan view sketch of flute M13-F1, with sampling area indicated.

3.3.1.2 M14- F1

Flute M14-F1 was located in an inter-drumlin area in the north-central portion of the Múlajökull forefield (UTM 27 W 611395 E 7172120 N). It was fully excavated during sampling, so only its boulder remains. The flute was positioned ~40 m downglacier of a pro-glacial lake. The 2008 moraine was located ~100 m downglacier from tail end of the flute. The boulder on its stoss end was 0.75 m tall, 0.75 m wide, and 1.25 m long. The boulder had a classic “bulleted” shape: a rounded stoss end, a plucked lee side, and numerous flow-parallel striations ([Fig. 3-4](#)). Immediately in the lee of its boulder, the flute was 0.70 m tall and ~1.0 m wide but tapered to being imperceptibly high and wide along its 5 m length ([Fig. 3-5](#)). The flute trends 119° directly in the lee of the boulder but curves slightly to the north down-flute. At the end of the flute, it trends 109°.



Figure 3-4. View of the boulder at the head of flute M14-F1 looking southwest.

Samples for 13 AMS fabrics were collected from six platforms that were dug into five sites at M14- F1 ([Fig. 3-6](#)). Two platforms were dug into site A at 0.30 m and 0.50 m below the top of the stoss-side boulder. Samples for these fabrics were collected from either side of the flute's central axis at the A-0.30 m platform, and samples for four fabrics (two on either side of the flute's central axis) were collected from the A-0.50 m platform. Samples for two fabrics were collected from each of the following: a platform at 0.46 m depth below the top of the boulder at site B, a platform at a depth of 0.20 m at site C, and a third platform at a depth of 0.52 m at site D. Samples for an additional fabric were collected from a platform at depth of 0.30 m immediately upglacier the flute's boulder.



Figure 3-5. View of flute M14-F1 looking upglacier.

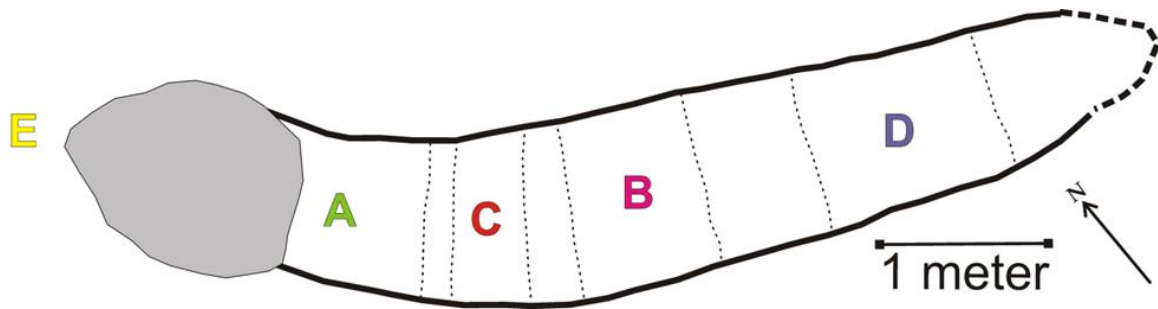


Figure 3-6. Plan view sketch of flute M14-F1, with sampling sites indicated.

3.3.1.3 M14- F2

The flute, M14-F2, is located in the southwestern portion of the Múlajökull forefield (UTM 27W 608565 E 7171433 N). This flute and the other flutes in its “swarm” are located on a highland that is bounded on either side by meltwater drainages. The highland is of relatively low relief but has been identified as a drumlin by [Johnson et al.](#)

(2010) and Jónsson et al. (2014). The upglacier end of the flute is located ~200 m from the 2014 glacier margin. The 2008 moraine is absent in this area of the forefield, but the boulder on the stoss end of M14-F2 is located upglacier of the 2008 glacier margin (Sigurkarlsson, 2015). This boulder has a “bulleted” shape (Fig. 3-7) and is 0.75 m high, 0.75 m wide, and 1.5 m long. The flute is ~250 m long, is of uniform width and height, and ends downglacier at a meltwater stream (Fig. 3-8 and 3-9A). The flute trends 226°. The depressed areas on either side of the flute are partially filled with sorted, sandy sediment - a result of deposition by meltwater (Fig. 3-9B).

Samples for 20 fabrics were collected from eight platforms at six sites in flute M14-F2 (Fig. 3-10). Samples for two fabrics were collected from each of the following: a platform at a depth of 0.36 m below the top of the boulder at site C, a platform at a depth of 0.45 m at site C, a platform at a depth of 0.50 m at site D, and a platform at a depth of 0.49 m at site F. Samples for three AMS fabrics were collected from both Site B platforms at a depth of 0.65 m and 0.40 m. Samples for four AMS fabrics were collected from a platform at a depth of 0.75 m at site A. Site A was located immediately in the lee of M14-F2’s stoss-side boulder, and was unique because the flute there had low relief and was draped by a layer of sorted sand (Fig. 3-7; Fig. 3-10). One fabric was collected from each of two pits (site E) dug 0.10 m into unfluted till.



Figure 3-7. View of flute M14-F2 looking to the south.



Figure 3-8. View of flute M14-F2 looking downglacier.

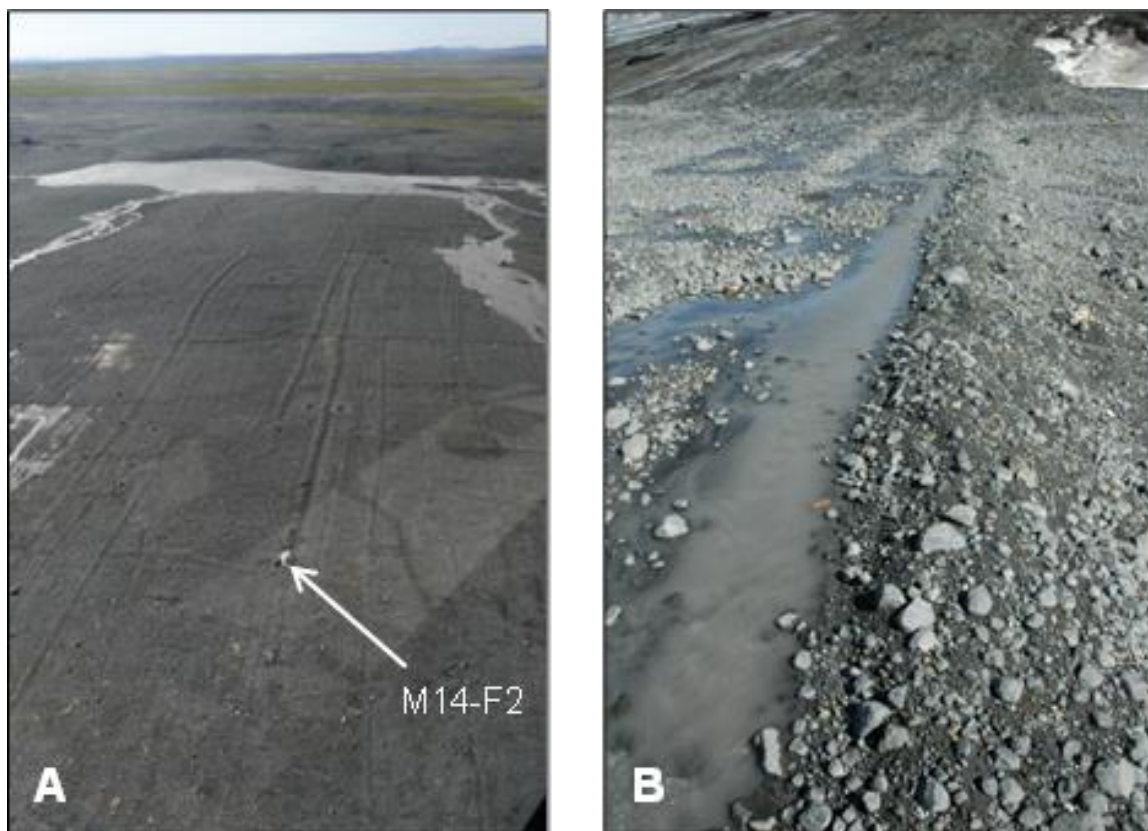


Figure 3-9. (A) View looking downglacier of M14-F2 and other flutes in the same “swarm.” (photo credit: Lucas Zoet). (B) View looking upglacier of several flutes emerging from beneath Múlajökull near M14-F2. Meltwater flows in the depressed areas on either side of the flutes and is carrying sediment in suspension.

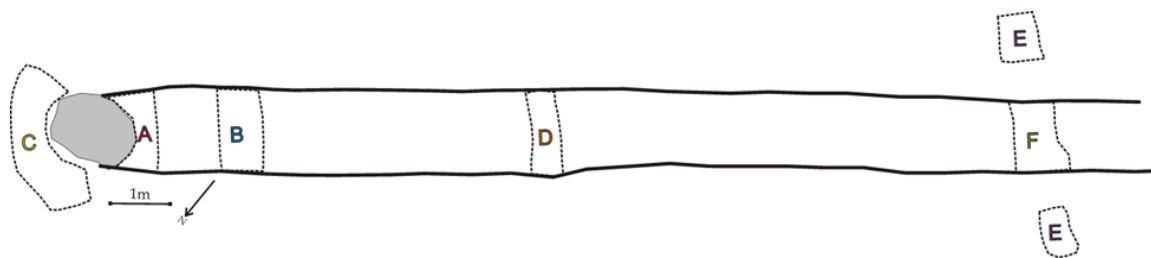


Figure 3-10. Plan view sketch of flute M14-F2, with sampling sites indicated.

3.3.2 Breiðamerkurjökull

Samples for AMS fabrics were collected from two flutes, B14-F1 and B14-F2, at Breiðamerkurjökull in August of 2014. Both flutes are long and parallel-sided with large, bulleted boulders at their heads. The flutes are located on the large, perennial island (dubbed Breiðalón after the adjacent proglacial lake) in front of the far western margin of Breiðamerkurjökull. Both flutes are primarily composed of diamicton, less than 1.0 m tall, and streamlined in the direction of glacier motion. These flutes have been exposed to sub-aerial weathering processes for several decades and are, therefore, greatly diminished in height relative to their boulders. Consequently, only the interior of B14-F1 and B14-F2 were sampled for AMS, because much of the flutes' exteriors appeared to have been slumped and winnowed.

3.3.2.1 B14- F1

Flute B14- F1 is the farther upglacier of the two Breiðamerkurjökull flutes. B14-F1 is located ~150 m upglacier of the 1998 margin (UTM 28 W 431258 E 7104287 N). The flute is ~40 m long and terminates at a transverse ridge ([Fig. 3-11](#)). The boulder at its stoss end is 0.93 m tall, 2.15 m long, 2.63 m wide, and has a “bulleted” shape ([Fig. 3-11](#) and [3-12](#)). This flute is primarily composed of a stony diamicton. The only observed exception is directly in lee of the stoss-end boulder, where there are deformed lenses of sorted, fine sand ([Fig. 3-13](#)).



Figure 3-11. *View of flute B14-F1 looking downglacier.*

Samples for 11 AMS fabrics were collected from four sites in this flute ([Fig. 3-14](#)). Samples for two fabrics were collected from each of the following: platforms at a depth of 0.30 m and 0.40 m below the top of the boulder at site A, platforms at a depth of 0.29 m and 0.50 m at site B, and a platform at a depth of 0.50 m at site C. Samples for a single fabric were collected from site D. Site D was located in unfluted till adjacent to the flute.



Figure 3-12. View looking northeast of the boulder at the head of flute B14-F1.

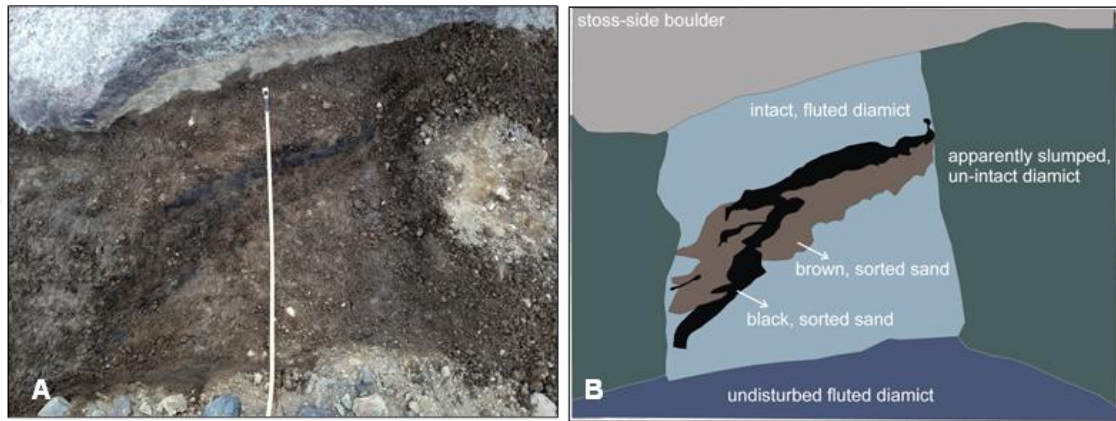


Figure 3-13. Deformed sand body in flute B14-F1 immediately downglacier of the flute's stoss-end boulder. (A) Photograph. (B) Sketch highlighting sedimentary features.



Figure 3-14. Plan view sketch of flute B14-F1, with sampling sites indicated. The hashed area in the center of the flute is where till was intact. Outer parts of the flute were either unconsolidated or had undergone slumping. AMS samples were collected only from the interior of the flute (as marked).

3.3.2.2 B14-F2

Flute B14-F2 is the farther downglacier of the two Breiðamerkurjökull flutes. The boulder at the flute's stoss end has a bullet-shaped shape and is 2.7 m wide, 3.8 m long, and 0.98 m tall and is located ~100 m upglacier of the 1965 margin and is immediately upglacier from an area of Breiðalón dominated by flow transverse ridges ([Fig. 3-15](#)). The flute is ~170 m long, trends 163° and terminates at a gully ([Fig. 3-16](#)). The flutes in this area of the forefield are ubiquitous but highly subdued.



Figure 3-15. View of flute B14-F2's stoss-end boulder looking northeast.

Six AMS fabrics were collected from three platforms in B14-F2 ([Fig. 3-17](#)). All platforms were near the base of the B14-F2, owing to its degradation ([Fig. 3-16](#)). Two fabrics were collected from a single platform at each site. The depth of the platform at site A was 1.01 m below the top of the boulder, at site B the depth was 0.85 m, and at site C the depth was 1.00 m.



Figure 3-16. View of flute B14-F2 looking downglacier. This flute is located on a densely fluted surface.

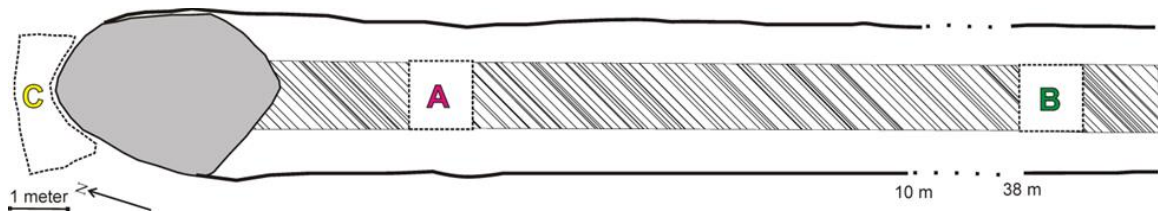


Figure 3-17. Plan view sketch of flute B14-F2, with sampling sites indicated. The hashed area in the center of the flute is where till was intact. Outer parts of the flute were either unconsolidated or had undergone slumping. AMS samples were collected only from the interior of the flute (as marked).

3.4 Magnetic mineralogy

To interpret till fabrics based on AMS measurements, the magnetic characteristics of the till being measured must be known. AMS-based fabrics have been used successfully to study deformation and strain in a number of Quaternary glacial deposits that have a small variety of magnetic mineral compositions ([Shumway and Iverson, 2009](#); [Thomason and Iverson, 2009](#); [Gentoso et al., 2012](#); [Fleming et al., 2013](#); [Vreeland et al.,](#)

[2015](#)). Several of these sediments have AMS signals dominated by magnetite ([Shumway and Iverson, 2009](#); [Thomason and Iverson, 2009](#)), whereas others are dominated by chlorite clays ([Fleming et al., 2013](#)) or maghemite ([Gentoso et al., 2012](#); [Hopkins et al., 2015](#)). In each case, knowing the magnetic mineralogy of the sediment was imperative to correctly interpreting the sediment's strain history.

The magnetic characteristics of the Múlajökull and Breiðamerkurjökull tills were identified using a series of standard geomagnetic measurements, including bulk susceptibility, susceptibility vs. temperature, susceptibility dependence on field frequency, magnetic hysteresis, and first-order reversal curves (FORC). Each of these measurements, in the order listed, provided progressively more specific diagnostic data for the magnetic characteristics of the Múlajökull and Breiðamerkurjökull tills. These tests can be used to identify specific magnetic minerals ([Table 3-1](#)), which can affect AMS measurements in different ways.

3.4.1 Bulk susceptibility

All materials, including those without a permanent magnetization, possess the property of magnetic susceptibility. The magnetic susceptibility magnitudes of ferromagnetic or ferrimagnetic materials are order(s) of magnitude larger than those that are paramagnetic or diamagnetic ([Fig. 3-18](#)). Therefore, if a small amount of a ferromagnetic or ferrimagnetic mineral is present in a sediment sample, that material will dominate the AMS signal and drown out any para- or diamagnetic contribution ([Tarling and Hrouda, 1993](#); [Tauxe et al., 2015](#)). Measuring the magnitudes of the Múlajökull and Breiðamerkurjökull tills' bulk susceptibilities allowed the estimation of the weight and volume percent of magnetic material present in the till ([Table 3-1](#); [Fig. 3-18](#)).

Table 3-1. Some generalized properties of ferromagnetic minerals. Table adapted primarily from Table 2.1 in [Tarling and Hrouda \(1993\)](#) and Table 6.1 in [Tauxe et al. \(2015\)](#). ⁽¹⁾[Dunlop and Özdemir \(1997\)](#); ⁽²⁾[Tarling and Hrouda \(1993\)](#); ⁽³⁾[O'Reilly \(1984\)](#); ⁽⁴⁾[Banerjee \(1971\)](#); ⁽⁵⁾[Dekkers \(1989\)](#); ⁽⁶⁾[Hunt et al. \(1995\)](#)

Name	Titanomagnetite 60		
	Magnetite	(TM60)	Hematite
Chemical Composition	$\alpha\text{-Fe}_3\text{O}_4$	$\text{Fe}_{2.4}\text{Ti}_{0.6}\text{O}_4$	$\alpha\text{-Fe}_2\text{O}_3$
Curie/Neel Temperature, °C, Section, Section 3.4.2	580 ^(1,2)	150 ⁽¹⁾	675-680 ^(2,3)
Saturation Magnetization, $\text{Am}^2\text{kg}^{-1}$, Section 3.4.5	90-93 ^(2,3)	24 ⁽¹⁾	0.2-0.5 ^(2,3)
Coercivity, mT, Section 3.4.5	10's, Variable ⁽³⁾	~8 ⁽¹⁾	10,000's, Widely Variable ⁽⁴⁾
Volume Susceptibility, SI, Section 3.4.1	1.0 – 5.7 ^(3,6)	0.13 – 0.62 ⁽⁶⁾	~0.001 ⁽⁵⁾
Mass Susceptibility, $\times 10^{-8} \text{ m}^3\text{kg}^{-1}$, Section 3.4.1	20,000 – 110,000 ⁽⁶⁾	2,500 – 12,000 ⁽⁶⁾	10 - 760 ^(2,6)
Density, kgm^{-3}	5197 ⁽¹⁾	4939 ⁽¹⁾	5271 ⁽¹⁾
Anisotropy Type	Shape	Shape	Magnetocrystalline

The bulk susceptibility of a material is the magnitude of a susceptibility measurement $\left(k = \frac{H}{M}\right)$ normalized by the measured sample's volume $\left(k_m = \frac{k}{V}\right)$ or mass $\left(\chi_m = \frac{k}{m}\right)$, where k is total susceptibility, χ_m is mass normalized bulk susceptibility, k_m is volume normalized bulk susceptibility, M is the magnetization, H is the applied field, V is the sample volume, and m is the mass of the sample. The volume-normalized bulk susceptibility of intact till samples was measured for this study, and their mass-normalized bulk susceptibility calculated.

The volume-normalized bulk susceptibility of each AMS sample was measured with an AGICO Geophysika MFK1-FA Multifunction Kappabridge located at University

of Wisconsin – Milwaukee. The average volume of the AMS sample boxes used in this study was measured to be 5.17 mm^3 . The mass-normalized bulk susceptibility of each AMS sample was calculated using the volume-normalized value determined with the Kappabridge to calculate the total susceptibility of the sample and then normalizing the total susceptibility value by the sample's dry unit weight. The dry unit weight of each AMS sample was measured as described in [Section 3.6.2](#) of this paper.

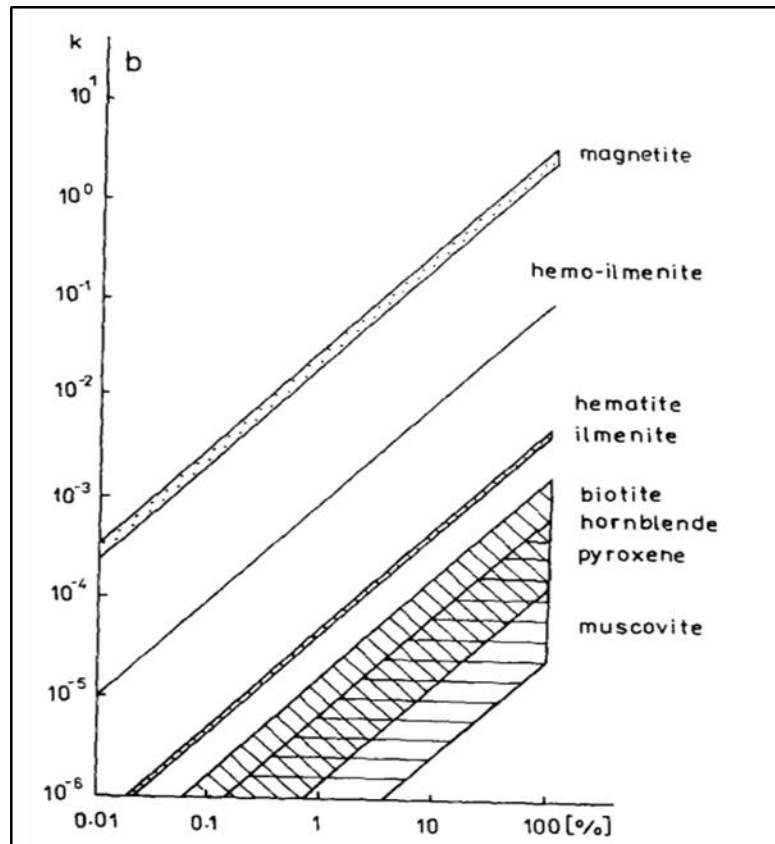


Figure 3-18. Volume normalized susceptibility (SI) vs. weight percent of mineral ([Hrouda and Kahan, 1991](#)).

3.4.2 Susceptibility vs. temperature

Experiments that reveal the relationship between susceptibility and temperature, herein called susceptibility vs. temperature experiments, were used to identify the

dominant magnetic mineralogy by identifying the temperatures from (10 K – 800 °C) at which the magnetic properties of two tills changed. The molecular exchange forces that cause the alignment of electrons in permanently magnetized materials are opposed by the thermal vibrations of those electrons ([Tarling and Hrouda, 1993](#)). For all materials there is a temperature above which the mineral will have paramagnetic characteristics ([Tarling and Hrouda, 1993](#)). This temperature is ~ 40 K for most paramagnetic materials, and ~ 580 °C for magnetite. This transition from ferro-, ferri-, or antiferromagnetic to paramagnetic can be caused either by the breakdown of links between individual electrons within a crystal lattice or through the destruction of links between internal magnetic lattices ([Tarling and Hrouda, 1993](#)). When the former occurs, the critical temperature is called the Curie temperature (T_c) and the latter occurs at the Néel temperature (T_N). For the purposes of this study, these two critical temperatures are effectively the same and can therefore be used as a method for determining the source of magnetic susceptibility in till ([Table 3-1](#)).

High-temperature susceptibility vs. temperature tests were performed at the University of Wisconsin – Milwaukee with an AGICO Geophysika MFK1-FA Multifunction Kappabridge. A small till sample was slowly heated from room temperature (~20 °C) to 800 °C and then cooled while continuously measuring the sample's total susceptibility. The “heating curve” for each sample was plotted on a graph of normalized susceptibility vs. temperature. The first derivative of each heating curve was calculated, and the temperature associated with the first derivative minima were the critical temperature(s) of the sample. The critical temperature(s) for each sample was then

compared to known magnetic mineral critical values to determine the till's primary magnetic component ([Table 3-1](#)).

Changes can also occur to a material's magnetic susceptibility at low temperatures (< 300 K), which can be diagnostic of that material's magnetic mineralogy. Magnetite, for example, undergoes a first-order, crystallographic phase transition from inverse cubic spinel to monoclinic symmetry between 110 – 125 K ([Fig. 3-19](#)) ([Verwey, 1939](#); [Verwey and Haayman, 1941](#); [Otsuka and Sato, 1986](#); [Moskowitz et al., 1998](#)). This transition is called the Verwey transition (T_v) and is marked by a sharp drop in susceptibility below that temperature ([Verwey, 1939](#); [Verwey and Haayman, 1941](#); [Moskowitz et al., 1998](#)). In oxidized magnetites and magnetites with significant cation substitution (e.g. titanomagnetite), this transition is smeared out and suppressed so that there is a gradual decrease in susceptibility with temperature ([Fig. 3-19](#)) ([Özdemir et al., 1993](#); [Moskowitz et al., 1998](#); [Kosterov, 2007](#)). The crystallographic orientation of magnetization in magnetite also undergoes a transition at ~ 130 K, where the preferred direction of magnetization in the mineral (or, "easy axis") shifts from $[111]$, where $T > \sim 130$ K, to $[100]$, where $T < \sim 130$ K ([Kakol, 1990](#); [Moskowitz et al., 1998](#); [Kosterov, 2007](#)). The magnetic susceptibility is at its maximum at this temperature, which is called the magnetic isotropic point (T_i) ([Moskowitz et al., 1998](#)). T_i is also obscured in low-temperature vs. susceptibility measurements of magnetites with increased oxidation or cation substitution ([Kakol and Honig, 1989](#); [Kakol, 1990](#); [Kakol et al., 1994](#); [Moskowitz et al., 1998](#); [Kosterov, 2007](#)).

Low-temperature vs. susceptibility measurements were performed using a Quantum Designs Magnetic Property Measurement System (MPMS) 5S ("Old Blue") at

the Institute for Rock Magnetism, University of Minnesota. One crushed bulk, representative till sample from each glacier was measured. Samples were cooled to 10 K and slowly heated up to 300 K. The in-phase (field-parallel) magnetic susceptibility (k') of the samples were measured at 10 K intervals in a 238.7 A/m AC field.

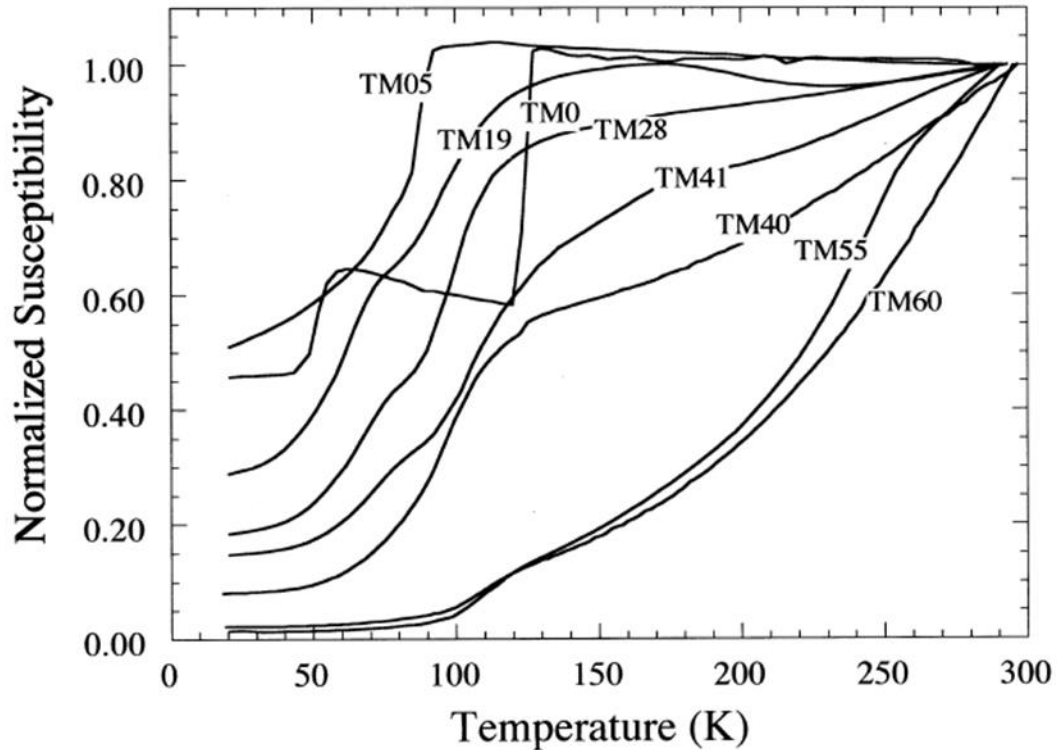


Figure 3-19. Normalized in-phase susceptibility curves of synthetic titanomagnetites during warming from 15 K to 300 K. Titanomagnetites with different degrees of titanium substitution are written as TMX, where X is the percent titanium substituting for iron in the crystal structure $[Fe_{(3-x)}Ti_xO_4]$. Single crystal samples are TM0, TM05, TM19, TM28, TM41, TM55 and polycrystalline samples are TM40 and TM60. The in-phase susceptibility was measured at 1000 Hz. Figure from [Moskowitz et al. \(1998\)](#).

3.4.3 Low-temperature magnetic remanence

Experiments that measure the magnetic remanence of sediment samples at low temperatures (20 K – 300 K) can be used to identify characteristic behaviors (like T_i and T_v), estimate oxidation state, and are much faster than those that measure susceptibility at

low temperatures ([Özdemir and Dunlop, 2010](#); [Bilardello and Jackson, 2013](#)).

Remanence vs. temperature measurements were performed on 11 sediment samples (six from Breiðamerkurjökull and five from Múlajökull) using the ‘Sweep-Cool-Warm’ sequence on a MPMS 5S (“Old Blue”) at the Institute for Rock Magnetism, University of Minnesota ([Bilardello and Jackson, 2013](#)). A 2.5 T saturation isothermal remanent magnetization (SIRM) was imparted upon each sample at room temperature. The samples were then cooled to 20 K in the absence of a magnetic field while their magnetization was measured. Another 2.5 T SIRM was imparted on the samples at 20 K. Each sample was then warmed up to 300 K while its magnetic remanence was measured.

3.4.4 Frequency dependence of magnetic susceptibility

Low-temperature MPMS experiments also included measurements of variation in magnetic susceptibility magnitude as a function AC field frequency. Frequency dependent susceptibility can be diagnostic of some magnetic minerals or of a mineral’s domain states ([de Wall and Worm, 2000](#); [Muxworthy, 2001](#)).

The percent dependence of susceptibility on frequency is defined as:

$$\chi_{FD} (\%) = 100 \cdot [(\chi_{LF} - \chi_{HF})/\chi_{LF}],$$

where χ_{LF} and χ_{HF} are susceptibilities measured in a low and high frequency AC field, respectively, χ_{ferri} is the ferrimagnetic contribution to susceptibility, and χ_{para} is the paramagnetic contribution to susceptibility ([Dearing et al., 1996](#); [Eyre, 1997](#); [Worm, 1998](#); [Muxworthy, 2001](#)). The susceptibility values used to calculate χ_{FD} for this study were measured in 238.7 A/m AC fields with frequencies of 1 Hz and 997.3 Hz at 300 K. The parameters χ_{ferri} and χ_{para} were calculated using data from magnetic hysteresis

measurements ([Section 3.4.3](#)). The χ_{LF} for each sample was then compared to known magnetic mineral properties to determine the till's primary magnetic component and, if applicable, domain state.

3.4.5 Magnetic hysteresis

Magnetic hysteresis is a property of all ferro-, ferri-, and antiferromagnetic materials that describes how the magnetization of such materials is dependent on their exposure to a magnetic field ([Krasa, 2007](#)). Magnetic hysteresis is measured by recording the magnetization (M) of a rock or sediment as a function of the magnitude of an externally applied magnetic field (B) ([Krasa, 2007](#); [Tauxe et al., 2015](#)). Magnetization is measured only in the direction of the applied field so that M and B can be treated as scalar quantities ([Krasa, 2007](#)). To measure an entire hysteresis “loop,” the applied external field is cycled from zero to a maximum positive value, back to zero, up to the maximum negative value, then back to the maximum positive value, while the corresponding M values are measured ([Krasa, 2007](#)).

Magnetic hysteresis measurements for this study were collected at room temperature using the Princeton Applied Research Vibrating Sample Magnetometer (VSM) “Old Gold” at the Institute for Rock Magnetism, University of Minnesota. A VSM measures the magnetization of a sample in an applied field by mechanically vibrating that sample at a fixed frequency passed several sensing coils. As the sample vibrates, the resulting magnetic flux induces a current in the sensing coils with electric potential proportional to the magnetization of the sample ([Krasa, 2007](#); [Williams, 2007](#)). The magnetic hysteresis of the bulk, fine and coarse fractions of three representative till samples from the two glaciers were measured at room temperature. One bulk

characteristic sample was selected from each flute (see [Section 3.3](#)) and from the well-sorted black sand at flute B14-F1 ([Section 3.3.2.1](#)).

A complete hysteresis loop yields five key measurements: the saturation magnetization (M_s), saturation remanence (M_{rs} or M_r), coercive field (B_c), coercivity of remanence (B_{cr}), and the work done during a hysteresis measurement (E_{hys}) ([Fig. 3-20](#)). M_s is the maximum magnitude of remanence magnetization a sample reaches during hysteresis measurement. M_{rs} is the magnitude of magnetization when $B = 0$ for the upper hysteresis branch. B_c is the magnitude of the applied field where $M = 0$ for the lower hysteresis branch. B_{cr} is derived from a “backfield curve” ([Krasa, 2007](#)). The backfield curve is measured by first applying the maximum magnetic field to the sample in the positive direction, and then measuring its remanence magnetization. Successively higher magnitude magnetic fields are then applied to the sample in the negative direction at discrete intervals. The remanence magnetization is measured following the application of every negative field interval. The applied field magnitude at which the remanence magnetization switches from positive to negative is B_{cr} . E_{hys} is defined as the area between the upper and lower branches of a hysteresis loop and corresponds to the energy dissipated by the magnetic system during hysteresis measurements ([Krasa, 2007](#)).

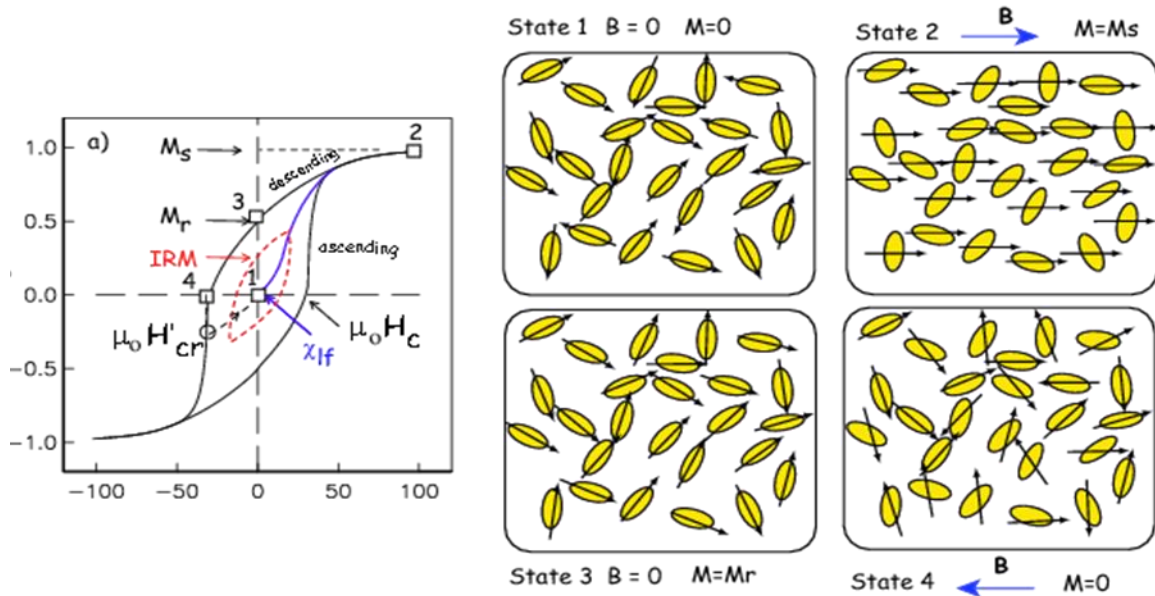


Figure 3-20. Behavior of idealized ferrimagnetic grains and associated magnetic hysteresis curve. At the beginning of the measurement (State 1) minerals are in their remanence state, so that M in the direction of the applied field is effectively zero. When M_s is reached (State 2) minerals are magnetized in the direction of the applied field. When the applied field is scaled down to zero, M_r is reached (State 3). As the applied field ramps up in the opposite direction, eventually M has no preferred orientation, and B_{cr} is measured (State 4.) Figure adapted from [Tauxe et al. \(2015\)](#).

The relative values of the five parameters M_s , M_{rs} , B_c , B_{cr} , and E_{hys} , and therefore the shape of a hysteresis loop, are dependent upon the type of permanent magnetism present (ferro-, ferri-, or antiferromagnetic), the presence or absence of paramagnetic and diamagnetic materials, the size and shape of magnetic grains, as well as the concentration and distribution of each contributing mineral ([Krasa, 2007](#)). Coercivity (B_c) and saturation magnetization (M_{rs}) magnitudes were used as diagnostic measures of the magnetic mineral content of the sample and the weight concentration of those minerals, respectively ([Table 3-1](#)).

Interpretations of hysteresis can also aid in determining the average domain state and/or mixing of domain states of the magnetic minerals present in a sample. Different

domain states (which are roughly related to the size of the magnetic mineral) behave differently during AMS measurements. Knowing the domain state, or magnetic grain size, of the magnetic minerals present in the till samples, aided in the interpretation of AMS fabrics. This can be done either quantitatively using tools like a Day plot, or qualitatively, using the shape of the hysteresis curve.

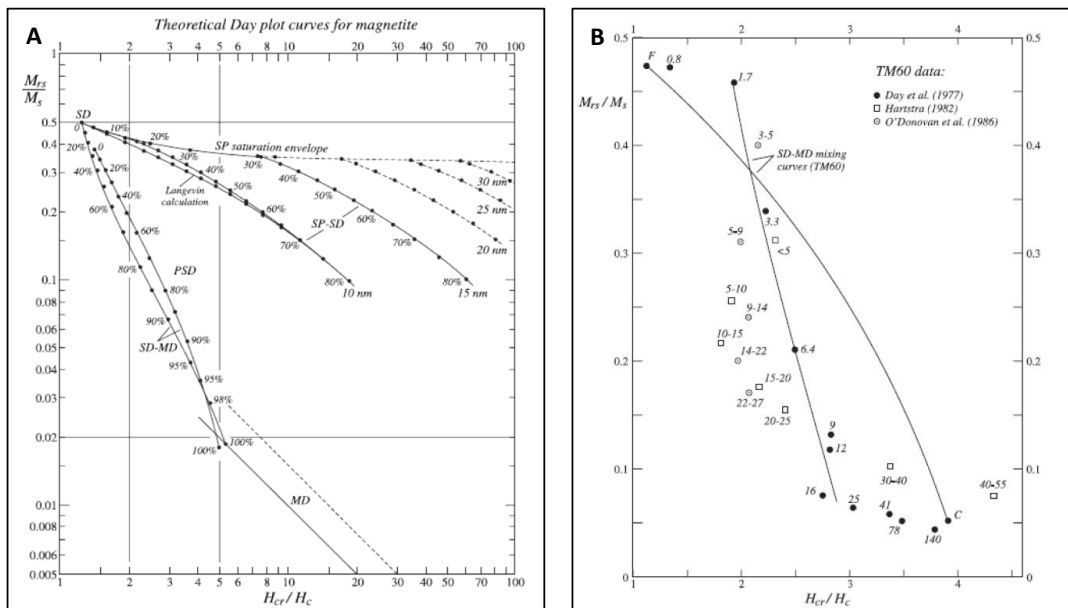


Figure 3-21. Day plots from [Dunlop \(2002\)](#) showing how hysteresis parameters can be a function of not only magnetic domain type but also of the degree of mixing between magnetic domain type and of magnetic grain size for (A) magnetite and (B) titanomagnetite.

Hysteresis results from each sample were analyzed using a Day plot ([Day et al., 1977](#); [Dunlop, 2002](#)). Day plots compare the ratios M_{rs}/M_s vs. H_{cr}/H_c ([Fig. 3-21](#)). The hysteresis parameters of various domain states and domain state mixtures of magnetite and titanomagnetite have been extensively measured, and their location on a Day plot is well constrained ([Dunlop, 2002](#); [Krasa, 2007](#)). Therefore, if a sample's magnetic signal is controlled by (titano)magnetite, the location of its hysteresis parameters on a Day plot

can be used to estimate its average domain state. Additionally, the average, grain size of the (titano)magnetite was determined by plotting the hysteresis parameters against those of (titano)magnetites of known grain sizes ([Fig. 3-21](#)) ([Dunlop, 2002](#)).

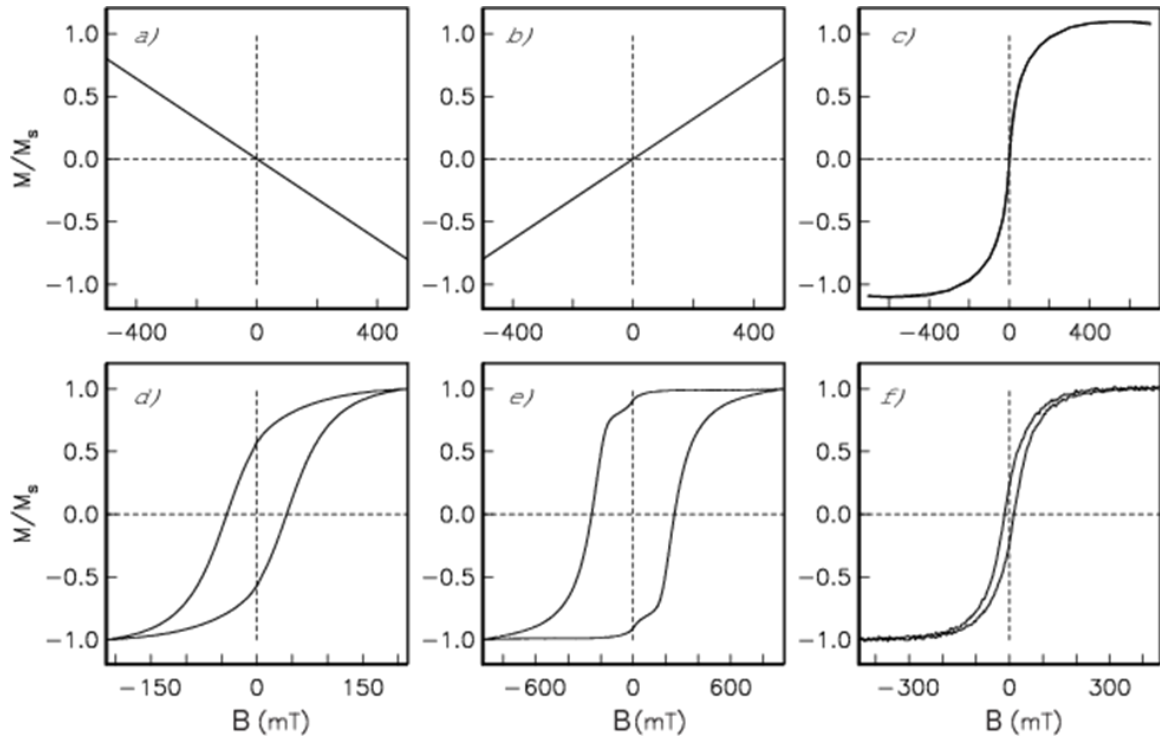


Figure 3-22. Idealized hysteresis loops of end-member behaviors: (a) diamagnetic, (b) paramagnetic, (c) superparamagnetic, (d) uniaxial, single domain, (e) magnetocrystalline single domain, and (f) pseudo-single domain. Figure adapted from [Tauxe et al. \(2015\)](#).

General information about the magnetic mineralogy can also be gleaned from a qualitative analysis of a hysteresis loop's shape ([Fig. 3-22](#)). Since diamagnetic and paramagnetic materials have negative and positive linear relationships, respectively, with applied field magnitudes, they have no magnetic hysteresis ([Fig. 3-22a, b](#)).

Superparamagnetic materials have no coercivity (B_c), but do have a saturation magnetization M_{rs} ([Fig. 3-22c](#)). Single-domain materials have relatively high coercivity values, and their shape will vary based on magnetic anisotropy type ([Fig. 3-22](#)

[d,e](#)). Pseudo-single-domain material will have relatively low coercivity values ([Fig. 3-22f](#)).

Since all ferrimagnetic minerals have a saturation magnetization, magnetic hysteresis curves can be used to estimate the fractions of a material's bulk susceptibility due to ferrimagnetism and para-, dia-, or antiferromagnetism. Naturally occurring rocks and sediments generally contain a mixture of paramagnetic, diamagnetic, antiferromagnetic, and ferrimagnetic materials, all of which contribute to that material's magnetic susceptibility. This idea can be represented simply as

$$\chi_m = \chi_{ferri} + \chi_{para} + \chi_{dia} + \chi_{antiferro}$$

([Richter and van der Pluijm, 1994](#)). The magnetic susceptibility of the paramagnetic, diamagnetic, and antiferromagnetic components of a material will continue to increase even after the ferrimagnetic component reaches saturation ([Fig. 3-22a, b](#)). Non-ferrimagnetic components will therefore contribute to a hysteresis loop in high fields, when $M > M_s$. The collective contribution of non-ferrimagnetic materials to χ_m is known as the high-field susceptibility, χ_{hf} ([Fig. 3-23](#)) ([Richter and van der Pluijm, 1994](#); [Tauxe et al., 2015](#)). High-field susceptibility can be estimated from a hysteresis loop by finding the slope of a best-fit linear regression of high-field hysteresis data, or

$$\tan \beta = \chi_{hf} = \chi_{para} + \chi_{dia} + \chi_{antiferro} ,$$

where β is the angle of χ_{hf} from horizontal ([Fig. 3-23](#)). If the high-field curve has a positive slope χ_{hf} the sample is dominated by paramagnetic materials ([Fig. 3-22b](#)) and if it has a negative slope χ_{hf} the sample is dominated by diamagnetic materials ([Fig. 3-22a](#)) ([Tauxe et al., 2015](#)). Any contribution by antiferromagnetic minerals was detected

through other tests described in this chapter. The ferrimagnetic component of susceptibility can be estimated, therefore, as:

$$\chi_{ferri} = \chi_m - \chi_{hf}.$$

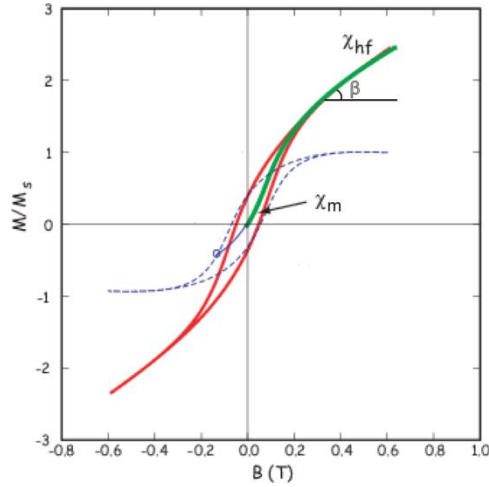


Figure 3-23. An uncorrected hysteresis curve (solid line) with a substantial high-field susceptibility (χ_{hf}) component, and a corrected hysteresis curve (dashed line) with the high-field component removed. Figure adapted from [Tauxe et al. \(2015\)](#).

3.4.6 First-order reversal curve (FORC) diagrams

Although magnetic hysteresis is able to identify the coercivity, saturation magnetization, and averaged grain size of a magnetic material, the method is unable to directly measure the distribution of magnetic domain type and hence grain size distributions in a sample ([Muxworthy and Roberts, 2007](#); [Tauxe et al., 2015](#)). FORC diagrams are advanced hysteresis tools that are used to graphically and quantitatively represent the distribution of magnetic grain sizes and specific minerals within a sample ([Muxworthy and Roberts, 2007](#); [Harrison and Feinberg, 2008](#); [Tauxe et al., 2015](#)).

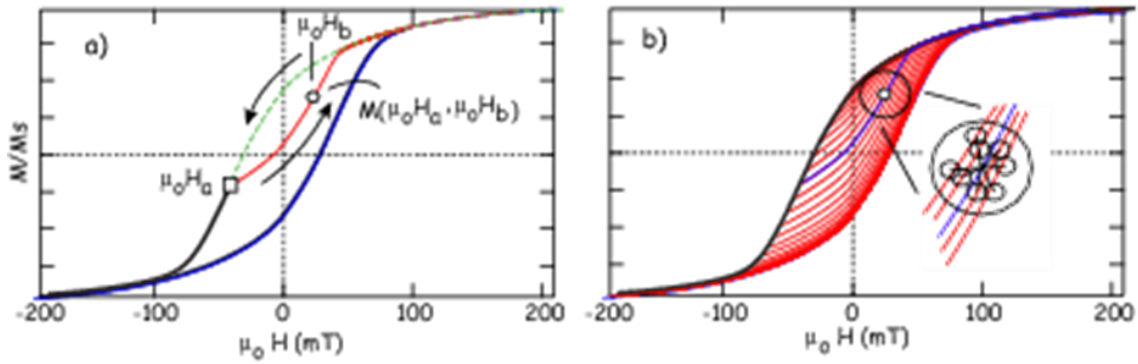


Figure 3-24. How a FORC is measured. (A) Components of a first-order reversal curve measurement. The dashed green line is the descending magnetization curve taken from H_{SAT} to some value H_A . The FORC is measured along the red line, as the applied field is increased to some magnitude $H_B > H_A$. (B) This plot shows a series FORC's measured from a single domain particle assemblage for many values of H_A . At any point for a set of FORC's there are a set of related "nearest neighbor" measurements (circles in inset). Figures were adapted from [Tauxe et al. \(2015\)](#).

FORC measurements for this study were made at room temperature with a Princeton Applied Research Vibrating Sample Magnetometer (VSM) at the Institute for Rock Magnetism, University of Minnesota. A single FORC is measured by saturating a sample in a field H_{SAT} , decreasing the field to a value H_A in the opposite direction of H_{SAT} , and finally sweeping the field back to H_{SAT} in a series of regular steps H_B ([Fig. 3-24](#)) ([Muxworthy and Roberts, 2007](#)). The magnetization M of the sample is measured at each step as a function of H_A and H_B ([Muxworthy and Roberts, 2007](#)). A function $M(H_A, H_B)$ can then be plotted as a function of H_A and H_B in field space, where a_i are fitted coefficients ([Harrison and Feinberg, 2008](#); [Tauxe et al., 2015](#)):

$$M(H_A, H_B) = a_1 + a_2 H_A + a_3 H_A^2 + a_4 H_B + a_5 H_B^2 + a_6 H_A H_B .$$

A FORC distribution (usually containing 100+ individual FORC curves from the same sample) is defined as the mixed second derivative of $M(H_A, H_B)$:

$$\rho(H_A, H_B) = -\delta^2 M \left(\frac{H_A}{H_B} \right) \frac{\delta H_A}{\delta H_B}.$$

The function $\rho(H_A, H_B)$ is then plotted as a contour plot with axes that are rotated by changing coordinates from (H_A, H_B) to $H_C = (H_B - H_A)/2$ and $H_U = (H_B + H_A)/2$ (Fig. 3-25A).

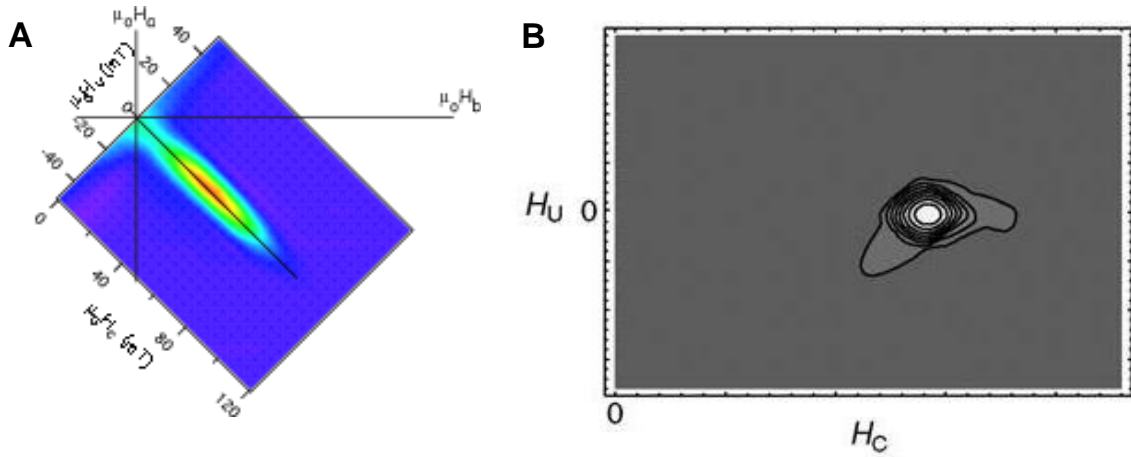


Figure 3-25. FORC diagrams. (A) An example of a FORC diagram with un-rotated axes. Figure modified from [Tauxe et al. \(2015\)](#). (B) An example of a FORC diagram with rotated axes. Figure from [Muxworthy and Roberts \(2007\)](#). Both FORC diagrams are examples from samples with single domain mineral assemblages.

Each domain state of a mineral will express itself differently in a FORC distribution diagram ([Fig. 3-25B](#); [Fig. 3-26](#)). The contour patterns of FORC diagrams were used to estimate the distribution of domain states and therefore magnetic grain sizes in the Múlajökull and Breiðamerkurjökull tills.

To restate, since MD, PSD, SD, and SP domain states of magnetic minerals all behave differently when exposed to an applied field, each type of domain state will contribute a unique signal to an AMS measurement. Knowing the distribution of magnetic mineral domain states in the Múlajökull and Breiðamerkurjökull tills improved

interpretation of AMS data. Because domain states of magnetic minerals are often controlled by the size of the magnetic mineral, knowing the distribution of domain states can contribute to understanding the physical controls on AMS fabrics.

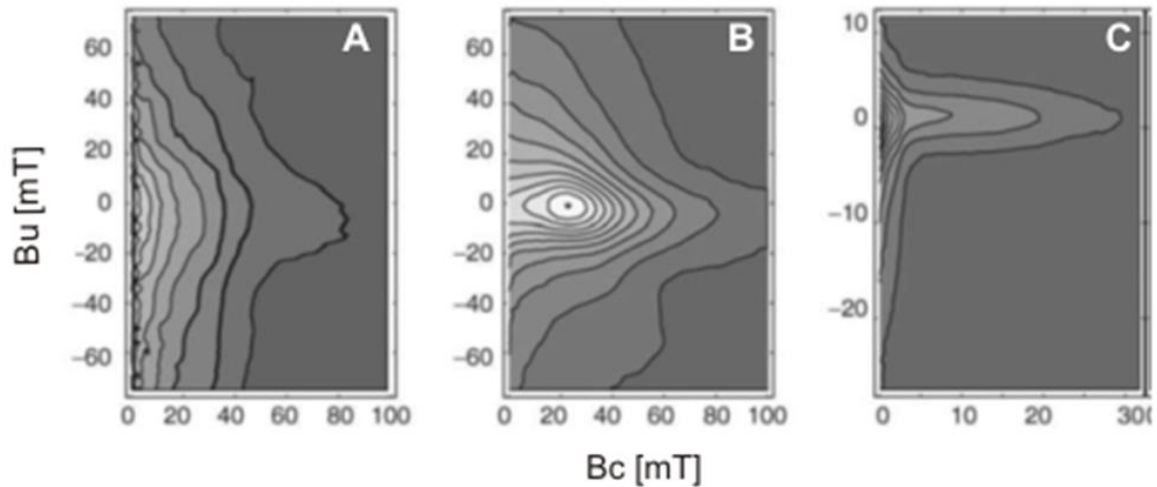


Figure 3-26. FORC diagrams have different contours depending on the magnetic grain sizes (domain states) present in the sample being measured. These diagrams show typical distributions for (A) multi-domain, (B) single-domain, and (C) pseudo-single domain magnetites. Figures are from [Muxworthy and Roberts \(2007\)](#).

3.4.7 Anisotropy of Magnetic Susceptibility Measurements

The AMS of each till sample was measured using an AGICO Geophysika MFK1-FA Multifunction Kappabridge located at University of Wisconsin - Milwaukee and processed using the accompanying Safyr4W software ([Jelinek, 1977, 1997](#); [AGICO, 2009](#)). AMS samples were measured in a 976 Hz applied field at room temperature with a 200 Am^{-1} peak intensity, using the MFK1-A's spinning specimen method ([Jelinek, 1997](#)). Each specimen was slowly rotated inside the Kappabridge's measuring coil about three perpendicular axes a1, a2, and a3, where a1 and a3 are, respectively, parallel to and perpendicular to the sampling surface ([Fig. 3-27](#)) ([AGICO, 2009](#)). 64 susceptibility

measurements were made about each axis, and the bulk susceptibility (no spin) of each sample was measured ([AGICO, 2009](#)). Second rank, primary magnetic susceptibility tensors and the associated eigenvectors (i.e., the principal susceptibility orientations) of each AMS box were calculated using the Safyr4W software ([Jelinek, 1977, 1997](#); [AGICO, 2011](#)). The azimuth of each AMS sample box as measured *in situ* was assigned to its a1 axis in the Safyr4W program, so that all resulting AMS orientation data were in geographic coordinates.

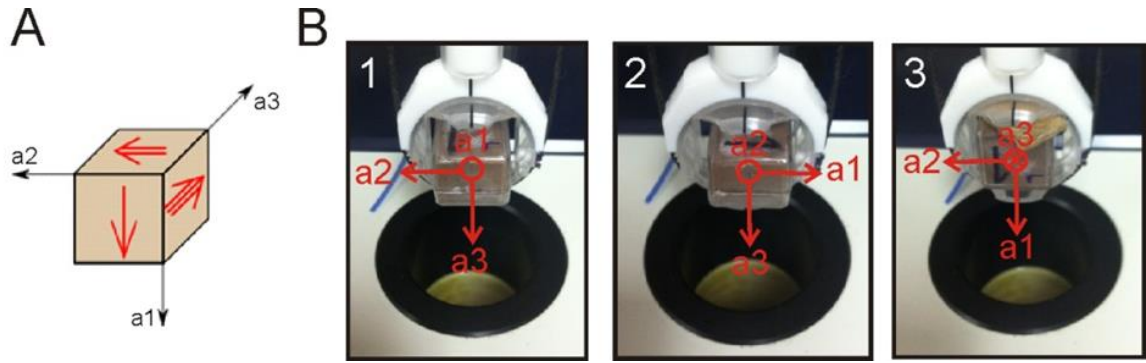


Figure 3-27. Visualizations of AMS measurements. (A) The three directions about which an AMS sample is measured in a Kappabridge (from [AGICO \(2011\)](#)). (B) The three positions of a sample box during AMS measurement.

These measurements yielded many data for each AMS sample, including the volume-normalized bulk susceptibility of the material, k_m , and symmetric second rank magnetic susceptibility tensor, \mathbf{k}_{ij} :

$$\mathbf{k}_{ij} = \begin{bmatrix} k_{11} & k_{12} & k_{13} \\ k_{21} & k_{22} & k_{23} \\ k_{31} & k_{32} & k_{33} \end{bmatrix}$$

The magnetic susceptibility tensor \mathbf{k}_{ij} is a three dimensional description of a sample's magnetic susceptibility, which is, as always, a function of the magnetic field applied to a sample (H_j) and the magnetization produced by the sample (M_i):

$$M_i = k_{ij}H_j,$$

which can be written as:

$$M_1 = k_{11}H_1 + k_{12}H_2 + k_{13}H_3$$

$$M_2 = k_{21}H_1 + k_{22}H_2 + k_{23}H_3$$

$$M_3 = k_{31}H_1 + k_{32}H_2 + k_{33}H_3.$$

([Hrouda, 2007](#); [Tauxe et al., 2015](#)). The orientations of k_1 , k_2 , and k_3 are defined by the eigenvectors of \mathbf{k}_{ij} and relative magnitudes that are the eigenvalues of \mathbf{k}_{ij} (τ_1 , τ_2 , and τ_3) (([Tauxe et al., 2015](#))). In a Cartesian coordinate system defined by these eigenvectors, the preceding equations simplify to:

$$M_1 = k_{11}H_1$$

$$M_2 = k_{22}H_2$$

$$M_3 = k_{33}H_3$$

([Hrouda, 2007](#)). The components $k_{11} > k_{22} > k_{33}$ will hereafter be noted as $k_1 > k_2 > k_3$.

3.4.7.1 Anisotropy parameters

Parameters calculated using the eigenvalues τ_1 , τ_2 , and τ_3 were used to determine the significance of each till sample's AMS ellipsoid. Three F statistics exist to describe anisotropy of second order tensors and were used determine if the principal susceptibilities k_1 , k_2 , and k_3 were significant from one another ([Hext, 1963](#); [AGICO, 2009](#); [Tauxe et al., 2015](#)). These F statistics, defined by [Hext \(1963\)](#), were calculated as follows:

$$F = 0.4 \frac{(\tau_1^2 + \tau_2^2 + \tau_3^2 - 3k_b^2)}{\sigma_v^2}$$

$$F_{12} = 0.5 \left(\frac{\tau_1 - \tau_2}{\sigma_v} \right)^2$$

$$F_{23} = 0.5 \left(\frac{\tau_2 - \tau_3}{\sigma_v} \right)^2$$

where $\sigma_v = \sqrt{\frac{S_o}{n_f}}$ is the estimated variance of the data, n_f is the number of degrees of freedom, given by the number of measurements less six ($n_f = N_{measure} - 6$), and S_o is the residual sum of squares ([Hext, 1963](#); [Tauxe et al., 2015](#)). The F parameter tests for the significance of overall anisotropy of the sample; F_{12} tests for a significant difference between k_1 and k_2 , and F_{23} tests for a significant difference between k_2 and k_3 . If any of the F values of a sample fell below critical values, the sample's AMS signal was considered to be isotropic and was not used in subsequent calculations of susceptibility parameters or fabric orientation.

If a sample had an AMS signal that was significantly anisotropic (passed all F -tests), then two shape parameters that are functions of the normalized susceptibility values k_1 , k_2 , and k_3 were used to describe its shape: lineation (P_1), and foliation (P_3) ([Balsley and Buddington, 1960](#); [Jelinek, 1981](#); [Tarling and Hrouda, 1993](#)). Lineation is defined as $P_1 = \frac{k_1}{k_2}$ and foliation as $P_3 = \frac{k_2}{k_3}$ ([AGICO, 2011](#)). Lineation and foliation were compared using a Flinn plot to help differentiate among magnetic minerals ([Fig. 3-28](#)) ([Flinn, 1962](#); [Hrouda, 2007](#)). Although the AMS fabric shape of rocks is often related to strain magnitude and type, ring-shear experiments on basal tills have identified no discernable relationship between AMS fabric shape and shear strain magnitude ([Hooyer](#)

[et al., 2008](#)). Although the anisotropy of a sedimentary AMS ellipsoid is generally less than 5%, its shape can still be controlled by the minerals contained in the sediment ([Weiler, 2007](#)).

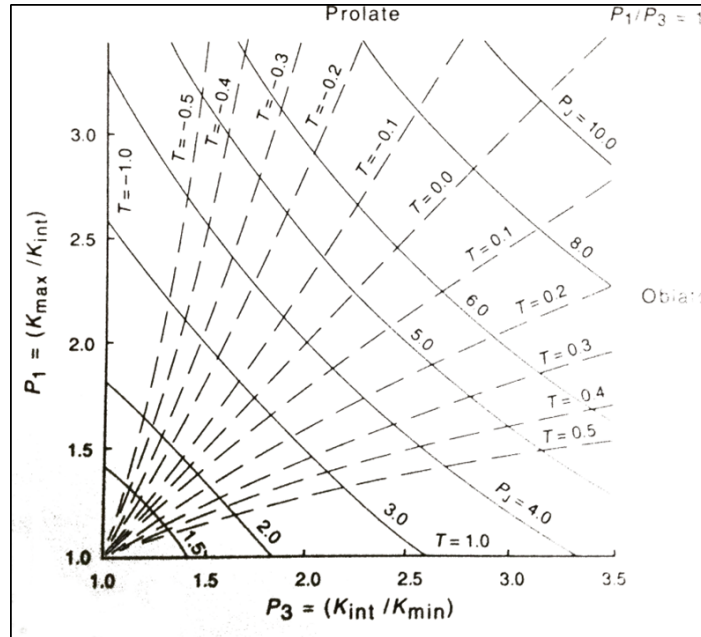


Figure 3-28. Bivariate Flinn plot of the lineation (P_1) vs. foliation (P_3) of an AMS ellipsoid. The shape parameter (T) and the corrected degree of anisotropy (P_j) are also shown. Figure is from [Tarling and Hrouda \(1993\)](#).

3.5 Fabric analyses

In order to describe the magnetic fabric of a sedimentary unit, the spatial distribution of the orientations of the maximum (k_1), intermediate (k_2), and minimum (k_3) susceptibilities measured for 25 or more AMS samples had to be statistically analyzed ([Hooyer et al., 2008](#); [Iverson et al., 2008](#)). Prior to statistical analysis, each AMS sample was assigned a three-dimensional coordinate describing its position in the flute. Sets of samples were then selected for analysis based on their position. This method of grouping was used to resample AMS data in order to identify the most statistically significant and consistent fabric trends. The orientations and shapes of the k_1 , k_2 and k_3 axes of each

fabric were then determined through principal component analyses. The distributions of principal susceptibility orientations were described using the appropriate probability density function or best-fit great circle.

3.5.1 Flute coordinate system

The coordinates of sample locations were measured in reference to the farthest downglacier, central point on the top of a flute's stoss-side boulder, so that x is the distance from the boulder, y is the distance from the center of the flute, and z is the depth below the boulder ([Fig. 3-29](#)). The x , y , and z coordinates of the AMS boxes were normalized in relation to the height of the flute's stoss-side boulder (D), width of the flute (W), and length of the flute (L), so that:

$$x' = \frac{x}{L}; y' = \frac{2 \cdot y}{W}; z' = 1 - \frac{z}{D}.$$

Every AMS sample box taken from a single sampling platform was assigned the same z value. Sampling platforms at Múlajökull and Breiðamerkurjökull were not perfectly horizontal due to the rocky nature of the tills. Each z measurement should therefore be considered to have an error of ± 2.5 cm. The x and y location of every AMS sample box was measured using photographs of the sampling site taken in the field. A Matlab script was used that allowed box locations to be manually selected from a photograph of the field site ([Appendix A](#)).

If the precise location of an individual measurement (either AMS or pebble) was unknown, that sample was assigned a location in the flute based on the location of its sample set.

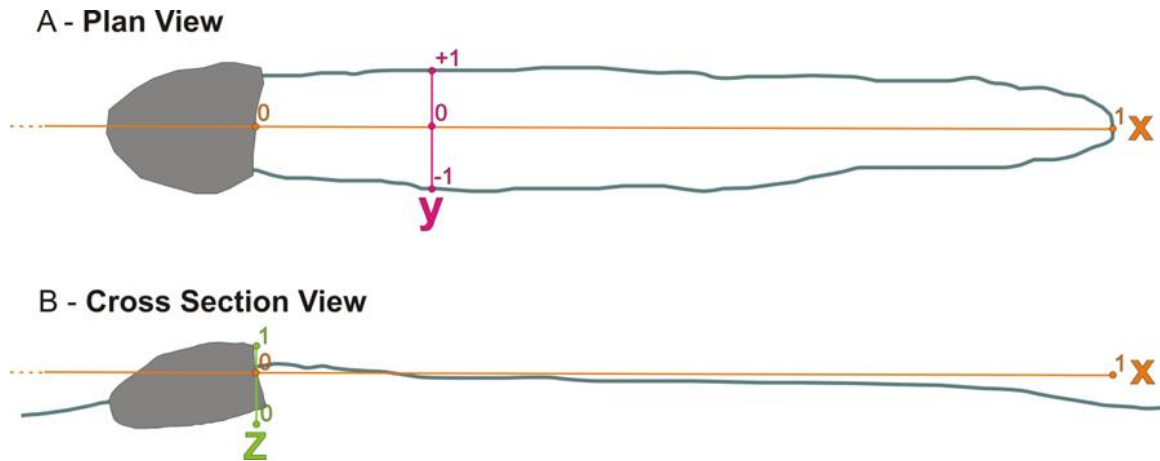


Figure 3-29. (A) Plan view and (B) cross sectional view of a “standard” flute with the orientation and magnitudes of the normalized, three-dimensional flute coordinate system used in this study.

3.5.2 Fabric directional analyses

Till that has experienced moderate to high shear strains (> 7) will produce a strongly triaxial fabric (orthogonally clustered k_1 , k_2 and k_3 orientations) that can be satisfactorily described using an orientation-tensor (i.e. principal component) analysis ([Hooyer et al., 2008](#); [Iverson et al., 2008](#)). Till subjected to smaller shear strains yield non-triaxial or weakly triaxial AMS fabrics whose distributions cannot be adequately described using only a principal component analysis. Both weakly-triaxial and non-triaxial AMS fabrics were common in the flute fabrics measured in this paper. To differentiate between and better describe AMS fabrics that are not strongly triaxial, spherical probability density analysis was employed, in addition to orientation tensor (principal component) analysis, to determine fabric orientation and shape. In geomagnetism, the application of spherical probability density functions (PDF's) is a common approach to describing the distribution of vectors ([Fisher, 1953](#); [Watson, 1966](#); [Bingham, 1974](#); [Fisher et al., 1987](#); [Borradaile, 2003](#); [Tauxe et al., 2015](#)). Because PDF's impose confidence limits to the data, fabric shape could be more accurately inferred.

3.5.2.1 Orientation tensor method

The purpose of the orientation-tensor method is to characterize the dispersal and principal orientation of a set of three dimensional axial data with an unknown distribution ([Watson, 1966](#)). The orientation tensor method, sometimes referred to as a principal component analysis or “eigenvalue” method, was developed to describe the principal orientation, often referred to colloquially as the “mean” orientation, for a set of three-dimensional vectors ([Scheidegger, 1964, 1965](#); [Watson, 1966](#)). Many geologic disciplines, including geomagnetism, use the orientation-tensor method to determine the principal orientation for a set of three-dimensional unit vectors ([Fara and Scheidegger, 1963](#); [Watson, 1966](#); [Mark, 1973](#); [Naylor and Woodcock, 1977](#); [Woodcock, 1977](#); [Love, 2007b](#)). Originally developed for the study of earthquake fault planes and paleomagnetic vectors, the orientation-tensor method has also been employed widely to describe clast fabrics of glacial sediments ([Mark, 1973](#); [Woodcock, 1977](#); [Benn, 1994a](#)).

The orientation tensor, \mathbf{T} , is a symmetric, second rank tensor that is described in detail in [Appendix C](#). This tensor has three eigenvalues:

$$\lambda_1 \geq \lambda_2 \geq \lambda_3 \geq 0; \lambda_1 + \lambda_2 + \lambda_3 = N,$$

where N is the number of samples. Eigenvalues are normalized so that:

$$S_1 = \frac{\lambda_1}{N}; S_2 = \frac{\lambda_2}{N}; S_3 = \frac{\lambda_3}{N}; S_1 + S_2 + S_3 = 1$$

The tensor \mathbf{T} also has three eigenvectors V_1 , V_2 , and V_3 , which are mutually orthogonal and describe the orientation of the maximum, intermediate and minimum clustering, respectively.

A Matlab script was written to calculate the orientation-tensor eigenparameters of AMS and pebble fabrics that are reported in the results section. This script, as well as details on the orientation tensor-method, is reported in [Appendix B](#).

3.5.2.2 Describing fabric shape using normalized eigenvalue ratios

The relative magnitudes of the normalized eigenvalues for any orientation tensor, \mathbf{T} , have been shown to reflect the distribution of vector data and are therefore widely used in glacial geology to describe the “shape” of till fabrics ([Watson, 1966](#); [Mark, 1974](#); [Woodcock, 1977](#); [Fisher et al., 1987](#); [Benn, 1994a](#)). Quantifying the shape of each AMS fabric in this study provided the criterion for whether a set of orientations had an isotropic, girdled, or clustered distribution. A perfectly isotropic fabric, with orientation data distributed evenly, would yield normalized eigenvalues of $S_1 = S_2 = S_3 = \frac{1}{3}$. Normalized eigenvalues that represent a girdled fabric, with unit vectors distributed about a great circle, would have values of $S_1 \approx S_2 \gg S_3$. A clustered fabric that consists of roughly aligned unit vectors would have normalized eigenvalues of $S_1 \gg S_2 \gg S_3$. In reality, there are continuums of fabric shapes that can be represented by the relative values of normalized eigenvalues. Two methods for quantitatively describing fabric shape were used in this study: an equilateral ternary diagram [Benn \(1994a\)](#) and a biaxial logarithmic plot [Woodcock \(1977\)](#).

The [Benn \(1994a\)](#) ternary diagram is a useful visual and quantitative aid for classifying sedimentary fabrics. The Benn ternary diagram compares the elongation index ($E = 1 - S_2/S_1$) and isotropy index ($I = S_3/S_1$) of a fabric ([Fig. 3-30](#)). The elongation index indicates the degree to which orientation data are clustered. The isotropy index

indicates the extent to which orientation data lie in a plane. [Benn \(1994a\)](#) also suggested the use of a cluster-girdle index ($CGI = (S_1 - S_2)/(S_1 - S_3)$). If $CGI = 0$ the axes are girdled, and if $CGI = 1$ the data are perfectly clustered. The quantitative divide between a clustered or girdled fabric is presumed to be $CGI = 0.5$.

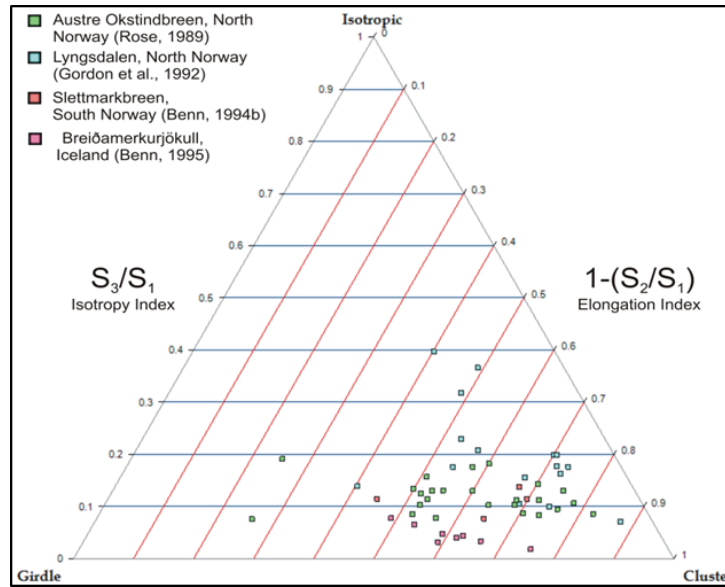


Figure 3-30. A Benn ternary diagram. Flute pebble fabric parameter from four studies at four different glaciers are plotted.

The parameters used in the [Woodcock \(1977\)](#) biaxial logarithmic plot can be used to quantify both the strength and shape of a fabric. This plot, which is based on the Flinn plot ([Fig. 3-28](#)), characterizes fabric shape using four normalized eigenvalue ratios: $r_1 = \ln(S_2/S_3)$, $r_2 = \ln(S_1/S_2)$, $K = (r_2/r_1)$, and $C = \ln(S_1/S_3)$ ([Fig. 3-31](#)). The meanings of these normalized eigenvalue ratios are very similar to E , I and CGI used in the Benn ternary diagram. If $r_1 = 0$, then $S_2 = S_3$, and orientations are perfectly clustered. If $r_2 = 0$, then $S_1 = S_2$, and orientations are perfectly girdled. The parameter K quantifies the extent to which a fabric is clustered or girdled. For an equal tendency toward both, $K = 1$, for girdled fabrics $0 \leq K < 1$, and for clustered fabrics $1 < K \leq \infty$.

The strength of the preferred orientation of a fabric is measured by the parameter C . If $C = 0$, orientations are isotropic, and the fabric will plot near the origin. For greater fabric strengths, the C parameter is larger. This plot does not characterize endmember (perfectly clustered or perfectly girdled) fabrics as well as a Benn ternary diagram (Benn, 1994a). The Woodcock biaxial log plot, on the other hand, displays intermediate fabrics with greater resolution.

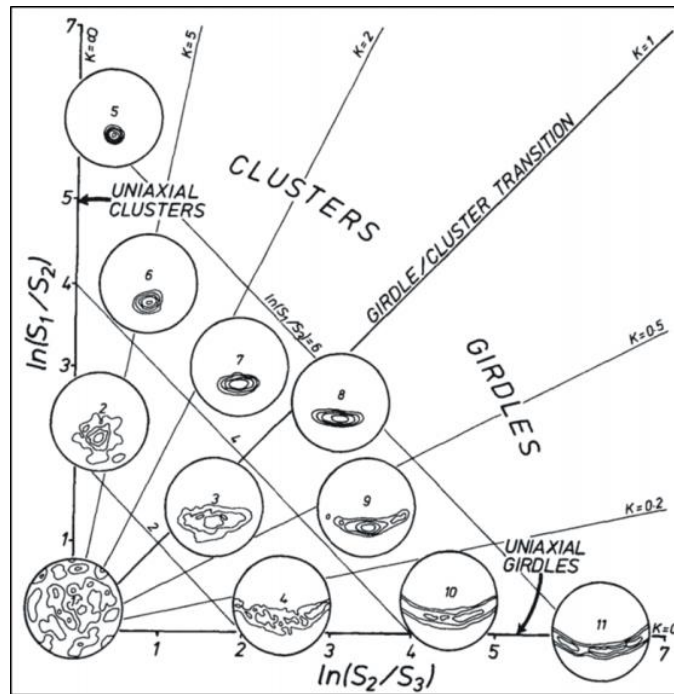


Figure 3-31. Woodcock biaxial logarithmic plot. Figure from [Woodcock \(1977\)](#).

A Matlab script was written, using sources cited in this section, to calculate normalized eigenvalue ratios. This script is reported and described in [Appendix B](#).

3.5.2.3 Spherical probability density functions

While the shape parameters associated with the orientation tensor method are useful in describing the general shape of a fabric, the method does not provide a means to determine if two sets of directional data are distinct. Because poorly clustered AMS data

were common in this study, a different analysis that included a confidence measure was needed. Spherical probability density functions (PDFs) are commonly used in paleomagnetism and structural geology to determine the characteristic orientation and directional confidence for a set of vectorial data. Several PDFs for spherical data exist that satisfactorily describe a confidence interval about a reference orientation for orientation data that have elliptical, girdled, and/or bimodal distributions – common distributions in the AMS data of this study. By characterizing two or more sets of AMS fabric data using PDF analysis, differentiating strain style and orientation in seemingly indistinct flute AMS and pebble fabric data was possible.

A spherical PDF describes how densely a population of data is clustered about a single vector, for an assumed distribution of that data. PDFs are determined for an area, defined by the angular difference from some unit vector, which encloses a certain fraction of the population of orientation data. For spherical data, the reference vector can either be the principal orientation that results from orientation-tensor analysis or the unit vector sum of the data. The principal component (V_I) was used as the reference vector for all PDF analysis in this study because the principal component more accurately reflects the orientation of apparent bimodal data. A set of nearly-parallel vectors that are close to horizontal but with subgroups plunging in opposite directions, like many of the k_1 and k_2 fabrics of this study, can appear to have a bimodal distribution to both human eyes and certain statistical analyses because their trends are separated by $\sim 180^\circ$ ([Fig. 3-32](#)).

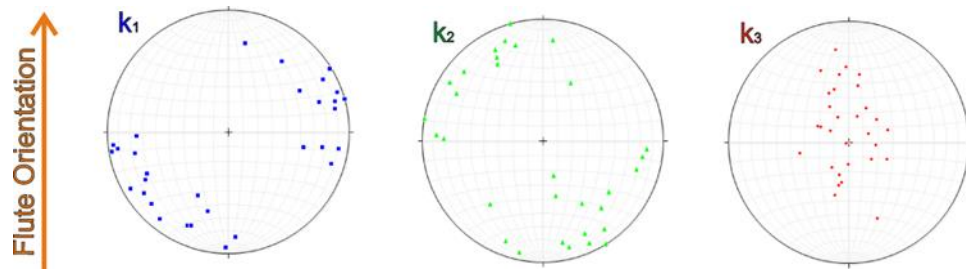


Figure 3-32. Examples of typical k_1 , k_2 , and k_3 AMS axial orientations displayed on lower hemisphere, equal area stereonet. The apparent bimodal distribution of k_1 and k_2 vectors is typical of AMS fabrics from all flutes used in this study. These data were measured from 31 AMS sample boxes collected from flutes M14-F2 and B14-F1, and their trend normalized by their respective flute orientations.

Since PDF's inherently assume a distribution, in order to accurately describe AMS and pebble fabric shape, the appropriate PDF must be used for a set of data. The fabrics considered in this study were unique on two accounts: both symmetric and non-symmetric distributions were common and apparent bimodal distributions were ubiquitous. The PDFs that can most accurately describe distributions with those characteristics are the Watson and Bingham distributions ([Fisher, 1953](#); [Bingham, 1964](#); [Watson, 1966](#); [Bingham, 1974](#); [Fisher et al., 1987](#); [Borradaile, 2003](#); [Love, 2007a](#); [Tauxe et al., 2015](#)). The Watson and Bingham distributions can both be applied to apparently bimodal data ([Fisher et al., 1987](#); [Tauxe et al., 2015](#)). The simplest and most widely used spherical PDFs, like the Watson, assume that data are symmetrically distributed about some “mean” vector, whereas others have been developed to describe non-symmetrical (elliptical) distributions of spherical data, like the Bingham ([Fisher, 1953](#); [Bingham, 1964](#); [Watson, 1966](#); [Bingham, 1974](#); [Fisher et al., 1987](#); [Borradaile, 2003](#); [Love, 2007a](#); [Tauxe et al., 2015](#)). A symmetrical PDF can accurately describe the distribution of only symmetrically clustered vectors and will misrepresent a set of vectors that has an elliptical distribution ([Fisher et al., 1987](#); [Borradaile, 2003](#)). Likewise, a non-symmetrical

PDF will misrepresent symmetrically distributed vectors ([Fisher et al., 1987](#); [Borradaile, 2003](#)).

The Watson PDF is defined as:

$$F_W = C_W \exp[\kappa \cos^2 \theta],$$

where $C_W = 1 / \left(4\pi \int_0^1 \exp -(\kappa u^2) du \right)$ and θ is the angular difference from the axis of symmetry (Fisher et al, 1987; Tauxe et al., 2014; Watson, 1966). The shape parameter κ is called the concentration parameter. For larger values of κ , the distribution about the principal orientation is more clustered. As $\kappa \rightarrow \infty$, the distribution of orientations approaches uniformity. The parameter κ can be estimated as $\kappa' \cong \frac{N-1}{N-R}$.

The Bingham PDF is a five parameter model and is defined as

$$F_B = C_b \exp(\kappa_1 \cos^2 \phi + \kappa_2 \sin^2 \phi) \sin^2 \alpha$$

where $C_b = 1 / \left(4\pi d(\kappa_1, \kappa_2) \right)$ (Tauxe et al., 2014). Here, α is the angle between a given direction and the axis of symmetry, and ϕ is the angle in the V_2 - V_3 plane. The function $d(\kappa_1, \kappa_2)$ provides a normalization factor given by:

$$d(\kappa_1, \kappa_2) = \frac{1}{4\pi} \int_0^{2\pi} \int_0^\pi \exp((\kappa_1 \cos^2 \phi + \kappa_2 \sin^2 \phi) \sin^2 \theta) \sin \theta d\theta d\phi,$$

where κ_1 and κ_2 are concentration parameters. Bingham or Watson distributions were fit to the appropriate AMS fabric data using the Fisher and Bingham functions of the PmagPy script eqarea_ell.py ([Tauxe, 2015](#)).

For every fabric, the general shape of each principal component distribution (V_1 , V_2 , and V_3) was determined prior to applying a specific PDF to the data ([Fig. 3-33](#)). For

this study, the distribution of a set of orientations (k_1 , k_2 , or k_3) was described as either isotropic, girdled, Watson-clustered, or Bingham-clustered. A set of orientations was considered to have an isotropic distribution if $I \geq 0.21$ and $C < 1.56$ ([Fig. 3-33](#); [Table 3-2](#)). No thresholds for isotropic fabrics are suggested in the literature. Therefore, threshold values for I and C are based on values from fabrics developed in ring-shear experiments, and flute AMS fabrics from this study. If orientations were anisotropic, they could either be girdled or clustered. A fabric was considered to have a girdled distribution if $K > 1$ or $CGI > 0.5$ ([Woodcock, 1977](#); [Benn, 1994a](#)). If orientations did not have an isotropic or a girdled distribution, data were considered to be clustered. A test for symmetrical uniformity was used to differentiate between Watson-clustered and Bingham-clustered axial distributions. If the mean vector length of the data was too small, then the data were considered to have a non-symmetrical distribution, and if the mean vector was sufficiently long, the data were considered to have a symmetrical distribution ([Appendix C](#)) ([Fisher et al., 1987](#)). The Watson and the Bingham PDFs were applied, respectively, to data that were symmetrically and unsymmetrically distributed. [Appendix C](#) describes in more detail the method used to differentiate between symmetrically and unsymmetrically distributed, clustered, orientation data.

Table 3-2. AMS fabric data from tills sheared in ring-shear experiments ([Hooyer et al., 2008](#); [Shumway and Iverson, 2009](#); [McCracken, 2015](#)).


(A) Batestown Till	B9			B12			B13			B10			B11			B7			B8		
Strain Magnitude	0			0.1			0.7			2			27.8			64.8			70		
Ellipsoid Shape	Isotropic			Isotropic			Isotropic			Sub-Prolate			Triaxial			Triaxial			Triaxial		
	k1	k2	k3	k1	k2	k3	k1	k2	k3	k1	k2	k3	k1	k2	k3	k1	k2	k3	k1	k2	k3
V1 dec	82.84	3.70	28.69	24.54	323.87	323.01	272.37	5.37	339.64	348.38	233.43	331.50	3.21	93.83	5.32	327.35	66.38	366.01	369.81	270.14	357.77
V1 inc	13.90	19.05	61.40	9.83	36.56	55.55	9.65	22.78	59.76	27.15	24.97	66.67	25.92	1.63	64.71	20.69	5.42	66.37	26.10	1.25	61.06
V2 dec	345.23	285.83	290.34	286.81	299.54	83.54	9.21	85.86	65.10	84.83	293.40	81.36	271.42	5.36	275.05	62.31	333.32	8.75	65.48	356.63	88.67
V2 inc	28.14	31.31	4.47	37.81	50.86	19.19	35.00	21.49	2.64	12.35	47.06	8.73	3.68	43.27	0.13	12.89	20.72	23.11	40.07	70.40	-0.50
V3 dec	16.21	67.32	17.94	305.67	44.76	3.92	349.19	317.18	333.57	16.86	340.66	355.01	363.91	2.10	4.98	2.15	349.33	278.75	292.97	0.58	368.95
V3 inc	58.04	52.14	28.19	50.48	12.06	27.37	53.30	57.79	30.10	59.73	32.32	22.52	63.78	46.68	25.29	65.30	68.52	4.66	38.77	19.56	28.94
S1	0.49	0.46	0.63	0.50	0.40	0.47	0.55	0.53	0.71	0.73	0.51	0.55	0.94	0.90	0.93	0.65	0.57	0.90	0.95	0.81	0.81
S2	0.41	0.34	0.22	0.34	0.37	0.33	0.34	0.30	0.15	0.21	0.32	0.35	0.05	0.06	0.06	0.31	0.27	0.06	0.03	0.16	0.17
S3	0.10	0.20	0.15	0.18	0.23	0.19	0.11	0.16	0.14	0.06	0.16	0.10	0.01	0.05	0.01	0.04	0.06	0.03	0.02	0.03	0.03
CGI (Benn, 1994a)	0.14	0.45	0.85	0.48	0.16	0.60	0.48	0.62	0.97	0.77	0.54	0.42	0.96	0.99	0.96	0.96	0.66	0.94	0.99	0.82	0.81
K (Woodcock, 1977)	0.22	0.54	2.73	0.49	0.15	0.64	0.43	0.91	13.33	0.94	0.66	0.38	2.06	11.52	1.89	0.36	0.60	2.29	18.05	0.89	0.69
I (Benn, 1994a)	0.20	0.44	0.24	0.32	0.59	0.41	0.20	0.31	0.19	0.08	0.31	0.18	0.01	0.05	0.01	0.06	0.09	0.03	0.02	0.03	0.02
C (Woodcock, 1977)	1.59	0.82	1.44	1.14	0.52	0.90	1.62	1.18	1.64	2.54	1.16	1.70	4.34	2.99	4.27	2.83	2.42	3.53	3.81	3.38	3.86
 Sense of Shear																					
Axial Distribution	Isotropic	Isotropic	Isotropic	Isotropic	Isotropic	Isotropic	Isotropic	Isotropic	Isotropic	Bingham	Isotropic	Isotropic	Watson	Bingham	Watson	Bingham	Bingham	Watson	Watson	Bingham	Bingham
Girdle																					
Strike																					
Dip																					
Watson (Fisher)																					
alpha													5.9		6.1			6.9	5		
Bingham																					
Ela										16.9				7.2		23.9				13.2	13.2
Zeta										8.1				5.9		6.4				4.6	4.6

Table 3-2, continued.

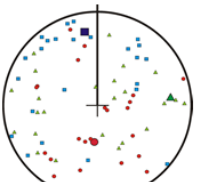
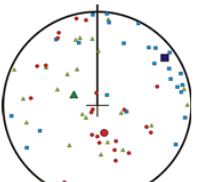
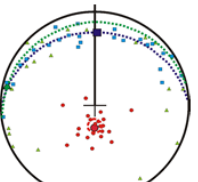
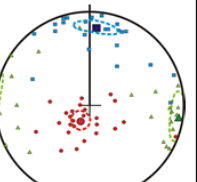
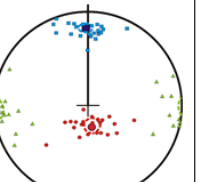
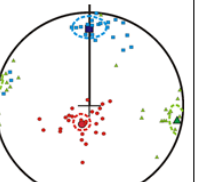
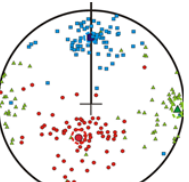
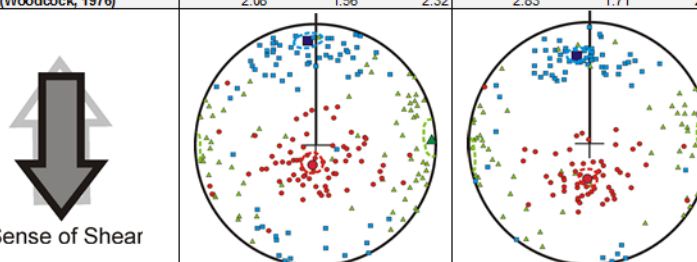
(B) Douglass Till	D3			D4			D5			D1			D6			D2			Shumway & Iverson (2009)			
Strain Magnitude	0			0.1			2.1			6.3			25			70			714			
Ellipsoid Shape	Isotropic			Isotropic			Oblate			Triaxial			Triaxial			Triaxial						
	k1	k2	k3	k1	k2	k3	k1	k2	k3	k1	k2	k3	k1	k2	k3	k1	k2	k3	k1	k2	k3	
V1 dec	350.41	83.91	356.35	54.57	304.41	345.79	2.02	281.86	357.31	5.12	277.55	28.96	358.38	266.45	347.62	5.52	279.58	25.42	359.30	272.71	17.97	
V1 inc	20.65	22.60	51.92	11.63	53.39	65.04	22.18	4.85	71.52	16.39	5.59	74.60	17.41	2.90	72.36	14.14	5.66	74.25	27.71	6.86	58.49	
V2 dec	80.84	76.93	349.89	323.08	343.41	319.68	271.45	12.84	84.50	277.21	7.08	270.66	274.13	353.92	83.39	274.55	4.15	68.19	273.92	10.46	272.64	
V2 inc	1.15	67.25	37.91	7.23	30.00	22.68	1.41	11.44	0.94	7.07	4.72	7.44	17.70	57.33	1.83	3.84	43.69	11.70	8.72	48.26	8.86	
V3 dec	353.89	352.88	82.34	21.85	61.96	53.85	357.99	349.27	354.19	29.73	57.09	358.88	46.72	0.30	353.97	349.70	15.41	336.01	19.80	356.72	357.48	
V3 inc	68.31	2.49	3.14	76.26	18.97	-9.87	67.77	77.55	-18.45	72.07	82.67	13.40	64.75	32.51	17.53	75.33	46.75	10.40	60.72	40.91	29.96	
S1	0.51	0.44	0.49	0.61	0.45	0.53	0.56	0.55	0.52	0.76	0.72	0.83	0.95	0.89	0.91	0.82	0.83	0.89	0.83	0.76	0.78	
S2	0.35	0.39	0.28	0.27	0.31	0.34	0.43	0.40	0.04	0.20	0.20	0.12	0.04	0.07	0.07	0.15	0.11	0.07	0.11	0.13	0.14	
S3	0.14	0.17	0.22	0.12	0.24	0.13	0.01	0.05	0.03	0.04	0.09	0.05	0.02	0.04	0.01	0.03	0.05	0.04	0.06	0.11	0.08	
CGI (Benn, 1994)	0.42	0.17	0.77	0.68	0.67	0.47	0.24	0.31	0.99	0.78	0.82	0.91	0.97	0.96	0.94	0.85	0.93	0.96	0.94	0.97	0.93	
K (Woodcock, 1976)	0.38	0.13	2.21	0.92	1.50	0.45	0.08	0.16	10.61	0.86	1.56	2.20	3.42	4.07	1.58	1.06	3.30	3.81	3.42	11.95	3.70	
I (Benn, 1994a)	0.27	0.38	0.45	0.19	0.54	0.23	0.03	0.09	0.04	0.06	0.12	0.06	0.02	0.04	0.02	0.04	0.07	0.04	0.07	0.14	0.11	
C (Woodcock, 1976)	1.32	0.96	0.80	1.66	0.62	1.45	3.63	2.41	3.35	2.88	2.12	2.85	4.14	3.14	4.16	3.31	2.62	3.18	2.66	1.93	2.23	
																						
Axial Distribution	Isotropic	Isotropic	Isotropic	Isotropic	Isotropic	Isotropic	Girdle	Girdle	Watson	Bingham	Bingham	Watson	Watson	Bingham	Watson	Watson	Bingham	Watson	Watson	Bingham	Watson	
Girdle																						
Strike							208	259.3														
Dip							22.2	12.4														
Watson (Fisher)																						
alpha									6.3			8.2		5		6.8		11.8		7.2	5	6.5
Bingham																						
Esa										15.6	16.3			8.3			10.3			6.5		
Zeta										6.6	9.7			5.9			7.4			6.4		

Table 3-2, continued.

(C) Múlaþökkull Till	1				2			
Strain Magnitude	31				37			
Ellipsoid Shape	Triaxial				Triaxial			
	k1	k2	k3		k1	k2	k3	
V1 dec	355.45	86.61	2.59		354.10	84.68	2.59	
V1 inc	13.83	3.79	77.12		25.00	3.48	66.56	
V2 dec	80.93	356.88	85.10		85.31	355.53	270.60	
V2 inc	17.74	4.07	1.71		2.59	13.71	-0.86	
V3 dec	301.32	313.76	354.71		0.84	340.74	0.23	
V3 inc	67.22	84.43	12.76		64.85	75.84	23.42	
S1	0.75	0.67	0.75		0.79	0.70	0.81	
S2	0.16	0.18	0.17		0.16	0.17	0.14	
S3	0.09	0.14	0.07		0.05	0.13	0.05	
CGI (Benn, 1994)	0.90	0.92	0.85		0.85	0.92	0.88	
K (Woodcock, 1976)	2.79	4.99	1.73		1.30	4.28	1.64	
I (Benn, 1994a)	0.12	0.21	0.10		0.06	0.18	0.06	
C (Woodcock, 1976)	2.08	1.56	2.32		2.83	1.71	2.80	
 <p>Sense of Shear</p>								
Axial Distribution	Bingham	Watson			Watson	Bingham	Watson	
Girdle								
Strike								
Dip								
Watson (Fisher)								
alpha			7.2		6.5		6.1	
Bingham								
Eta	7.8	9.2				9.7		
Zeta	6.0	7.8				7.6		

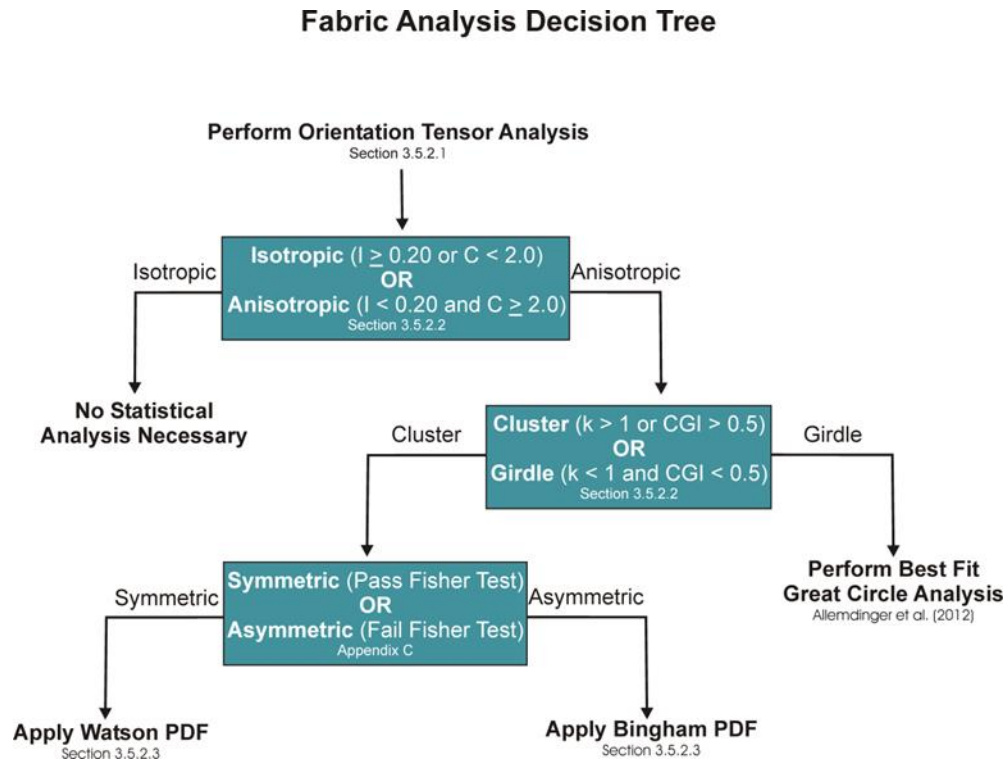


Figure 3-33. The decision tree used to determine the best analysis AMS orientation data.

3.5.3 Strain

3.5.3.1 Fabric shape

The shape of an AMS till fabric is a product of the style, orientation, and magnitude of strain experienced by the sediment ([Hooyer et al., 2008](#); [Iverson et al., 2008](#)). The shape of an AMS fabric is defined by the orientation distributions of its k_1 , k_2 , and k_3 components, as characterized by their orientation tensors and the confidence limits determined using the appropriate probability density function as described in the previous section.

An AMS fabric can be triaxial, oblate, prolate, or isotropic ([Fig. 3-34](#)). Triaxial AMS fabrics have k_1 , k_2 , and k_3 orientation distributions that are all statistically distinct

from one another. Oblate fabrics have k_1 and k_2 orientation distributions that are indistinct from one another, and a distinct k_3 distribution. A fabric is prolate if the k_2 and k_3 distributions are statistically indistinct, and the k_1 distribution is distinct. A fabric is isotropic if none of the distributions of principal susceptibility orientations is distinct from the others.

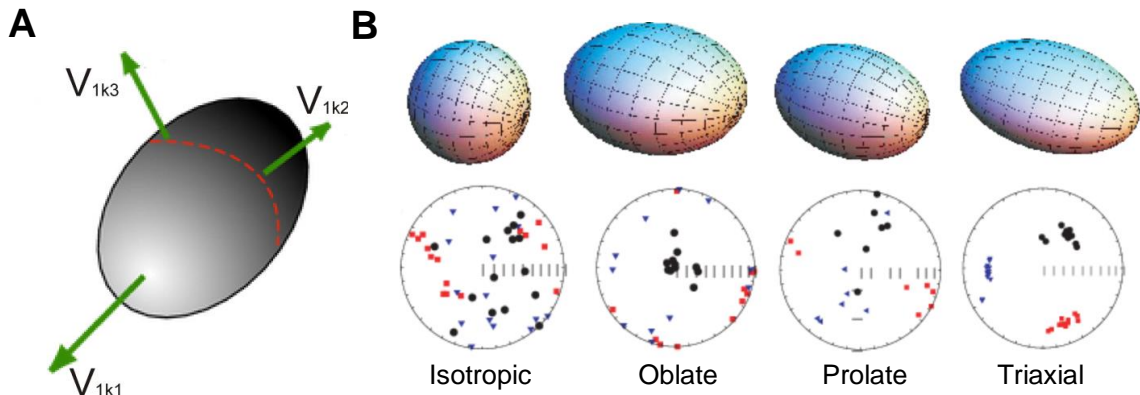


Figure 3-34. Visualizations of AMS fabric end-member shapes. (A) AMS fabrics can be visualized as three dimensional ellipsoids where V_{1k1} is the longest axis and V_{1k3} is the shortest axis. (B) Visualization of the four end-member shapes – isotropic, oblate, prolate, and triaxial – accompanied by associated AMS fabrics projected on equal area, lower hemisphere stereonets. Red squares are k_1 orientations, blue triangles are k_2 orientations and black circles are k_3 orientations. Figures adapted from [Tauxe et al. \(2015\)](#).

3.5.3.2 Strain type and orientation

Ring-shear experiments have shown that the magnitude of shear strain can be inferred from the shape of a till's AMS fabric ([Hooyer et al., 2008](#); [Iverson et al., 2008](#)). At strains less than ~ 2 , k_1 , k_2 , and k_3 were generally isotropically distributed ([Table 3-2](#)). At strains of ~ 2 , till developed an oblate AMS fabric where the k_1 and k_2 girdled along a plane with a slight upglacier dip, and the k_3 axes clustered near the vertical with a steep plunge 72° downglacier ([Table 3-2B](#); D5). At shear strains greater than ~ 6 , the sediments

developed triaxial fabrics that with sufficient further strain attained steady strengths (i.e., steady S_I values) ([Table 3-2A, B](#)) (Iverson et al. 2008; Hooyer et al., 2008). Similarly, triaxial fabrics developed in Múlajökull till when it was subjected to moderate strains (31 and 37) in ring-shear experiments ([Table 3-2C](#)) ([McCracken et al., 2014](#)).

The orientation of a triaxial or oblate AMS fabric can indicate the orientation of shear strain experienced by a till. In ring-shear experiments, triaxial fabrics aligned so that the k_I orientations clustered and plunged 15°-25° upglacier, and k_3 orientations clustered and plunged 65°-75° downglacier, with the orientations of both of these principal susceptibilities parallel to shear ([Table 3-2](#)) ([Hooyer et al., 2008](#); [Iverson et al., 2008](#); [McCracken et al., 2014](#)). Therefore, in triaxial AMS fabrics, the trend of the great circle that includes both V_{Ik1} and V_{Ik3} defines the orientation of shear ([Table 3-2](#)) ([Shumway and Iverson, 2009](#)). Also in ring-shear experiments, k_2 orientations of triaxial fabrics clustered in the horizontal plane of shear and perpendicular to the direction of shear ([Table 3-2](#)). Therefore, in triaxial fabrics, the orientation of the shear plane can be inferred from V_{Ik1} , which plunges, as noted, 15°-25° upglacier relative to the shear plane, and from V_{Ik2} , which lies within the shear plane ([Shumway and Iverson, 2009](#)). For this study, the apparent shear plane of a fabric was, therefore, determined by rotating V_{Ik1} and V_{Ik3} 20° ± 5° down-glacier about the pole defined by V_{Ik2} . The great circle that included V_{Ik2} and the rotated V_{Ik1} defined the apparent plane of simple shear. Implicit in using this method is the assumption that simple shear dominated the state of strain, as in a ring-shear test. Although this assumption is supported by the triaxial distributions of principal susceptibility orientations and the subglacial sampling environment, where simple shear

should generally predominate, the possibility that a component of pure shear affected fabric orientations cannot be strictly precluded.

For oblate fabrics, a similar method was used to determine the orientation of shear strain. In such fabrics from ring-shear tests (D5), k_3 orientations clustered and plunged $\sim 70^\circ$ downglacier along the longitudinal flow plane associated with shear. The plane that best defined the girdles of the k_1 and k_2 distributions strikes transverse to the longitudinal flow plane. The k_1 girdle plane of D5 dips 22° up-glacier. For this study, the relationships among the k_1 girdle plane, k_2 girdle plane, and V_{Ik3} of oblate fabrics were used to infer the orientation of shear strain. The plane P was defined by the acute angle bisection k_1 and k_2 girdle planes ([Allmendinger et al., 2012](#)). The longitudinal flow plane was defined by the trend of a great circle that fitted V_{Ik3} and an axis defined by the dip and dip direction of P . To determine the plane of simple shear for an oblate fabric, V_{Ik3} and P were rotated 22° down-glacier about a pole defined by the strike of P . Again, however, this interpretation—predicated on simple shear being predominant—is not unique; for example, an oblate fabric could also result from compression along an axis dipping steeply downglacier, with extension perpendicular to that axis to girdle k_1 and k_2 orientations ([Ankerstjerne et al., 2015](#)).

3.6 Physical analyses

3.6.1 Grain -size distribution

The grain-size distribution (GSD) of the tills from both fluted and unfluted sediments in the forefields of both glaciers was measured. The variation in grain-size

distribution between fluted till and adjacent, unfluted till has been used to infer possible depositional processes contributing to flute formation ([Rose, 1989](#); [Benn, 1995](#)). [Benn \(1995\)](#) observed that the grain-size distribution within flutes at Breiðamerkurjökull matched very closely that of surrounding, unfluted tills, and he used this grain-size similarity to support the till-squeeze hypothesis. [Rose \(1989\)](#), in contrast, found that although fluted till had an almost identical grain-size distribution to adjacent, unfluted till, it was likely to contain more gravel ($> 1 \phi$). [Rose \(1989\)](#) concluded that this gravel was likely added to the fluted material by basal melt-out. This enrichment in gravel has not been seen by others. In contrast, no published studies have reported attempts to determine if GSD varies systematically within flutes. Grain-size distributions were measured in this study to both identify trends between fluted and unfluted tills and search for trends within flutes.

The grain-size distributions of 13 samples were analyzed using the sieve and hydrometer method ([ASTM, 2007](#)). Characteristic, bulk sediment samples that weighed ~300 g were collected from every AMS sample site and other locations of interest in or adjacent to flutes. Samples were first allowed to air dry at room temperature. The sample was then hand-sieved through a No. 10 (2 mm) sieve. The sediment remaining on the sieve was washed, oven dried, and weighed. The portion passing the No. 10 sieve was oven dried, weighed, and then soaked in 125 mL of a sodium hexametaphosphate solution (40g/L) for at least 16 hours and subjected to hydrometer analysis. Hydrometer readings were recorded at intervals of 1, 2, 4, 8, 15, 30, 60, 120, 240, 480, and 1440 minutes. The sediment was then removed from the settling tube and washed through a No. 200 (75 μm) sieve until the water ran clear. The remaining sand was oven dried and

run through a No. 18 (1 mm), No. 35 (0.5 mm), No. 60 (250 μm), and No. 120 (125 μm) sieve stack.

3.6.2 Dry bulk density

The bulk density of each AMS sample was measured. The bulk densities were used to detect differences in sediment consolidation across flutes. These differences, in the absence of significant grain-size variations, will reflect differences in effective pressure on the bed—a key variable affecting till strength and mobility ([Iverson, 2010](#)). Prior to the measurement of each sample mass, the samples were uncapped and oven dried at 90°C - a temperature sufficiently small to avoid melting the boxes. The mean mass and volume of 10 clean, empty sample boxes was subtracted from the mass of every sample prior to the calculation of bulk density.

3.7 Resampling and reanalyzing clast fabrics from the literature

To compare AMS fabric data from this study with clast fabrics published in the literature, data from published journal articles were imported to a useable format and reanalyzed using the statistical techniques outlined earlier in this chapter.

3.7.1 Importing data from literature

Pebble fabric data were imported only from papers that included the orientations of all clasts measured either as lines on equal-area, lower hemisphere stereonet or as supplementary data. Clast fabric data from articles that included only the resulting eigenvectors ([Benn, 1995](#)), contour density plots ([Boulton, 1976](#); [Hubbard and Reid, 2006](#)), or rose diagrams ([Glasser and Hambrey, 2001](#)) were not used. Locations where clast fabrics were measured in the flute also needed to be reported for them to be usable.

3.7.2 Application of fabric analyses

Fabrics based on k_I orientations from AMS fabrics are commonly similar to the V_I orientations of clast fabrics measured from the same location. Both laboratory experiments ([Hooyer and Iverson, 2000](#); [Iverson et al., 2008](#)) and field observations ([Gentoso et al., 2012](#)) have shown as much. Imported clast fabric data from flutes were analyzed using the orientation tensor and PDF methods outlined in [Sections 3.5.1](#) and [3.5.2](#) in order to directly compare clast-fabric data to the AMS data collected for this study.

CHAPTER 4. RESULTS

4.1 Magnetic mineralogy

4.1.1 Susceptibility vs. Temperature

Heating curves from high-temperature thermomagnetic experiments provide Curie temperature (T_c) values for the different sediment types of this study. Múlajökull tills have at least two Curie temperatures with values of 182 °C, 485 °C, or ~550 °C ([Fig. 4-1A](#)). The susceptibility of each Múlajökull sample gradually increased between 20 °C and 130 °C. The black, sandy sediment in B14-F1, site A, has a Curie temperature of 550 °C ([Fig. 4-1B](#)). Samples B14-F1, site B and B14-F2, site B are bulk samples from diamictaceous till at the centers of Flute 1 and Flute 2, respectively, and have Curie temperature of ~320 °C, ~490 °C, and ~550 °C. The relative magnitude of susceptibility loss at each Curie temperature indicates the degree to which the magnetic mineral represented by the T_c contributed to the till's overall susceptibility.

Low-temperature thermomagnetic curves were determined for one Múlajökull ([Fig. 4-2A](#)) and one Breiðamerkurjökull ([Fig. 4-2B](#)) till sample from flute interiors. Magnetic behaviors at low temperatures can be indicative of certain magnetic minerals, like magnetite. Neither curve was corrected for paramagnetic contributions to susceptibility, which increase markedly at low temperatures (<60 K) as paramagnetic minerals reach their T_c . The susceptibility of the Múlajökull sample decreases gradually with temperature, until reaching the paramagnetic T_c . The susceptibility of the Breiðamerkurjökull sample peaks around 130 K and decreases abruptly at around 120 K,

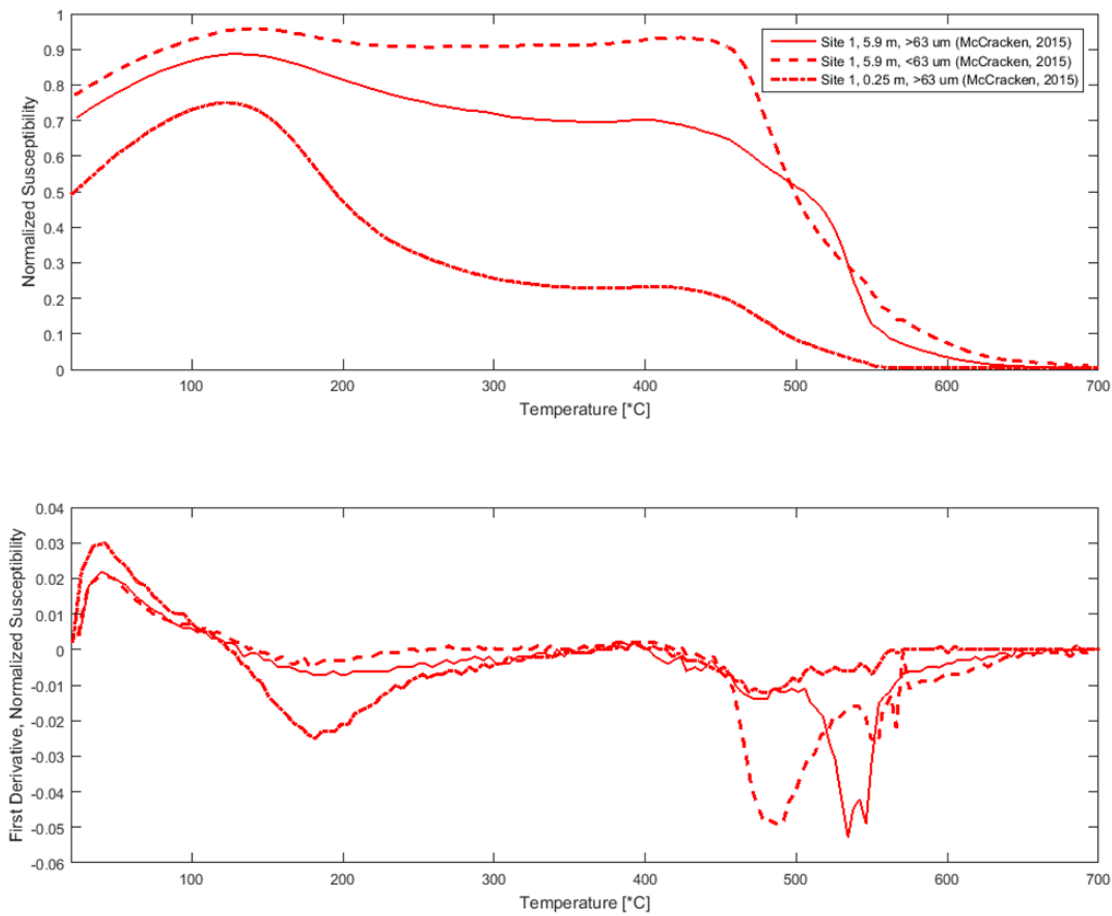


Figure 4-1. Normalized susceptibility vs. temperature heating curves for (A) Múlajökull till and (B) Breiðamerkurjökull sediment samples and first derivative of those curves. The Curie temperature(s) of each sample is represented by the minimum or minima of its first derivative.

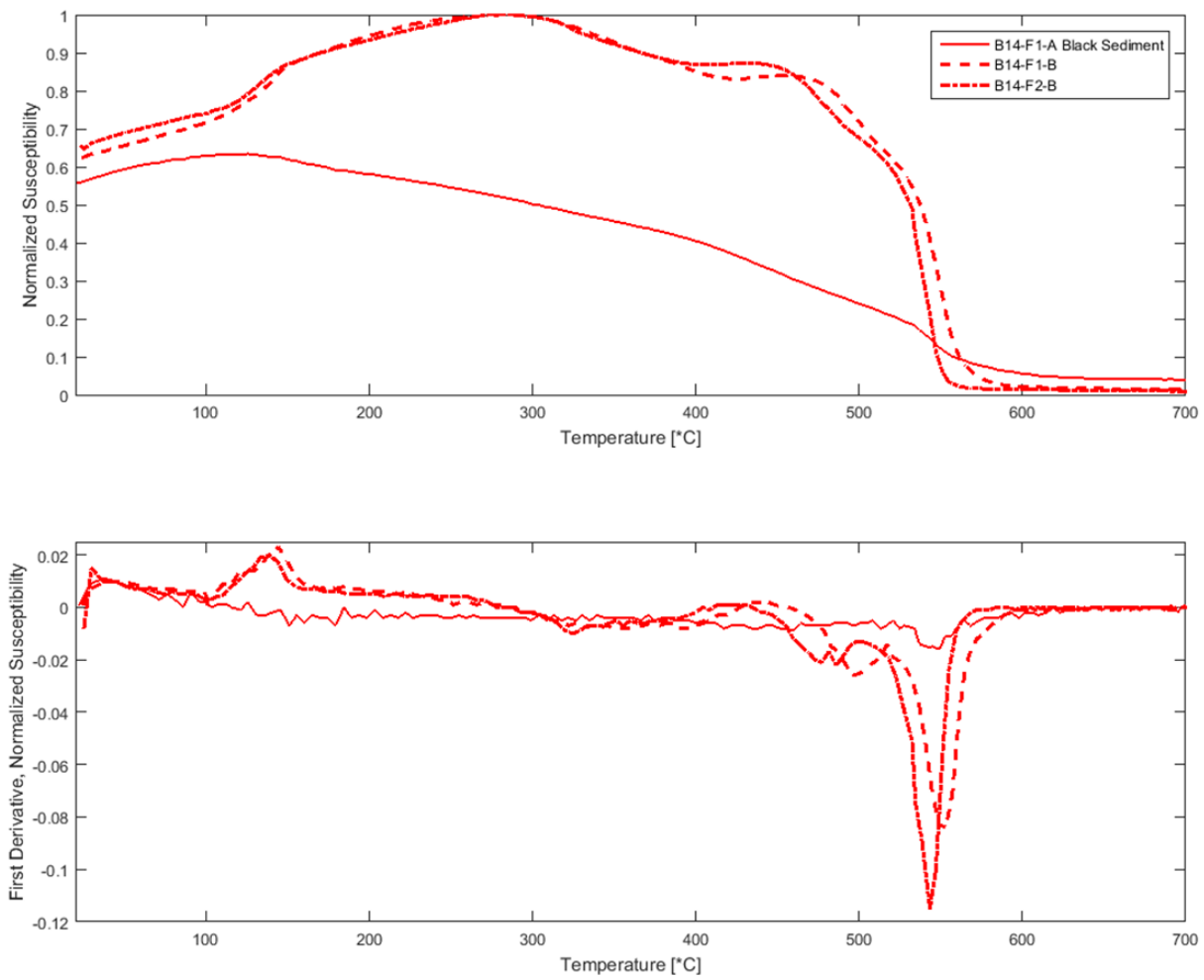


Figure 4 1B.

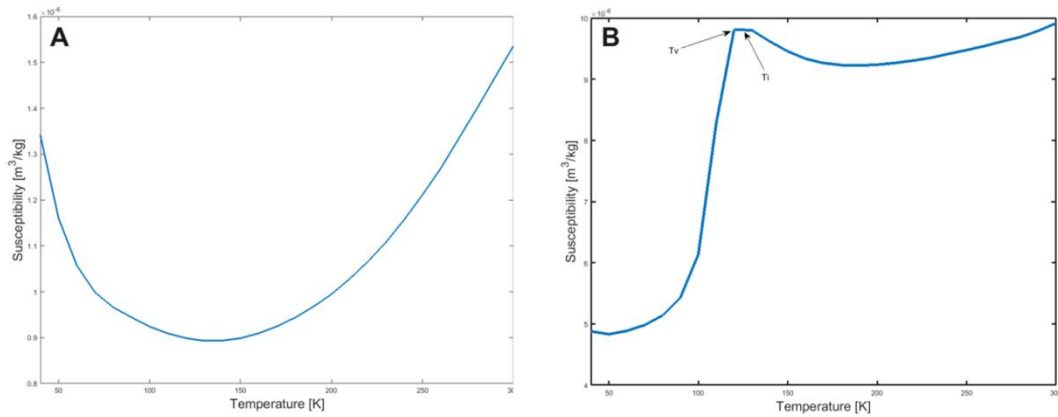


Figure 4-2. In-phase susceptibility vs. low temperature curves for a bulk sediment sample from (A) Flute M14-F2 and (B) Flute B14-F1. T_v indicates the Verwey Transition and T_i indicates the isotropic point, both of which are indicative of phase changes that occur in magnetite at low temperatures.

4.1.2 Frequency dependence of magnetic susceptibility

The in-phase, room temperature frequency dependence of magnetic susceptibility for one Múlajökull till sample was 5.38%. The in-phase, room temperature frequency dependence of magnetic susceptibility for one Breiðamerkurjökull diamicton sample was 1.73%. Frequency dependence on susceptibility provides information about mineralogy and domain state.

4.1.3 Low temperature remanence

SIRM cooling curves show that the magnetization of sediment samples from Múlajökull and Breiðamerkurjökull increased until temperatures of either ~260 K or ~150 K and then gradually decreased as the temperature continued to drop (Fig. 4-3, left, middle and bottom panels). Curves that indicate SIRM zero-field remanence during warming showed that the magnetization of all samples decreased as the temperature

increased but experienced rapid decreases in magnetization around temperatures of 70 K, 120 K, or both ([Fig. 4-3](#), right, middle and bottom panels). Transitions in both warming and cooling curves around 120 K are indicative of the Verwey transition in magnetite ([Özdemir et al., 1993](#)). Suppressed transitions and lower-temperature (70 K) transitions indicate either titanomagnetite or maghemite ([Özdemir et al., 1993](#); [Moskowitz et al., 1998](#)).

Remanent magnetization changes with temperature were mostly consistent among Breiðamerkurjökull diamict samples and among Múlajökull till samples, with the exception of M14-F2-B. The M14-F2-B sample has a strong transition at 120 K, which is characteristic of stoichiometric magnetite. Other Múlajökull samples did not have a transition at 120 K. For diamicts from both glaciers, low-temperature remanence properties were consistent among different grain sizes, which is a characteristic expected in tills.

The low-temperature remanence properties of the black, sandy sediment (B14-F1-A) did not closely resemble those of the other Breiðamerkurjökull till samples because the Verwey transition at 120 K is suppressed ([Fig. 4-3](#), top panel). The fine-grained portion of the B14-F1-A sediment had remanence properties dissimilar from coarse-grained and bulk samples from the same sediment, which is expected in sediments that have experienced transport and sorting.

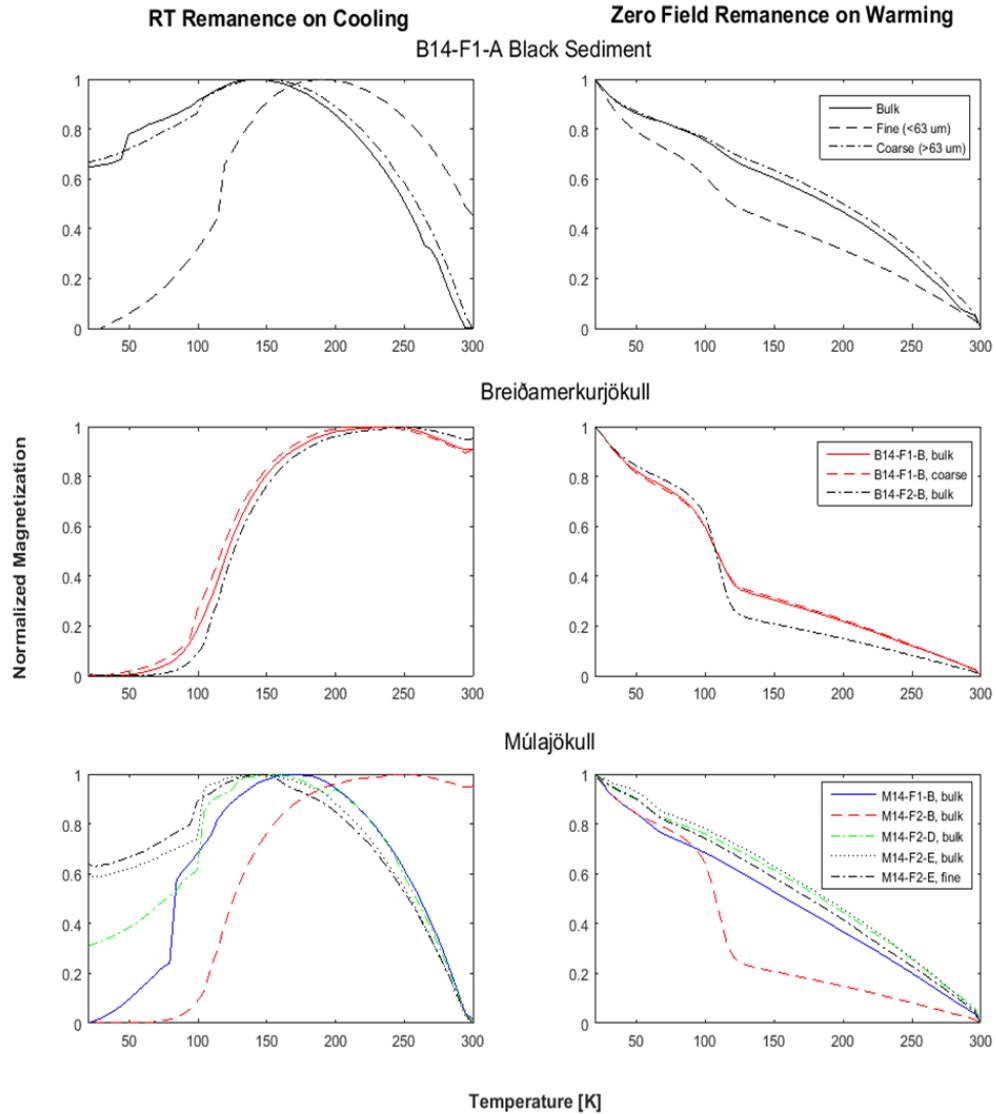


Figure 4-3. Normalized SIRM on cooling from 300 to 20 k (Room Temperature Remanence on Cooling) and Normalized SIRM on warming from 20 to 300 k (Zero Field Remanence on Warming) curves for the B14-F1-A black sediment, Breiðamerkurjökull tills, and Múlajökull tills. Abrupt decreases in magnetization magnitude at low temperatures in RT-Remanence-on-cooling curves are likely due to movement in the sample due to physical contraction and crystalline phase changes that can occur low temperatures.

Table 4-1. Hysteresis parameters for sediment samples from Múlajökull and Breiðamerkurjökull. χ_{hf} is the high field mass susceptibility, χ_0 is the totally mass susceptibility, χ_{ferri} is the ferrimagnetic contribution to mass susceptibility.

Sample Location	M_s [Am ² /kg]	M_r [Am ² /kg]	B_c [mT]	B_{cr} [mT]	χ_{hf} [m ³ /kg]	χ_0 [m ³ /kg]	χ_{ferri} [m ³ /kg]	χ_{ferri} [percent]	M_r/M_s	B_{cr}/B_c
B14-F1-A-0.40 blk sed	0.14	0.06	33.52	65.55	2.29E-07	1.88E-06	1.65E-06	87.84%	0.39	1.96
B14-F1-A-0.40 blk sed fine	0.19	0.04	15.95	48.60	1.92E-07	3.27E-06	3.08E-06	94.13%	0.22	3.05
B14-F1-B bulk	1.64	0.30	14.93	42.72	1.72E-07	2.32E-05	2.30E-05	99.26%	0.18	2.86
B14-F1-B coarse	1.07	0.23	16.33	42.89	2.19E-07	1.64E-05	1.62E-05	98.66%	0.22	2.63
B14-F1-B fine	1.07	0.23	13.64	47.87	2.19E-07	1.64E-05	1.62E-05	98.66%	0.22	3.51
B14-F2-B interior bulk	1.51	0.23	9.82	20.09	1.91E-07	2.64E-05	2.62E-05	99.27%	0.15	2.05
B14-F2-B interior coarse	1.53	0.35	19.37	52.17	1.51E-07	2.06E-05	2.04E-05	99.27%	0.23	2.69
B14-F2-B interior fine	1.35	0.25	12.45	27.61	2.91E-07	2.28E-05	2.25E-05	98.72%	0.18	2.22
M14-F1-B-0.68 interior	0.37	0.12	17.29	20.77	2.30E-07	7.32E-06	7.09E-06	96.86%	0.32	1.20
M14-F1-B-0.68 interior	0.29	0.10	23.25	43.72	2.01E-07	4.72E-06	4.52E-06	95.75%	0.36	1.88
M14-F1-B-0.68 interior	0.45	0.12	14.40	30.37	2.07E-07	9.23E-06	9.02E-06	97.76%	0.27	2.11
M14-F2-D-0.50 interior	0.30	0.13	27.00	42.87	2.20E-07	4.49E-06	4.27E-06	95.11%	0.43	1.59
M14-F2-D-0.50 interior	0.34	0.10	13.27	7.62	2.30E-07	7.58E-06	7.35E-06	96.96%	0.29	0.57
M14-F2-D-0.50 interior	0.25	0.10	27.06	49.98	2.31E-07	7.58E-06	7.35E-06	96.96%	0.39	1.85
M14-F2-EN bulk	0.36	0.14	23.72	35.56	1.76E-07	5.24E-06	5.06E-06	96.64%	0.39	1.50
M14-F2-EN coarse	0.39	0.13	19.49	33.40	1.84E-07	6.33E-06	6.15E-06	97.10%	0.32	1.71
M14-F2-EN fine	0.42	0.17	25.80	46.30	2.31E-07	6.52E-06	6.29E-06	96.46%	0.41	1.79
Múlajökull 13-01-0.25	0.33	0.12	19.35	35.82	2.08E-07	6.26E-06	6.05E-06	96.68%	0.35	1.85
Múlajökull 13-01-0.25 fine	0.46	0.14	18.28	43.87	2.18E-07	8.28E-06	8.06E-06	97.37%	0.30	2.40
Múlajökull 13-01-5.9	0.30	0.11	20.50	45.39	2.18E-07	5.43E-06	5.21E-06	95.98%	0.35	2.21
Múlajökull 13-01-5.9 fine	0.55	0.15	16.35	38.87	2.05E-07	1.01E-05	9.89E-06	97.97%	0.28	2.38

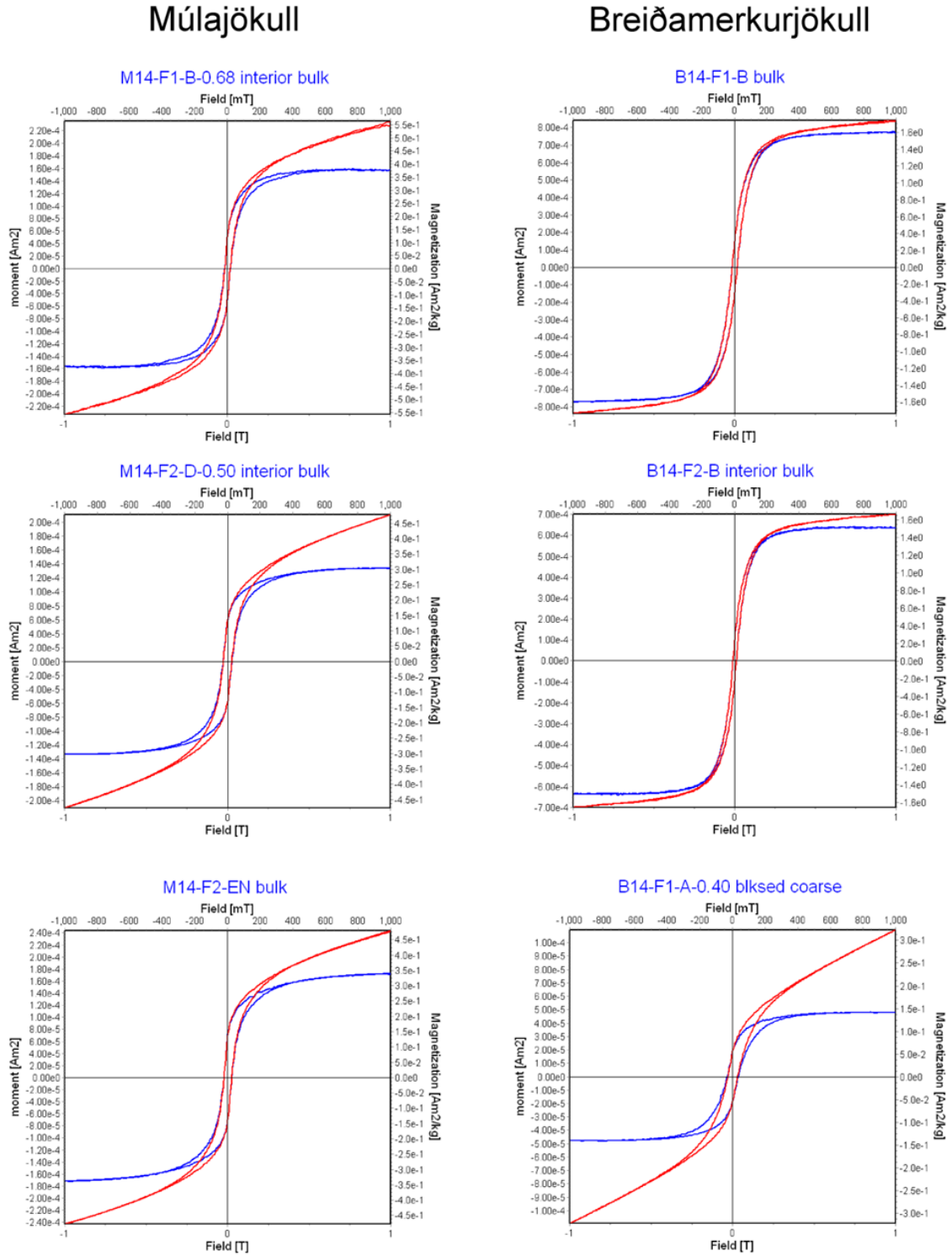


Figure 4-4. Magnetic hysteresis curves of bulk sediment samples from Múlajökull and Breiðamerkurjökull. Blue hysteresis curves are corrected (paramagnetic contribution removed), and red hysteresis curves are uncorrected.

4.1.4 Magnetic hysteresis

Magnetic hysteresis parameters can be used to infer the magnetic mineralogy of a sediment as well as domain states and grain sizes. Hysteresis results for the bulk, coarse, and fine fractions of Múljökull and Breiðamerkurjökull samples are displayed in [Table 4-1](#). The hysteresis loops for the bulk of each sample are shown in [Figure 4-4](#).

The hysteresis parameters of Múljökull tills are similar among grain sizes and between forefield locations. Tills from Múljökull have saturation remanence values (M_s) that range from 0.25 – 0.55 [Am^2/kg], and coercivities (B_c) between 16 and 27 mT. All Múljökull tills have paramagnetic contributions $\leq 5\%$ of total bulk susceptibility (χ_m). The hysteresis parameters of Múljökull tills are similar to natural and synthetic titanomagnetite samples with known grain sizes ranging from 1.5 μm to 11.5 μm ([Fig. 4-5A](#)) ([Dunlop, 2002](#)).

The magnetic hysteresis parameters of Breiðamerkurjökull diamictons ([Table 4-1](#)) from B14-F1 and B14-F2 are similar to one another and among grain sizes. The diamictons have saturation remanence values (M_s) of 1.07 – 1.61 [Am^2/kg], and coercivities (B_c) of 9.8 – 19.4 mT. The contribution of paramagnetic material to χ_m is $< 2\%$. Both diamictons plot in the middle PSD range of a traditional Day plot, near synthetic magnetite of known grain sizes between 0.11 μm and 0.80 μm ([Fig. 4-5B](#)) ([Day et al., 1977](#); [Dunlop, 2002](#)).

Hysteresis parameters of the B14-F1, site A black sandy unit differ among grain sizes and from the surrounding diamict. The fine fraction ($< 63 \mu\text{m}$) of the black, sandy unit has an M_s value of 0.19 [Am^2/kg] and a B_c value of 15.95 mT. The coarse fraction

(> 63 μm) of the black, sandy unit has an M_s value of 0.14 [Am^2/kg] and a B_c value of 33.52 mT. Paramagnetic materials contribute ~6% to χ_m in the sediment's fine portion but ~12% to the sediment's coarse portion.

4.1.5 FORCs

FORCs use coercivity measurements to infer the domain state composition of ferrimagnetic minerals. Single domain (SD) minerals can give rise to inverse or intermediate AMS fabrics, so identifying their presence or absence is integral to the accurate interpretation of fabric orientation. FORC distributions of Múlajökull tills indicate that the magnetic properties of the sediment are controlled by primarily pseudo-single domain (PSD) grains with some multi domain (MD) grains ([Fig. 4-6A](#)). FORC distributions of the Breiðamerkurjökull diamicts indicate that their magnetic properties are primarily controlled by PSD minerals with minor MD and SD components ([Fig. 4-6B](#), 10-11). The black sandy sediment's fine and coarse fractions have different FORC distributions. The coarse fraction's FORC indicates primarily PSD and SD domain states ([Fig. 4-6B](#), 8). The fine fraction of the black sediment indicates mostly PSD grains with some MD grains present ([Fig. 4-6B](#), 9). See [Figure 3-25](#) for how SD magnetite plots on a FORC diagram, and [Figure 3-26](#) for MD and PSD.

4.2 Anisotropy of magnetic susceptibility

4.2.1 Flute fabrics

Flutes at both Múlajökull and Breiðamerkurjökull yielded primarily triaxial (k_1 , k_2 , and k_3 clustered) and oblate (clustered k_3 , girdled k_1 and k_2) AMS fabrics, which are indicative of moderate-to-high and small shear strains, respectively ([Fig. 4-7](#), [Fig. 4-8](#),

[Fig. 4-9](#), [Fig. 4-10](#), [Fig. 4-11](#); [Tables 4-2](#), [4-3](#), [4-4](#), [4-5](#), [4-6](#)). Planes of shear (of which V_{1k3} is the pole) were near-horizontal in almost all fabrics. Shearing azimuths, as indicated by k_1 orientations of individual fabrics, could be strongly divergent (fabrics 12 and 13 of flute M14-F2, [Fig. 4-9B](#)) or weakly divergent (fabrics 3 and 4 of flute M13-F1, [Fig. 4-7B](#)) about the flute's central axis, strongly convergent (fabrics 1 and 2 of flute M13-F1, [Fig. 4-7B](#)) or weakly convergent (fabrics 17 and 19 of flute M14-F2, [Fig. 4-9B](#)) about the central axis, parallel to the flute long axis (fabric 7 of flute B14-F1, [Fig. 4-10B](#)), or unidirectional across the flute's central axis (fabrics 9, 10, and 11 of flute M14-F2, [Fig. 4-9B](#)). Shearing azimuths could change considerably over small changes in depth within, or with distance along, a single flute. Fabrics did not consistently display either herringbone or flow-parallel fabrics, as predicted by the cavity propagation and freeze-on hypotheses.

The exception to these AMS fabric patterns are from sediments directly on the lee side of B14-F1's boulder (site A) ([Fig. 4-12](#)) ([Table 4-7](#)). These fabrics are mostly triaxial, with uniform V_{1k1} orientations. The pole-to-plane of the apparent shear planes (V_{1k3}) of triaxial fabrics on the left side of the figure are near-horizontal ([Fig. 4-12](#)). These patterns likely are not the result of unique magnetic mineralogy in the black and brown sediments, as fabric shapes and orientations are similar between lithologies on either side of the flute axis ([Fig. 4-12](#)).

For all flute AMS fabrics with anisotropic (clustered or girdled) k_2 distributions, shear planes indicated by these distributions were usually near horizontal, meaning that corrected shear azimuths rarely deviated more than 5° from uncorrected azimuths. This

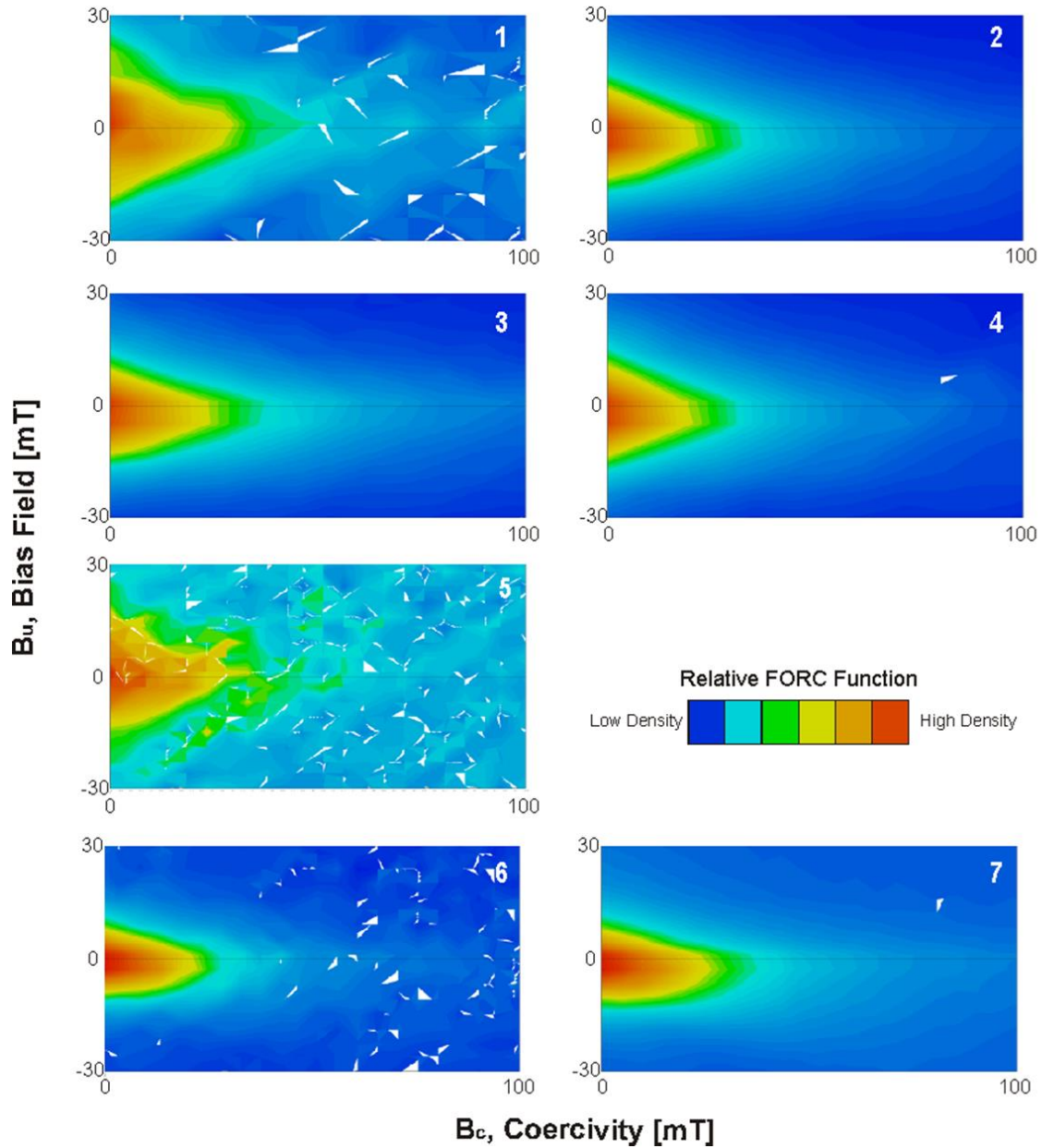


Figure 4-6. First Order Reversal Curves of (A) Múlajökull sediments from: (1) McCracken (2015), site 1, 0.25 m depth, $> 63 \mu\text{m}$; (2) McCracken (2015), site 1, 0.25 m depth, $< 63 \mu\text{m}$; (3) McCracken (2015), site 1, 5.9 m depth, $> 63 \mu\text{m}$; (4) McCracken (2015), site 1, 5.9 m depth, $< 63 \mu\text{m}$; (5) M14-F1, site B, bulk; (6) M14-F2, site E, side A, bulk; (7) M14-F2, site E, side A, $< 63 \mu\text{m}$, and (B) Breiðamerkurjökull sediments from: (8) B14-F1, site A, black sediment, $> 63 \mu\text{m}$; (9) B14-F1, site A, black sediment, $< 63 \mu\text{m}$; (10) B14-F1, site B, bulk; (11) B14-F1, site B, $> 63 \mu\text{m}$.

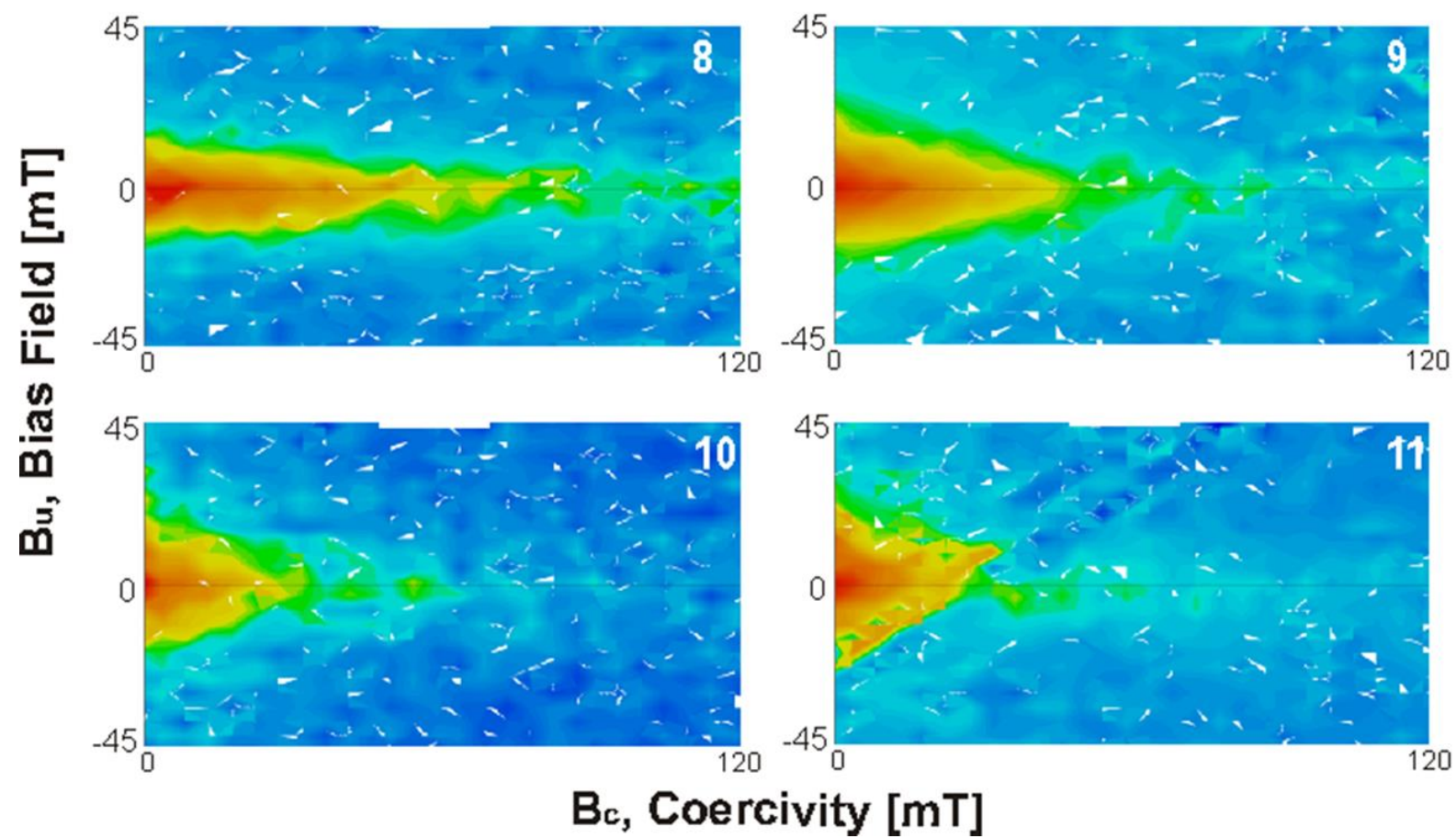


Figure 4-6B.

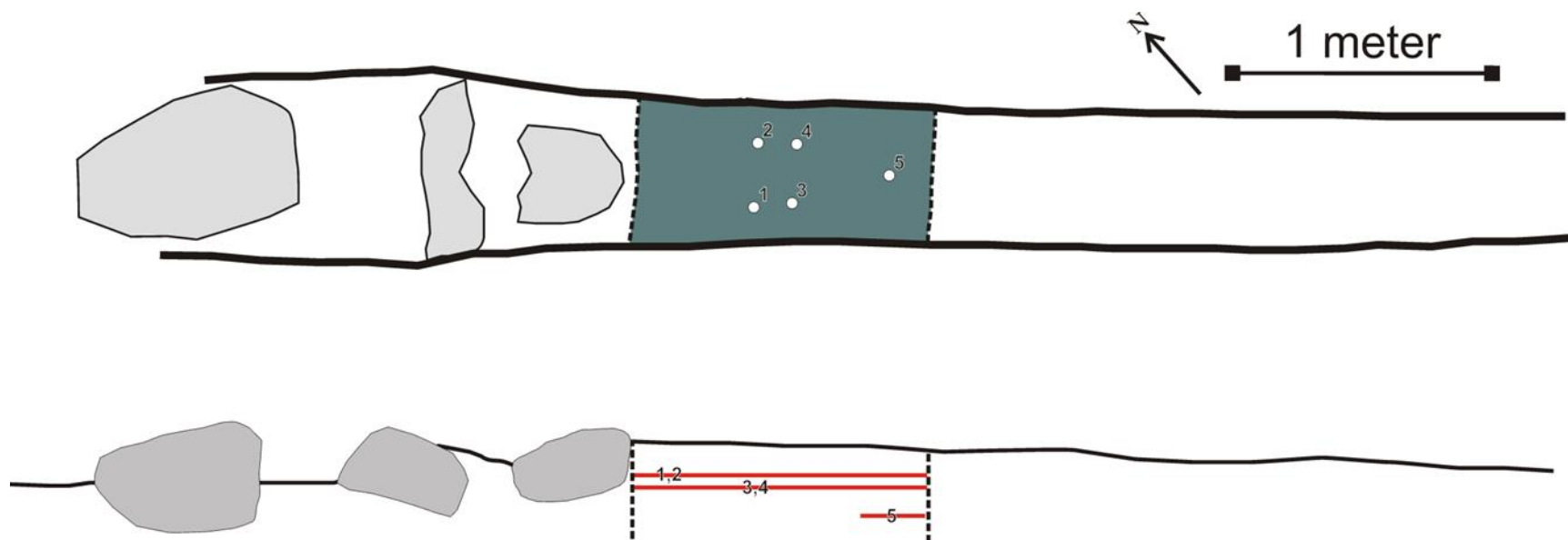


Figure 4-7. (A) Plan and longitudinal views of flute M13-F1, with the approximate mean location of samples used in each fabric indicated. (B) AMS fabrics and fabric analysis results from flute M13-F1. Numerical results shown in [Table 4-2](#). All data are displayed on equal-area, lower-hemisphere stereonet.

Flute M13-F1

AMS Principal Susceptibility
and Shear Orientation Data

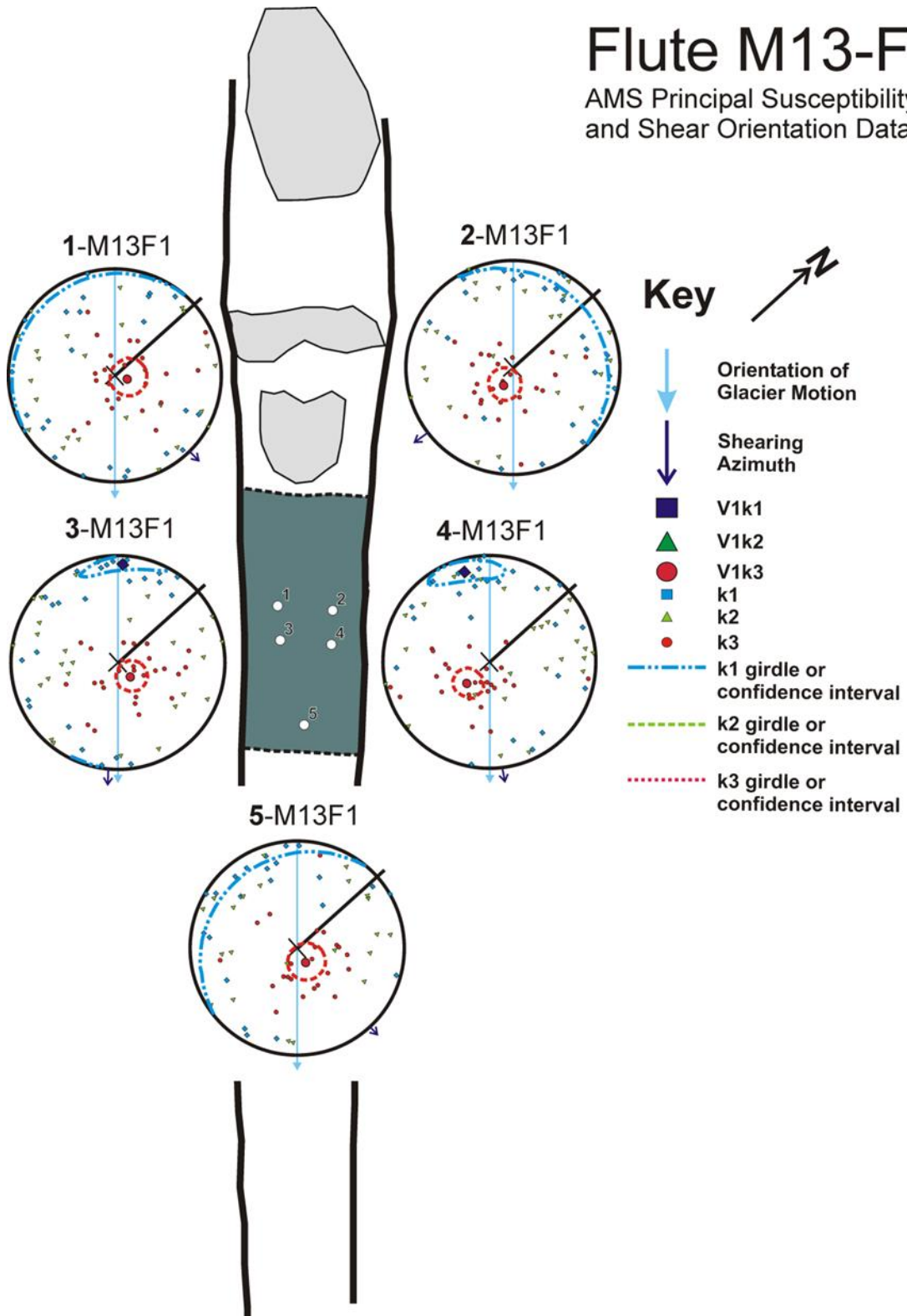
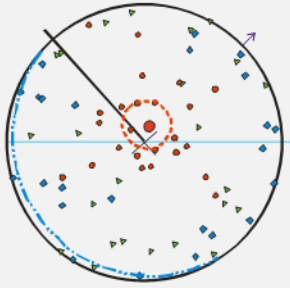
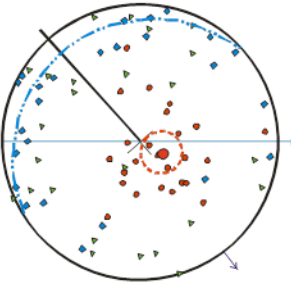
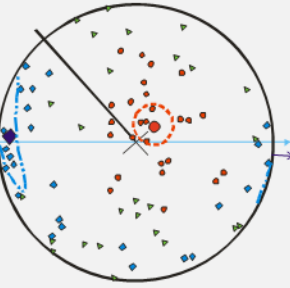
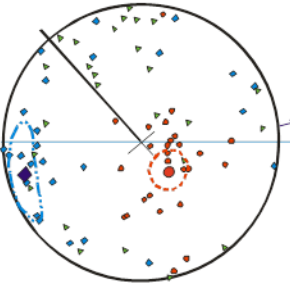
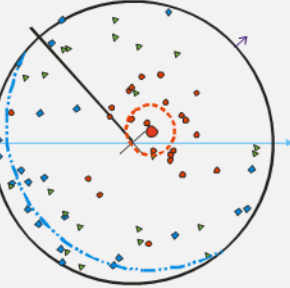


Figure 4-7B.

Table 4-2. AMS fabric results from flute M13-F1.

Ellipsoid Shape	M13-F1-15B			M13-F1-15A			M13-F1-10B			M13-F1-10A			M13-F1-10?		
	Oblate?			Oblate?			Triaxial?			Triaxial?			Oblate?		
	k1	k2	k3	k1	k2	k3	k1	k2	k3	k1	k2	k3	k1	k2	k3
V1 dec			61.90			166.60		315.80	82.00		297.50	172.30			99.70
V1 inc			81.40			75.00		8.30	76.50		12.80	69.00			73.50
CGI (Benn, 1994a)	0.48	0.61	0.94	0.28	0.31	0.96	0.55	0.84	0.89	0.65	0.72	0.84	0.37	0.61	0.96
K (Woodcock, 1976)	0.42	0.96	6.61	0.17	0.27	7.35	0.36	3.25	2.51	0.67	1.42	1.59	0.22	1.02	8.49
I (Benn 1994a)	0.19	0.36	0.19	0.15	0.35	0.15	0.06	0.38	0.12	0.13	0.31	0.10	0.11	0.42	0.17
C (Woodcock, 1976)	1.65	1.02	1.68	1.93	1.06	1.92	2.73	0.96	2.14	2.06	1.18	2.32	2.17	0.86	1.78
Fisher Test	N/A	N/A	Pass	N/A	N/A	Pass	Fail	N/A	Pass	Fail	N/A	Pass	N/A	N/A	Pass
Principal Susceptibility Orientations															
Axial Distribution	Girdle	Isotropic	Watson	Girdle	Isotropic	Watson	Bingham	Isotropic	Watson	Bingham	Isotropic	Watson	Girdle	Isotropic	Watson
Shearing Azimuth		87.5			186.1			134.2			121.4			89	
Girdle															
Dip		7.1			15.8									17.1	
Dip Direction		268			7.6									268	
Watson (Fisher)															
alpha			14.3			12.4			11.8			11.5			14.3
Bingham															
Eta							27.8			24					
Zeta							6.9			10					

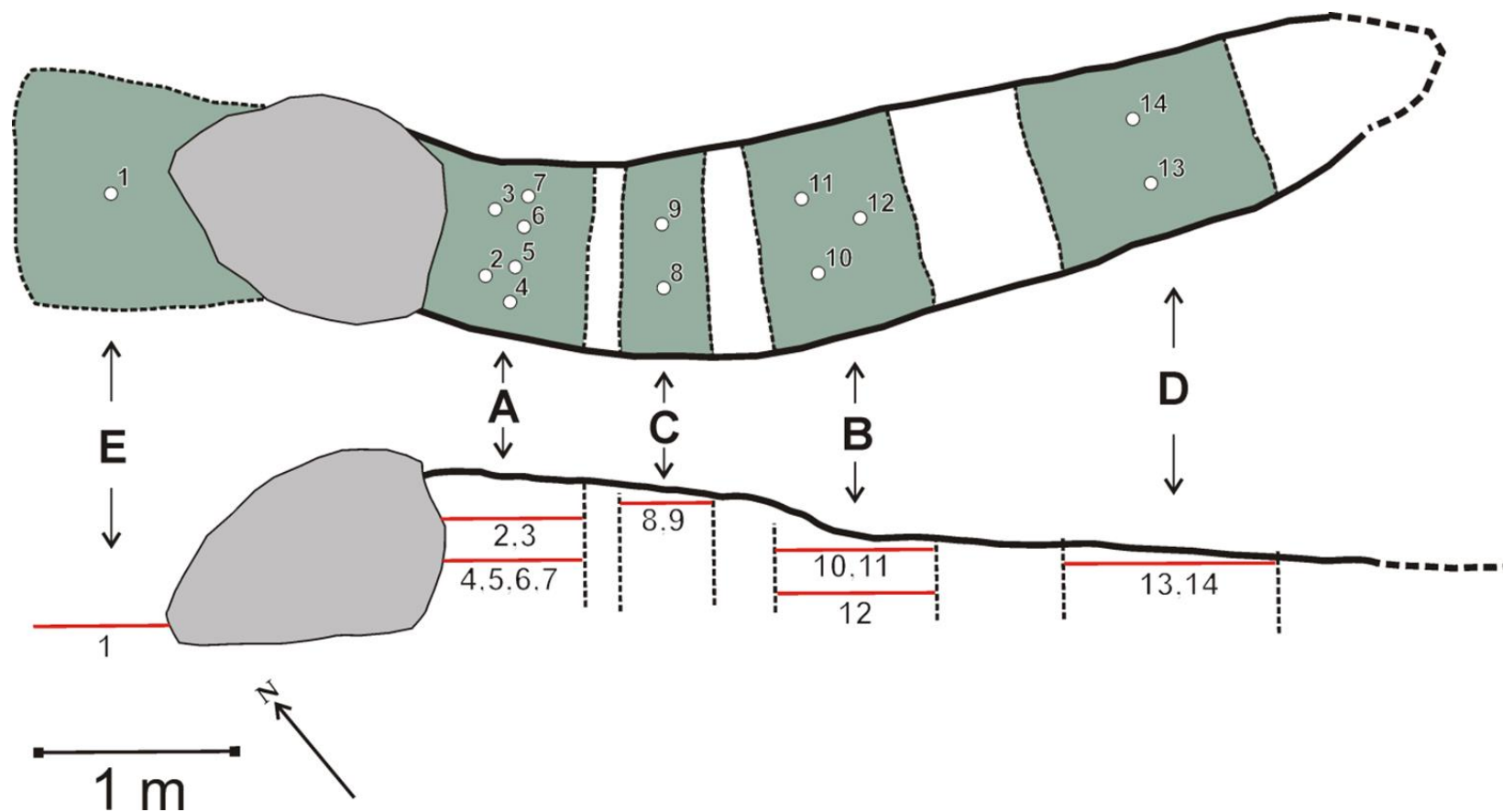


Figure 4-8. (A) Plan and longitudinal views of flute M14-F1, with the approximate mean location of samples used in each fabric indicated. (B) AMS fabrics and fabric analysis results from flute M14-F1. Numerical results shown in [Table 4-3](#). All data are displayed on equal-area, lower-hemisphere stereonet. Bold lines on stereonet indicate true north. (C) Corrected shear plane attitudes (yellow lines) and pole-to-plane confidence intervals (purple circles) derived from AMS fabrics of flute M14-F1. Numerical results shown in [Table 4-3](#). All data are displayed on equal-area, lower-hemisphere stereonet.

Flute M14-F1

AMS Principal Susceptibility
and Shear Orientation Data

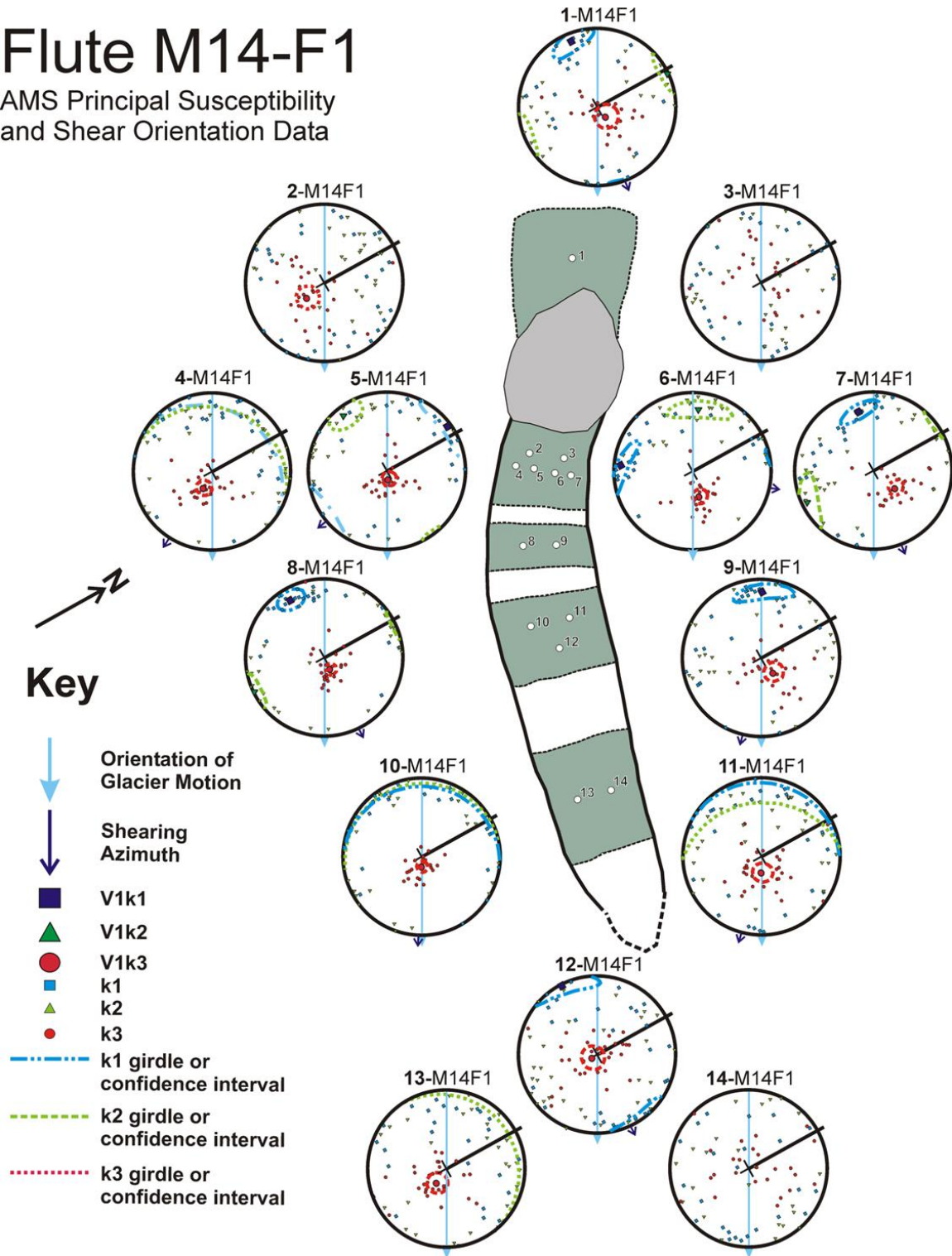


Figure 4-8B.

Flute M14-F1

AMS Shear Planes and
Poles to Shear Planes

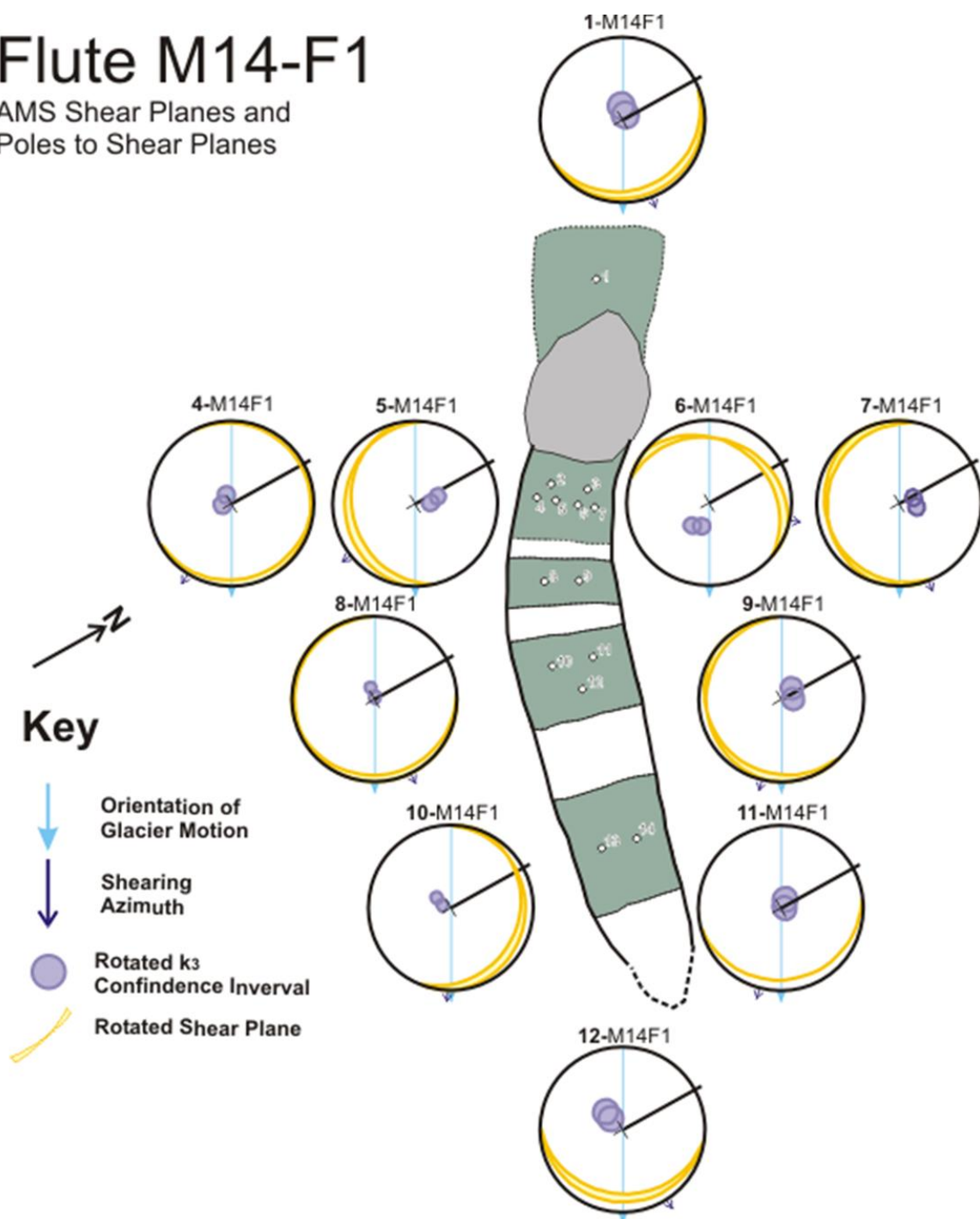


Figure 4-8C.

Table 4-3. AMS fabric results from flute M14-F1.

Ellipsoid shape	1-M14F1			2-M14F1			3-M14F1			4-M14F1			5-M14F1			6-M14F1			7-M14F1		
	K1	K2	K3	K1	K2	K3	K1	K2	K3	K1	K2	K3	K1	K2	K3	K1	K2	K3	K1	K2	K3
Vl dec	278.10	4.70	72.00				173.40	263.90	187.10	66.30	212.50	303.70	99.70	361.20	268.60	100.10	302.20	34.00	142.90		
Vl inc	9.60	0.60	77.60				66.20	23.90	11.10	61.00	11.00	21.60	63.60	3.30	11.20	79.80	17.90	4.20	70.80		
COI (Benn 1994a)	0.7922	0.9304	0.9448	0.29	0.32	0.78	0.17	0.59	0.51	0.84	0.59	0.46	0.94	0.59	0.57	0.97	0.43	0.59	0.98		
K (Woodcock, 1976)	1.1903	1.838	3.433	0.21	0.40	1.40	0.10	0.54	1.81	0.35	0.78	2.77	0.41	0.80	5.33	0.53	0.41	5.98	0.27	0.26	3.63
K (Benn 1994a)	0.3684	0.1707	0.1376	0.22	0.67	0.23	0.22	0.26	0.13	0.04	0.16	0.08	0.07	0.11	0.08	0.12	0.07	0.08	0.10	0.13	0.08
C (Woodcock, 1976)	1.0273	1.702	2.934	1.50	0.39	1.40	1.52	1.35	2.00	3.22	1.85	3.08	2.71	2.17	2.97	2.14	2.60	2.05	2.33	2.05	3.85
Fisher Test	Fail	Fail	Pass	NA	NA	NA	NA	NA	Pass	Fail	Fail	Pass	Fail	Fail	Pass	Fail	Pass	Pass	NA	NA	Pass
Principal Susceptibility Orientations																					
Local Distribution	Bingham	Bingham	Fisher	Isotropic	Isotropic	Isotropic	Isotropic	Isotropic	Vielson	Bingham	Bingham	Vielson	Bingham	Bingham	Vielson	Bingham	Vielson	Vielson	Girdle	Girdle	Vielson
Streaming Amplitude			97.2			NA			NA			97.1			170.6						
Girdle																					
Chi																			20.6	18.9	
Chi Direction																			333.1	316.5	
Vielson (Fisher)																					
Mean			12.3						12.1			8.0			7.8			16.4	7.6		7.8
Stia																					
Chi	20.4	18.3						23.6	24.7		26.2	28.9		28							
Chi	11.3	12.2						4.6	11.4		7.2	10.7		10.5							
Ellipsoid shape	8-M14F1			9-M14F1			10-M14F1			11-M14F1			12-M14F1			13-M14F1			14-M14F1		
	K1	K2	K3	K1	K2	K3	K1	K2	K3	K1	K2	K3	K1	K2	K3	K1	K2	K3	K1	K2	K3
Vl dec	297.30	189.20	77.10	271.90	182.20	86.00				119.60			272.40			126.20					
Vl inc	16.50	9.40	70.50	16.70	3.00	76.00				73.90			80.30			88.90					
COI (Benn 1994a)	0.6387	0.7459	0.9448	0.75	0.82	0.94	0.51	0.39	0.93	0.40	0.35	0.97	0.59	0.51	0.96	0.59	0.58	0.63	0.29	0.29	0.94
K (Woodcock, 1976)	0.5781	1.133	3.726	0.39	1.23	2.08	0.44	0.31	5.38	0.18	0.20	2.97	0.55	0.37	1.48	0.79	0.38	0.78	0.20	0.19	4.27
K (Benn 1994a)	0.1362	0.0799	0.0912	0.03	0.08	0.03	0.16	0.21	0.12	0.04	0.08	0.02	0.17	0.28	0.12	0.42	0.47	0.22	0.23	0.18	0.11
C (Woodcock, 1976)	1.1382	1.978	2.934	3.49	2.97	3.35	1.95	1.95	2.00	3.21	2.99	3.90	1.75	1.36	2.10	0.96	0.75	1.35	1.47	1.69	3.20
Fisher Test	Fail	NA	Pass	Pass	Fail	Pass	NA	NA	Pass	NA	NA	Pass	Fail	NA	Pass	NA	NA	NA	NA	NA	Pass
Principal Susceptibility Orientations																					
Local Distribution	Bingham	Isotropic	Vielson	Vielson	Bingham	Vielson	Girdle	Girdle	Vielson	Girdle	Girdle	Vielson	Bingham	Isotropic	Fisher	Isotropic	Isotropic	Isotropic	Isotropic	Girdle	Fisher
Streaming Amplitude			113.7			91.6									92.4						
Girdle																					
Chi							8.1	32.8		11.8	7.7									10.7	
Chi Direction							315.7	295.1		302.1	298.1									350.5	
Vielson (Fisher)																					
Mean			10.2		12.4	5.8						5.7			12						10.7
Stia																					
Chi	26.3	7.6			5.4	13.7				10			29.9							11	
Chi						7.9							13.3								

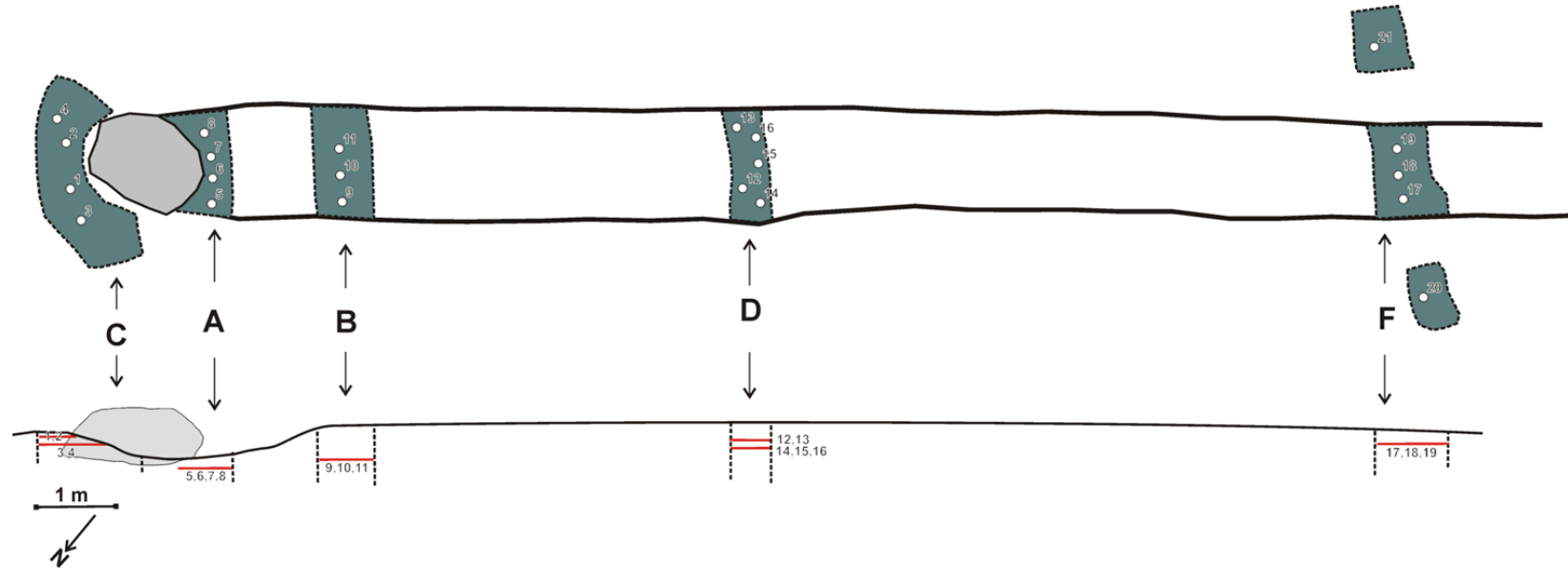


Figure 4-9. (A) Plan and longitudinal views of flute M14-F2, with the approximate mean location of samples used in each fabric indicated. (B) AMS fabrics and fabric analysis results from flute M14-F2. Numerical results shown in [Table 4-4](#). All data are displayed on equal-area, lower-hemisphere stereonet. Bold lines on stereonet indicate true north. (C) Corrected shear plane attitudes (yellow lines) and pole-to-plane confidence intervals (purple circles) derived from AMS fabrics of flute M14-F2. Fabric analysis results shown in [Table 4-4](#). All data are displayed on equal-area, lower-hemisphere stereonet

Flute M14-F2

AMS Principal Susceptibility
and Shear Orientation Data

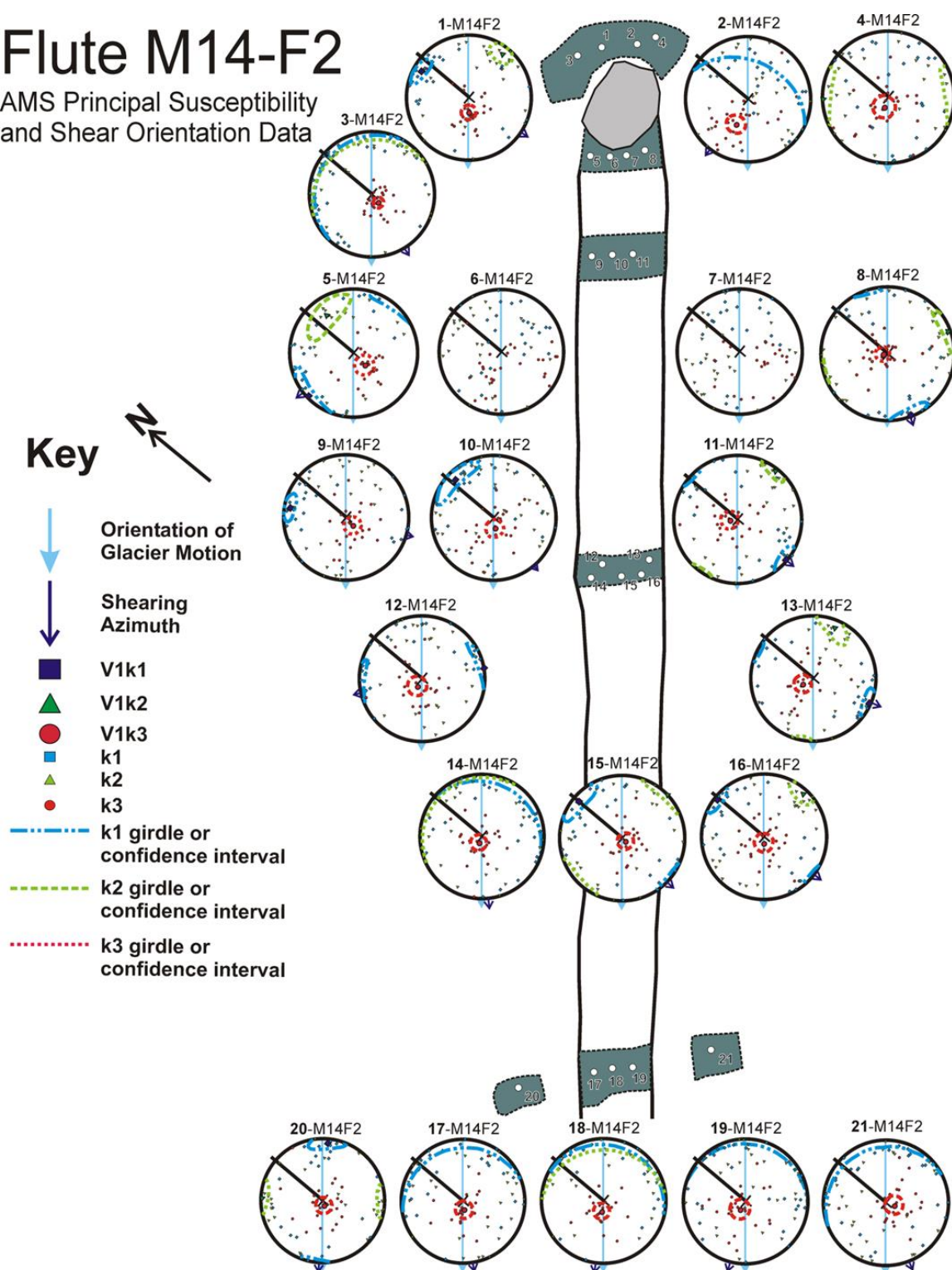


Figure 4-9B.

Flute M14-F2

AMS Shear Planes and
Poles to Shear Planes

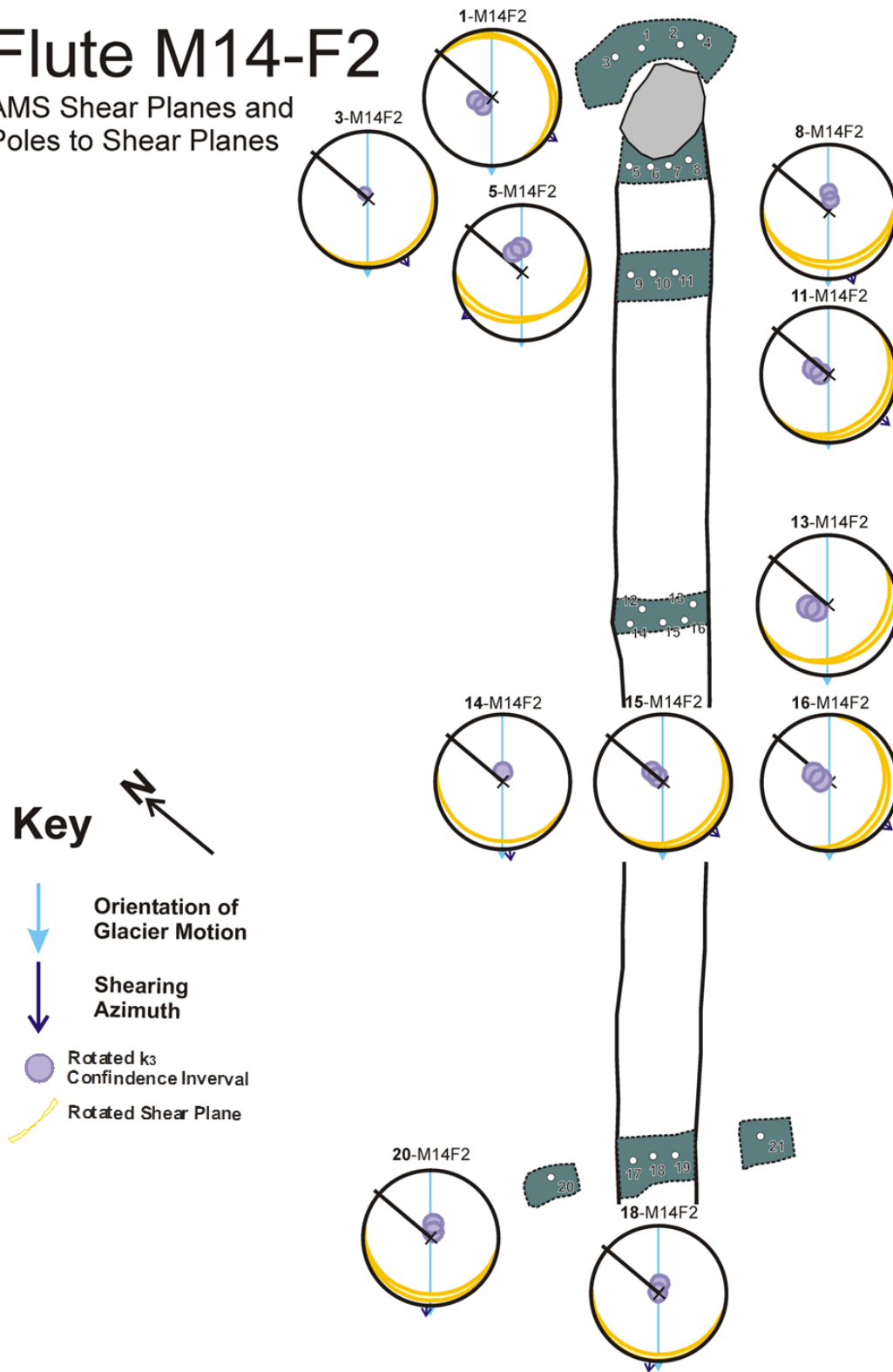


Figure 4-9C.

Table 4-4. AMS fabric results from flute M14-F2.

	1-M14F2			2-M14F2			3-M14F2			4-M14F2			5-M14F2			6-M14F2			7-M14F2			8-M14F2		
Ellipsoid Shape	TriBI			Near-TriBI			CoBI			Near-TriBI			TriBI			Not-50%			Isotropic			TriBI		
K1	K2	K3	K1	K2	K3	K1	K2	K3	K1	K2	K3	K1	K2	K3	K1	K2	K3	K1	K2	K3	K1	K2	K3	
Vf dec	349.7	88.9	221.6			261.1			192.6			279.2	14.4	164.7							211.3	121.2	318.8	
Vf Inc	14.7	14.5	69.2			69.2			78.9			4.3	27.1	65.2							3.4	5.3	83.1	
CD (Binn, 1994a)	0.77	0.82	0.94	0.24	0.38	0.73	0.37	0.36	0.68	0.71	0.62	0.90	0.88	0.84	0.96	0.81	0.88	0.82	0.83	0.82	0.89	0.72	0.68	
K (Woodcock, 1976)	1.07	1.63	3.83	0.15	0.37	0.88	0.20	0.20	0.97	1.32	0.74	3.42	0.40	0.82	7.11	2.26	2.92	0.82	2.41	2.63	3.85	0.88	0.84	3.10
I (Bennett 1994a)	0.10	0.13	0.07	0.19	0.49	0.10	0.08	0.10	0.05	0.29	0.20	0.16	0.08	0.20	0.12	0.31	0.29	0.28	0.27	0.33	0.24	0.12	0.10	0.06
C (Woodcock, 1976)	2.28	2.02	2.61	1.67	0.71	2.31	2.37	2.34	3.05	1.26	1.62	1.80	2.52	1.59	2.09	1.18	1.22	1.40	1.29	1.10	1.43	2.13	2.26	2.77
Fisher Test	Fail	Pass	Pass	NA	NA	Pass	Fail	Fail	Pass	NA	Fail	Pass	Fail	Fail	Pass	NA	NA	NA	NA	NA	NA	Fail	Fail	Pass
Principal Susceptibility Orientations																								
Rotated Shear Plane and V13 Orientations																								
Local Distribution	Bingham	Vatson	Vatson	Girdle	Isotropic	Vatson	Girdle	Girdle	Vatson	Isotropic	Bingham	Vatson	Bingham	Bingham	Vatson	Isotropic	Isotropic	Isotropic	Isotropic	Isotropic	Isotropic	Bingham	Bingham	Vatson
Shearing Azimuth				174		267			196					262								211		
Chi										11.6	16.5													
Chi Direction										0.1	20.9													
Vatson (Fisher)																								
Mean																								
Bingham																								8.6
Eta	16.6									29.6			31.8	33.3								18.4	22.5	
Phi	9.1									13.3			9.6	16.4								9.1	9.3	
Ellipsoid Shape	9-M14F2			10-M14F2			11-M14F2			12-M14F2			13-M14F2			14-M14F2			15-M14F2			16-M14F2		
K1	K2	K3	K1	K2	K3	K1	K2	K3	K1	K2	K3	K1	K2	K3	K1	K2	K3	K1	K2	K3	K1	K2	K3	
Vf dec	330.3	8.2	197.8	8.2		224.8	180.4	86.9	319.0	127.2		248.2	164.7	72.2	288.0				0.6	96.1	187.8	357.0	88.1	238.2
Vf Inc	8.3		75.2	14.0		75.0	3.4	4.5	79.4	2.7		79.0	3.3	15.2	71.0				80.5	8.7	0.1	82.3	3.5	8.2
CD (Binn, 1994a)	0.94	0.90	0.88	0.84	0.38	0.88	0.97	0.95	0.91	0.94	0.71	0.93	0.84	0.85	0.79	0.49	0.37		0.75	0.63	0.92	0.90	0.95	
K (Woodcock, 1976)	1.61	3.76	2.33	0.83	0.82	1.13	2.38	1.89	2.96	0.35	1.32	4.26	1.60	0.89	0.96	0.81	0.82		1.09	0.82	2.97	3.19	7.27	
I (Bennett 1994a)	0.11	0.21	0.10	0.19	0.81	0.09	0.15	0.12	0.10	0.07	0.30	0.13	0.10	0.17	0.07	0.13	0.19		0.18	0.12	0.08	0.15	0.19	
C (Woodcock, 1976)	2.23	1.55	2.30	1.64	1.38	2.40	1.91	2.10	2.34	2.70	1.21	2.07	2.31	1.77	2.72	1.91	1.66		1.72	1.30	2.49	1.90	1.66	
Fisher Test	Fail	NA	Pass	Fail	NA	Pass	Fail	Fail	Pass	Fail	NA	Pass	Fail	Fail	Pass	NA	NA	Pass	Fail	Fail	Pass	Fail	Fail	Pass
Principal Susceptibility Orientations																								
Rotated Shear Plane and V13 Orientations																								
Local Distribution	Bingham	Isotropic	Vatson	Bingham	Isotropic	Vatson	Bingham	Bingham	Vatson	Bingham	Isotropic	Vatson	Bingham	Bingham	Vatson	Girdle	Girdle	Vatson	Bingham	Bingham	Vatson	Bingham	Bingham	Vatson
Shearing Azimuth			151.9			190.4		0			306.8			163			244.2			181			178	
Chi																			14.2	6.6				
Chi Direction																			81.1	16.6				
Vatson (Fisher)																								
Mean					11.1			11.6		10.9						11.5					10.4			10.5
Bingham																								
Eta	14.3				31.2			14.7	14.4		28.8		14.4	28.1					23.6	28.3		14.7	14	
Phi	9.1				11.3			10.5	9.2		7.1		9.2	11.8					13.1	10.4		10.6	10.8	

Table 4-4., continued

Ellipsoid Shape	17-M14F 2			18-M14F 2			19-M14F 2			20-M14F 2			21-M14F 2		
	Near-Oblate			Oblate			Near-Oblate			Triaxial			Near-Oblate		
	k1	k2	k3	k1	k2	k3	k1	k2	k3	k1	k2	k3	k1	k2	k3
V1 dec			229.0			242.3			261.8		54.1	322.9	201.4		168.0
V1 inc			77.2			76.3			77.6		6.8	1.3	80.2		77.5
CGI (Benn, 1994a)	0.04	0.27	0.88	0.28	0.32	0.98	0.40	0.41	0.98	0.76	0.83	0.96	0.08	0.13	0.92
K (Woodcock, 1976)	0.02	0.21	1.93	0.14	0.23	12.71	0.31	0.41	5.04	1.20	1.96	8.49	0.04	0.08	3.82
I (Bennm 1994a)	0.15	0.28	0.08	0.09	0.20	0.09	0.19	0.33	0.15	0.14	0.17	0.13	0.19	0.28	0.12
C (Woodcock, 1976)	1.91	1.28	2.57	2.37	1.63	2.46	1.64	1.11	1.87	1.96	1.78	2.04	1.67	1.27	2.08
Fisher Test	N/A	N/A	Pass	N/A	N/A	Pass	N/A	N/A	Pass	Fail	Fail	Pass	N/A	N/A	Pass
Principal Susceptibility Orientations															
Rotated Shear Plane and V1K3 Orientations															
Axial Distribution	Girdle	Isotropic	Watson	Girdle	Girdle	Watson	Girdle	Isotropic	Watson	Bingham	Bingham	Watson	Girdle	Isotropic	Watson
Shearing Azimuth		219.4			238.6			246.3			233.5			206	
Girdle															
Dip	14.7			11.2	19		8.3						11.6		
Dip Direction	38.8			74.5	48.8		65.8						27.6		
Watson (Fisher)															
alpha			11.4			10.4			12.9				10.7		11.7
Bingham															
Eta										19.7	17				
Zeta										11	12.1				

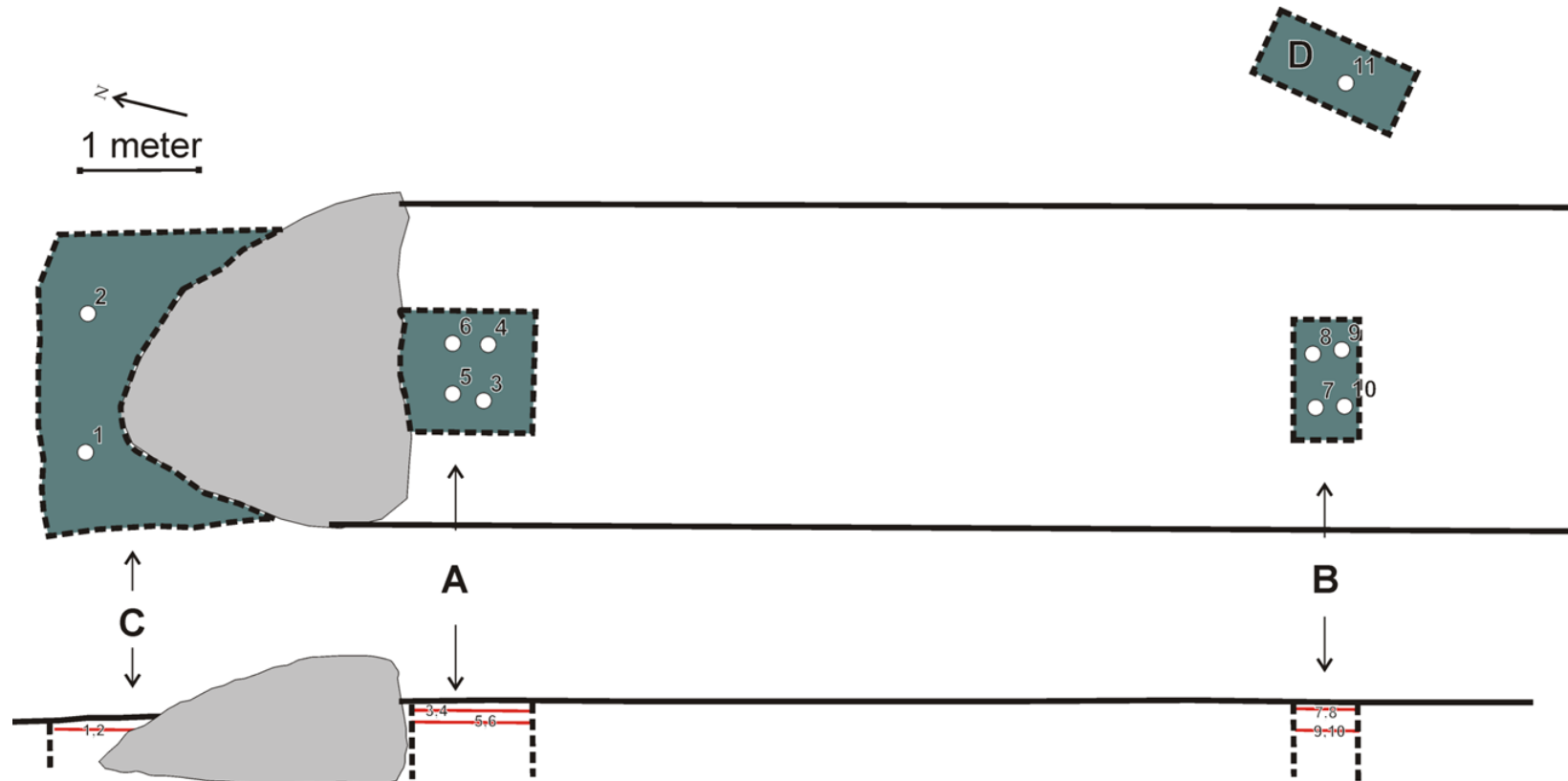


Figure 4-10. (A) Plan and longitudinal views of flute B14-F1, with the approximate mean location of samples used in each fabric indicated. (B) AMS fabrics and fabric analysis results from flute B14-F1. Numerical results shown in [Table 4-5](#). All data are displayed on equal-area, lower-hemisphere stereonets. Bold lines on stereonet indicate true north. (C) Corrected shear plane attitudes (yellow lines) and pole-to-plane confidence intervals (purple circles) derived from AMS fabrics of flute B14-F1. Fabric analysis results shown in [Table 4-5](#). All data are displayed on equal-area, lower-hemisphere stereonets.

Flute B14-F1

AMS Principal Susceptibility
and Shear Orientation Data

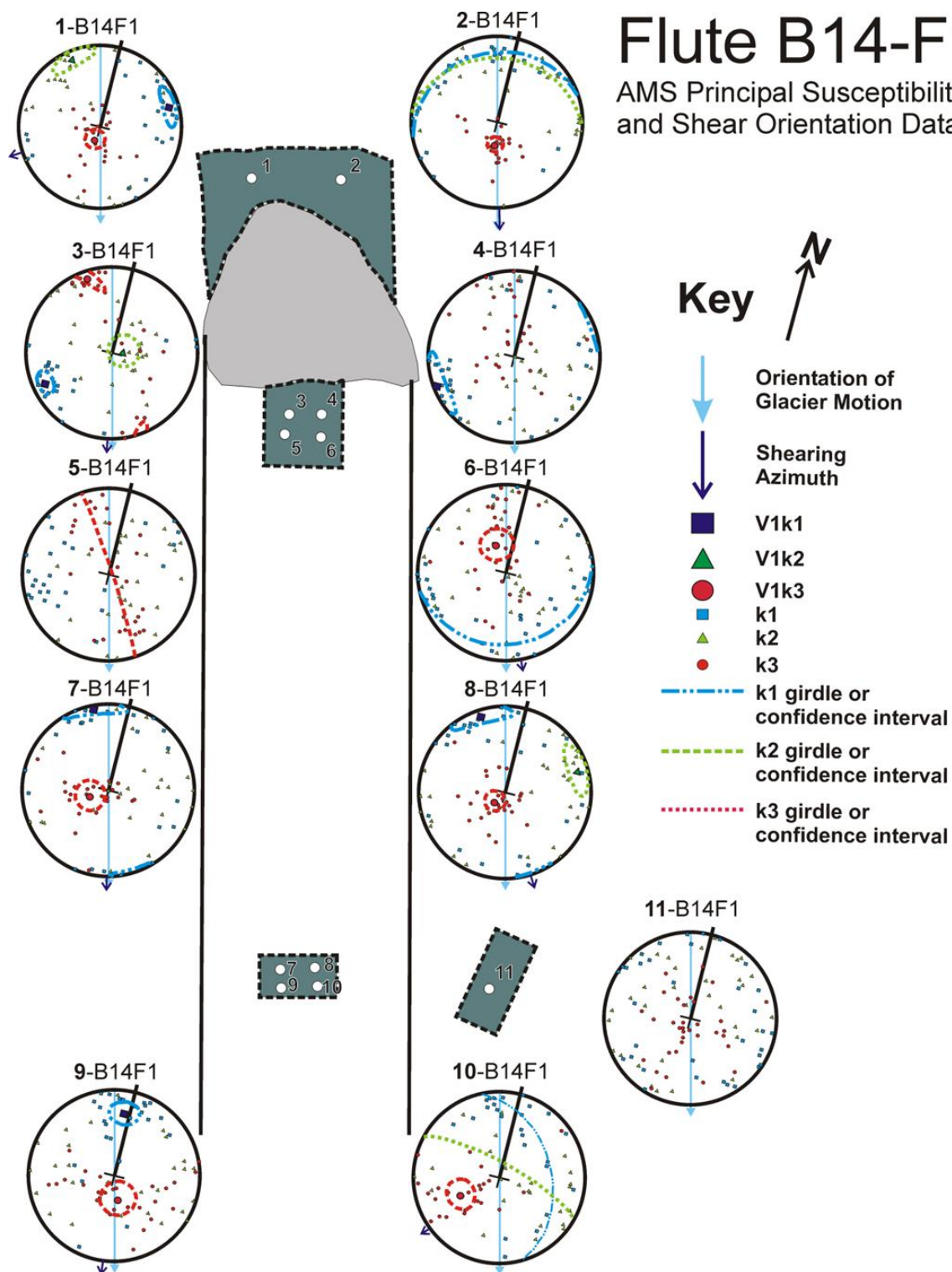


Figure 4-10B.

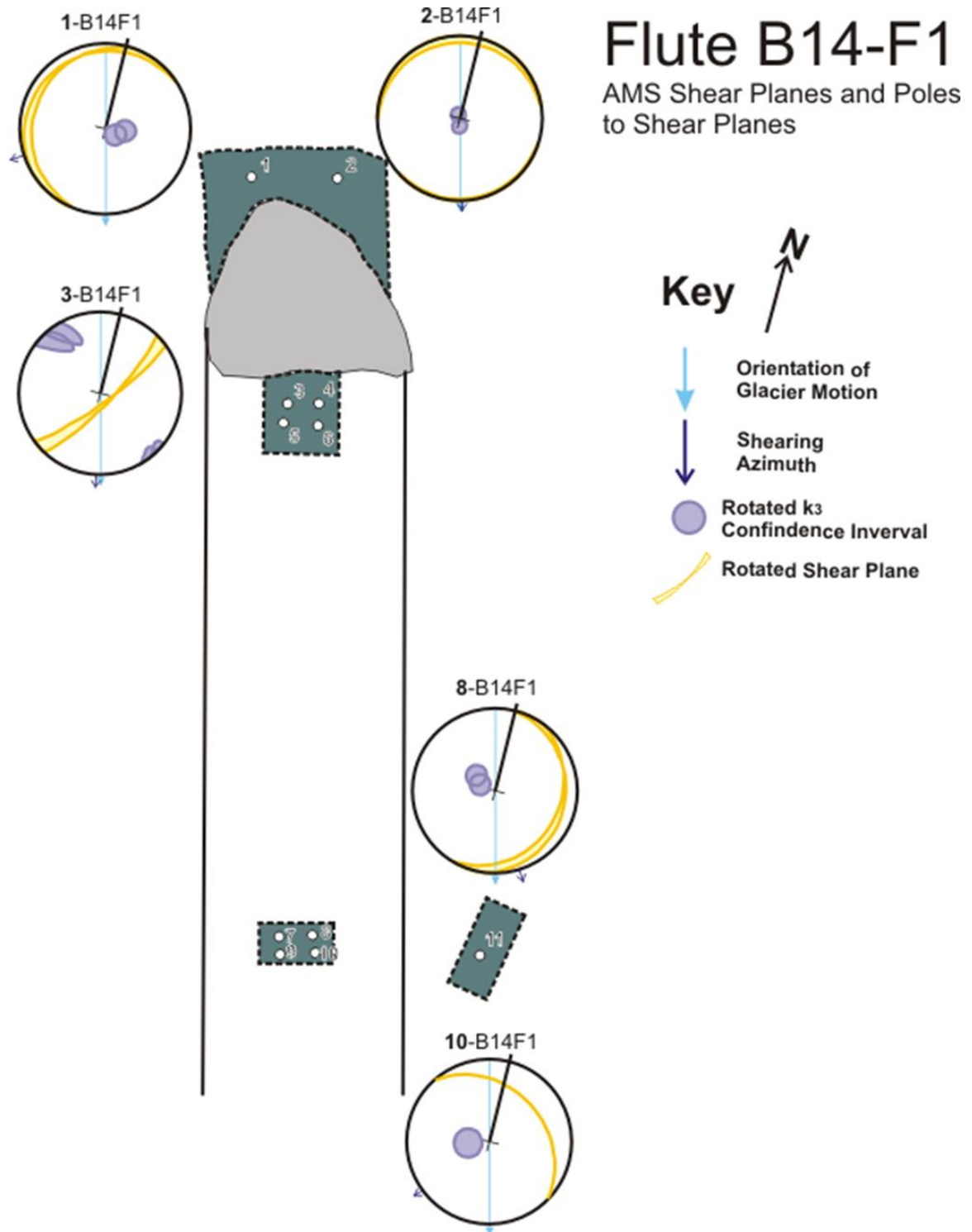


Figure 4-10C.

Table 4-5. AMS fabric results from flute B14-F1.

Elipsoid shape	1-B14F1 Trial#1			2-B14F1 COBSE			3-B14F1 Trial#1			4-B14F1 isotropic K7			5-B14F1 isotropic			6-B14F1 COBSE7		
	K1	K2	K3	K1	K2	K3	K1	K2	K3	K1	K2	K3	K1	K2	K3	K1	K2	K3
Vf dec	60.70	325.80	191.00				166.30	232.40	81.00	327.90	233.10							
Vf inc	12.60	11.20	79.10				67.70	18.70	75.20	8.60	8.20							
CO (Benn, 1994a)	0.77	0.72	0.92	0.39	0.41	0.95	0.96	0.96	0.77	0.62	0.65	0.82	0.67	0.95	0.63	0.41	0.50	0.63
K (Woodcock, 1976)	0.96	0.88	2.55	0.21	0.24	2.82	5.79	1.39	0.40	0.64	2.66	0.94	0.85	1.04	0.28	0.40	1.33	0.42
K (Benn 1994a)	0.08	0.11	0.07	0.08	0.10	0.04	0.08	0.18	0.04	0.11	0.37	0.21	0.22	0.38	0.14	0.14	0.62	0.12
C (Woodcock, 1976)	2.46	2.17	2.65	2.51	2.35	3.35	2.58	1.71	1.17	2.18	0.95	1.95	1.51	0.95	1.95	1.95	0.67	2.58
Fisher Test	Fail	Fail	Pass	NA	NA	Pass	Pass	Pass	Fail	Fail	NA	NA	NA	NA	NA	NA	NA	Pass
Principal Susceptibility Orientations																		
Axis Distribution	Bingham	Bingham	Watson	Girdle	Girdle	Watson	Watson	Watson	Bingham	Bingham	isotropic	isotropic	isotropic	isotropic	Girdle	Girdle	isotropic	Watson
Shear Sense	239			165			169									156		
Chi				20.4			26.6									86.2		
Chi Direction				334.1			351.6									87.8		
Watson (Fisher)				9.7			7.1									15.2		
Chi																		
Chi																		
Chi																		
Chi																		
Chi																		
Chi																		
Chi																		
Chi																		
Chi																		
Chi																		
Chi																		
Chi																		
Chi																		
Chi																		
Chi																		
Chi																		
Chi																		
Chi																		
Chi																		
Chi																		
Chi																		
Chi																		
Chi																		
Chi																		
Chi																		
Chi																		
Chi																		
Chi																		
Chi																		
Chi																		
Chi																		
Chi																		
Chi																		
Chi																		
Chi																		
Chi																		
Chi																		
Chi																		
Chi																		
Chi																		
Chi																		
Chi																		
Chi																		
Chi																		
Chi																		
Chi																		
Chi																		
Chi																		
Chi																		
Chi																		
Chi																		
Chi																		
Chi																		
Chi																		
Chi																		
Chi																		
Chi																		

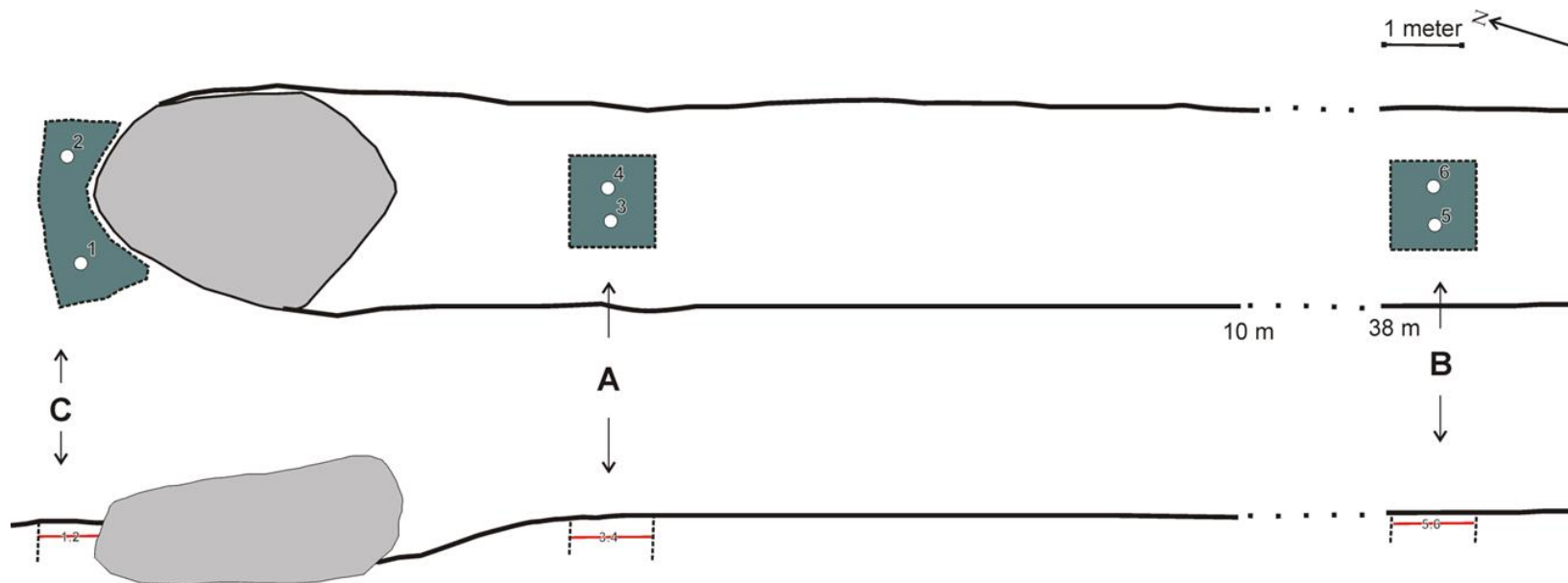


Figure 4-11. (A) Plan and longitudinal views of flute B14-F2, with the approximate mean location of samples used in each fabric indicated. (B) AMS fabrics and fabric analysis results from flute B14-F2. Numerical results shown in [Table 4-6](#). All data are displayed on equal-area, lower-hemisphere stereonet. Bold lines on stereonet indicate true north. (C) Corrected shear plane attitudes (yellow lines) and pole-to-plane confidence intervals (purple circles) derived from AMS fabrics of flute B14-F2. Fabric analysis results shown in [Table 4-6](#). All data are displayed on equal-area, lower-hemisphere stereonet

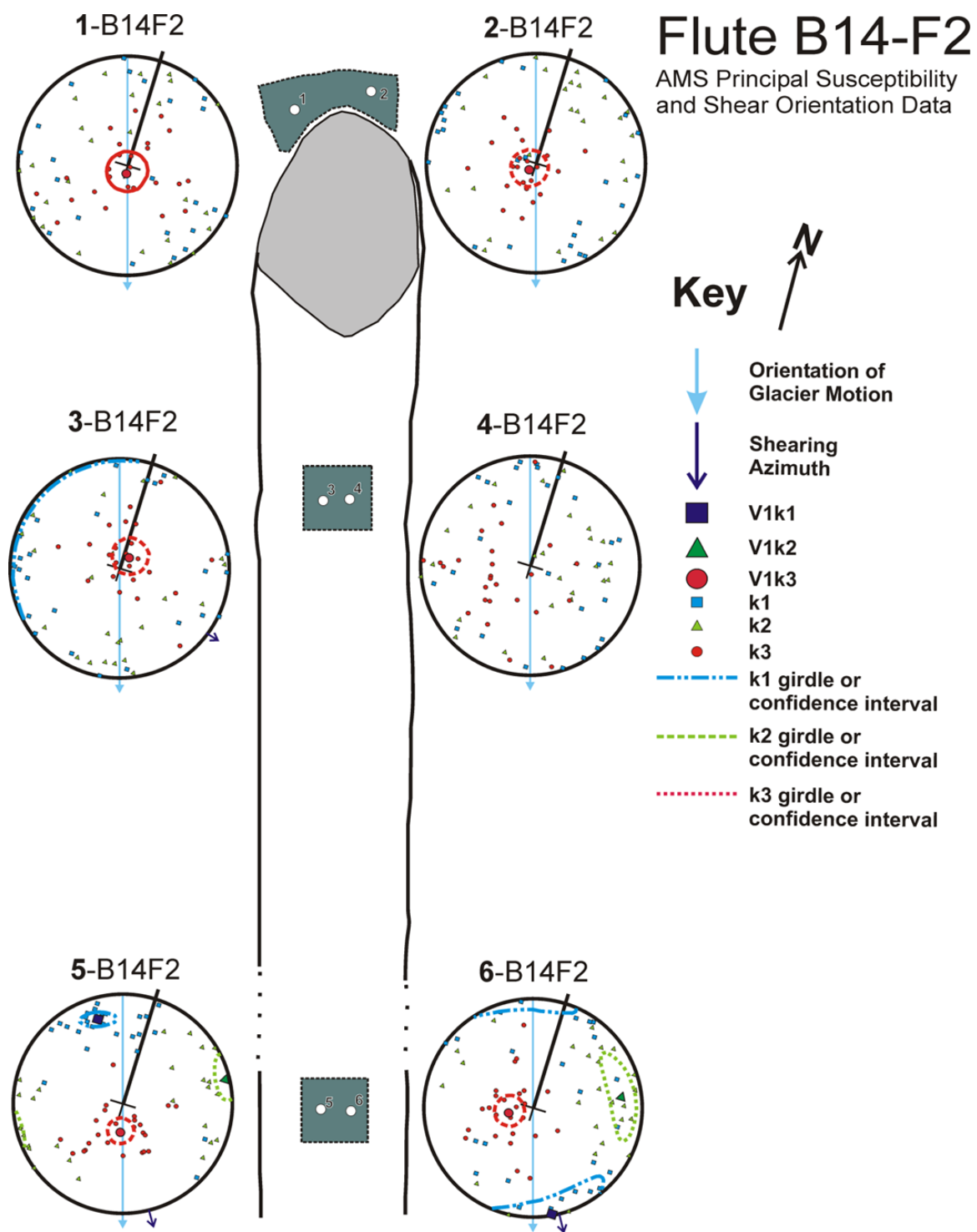


Figure 4-11B.

Flute B14-F2

AMS Shear Planes and Poles to Shear Planes

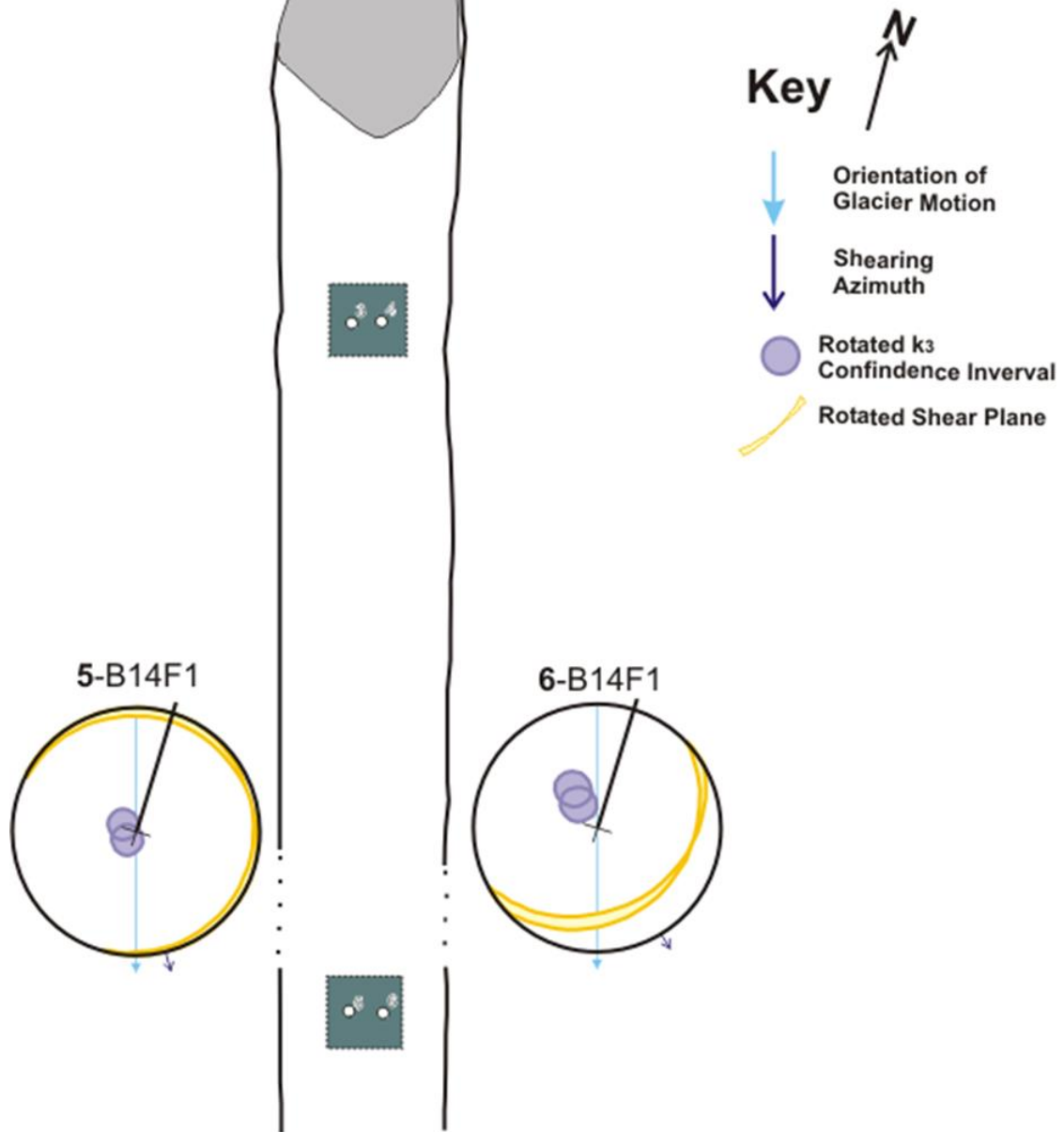


Figure 4-11C.

Table 4-6. AMS fabric results from flute B14-F2.

Ellipsoid Shape	1-B14F2			2-B14F2			#B14F2			4-B14F2			5-B14F2			6-B14F2		
	Isotropic?			Isotropic?			Oblate?			Isotropic			Triaxial			Triaxial		
Vl dec			112.20			231.00			7.70				324.80	55.90	167.50	149.80	62.80	240.50
Vl inc			87.10			81.10			80.50				21.00	4.70	69.30	3.70	19.70	71.10
CGI (Benn, 1994a)	0.24	0.28	0.82	0.64	0.63	0.93	0.45	0.65	0.99	0.56	0.82	0.88	0.96	0.92	0.91	0.58	0.82	0.89
K (Woodcock, 1976)	0.17	0.22	1.80	0.82	0.82	4.94	0.31	1.03	4.81	0.88	2.86	3.58	1.33	4.28	2.41	0.83	0.85	2.14
I (Benn 1994a)	0.27	0.38	0.17	0.21	0.24	0.16	0.12	0.32	0.15	0.28	0.38	0.26	0.05	0.15	0.07	0.21	0.15	0.09
C (Woodcock, 1976)	1.33	0.97	1.77	1.55	1.43	1.80	2.09	1.15	1.91	1.26	0.96	1.34	2.96	1.92	2.69	1.57	1.91	2.44
Fisher Test	N/A	N/A	Pass	N/A	N/A	Pass	N/A	N/A	Pass	N/A	N/A	N/A	Fail	Fail	Pass	Fail	Fail	Pass
Principal Susceptibility Orientations																		
Rotated Shear Plane and Vt3 Orientations																		
Axial Distribution	Isotropic	Isotropic	Watson	Isotropic	Isotropic	Watson	Girdle	Isotropic	Watson	Isotropic	Isotropic	Isotropic	Bingham	Bingham	Watson	Bingham	Bingham	Watson
Shearing Azimuth								105						147.6			328.5	
Girdle																		
Dip							4.1											
Dip Direction							284.9											
Watson (Fisher)			15			13.7			13.7						9.8			11.3
alpha																		
Bingham																		
Eta													11.5	13.2		34.9	28	
Zeta													6.1	10.2		14	11.7	

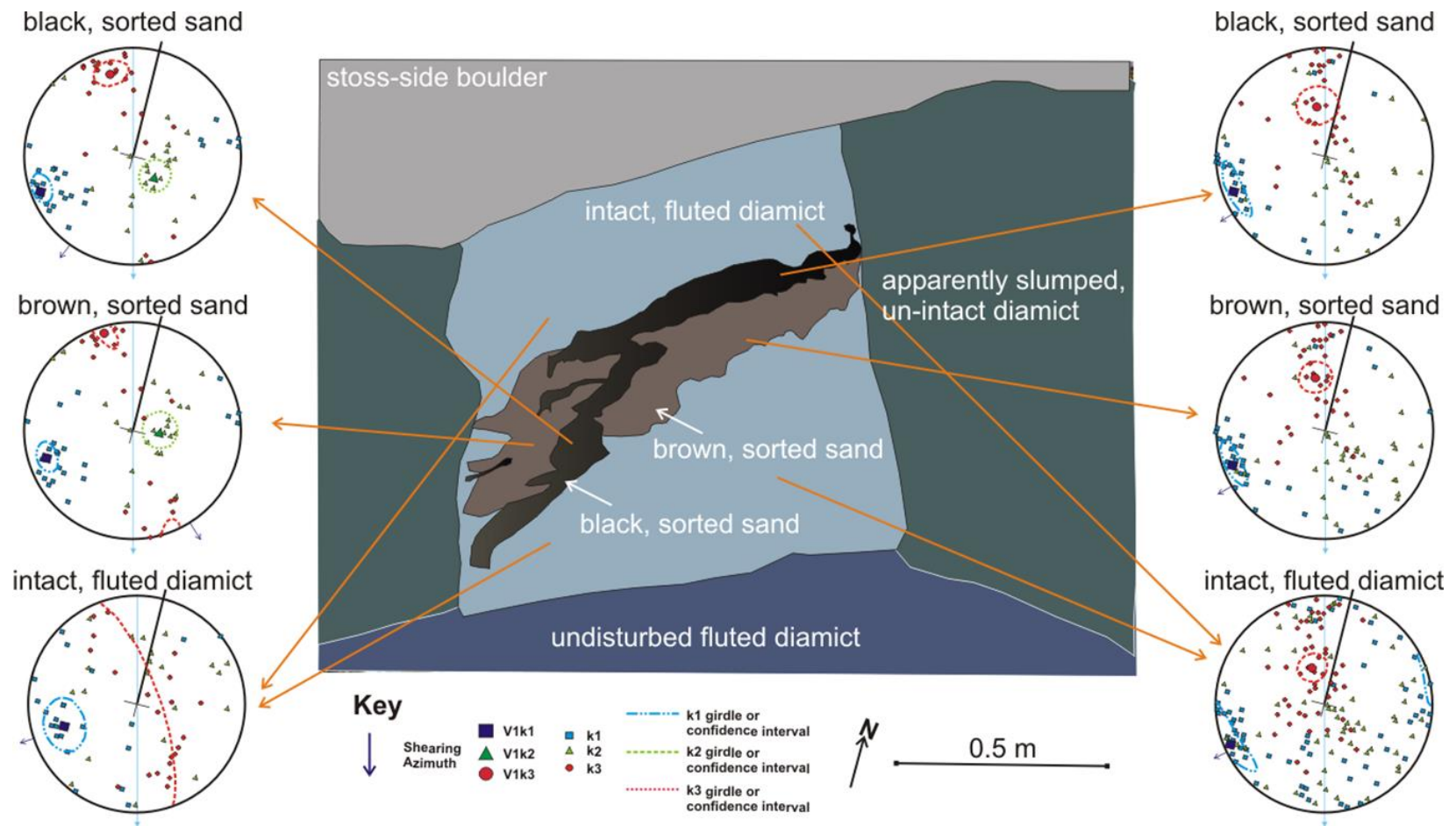


Figure 4-12. AMS fabrics from B14-F1, site A, immediately downglacier from the headward boulder. AMS samples were regrouped by sediment type and flute side and their fabrics reanalyzed. See [Figures 4-19](#) and [4-20](#) for comparison with original fabrics. Fabric analysis results shown in [Table 4-7](#). All data are displayed on equal-area, lower-hemisphere stereonets.

Table 4-7. AMS fabric results from flute B14-F2, site A . AMS samples were regrouped by sediment type and reanalyzed. All data are displayed on equal-area, lower-hemisphere stereonet.

Ellipsoid Shape	B14F1A-BlkSedB				B14F1A-BlkSedA				B14F1A-BwnSedB				B14F1A-BwnSedA				B14F1A-TiIB				B14F1A-TiIA			
	Triaxial				Triaxial?				Triaxial				Triaxial?				Prolate?				Triaxial?			
	k1	k2	k3		k1	k2	k3		k1	k2	k3		k1	k2	k3		k1	k2	k3		k1	k2	k3	
V1 dec	236.40	114.20	330.50		235.04		339.51		57.76	75.91	149.60		236.05		336.34		57.90	11.47			233.95		328.86	
V1 inc	12.80	66.00	19.30		12.19		46.81		18.62	68.47	5.74		10.52		43.89		24.86	44.34			6.94		60.94	
CGI (Benn, 1994a)	0.89	0.89	0.86		0.72	0.88	0.65		0.99	0.87	0.72		0.75	0.95	0.74		0.78	0.75	0.49		0.53	0.88	0.62	
K (Woodcock, 1976)	1.51	2.79	1.39		0.81	3.94	0.72		15.47	2.59	0.60		1.01	10.86	0.95		1.52	1.91	0.36		0.54	5.35	0.68	
J (Benn, 1994a)	0.04	0.14	0.06		0.09	0.32	0.14		0.08	0.16	0.05		0.11	0.30	0.12		0.18	0.42	0.12		0.21	0.53	0.17	
C (Woodcock, 1976)	3.26	1.95	2.80		2.39	1.13	1.99		2.52	1.83	3.09		2.23	1.19	2.15		1.69	0.87	2.12		1.57	0.64	1.80	
Fisher Test	Pass	Pass	Pass		Fail	N/A	Pass		Pass	Pass	Fail		Fail	N/A	Pass		Pass	N/A	N/A		Fail	N/A	Pass	
Principal Susceptibility Orientations																								
Axial Distribution	Watson	Watson	Watson		Bingham	Isotropic	Watson		Watson	Watson	Bingham		Bingham	Isotropic	Watson		Fisher	Isotropic	Girdle		Bingham	Isotropic	Fisher	
Shearing Azimuth	204				224				134				226				238				230			
Girdle																								
Dip																					72.3			
Dip Direction																					56.4			
Watson (Fisher)																								
alpha	8.9	12.1	11.1				15.2		9.4	13.5					12.2		17.6							11.0
Bingham																								
Eta					18						19.2		14.8								22.6			
Zeta					7.9						5.2		8								8.7			

observation justifies using uncorrected shear azimuths in this analysis, which allowed shear azimuths to be estimated from fabrics with isotropic k_2 distributions. This use of uncorrected shear azimuths follows standard practice in the analysis of clast fabrics in which, unlike the case for AMS analysis, no ancillary information about shear-plane orientation is available and all measurements are thus “uncorrected.”

4.2.2 Generalized AMS fabrics

In order to generalize flute AMS fabrics, the orientation and position of individual AMS samples were referenced to their host flute’s orientation and size as described in [Section 3.5.1](#). Flute-referenced AMS samples from M14-F1, M14-F2, B14-F1 (excluding site A), and B14-F2 were grouped by their flow-transverse position within the flute ([Fig. 4-13](#)), with A being the left side of the flute (viewed looking downglacier), Center being a strip down the flute axis, and B the right side. The fabrics based on these new groupings were analyzed using the methods described in [Section 3.5](#) ([Fig. 4-13](#), [Table 4-8](#)). The fabrics of A, Center, and B have isotropic k_2 distributions and strongly clustered k_3 distributions. The k_3 distributions, which are indicative of shear-plane orientation, for A and B (the flute exterior) are statistically distinct and plunge steeply into the flute. The k_3 distribution for the Center (flute interior) is not statistically distinct from the k_3 distribution of either A or B. Importantly, the k_1 distributions for A and Center were girdled and thus indicate shearing azimuth. The apparent orientation of shear for the Center fabric ([Fig. 4-13](#), solid blue arrow) is almost parallel to the flute long axis. In contrast, the shearing azimuth of the A fabric ([Fig. 4-13](#), dashed blue arrow) trends ~40° inward toward the flute centerline.

This same shear convergence is evident when uncorrected shear azimuths are grouped similarly (Fig. 4-14). The mean flute-referenced shear azimuths for both side A and side B have slightly convergent trends. However, orientations with the highest concentration of shear azimuths for both sets of data point slightly outward from the flute's central axis, indicating a discrete population of fabrics with divergent trends. In the context of Figure 4-13, this distribution of flute-referenced shear azimuths illustrates that, although convergent fabrics are dominant in flutes, substantial localized variability exists, including divergent and flow-parallel fabrics.

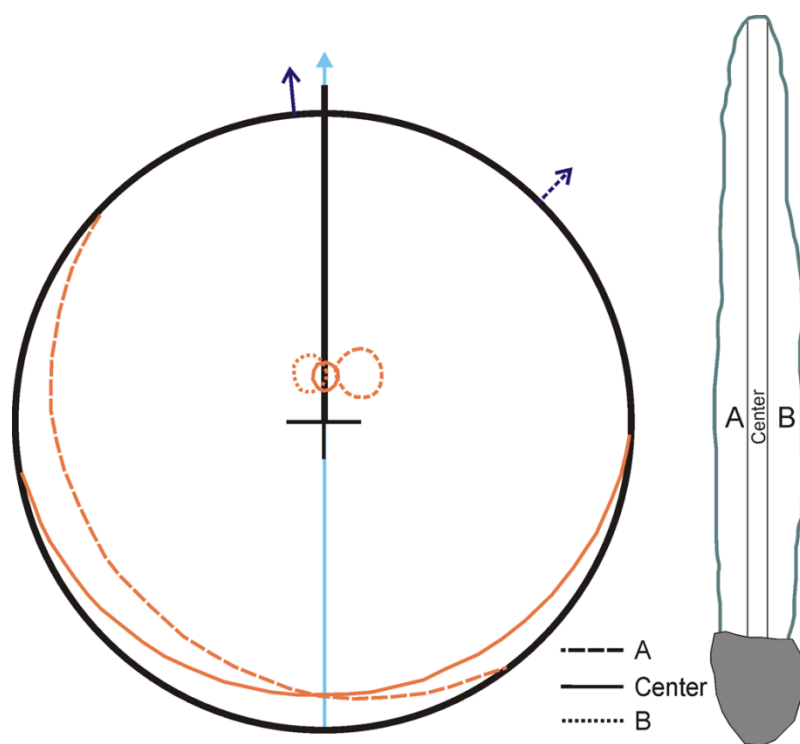
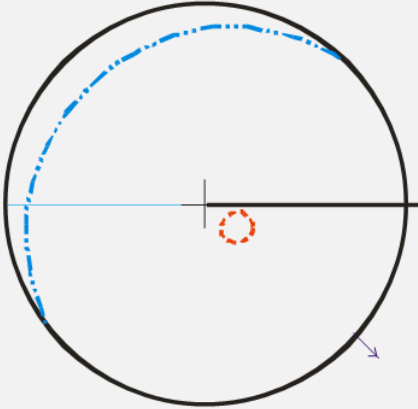
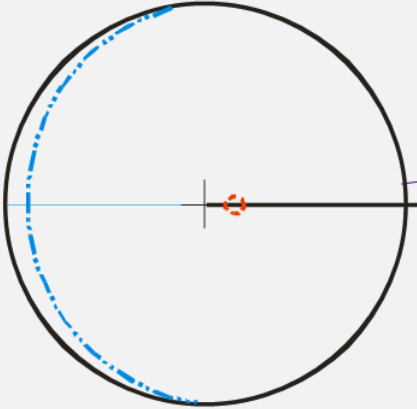
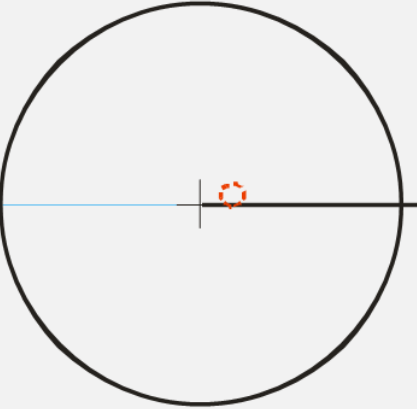


Figure 4-13. Fabric analysis of AMS principal susceptibilities from flutes M14-F1, M14-F2, B14-F1 (excluding site A), and B14-F2, referenced to flute axes. The planes represent the k_1 best-fit girdles for the “A” side of the flute and the center of the flute. The “B” side of the flute had an isotropic k_1 distribution. The confidence intervals represent the k_3 distribution of AMS samples from the “A” side of the flutes, the “B” side of the flute, and the center of the flute. The distribution of k_2 orientations was isotropic in the three cases. Fabric analysis results are shown in Table 4-8. Sample numbers are $N_A = 72$, $N_{center} = 265$, and $N_B = 277$. Data are displayed on equal-area, lower-hemisphere stereonets

Table 4-8. AMS fabric results from flute fabrics displayed in [Figure 4-13](#) AMS samples were reference to a common flute orientation, regrouped by flute position, and reanalyzed. All data are displayed on equal-area, lower-hemisphere stereonet.

	A			Center			B		
Ellipsoid Shape	Oblate?			Oblate?					
	k1	k2	k3	k1	k2	k3	k1	k2	k3
V1 dec	323.66	234.99	36.74	143.91	235.01	1.04	358.96	82.99	340.39
V1 inc	2.94	12.08	74.54	11.35	8.78	76.97	13.75	0.58	77.47
CGI (Benn, 1994a)	0.42	0.55	0.97	0.35	0.42	0.99	0.29	0.32	0.95
K (Woodcock, 1976)	0.31	0.64	11.42	0.23	0.38	42.98	0.21	0.30	7.62
I (Bennm 1994a)	0.15	0.26	0.14	0.14	0.25	0.13	0.24	0.36	0.19
C (Woodcock, 1976)	1.87	1.34	1.98	1.96	1.38	2.06	1.43	1.01	1.66
Fisher Test	N/A	N/A	Pass	N/A	N/A	Pass	N/A	N/A	Fail
Principal Susceptibility Orientations									
Axial Distribution	Girdle	Isotropic	Watson	Girdle	Isotropic	Watson	Isotropic	Isotropic	Bingham
Shearing Azimuth	44			354.5					
Girdle									
Dip	18.8			13.1					
Dip Direction	225			174.1					
Watson (Fisher)									
alpha	6.6			3.2					
Bingham									
Eta							4.6		
Zeta							4.3		

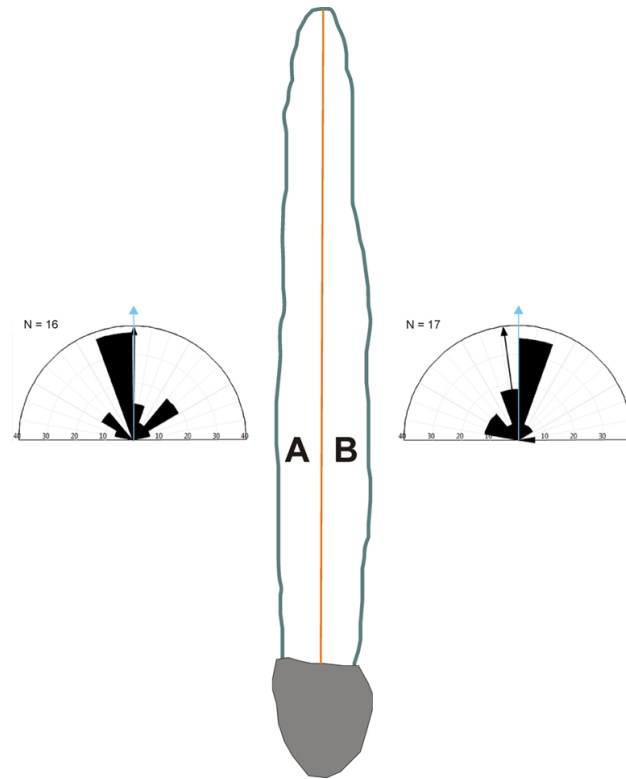


Figure 4-14. Uncorrected shear orientations derived from AMS fabrics referenced to the flute axes, grouped by their position in flutes, and plotted on rose diagrams. The blue arrow indicates flute orientation, and the black arrow indicates mean orientation for the dataset. Shear azimuths are grouped in 20° intervals and the exterior of the rose diagram represents 40% of the population. Shear azimuths of fabrics that straddled the flute axis were not included in these analyses because of the small number of samples on each side.

4.3 Relative density

The dry bulk densities of the till collected in AMS sample boxes from flutes M14-F1, M14-F2, B14-F1, and B14-F2 display several spatial patterns ([Fig. 4-15A-D](#)): (1) densities are typically larger on the stoss sides of headward boulders than elsewhere, (2) densities of till adjacent to the flutes are similar to, or slightly higher than, the mean density of the flute's till, (3) densities do not vary systematically with depth in flutes, which may reflect poor depth resolution due to sampling from horizontal platforms, and (4) densities increase from the edges of flutes toward their centerlines.

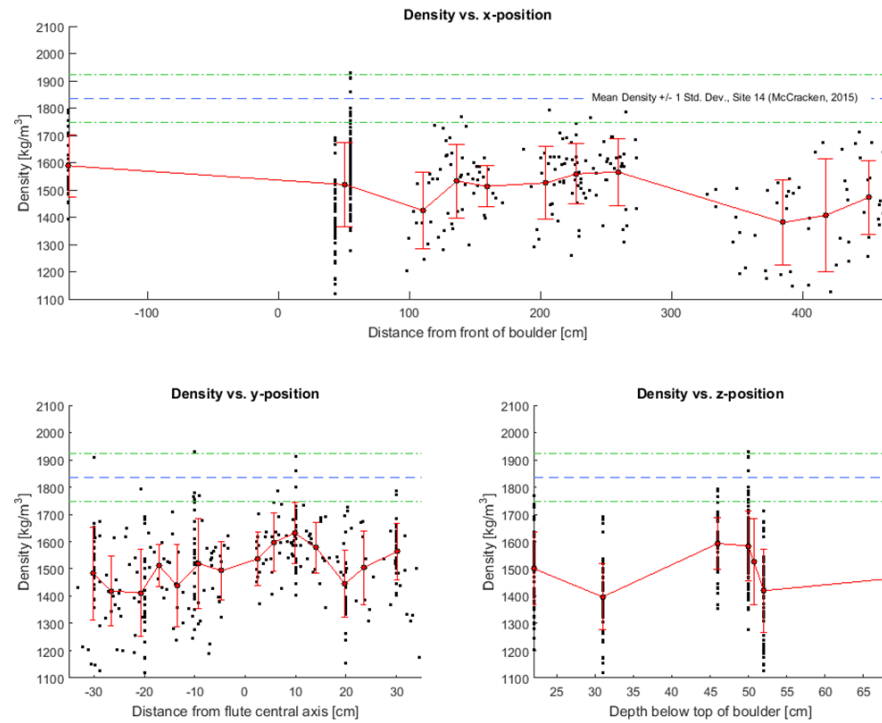


Figure 4-15. Variations in dry bulk density of AMS samples along the x, y, and z axes of flutes (A) M14-F1, (B) M14-F2, (C) B14-F1, and (D) B14-F2. The means and standard deviations (error bars, ± 1 S.D.) of density values were calculated for a set of at least 10 AMS boxes and at various mean x, y, or z positions of the AMS samples. Density values plotted along the x-axis do not contain values from AMS samples collected outside of the flute's width. Density values plotted along the y-axis do not contain values from AMS samples collected on the stoss side of the boulder. Density values plotted along the z-axis do not contain values from AMS samples collected from either outside the flute's width or on the stoss side of the boulder. For (A) the mean and standard deviation of AMS sample densities from site 14 in McCracken (2015) are also shown here. Site 14 was unfluted and located < 100 m from Flute M14-F1. For (C) the density of each sample was normalized using the minimum and maximum density value of its sediment type in Flute B14-F1, to account for the effect of texture on density.

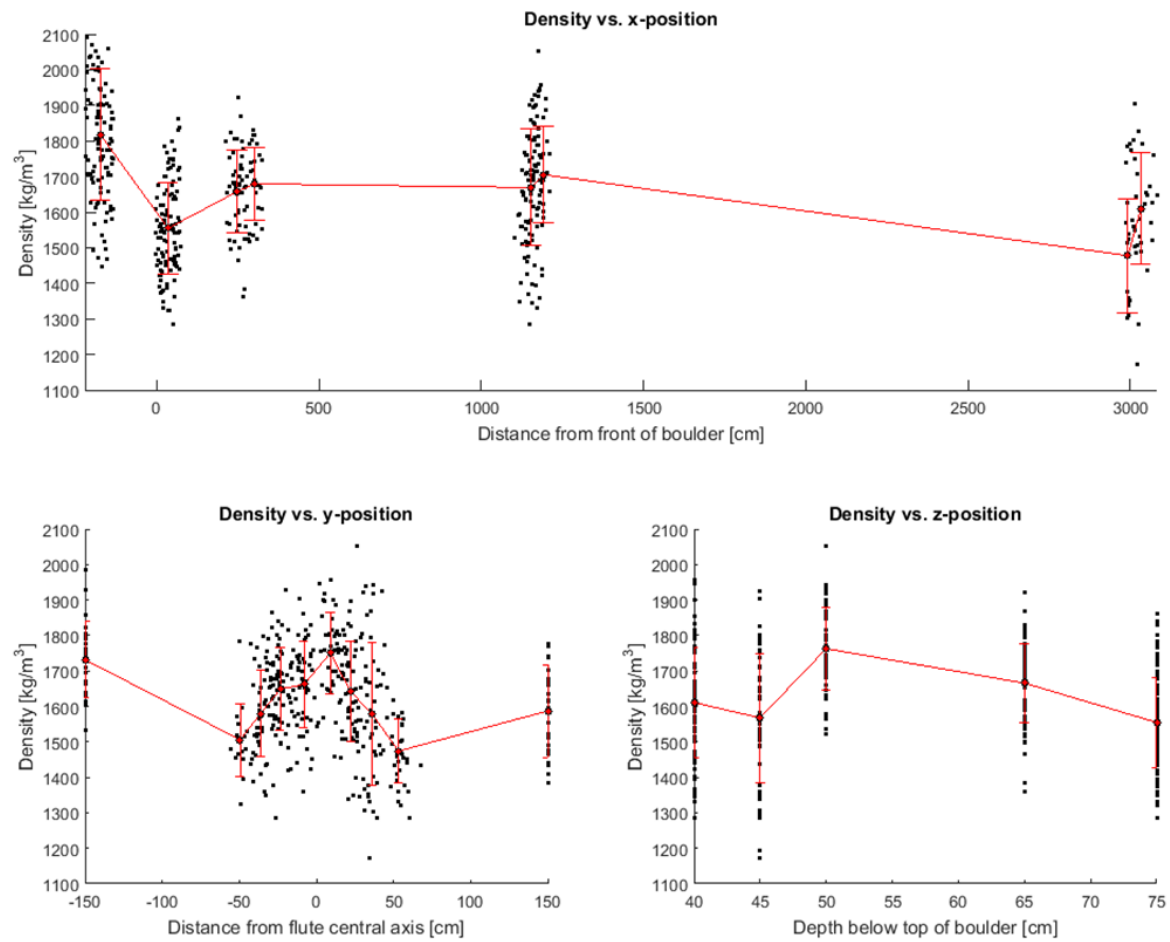


Figure 4-15B.

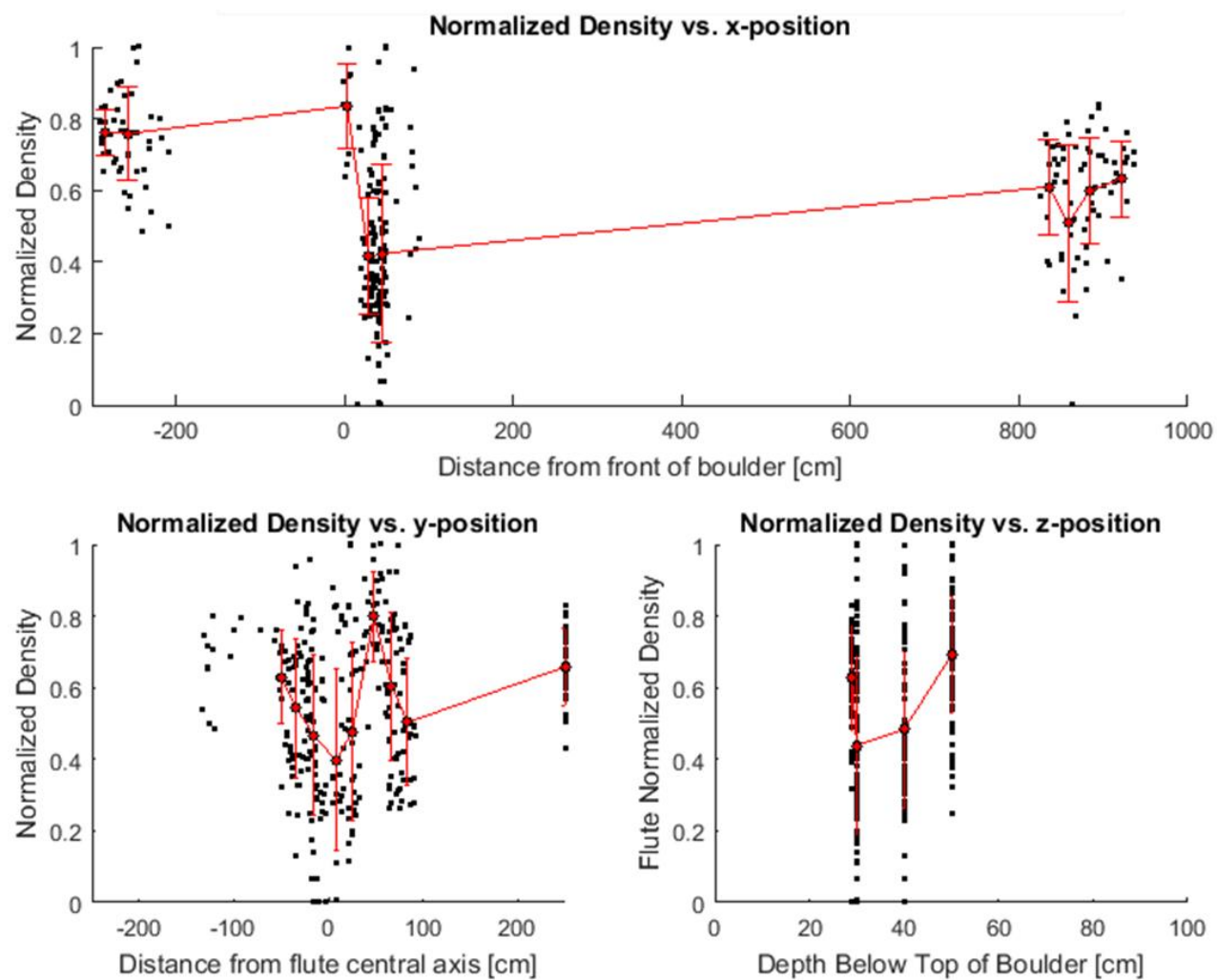


Figure 4-15C.

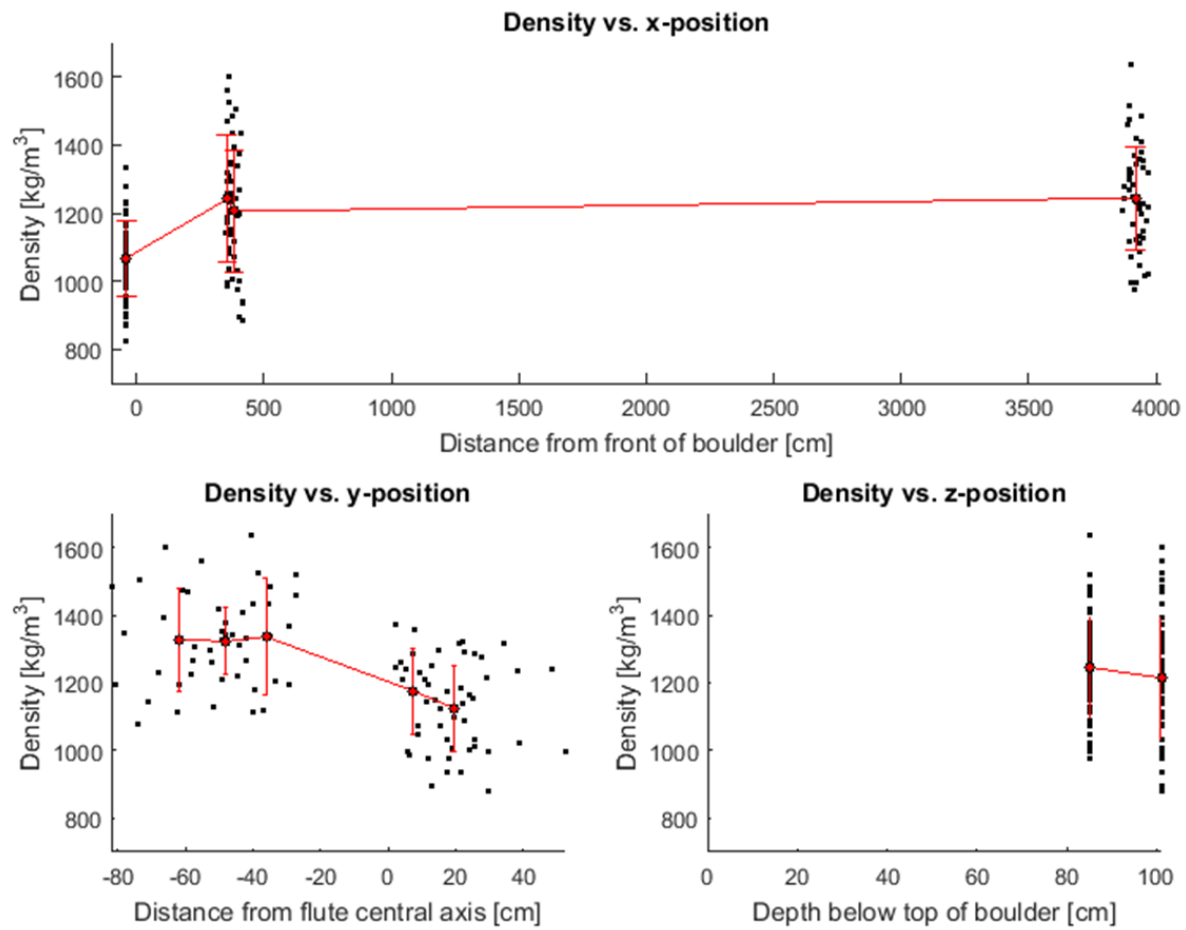


Figure 4-15D.

Till densities are generally higher on the stoss sides of boulders than in flutes downstream of boulders ([Fig. 4-15](#), A-C, uppermost plots). In one case, however, on the stoss side of the B14-F2 boulder, densities are lower than in the flute ([Fig. 4-15D](#)). Perhaps related to this observation is that AMS fabrics from this location are isotropic ([Fig. 4-11B](#)), unlike stoss-side fabrics at other flutes.

The most significant of these trends is the increase in till density from the edge of flutes toward their centerlines. The trend is most pronounced in M14-F2, which is a long, parallel-sided flute ([Fig. 4-15B](#)) and, significantly, is far less distinct in M14-F1, which is a short, tapered flute ([Fig. 4-15A](#)). This trend was not measured in either Breiðamerkurjökull flute because AMS samples were collected only from the interiors of those flutes.

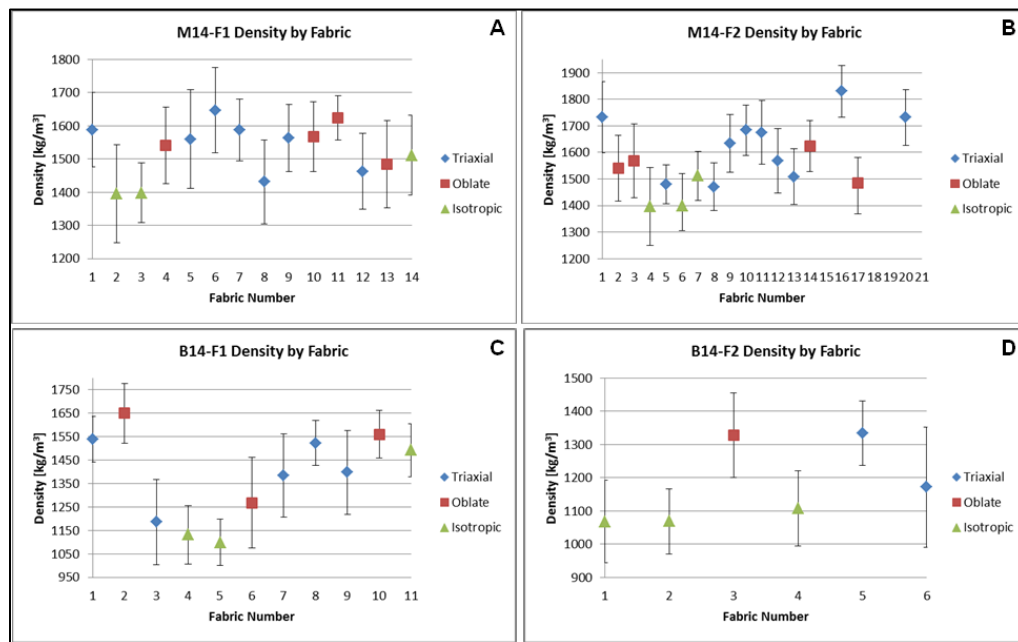


Figure 4-16. Mean densities and standard deviations (error bars, ± 1 S.D.) of individual AMS fabrics grouped by fabric shape for flute (A) M14-F1, (B) M14-F2, (C) B14-F1, and (D) B14-F2. The location of individual fabrics in each flute are shown in [Fig. 4-7A](#), [Fig. 4-8A](#), [Fig. 4-9A](#), [Fig. 4-10A](#), and [Fig. 4-11A](#). These data are also shown in [Table 4-9](#).

Table 4-9. Mean and standard deviation of sediment dry bulk density by fabric shape.

Fabric Number	Mean Dry Density, kgm ⁻³	Standard Deviation	Number of Samples,	AMS Fabric Shape
M14-F1				
1	1588	112	24	Triaxial
2	1396	148	25	Isotropic
3	1398	90	27	Isotropic
4	1541	116	25	Oblate
5	1560	148	24	Triaxial
6	1647	128	25	Triaxial
7	1587	93	26	Triaxial
8	1431	126	25	Triaxial
9	1564	101	28	Triaxial?
10	1567	106	29	Oblate
11	1624	67	24	Oblate
12	1463	114	29	Triaxial?
13	1484	131	26	Oblate?
14	1512	121	28	Isotropic
M14-F2				
1	1733	134	26	Triaxial
2	1733	123	26	Oblate?
3	2024	139	26	Oblate
4	1781	147	25	Isotropic
5	1480	74	26	Triaxial
6	1637	123	29	Isotropic
7	1639	92	24	Isotropic
8	1470	89	30	Triaxial
9	1634	110	23	Triaxial?
10	1683	94	29	Triaxial?
11	1675	120	25	Triaxial
12	1569	121	24	Triaxial?
13	1508	104	24	Triaxial
14	1701	97	26	Oblate
16	1830	97	24	Triaxial
17	1631	115	24	Oblate?
19	1505	209	27	Oblate?
20	1732	105	24	Triaxial
21	1587	128	26	Oblate?
B14-F1				
1	1538	97	25	Triaxial
2	1650	127	25	Oblate
3	1186	181	24	Triaxial
4	1132	124	24	Isotropic
5	1099	99	25	Isotropic
6	1269	193	29	Oblate?
7	1385	179	23	Triaxial?
8	1522	96	24	Triaxial
9	1398	178	26	Triaxial?
10	1560	101	24	Oblate
11	1492	113	33	Isotropic
B14-F2				
1	1068	98	24	Isotropic
2	1068	121	24	Isotropic
3	1328	142	24	Oblate?
4	1107	135	25	Isotropic
5	1335	138	25	Triaxial
6	1171	116	24	Triaxial

The mean and standard deviations of density values of the flutes are shown in [Table 4.9](#), as are values from individual AMS fabrics. Although there is generally not a good correspondence between fabric shape (triaxial, oblate, or isotropic) and density, isotropic fabrics are generally more likely to have lower densities than oblate and triaxial fabrics ([Fig. 4.16](#)).

4.4 Grain size distribution

Till in and adjacent to flutes from the Múlajökull and Breiðamerkurjökull forefields are, unsurprisingly, poorly sorted. There were also no consistent spatial variations in the texture of the tills of either flute M14-F1 or M14-F2 ([Fig. 4-17](#) and [Fig. 4-18](#)). Nor was there a significant difference in texture between sediments on the stosses and lees of headward boulders ([Fig. 4-17](#) and [Fig. 4-18](#)). Sediment adjacent to flute M14-F2 was slightly coarser overall than sediments in the flute ([Fig. 4-18](#)). The gravel content of the Múlajökull tills was unsystematically variable ([Table 4-10](#)), although this could be due to human error in selection of “bulk” samples for analysis. The grain size distribution of till from the B14-F1 is nearly identical to that measured by others in the Breiðalón area ([Boulton et al., 1974](#); [Boulton and Hindmarsh, 1987](#)). The black sediment from site B14-F1-A was much better sorted than till from the same flute ([Fig. 4-19](#)).

4.5 Analysis of pebble fabrics from the literature

Pebble orientations reported as 83 flute clast fabrics from five different glaciers in five papers were re-analyzed using the methods outlined in [Section 3.5](#). Clast fabric data from the following glaciers were used: Austre Okstindbreen, Norway ([Rose, 1989](#)); Lyngsdalen, Norway ([Gordon et al., 1992](#)); Slettmarkbreen (temperate), Norway

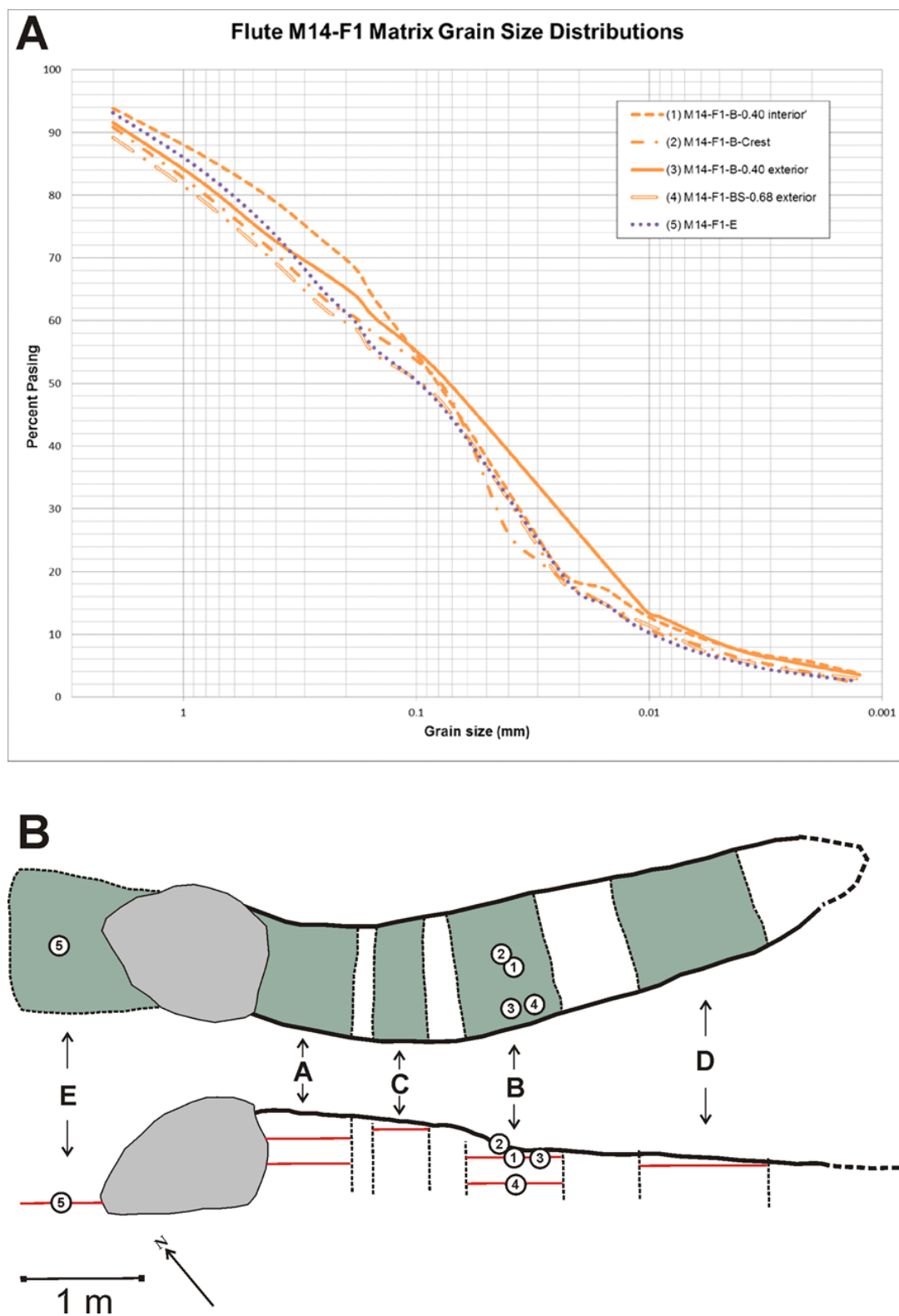


Figure 4-17. (A) Cumulative grain size distributions for bulk sediment sample fractions of < 4 mm, from locations in flute M14-F1 shown in (B).

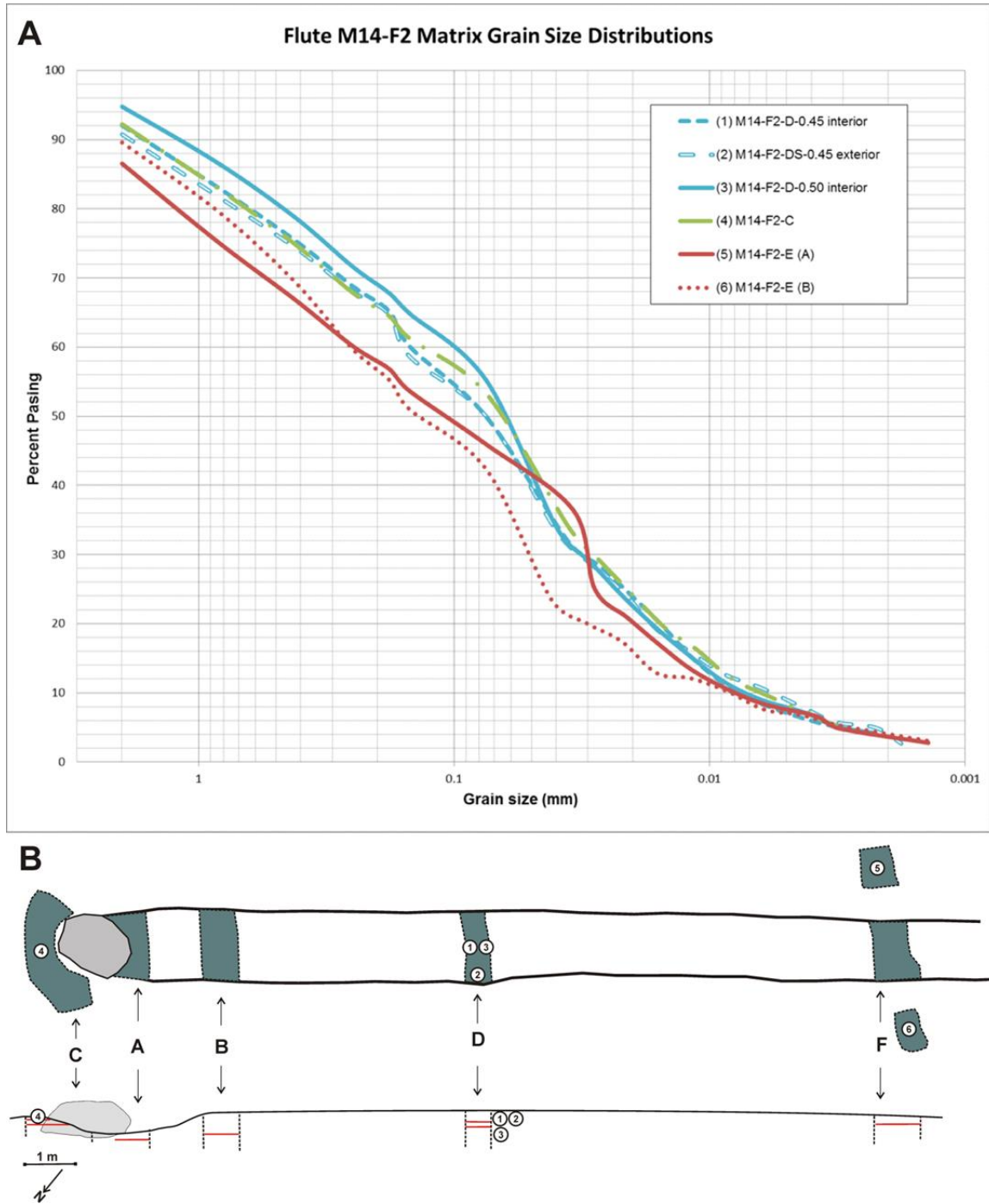


Figure 4-18. (A) Cumulative grain size distributions for bulk sediment sample fractions of < 4 mm, from locations in flute M14-F2 shown in (B).

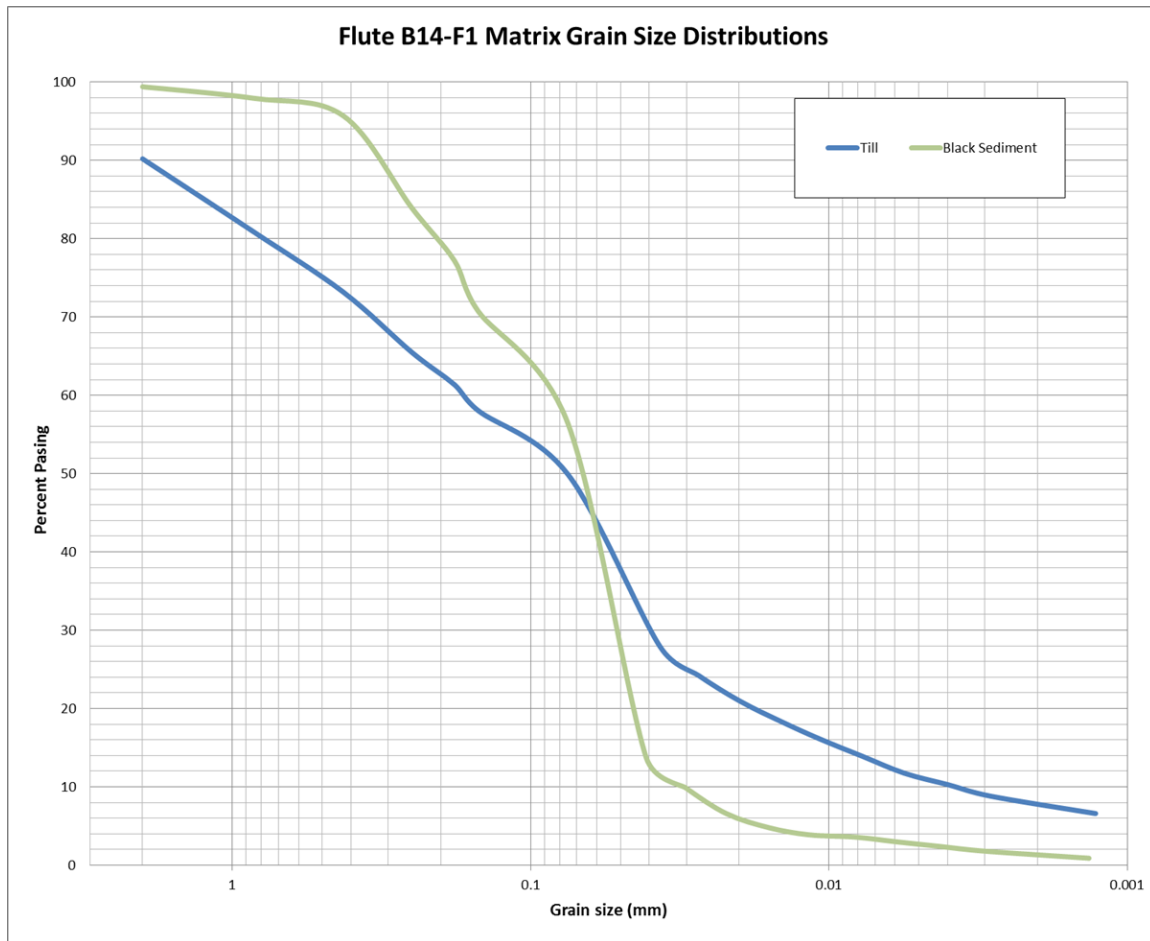


Figure 4-19. Cumulative grain size distributions for bulk sediment sample fractions of < 4 mm from B14-F1, site A.

Table 4-10. Grain size data for sediment in and adjacent to flutes. Size fraction is reported in mass percent.

Flute M14-F1						
Location Number	1	2	3	4	5	
Flute Position	interior	interior	exterior	exterior	stoss	
Gravel (> 2 mm)	16.0	33.8	20.6	37.0	19.2	
Sand (2 mm - 75 μ m)	40.8	30.5	35.5	30.3	41.2	
Silt (75 μ m - 4 μ m)	36.6	31.0	37.8	28.5	35.7	
Clay (< 4 μ m)	6.6	4.7	6.1	4.2	5.1	

Flute M14-F2						
Location Number	1	2	3	4	5	6
Flute Position	interior	exterior	interior	stoss	adjacent	adjacent
Gravel (> 2 mm)	33.2	27.5	10.5	27.4	37.6	29.6
Sand (2 mm - 75 μ m)	30.6	32.6	37.4	30.6	29.3	37.2
Silt (75 μ m - 4 μ m)	31.9	33.8	46.3	36.2	28.4	27.9
Clay (< 4 μ m)	4.4	6.1	5.8	5.7	4.8	5.4

Flute B14-F1, site A			
Location Number	1	2	
Sediment Type	Black Sand	Diamict	
Gravel (> 2 mm)	0.6	23.2	
Sand (2 mm - 75 μ m)	43.0	34.3	
Silt (75 μ m - 4 μ m)	54.0	33.7	
Clay (< 4 μ m)	2.4	8.7	

([Benn, 1994b](#)); Sandfellsjökull, Iceland ([Evans et al., 2010](#)); and Saskatchewan Glacier, Canada ([Eyles et al., 2015](#)).

When pebble orientations from these studies are referenced to their flute orientations, regrouped by flute position, and then analyzed, the results are very similar to those of the same analyses performed on AMS data from Múlajökull and Breiðamerkurjökull ([Fig. 4-20](#), [Fig. 4-21](#), [Table 4-11](#)). The pebble orientations from the A and B sides of the flute form girdles with orientations that indicate shear convergence, and pebble orientations

from the center of the flute cluster, indicating shear parallel to the flute orientation ([Fig. 4-20](#)). The apparent shear azimuths of pebble fabrics in flutes are also similar to shear azimuths from the AMS fabrics of this study: overall shear azimuths tend to parallel the flute axis, with clast populations along the flute edges (A and B) that indicate small components of inwardly and outwardly directed shear ([Fig. 4-21](#)).

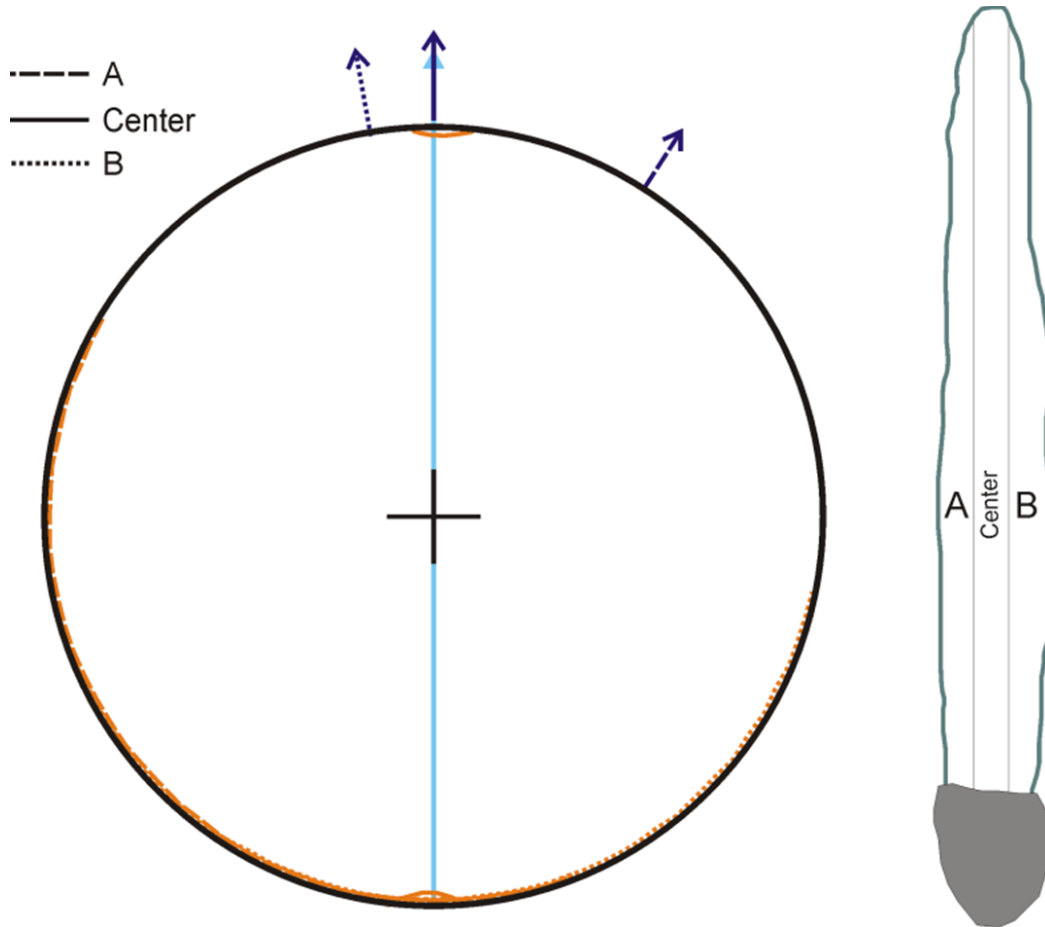
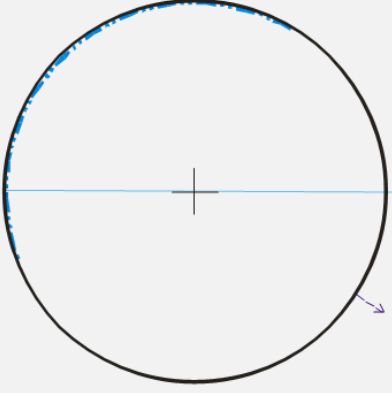
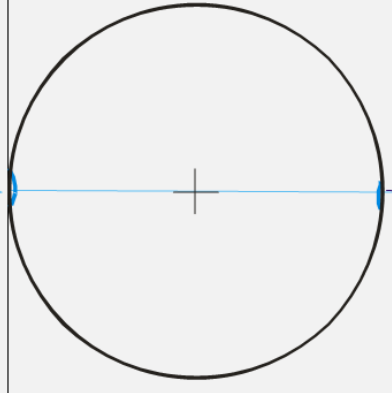
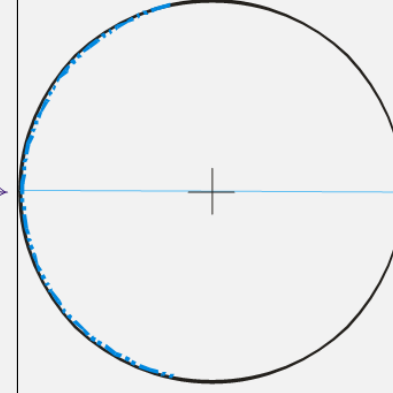


Figure 4-20. Fabrics regrouped by flute position (A, center, and B) and referenced to a common flute orientation, based on 2594 pebble orientations compiled from 83 fabrics measured in five different glacier forefields ([Rose, 1989](#); [Gordon et al., 1992](#); [Benn, 1994b](#); [Evans et al., 2010](#); [Eyles et al., 2015](#)). The planes represent the best-fit girdles to pebble orientations for the “A” (dashed orange line) and “B” (dotted orange line) sides of the flutes. The confidence interval (solid orange line) represents the distribution of pebble orientations from the center of the flutes. Fabric analysis results are shown in [Table 4-10](#). Individual pebble fabric analysis and results from each paper are reported in [Appendix D](#). Numbers of pebbles in each area: $N_A = 629$, $N_{center} = 951$, and $N_B = 1014$. Data are displayed on equal-area, lower-hemisphere stereonets.

Table 4-11. Flute pebble fabrics displayed in [Figure 4-20](#) . Pebble orientation measurements were referenced to a common flute orientation, regrouped by their position and reanalyzed. All data are displayed on equal-area, lower-hemisphere stereonet.

	A			Center			B		
Fabric Shape	Girdle			Cluster			Girdle		
	V1	V2	V3	V1	V2	V3	V1	V2	V3
Declination	13.48	103.49	32.81	0.95	270.92	306.99	176.13	266.12	349.77
Inclination	1.44	0.51	88.47	1.07	1.47	88.18	1.80	0.20	88.19
Sn	0.52	0.42	0.06	0.57	0.31	0.12	0.53	0.40	0.07
CGI (Benn, 1994a)		0.21			0.57			0.29	
K (Woodcock, 1976)		0.10			0.62			0.17	
I (Bennm 1994a)		0.11			0.21			0.13	
C (Woodcock, 1976)		2.18			1.55			2.08	
Fisher Test	N/A			Fail			N/A		
Principial Susceptibility Orientations									
Axial Distribution	Girdle			Bingham			Girdle		
Shearing Azimuth	32.8			1			349.8		
Girdle									
Dip	1.5						1.8		
Dip Direction	212.8						169.8		
Watson (Fisher)									
alpha									
Bingham									
Eta				5.7					
Zeta				2.3					

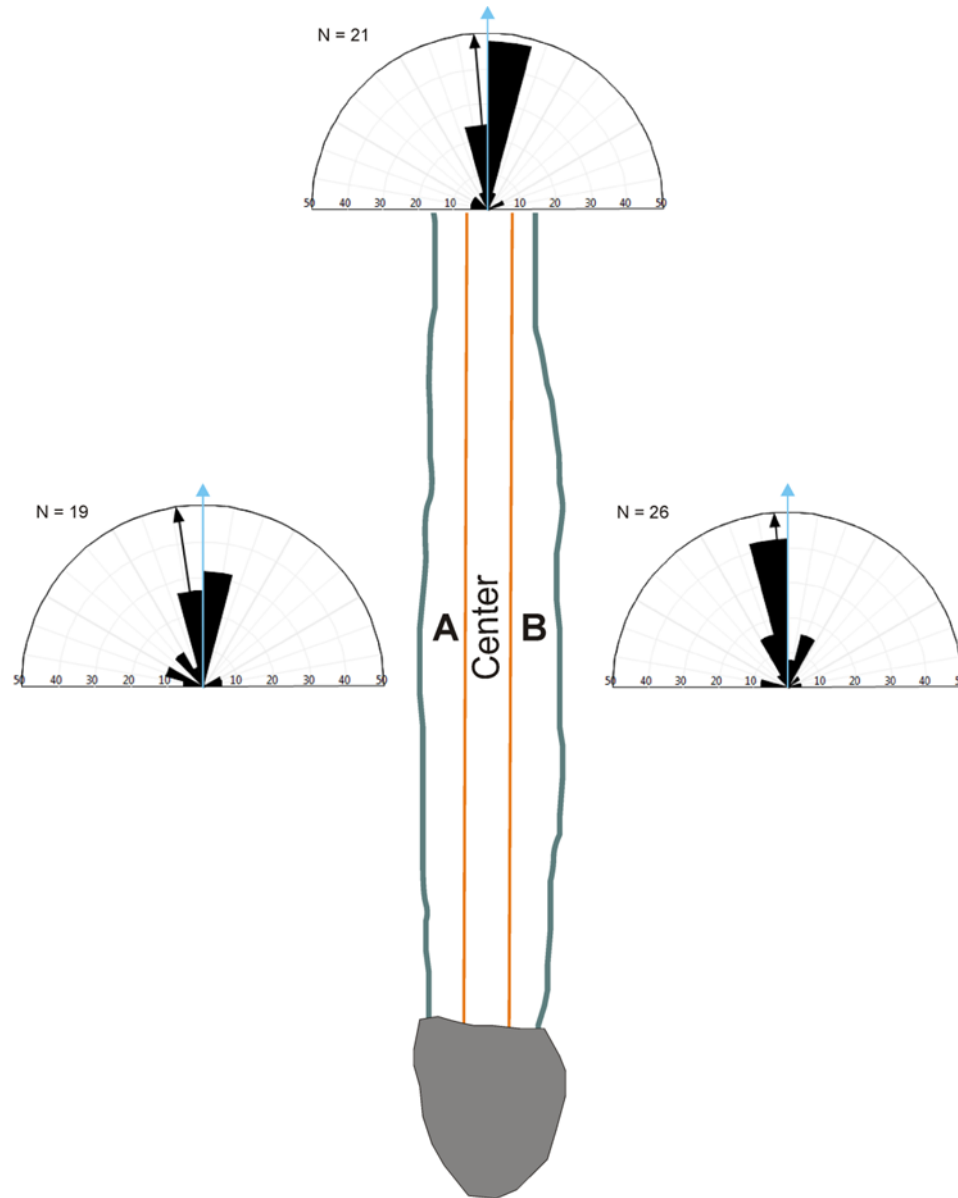


Figure 4-21. Uncorrected shear orientations derived from pebble fabrics in flutes and referenced to a common flute orientation from five different glacier forefields ([Rose, 1989](#); [Gordon et al., 1992](#); [Benn, 1994b](#); [Evans et al., 2010](#); [Eyles et al., 2015](#)) grouped by their position and plotted on rose diagrams. The blue arrow indicates flute orientation, and the black arrow indicates mean orientation for the dataset. Shear azimuths are grouped in 15° intervals, and the exterior of the rose diagram represents 50% of the population.

CHAPTER 5. DISCUSSION

5.1 Magnetic Characteristics

The magnetic susceptibilities from samples measured in this study are dominated by pseudo-single domain (PSD) and multi-domain (MD), ferrimagnetic, shape-anisotropic, iron oxides – specifically titanomagnetite and titanomaghemite at Múlajökull and magnetite and maghemite at Breiðamerkurjökull. The interpretation of magnetic mineralogy of the Múlajökull and Breiðamerkurjökull sediments is discussed in [Appendix D](#).

FORC analyses ([Fig. 4-6](#)) show that magnetic hysteresis properties of the Múlajökull and Breiðamerkurjökull sediments ([Fig. 4-5](#)) have dominantly PSD domain states and not a mixture of MD and single-domain (SD) particles. SD magnetite and titanomagnetite particles have inverse shape anisotropy, and their presence could result in inverse (switched k_1 and k_3 orientations), intermediate (switched k_1 and k_2 orientations), or offset AMS fabrics that do not directly represent the strain conditions of their host sediment. Identifying the absence of SD grains in Múlajökull and Breiðamerkurjökull sediments allows for a straightforward interpretation of AMS fabrics in this study. In the future if ferrimagnetic iron oxides are identified as the primary carrier of magnetic susceptibility in sediments and if there is any ambiguity in the domain state (for example, PSD vs. a mixture of MD and SD) methods should be used that wholly characterize the range of domain states, particularly if shear experiments are not conducted to calibrate fabric patterns to the state of strain.

Magnetic hysteresis data indicate that the grain sizes of magnetic particles are less than 11 μm in the Múlajökull tills and less than 7.5 μm Breiðamerkurjökull sediments ([Fig. 4-5](#)). These data support the hypothesis suggested by [Hooyer et al. \(2008\)](#) that triaxial AMS fabrics in sediment are a result of the alignment of silt-sized magnetic particles.

The results from ring-shear experiments performed on till from Múlajökull ([McCracken, 2015](#)), together with magnetic mineralogy data from this study, confirm results from [Hooyer et al. \(2008\)](#) that triaxial AMS fabrics form when till experiences moderate to high shear strains, as long as that till has a magnetic susceptibility signal controlled by PSD or MD, shape-anisotropic, ferrimagnetic minerals. The magnetic mineralogy of all sediments whose AMS was measured for this study fit these criteria, so the assumption can safely be made that AMS fabrics from the Múlajökull and Breiðamerkurjökull forefields reflect the strain experienced by those sediments.

5.2 Till density and estimated effective stress distribution

The distribution of AMS sampling in flutes at Breiðamerkurjökull was limited to their centers, so that there are no data for at least one half of each flute's total width; thus, the discussion of patterns of till matrix density will be limited to Múlajökull flutes.

The tills that comprise the flutes at Múlajökull have average dry bulk densities ($\overline{\rho_b}$) of 1400 – 1750 [kg m^{-3}] ([Fig. 4-16](#)). The grain size distributions and lithologies of Múlajökull tills have little variability throughout the forefield ([Fig. 4-17](#); [Fig. 4-18](#)). Therefore, the differences in densities between the flutes and adjacent till, and within the flutes themselves, are more likely due to variations in compaction and, therefore,

porosity. Differences in compaction are most likely due to differences in maximum past effective stress:

$$\sigma' = \sigma - P_w,$$

where σ is the total normal stress and P_w is the pore-water pressure. The trends in sediment matrix density present in fluted tills at Múlajökull, discussed in [Section 4.3](#), can therefore be used as proxies for trends in past effective stress. [McCracken \(2015\)](#) empirically related $\overline{\rho_b}$ to σ' for Múlajökull tills using results of consolidation experiments on intact till specimens:

$$\overline{\rho_b} = 86.308 \ln(\sigma') + 1319.6.$$

Using this relationship but noting its uncertainty (McCracken, 2015), patterns of past maximum effective stress can be inferred in the flutes. For example, the difference in effective stress between the interior and exterior of the Flute M14-F1 was likely ~30 kPa, whereas at Flute M14-F2 this difference was likely ~150 kPa. From these estimates the inference can be made that the transverse effective stress gradient was significant in both flutes but higher in Flute M14-F2. Additionally, the past maximum effective stress was likely much larger upglacier of the boulder than within the flute at both M14-F1 and M14-F2 ([Fig. 4-15A,B](#)).

Other factors being equal (e.g. grain size distribution), less porous sediments will have larger shear strengths ([Lambe and Whitman, 1969](#)). The porosity (n) of the till matrix at Múlajökull can be estimated using the relationship:

$$n = 1 - \frac{\overline{\rho_b}}{\rho_{sediment}}$$

where $\rho_{sediment}$ is the density of basalt, $\sim 2900 \text{ [kg m}^{-3}\text{]}$. Densities across the width of Flute M14-F1 indicate porosities of 0.52 in the flute's exterior and 0.44 in the flute's interior. Similarly, porosities across the width of Flute M14-F2 are estimated to be 0.40 at the center and 0.48 at its edge. Till compressibility increases with increasing porosity, so the equal differences in porosity across the two flutes result in smaller effective stress differences implied for flute M14-F1 ($\sim 30 \text{ kPa}$) than for the less porous Flute M14-F2 ($\sim 150 \text{ kPa}$).

5.3 Fabrics

5.3.1 Fabric Shape

Flutes at both glaciers yielded AMS fabrics that had triaxial, oblate, and isotropic ellipsoids. The shape of AMS fabrics can be used to infer shear-strain magnitude.

AMS fabrics collected from flutes at Múlajökull and Breiðamerkurjökull were dominantly triaxial and oblate with apparent shear planes oriented near horizontally. These fabric shapes indicate that most of the fluted till was sheared during basal slip of the glacier. Triaxial AMS fabrics form at moderate strains of ~ 7 and stay constant at higher strains, so strains of at least ~ 7 are indicated by some the till ([Hooyer et al., 2008](#)) ([Table 3-2](#)). However, the prevalence of oblate fabrics indicates that much of the fluted till was sheared unidirectionally to only low strains (~ 2) ([Hooyer et al., 2008](#)) ([Table 3-2](#)); that is, shear strains were insufficient for k_1 orientations to organize in a cluster. There is no systematic spatial distribution of oblate and triaxial AMS ellipsoids within the flutes, so unless very steep strain gradients were present—unlikely given the lack of

abrupt geometric changes of flutes along their lengths—the fluted till likely experienced shear strain nowhere much in excess of the threshold value of ~ 7 .

AMS fabrics with isotropic ellipsoids provide no information on strain orientation and could be the result of either the absence of strains greater than ~ 2 in a single orientation or disturbance of the till by post-glacial processes or during sampling. Ten of the twelve isotropic fabrics reported in Chapter 3 were collected from sediments with relatively low densities, and six of those fabrics are from sites immediately in the lee of the flute's boulder ([Fig. 4-16](#)). Sampling disturbance that results from AMS cubes being pushed into under-consolidated sediments is feasible. If sampling disturbance is not the cause of isotropic fabric ellipsoids, then they are likely the result of low strains. Less dense sediment experiencing lower strains than more dense sediment is counterintuitive because more porous sediments should have been weaker and more likely to have deformed than less porous sediment. This coincidence of porous sediments and isotropic AMS ellipsoids therefore implies—in the absence of sampling disturbance—that shearing and compaction may be related processes.

5.3.2 Fabric Orientations

Discrete AMS flute fabrics show large variability in shear orientations ([Fig. 4-14](#), [Fig. 4-21](#)). Fabrics had shear azimuths that were either flow-parallel, or unidirectional, divergent, or convergent across the flute's long axis. These fabric patterns imply transverse and longitudinal components of till flow, the relative importance of which varied from place to place ([Benn, 1994b](#)). Components of strain that were parallel to glacier flow (and the flute's axis) were likely the result of glacier slip dominating strain history. Flow-transverse components of till strain cannot be attributed to glacier slip

alone. Convergent till flow can be explained by till squeezing into a cavity, which is part of both the cavity-propagation and freeze-on hypotheses. Transverse strain that would cause divergent AMS fabrics (i.e., flow out of the cavity) is not readily explained by either hypothesis.

Although local shear orientations in flutes were highly variable, dominant shear orientations are apparent when both AMS and pebbles fabrics orientations from flutes are referenced to a single flute orientation ([Fig. 4-13](#), [Fig. 4-20](#)). These data indicate that flow-parallel shear dominates the inner portion of the flute, and that flute edges exhibit a tendency for convergence, consistent with till squeezing laterally into a cavity.

5.3.3 B14-F1-A

The AMS fabrics directly in the lee of the boulder at Flute B14-F1 indicate that those sediments experienced flow-parallel shear strain along a steeply-dipping shear plane ([Fig. 4-21](#), left side of figure). This strain state was observed nowhere else. The sediments at B14-F1-A are most probably the remnant of a till wedge formed during the lodgement of B14-F1's boulder. The orientation of shear planes (inferred from V_{Ik3}) dip steeply downglacier in a similar manner to deformed sands and silts in the lee of a lodged boulder described by [Eklund and Hart \(1996\)](#) ([Fig. 5-1](#)). [Boulton \(1976\)](#) noted that till wedges in the lee of boulders were prominent features in Breiðamerkurjökull flutes. Additionally, the black sediment at B14-F1, site A is probably not of subglacial origin because it is well sorted ([Fig. 4-19](#)), oxidized ([Appendix D](#)), and likely not laterally continuous, given that it has not been described in other studies of the Breiðdalón area ([Boulton et al., 1974](#); [Boulton and Hindmarsh, 1987](#); [Benn, 1995](#)). These characteristics indicate the black sediment at B14-F1 is the remnant of an aeolian or fluvial unit that was

buried by till deposition during a later advance of western Breiðamerkurjökull, and shoved upward into a wedge during lodgement of the boulder.

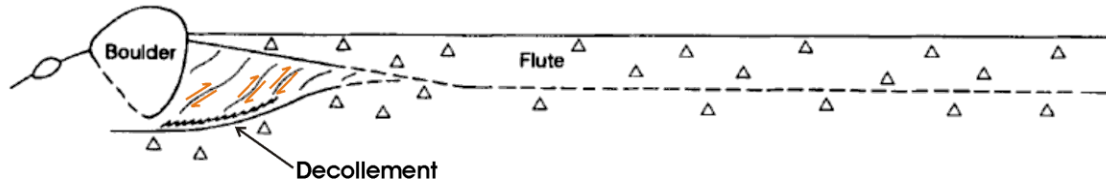


Figure 5-1. Transverse cross-section of a flute in the forefield of Isfallsglaciären, Sweden. Laminated silts and sands (no triangles) were deformed downstream of a flute's headward boulder. The pattern of deformation indicated by the structures in the silt and sand are similar to patterns of strain indicated by fabrics from B14-F1, site A. Orange arrows indicate the likely orientation of shear. Figure adapted from [Eklund and Hart \(1996\)](#).

5.4 Flute Formation

These data and observations suggest that the cavity-propagation hypothesis provides the best explanation for flute formation, and, importantly, provide an explanation for how weak till that has flowed into a cavity can support the growth of a cavity downstream from that till—a previously unexplained aspect of the hypothesis (see [Section 1.1.3.2](#)). In this section, I argue that flutes are initiated and grow through cavity extension during periods of high subglacial water pressure and sliding speed but that newly accreted till at the flute end is strengthened during periods of lower subglacial water pressure and sliding speed, thereby providing the rigid take-off point for a cavity during subsequent glacier acceleration ([Fig. 5-2](#)). Flute formation is initiated during transient high subglacial water pressure when till, weakened by low effective stresses, flows into a cavity on the lee side of a lodged boulder. When water pressure and sliding speed eventually decrease and the cavity begins to shrink, stress is transferred to the fluted till in the same way that decreasing water pressure in a cavity focuses normal stress on the bed immediately

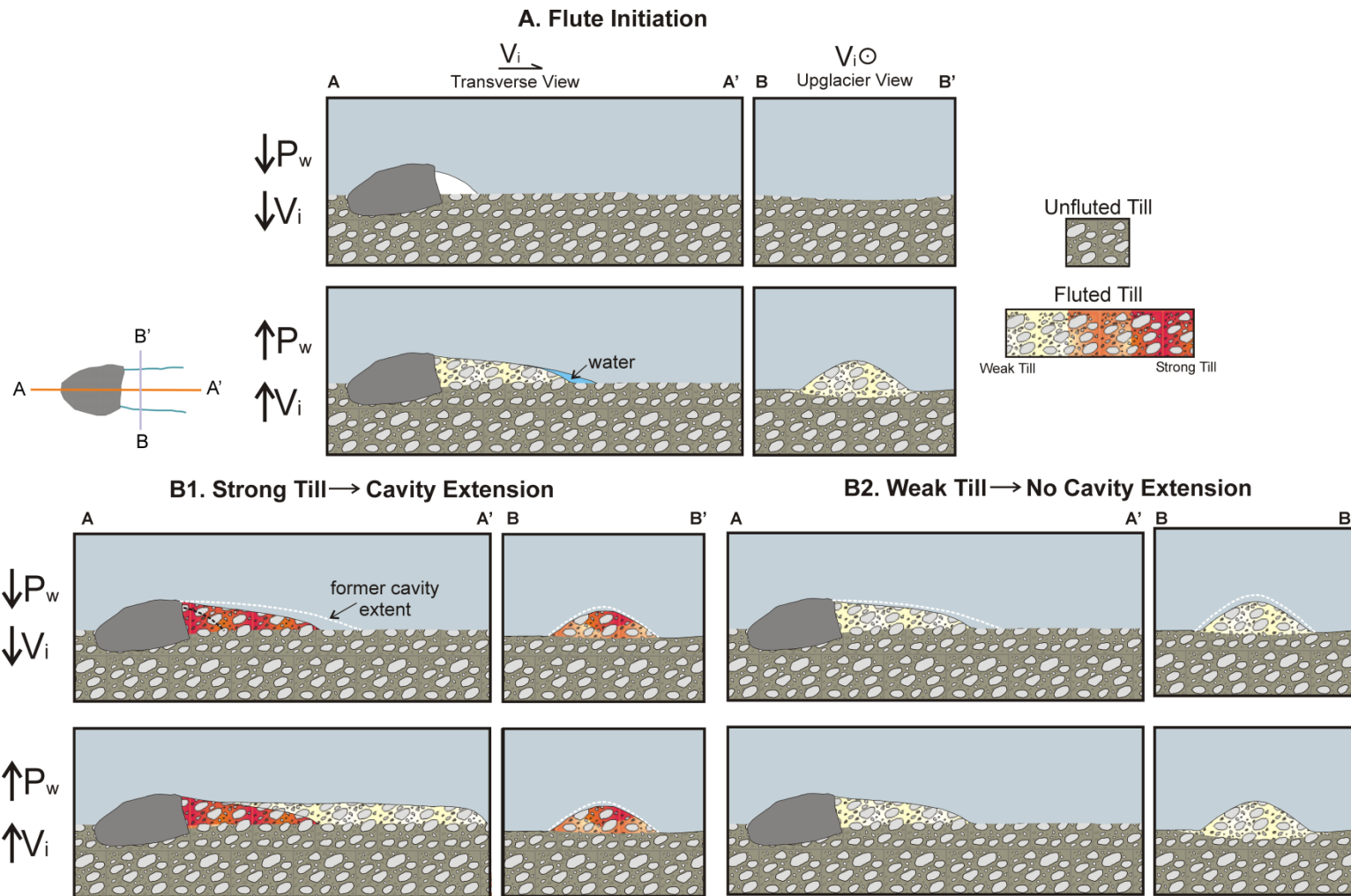


Figure 5-2. Illustration of the flute formation model outlined in the text , where A–A' is cross-sectional view of the flute transverse to glacier flow and B–B' is a view looking upglacier, P_w is basal water pressure, and V_i is ice sliding velocity. (A) Flute formation is

(Fig. 5-2, continued.) unlikely to occur during periods of low P_w because cavities will be small and till relatively strong. Flutes are most likely to be initiated during high P_w events when cavities will be longer and till weaker. When till is squeezed into the cavity where effective stresses are lower the till will dilate, and its strength will decrease further. (B1) Flutes are most likely to grow when the till in them strengthens due to increased normal stress during periods of low P_w and V_i . The increased normal stress will consolidate and strengthen the fluted till, perhaps most severely near the till surface where water drainage out of the till may occur most readily. During the next high P_w and V_i event, the cavity will be extended farther downglacier, owing to the rigid till that will enable cavity growth, and the flute will grow. (B2) Conversely, flutes will not grow if till is unable to compact and strengthen sufficiently to allow a cavity to extend downstream during a subsequent period of high P_w and V_i .

upstream ([Iverson, 1991](#); [Cohen et al., 2006](#)). The increase in downward total stress on the till, probably in conjunction with a decrease in till pore-water pressure associated with the reduction in basal water pressure, will result in till compaction and strengthening. In this scenario, the compacted till is strong enough so that during the next high water-pressure event that accelerates sliding the till will act rigidly and move the take-off point for the cavity downglacier, allowing additional till inflow to add to the flute's length.

Alternatively, if the increase in total downward stress on the till and the decrease in till pore-water pressure are not sufficient to consolidate and strengthen the till, the till will not act rigidly, so a cavity will not form during the next period of high water pressure and sliding velocity, and the flute will not extend.

5.4.1 Freeze-on vs. cavity-propagation

None of the data collected in this study clearly supports the freeze-on hypothesis for flute formation. The differences in density across the width of the flutes at Múlajökull are irreconcilable with the mechanism for flute deposition (likely lodgement) at temperate glaciers implicated by the freeze-on hypothesis. The dominance of convergent (herringbone) fabrics in both the AMS and pebble fabric data also supports the cavity-

propagation hypothesis over the freeze-on hypothesis, because the englacial transport of debris and subsequent lodgement required by the freeze-on hypothesis would impart a dominantly flow-parallel fabric (see [Section 1.1.3](#)). Similarly, the variability in shearing azimuths throughout flutes and the prevalence of oblate fabrics indicative of low strains is more easily explained by the cavity-propagation hypothesis.

5.4.2 Till strengthening and pore-water-pressure changes

As noted, the primary deficiency of the cavity-propagation hypothesis is its inability to explain how till that is weak enough to flow into a cavity then strengthens sufficiently to support stress from the surrounding ice and extend the cavity downglacier, thereby growing the flute. Till strength (τ_s) is the minimum shear stress necessary to initiate permanent strain and is given by the Coulomb equation:

$$\tau_s = \sigma' \tan \varphi + c,$$

where φ is the till's angle of internal friction and c is cohesion. Cohesion is generally assumed to be negligible in sandy tills like those at Múlajökull, Breiðamerkurjökull, and many other glaciers ([Cuffey and Paterson, 2010](#)). Till strength is, therefore, a function of φ , σ , and P_w . Importantly, the internal friction angle of a till is dependent on its porosity. In sands, for example, for which there are ample data, friction angle can increase from 33° to 41° with a porosity decrease from 0.43 to 0.35 ([Lambe and Whitman, 1969](#)). The patterns of matrix density across the width of flutes at Múlajökull—higher density near the centers of flutes and low density near their exteriors—indicate that differential compaction is central to discerning how fluted till is strengthened.

The till within a flute is generally less dense than the adjacent till outside the flute ([Fig. 4-15B, C](#)). The most likely explanation for this difference in density is that porosity increases as till flows into the lee of flutes, where total normal stresses on the bed will be reduced relative to the ice overburden pressure due to sliding past the obstacle presented by the flute (e.g., [\(Weertman, 1964\)](#)).

The decrease in density from the center of the flute toward its sides that develops subsequently provides a key clue to how till becomes strengthened in the lee of the flute. Owing to the inherent unsteadiness of basal water pressure and sliding speed during surges (e.g., [\(Kamb et al., 1985\)](#)) and during normal flow of temperate glaciers, the effect of decreases in water pressure and sliding speed on the till density gradient across flutes requires consideration. A reduction in sliding speed and water pressure in a cavity in the lee of a flute will cause a large increase in downward stress on till at the end of the flute for two reasons: (1) the reduction in sliding speed will reduce the pressure shadow in the lee of the flute, thereby increasing the normal stress where ice is in contact with till, and (2) the water-pressure reduction in the cavity will shift some of the weight of the ice to the zone of ice-till contact immediately upglacier, as indicated by studies of glacial quarrying ([\(Iverson, 1991; Cohen et al., 2006\)](#)). Note that the first of these effects will occur even if a cavity is absent. Of critical importance is that, owing to the transverse decrease in height of flutes toward their edges and its expected effect on transverse differences in pressure-shadow reduction and cavity length (see sliding theory, e.g. [\(Weertman, 1964; Kamb, 1987\)](#)), the downward increase in stress on till that accompanies sliding speed and water pressure decreases will be largest along the flute centerline and decrease toward its edges, with little or no effect outside its edges. The result should be

till that is most compacted at its centerline and is sometimes sufficiently strong there to support the takeoff point for a cavity during the next period of high water pressure and rapid sliding. Importantly, during the next period of rapid flow, the consolidated till will not lose its strength unless shear dilates it. Thus, central to this hypothesis is the irreversibility of till compaction in response to decreases in till effective stress.

This interpretation is indirectly supported by quarried boulders at the heads of flutes. The lee sides of boulders are often quarried at or below the height of their flute ([Fig. 5-3](#)), indicating that lee-side cavities were likely present and fluctuating stresses – likely required for quarrying – were acting on these boulders prior to the emplacement of fluted till ([Iverson, 1991](#); [Cohen et al., 2006](#)). Although rates of quarrying are variable and depend on a number of factors, the ample evidence of quarrying of boulders at the heads of some flutes suggests that significant periods of time can pass between when a lodged boulder is emplaced and the formation of a flute. Thus, a reasonable inference is that subglacial conditions that engender flute formation are fundamentally transient.

Additional evidence for this interpretation comes from some of the flute AMS fabrics. Localized divergent fabric orientations indicate that some parts of flutes experience a component of shear strain oriented outward from their centerlines. Outward strain is most simply explained as being the result of till being squeezed towards the edges of a cavity, owing to transient total normal stresses on till that are highest near the flute centerline. The squeezing of till outward could occur instead of, or in addition to, consolidation of till. Outward squeezing in the absence of sufficient compaction could leave till strengthened insufficiently to allow growth of the flute during the next phase of

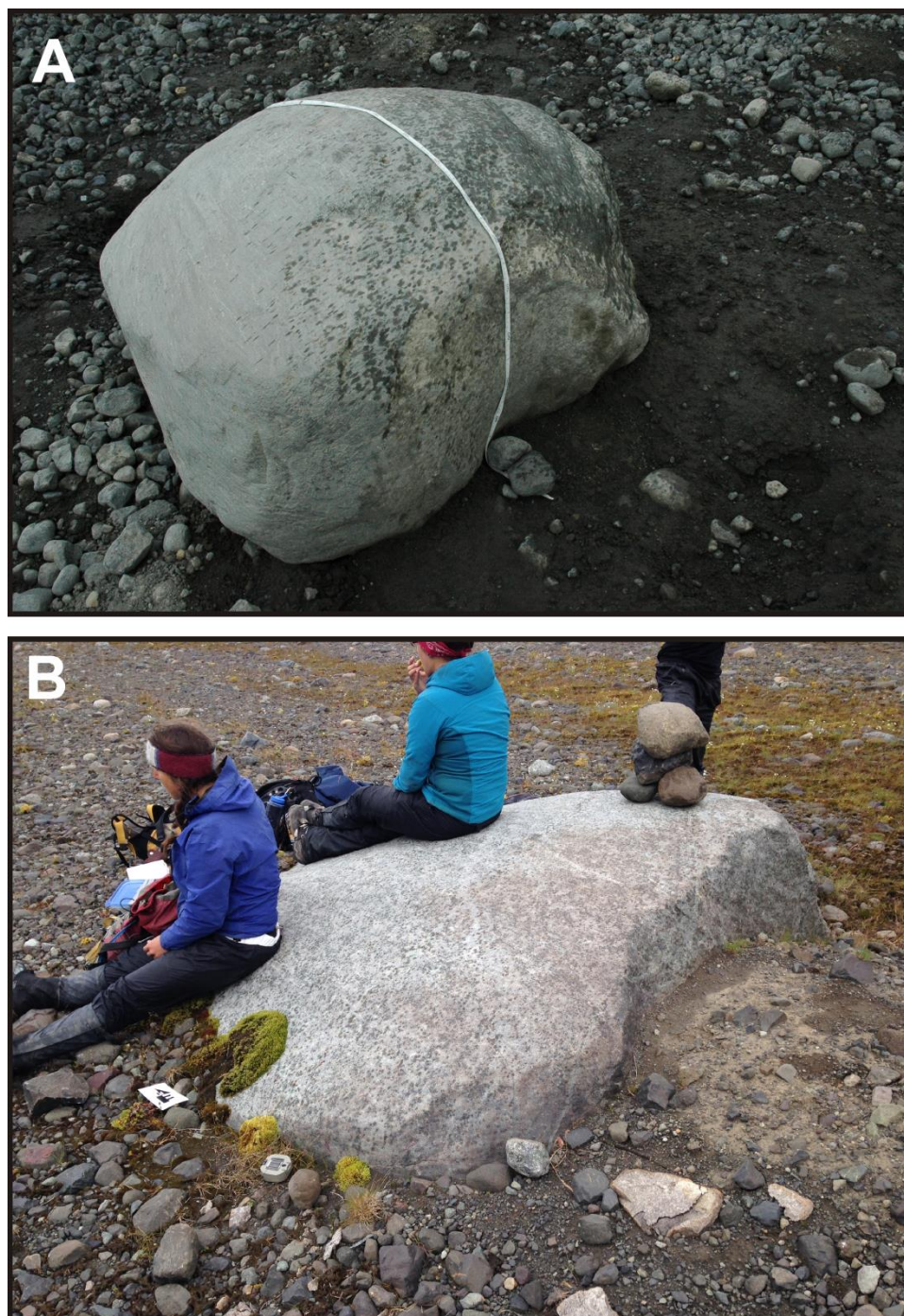


Figure 5-3. Examples of headward boulders of flutes with extensive quarrying from (A) M14-F1, following AMS sampling, and (B) B14-F1, prior to AMS sampling. Ice flow in both pictures is from the upper left to lower right corners.

high water pressure and sliding. This scenario is most feasible under glaciers with fine-grained till beds with associated low hydraulic diffusivities. Low till diffusivity will slow dissipation of pore-water pressure in response to either loading by ice or water pressure decreases in nearby connected parts of the hydrologic system. Slow pore-pressure dissipation will inhibit consolidation and strengthening.

5.4.3 Strain orientation and magnitude

The herringbone patterns that are present in generalized flute fabrics are consistent with the hypothesis presented here ([Fig. 4-13](#), [Fig. 4-20](#)). Because this hypothesis requires that till strengthen and become rigid once it flows laterally into the zone immediately downglacier from the flute, strain in the till due to subsequent down-glacier flow across it should be small, so complete re-setting of fabrics in the down-flow direction is unlikely. Transverse components of flow should, therefore, be preserved to some extent.

The prevalence of oblate fabrics in fluted tills indicates that low shear strains are common and that triaxial fabrics are likely indicative of moderate, instead of high, strains. Flow-parallel fabrics measured at depth in flutes, and the tendency for shear orientation to vary unsystematically with depth, suggest that low strains in flutes may be partly due to the vertical migration of bed-parallel shear zones. Till deformation likely concentrates in narrow bands that shift throughout the depth of till due to changes in effective stress ([Tulaczyk, 1999](#); [Tulaczyk et al., 2000](#); [Iverson and Iverson, 2001](#)). Glacier-wide changes in basal water pressure could cause the fluctuations in P_w that would lead to the migration of shear zones.

5.5 Implications

The hypothesis for flute formation presented here suggests that sediment texture (which helps control till strength and diffusivity) could be a relevant variable in flute formation. During a reduction in basal water pressure and sliding speed, the rate of pore-water pressure decrease in a till in response to both loading and water pressure decreases in connected parts of the subglacial hydraulic system would depend on the till's hydraulic diffusivity, which increases as grain size increases due to the overriding effect of permeability on diffusivity. Coarser-grained and more permeable tills are, therefore, likely to strengthen more quickly in response to loading by the glacier and are more likely to propagate cavities than finer-grained and less permeable tills. However, the claim cannot be made that coarse tills are more likely to form flutes because they are also less likely to deform into a cavity and initiate flute formation ([Hubbard and Reid, 2006](#)).

Long, parallel-sided and short, tapered flutes are possibly end members of a continuum that represents the degree of till strengthening following high water-pressure events. Flutes M14-F2 (long, parallel-sided) and M14-F1 (short, tapered) represent these end members because they have similar sediment textures and boulder sizes but drastically different morphologies. The notable difference between M14-F2 and M14-F1, besides morphology, is the magnitude of the density gradients across the width of either flute ([Fig. 4-15A, B](#)). Larger density gradients in M14-F2 suggest that till compaction in the flute was significant, indicating that the till in M14-F2 strengthened sufficiently by compaction to enable repeated downglacier growth of the flute during periods of high water pressure and rapid flow. Conversely, the smaller density gradients in M14-F1 indicate that strengthening associated with compaction was not as prevalent, for reasons

that cannot be discerned with the data at hand. Thus, this flute could not generate the pressure shadow and cavity necessary for the flute to accrete downglacier when water pressure and sliding speed were high. Rather it grew by deformation of weak till into the pressure-shadow and cavity caused by its boulder but no farther because its till was insufficiently rigid to propagate a pressure-shadow and cavity downstream. Thus, these data provide an explanation for why some flutes are parallel-sided and others are tapered.

This hypothesis is based on observations from temperate glaciers but cannot be precluded as a mechanism for flute formation at glaciers with frozen margins, for reasons argued by [Åmark \(1980\)](#) and [Eklund and Hart \(1996\)](#). The presence of melt-water in the ice of frozen flutes, as observed by [Roberson et al. \(2011\)](#), could easily be explained as pore-water that froze like the rest of a bed beneath the toe of a polythermal glacier.

This hypothesis for flute formation, unlike previous ones, requires unsteady subglacial water pressures and sliding speeds. It highlights how the variability of water pressure and sliding speed and bed textural properties could combine to influence flute formation. Thus, this hypothesis may help explain why flutes are present in some forefields of sediment-floored glaciers but absent in others.

CHAPTER 6. CONCLUSIONS

6.1 Flute Formation

Patterns of magnetic fabrics and bulk densities of fluted till in the forefield of Múlajökull and more limited data from fluted till in the Breiðamerkurjökull forefield indicate that flutes form by a cavity-propagation process similar to that suggested by [Benn \(1994b\)](#) but that flute growth requires unsteady subglacial water pressures and sliding speeds. Flutes are initiated and grow through till deformation into cavities in the lee of lodged boulders during periods of high subglacial water pressure and sliding speed. Newly accreted till at the end of flutes is consolidated and strengthened during periods of lower subglacial water pressure and sliding speed, thereby providing the rigid take-off point for a cavity farther downglacier during subsequent glacier acceleration ([Fig. 5-2](#)). This mechanism addresses the previously unexplained aspect of the cavity-propagation hypothesis of how fluted till can become strengthened and extend the take-off point of a cavity downglacier. Long, parallel-sided flutes and short, tapered flutes are likely end members of a continuum and represent a high and low degree, respectively, of till strengthening following till emplacement during high water-pressure events.

The presence of a cavity during flute formation is suggested by generally herringboned AMS fabrics from this study and pebble fabrics published in other studies ([Section 5.3.2](#)), indicative of inward till flow. Also, till matrix densities that are higher near the centers of flutes than near their edges indicate larger stress concentrations on till where cavities were largest ([Section 5.4.2](#)), and consequent strengthening of till is responsible for the preservation of fabrics that indicate transverse components of flow ([Section 5.4.3](#)). Transient basal water pressures during flute formation are also indirectly

supported by headward boulders with quarried lee sides ([Section 5.4.2](#)), indicative of both the water pressure fluctuations that help accelerate quarrying and a transient period when conditions were sufficient for quarrying but insufficient for flute formation. Locally divergent fabrics ([Section 5.4.2](#)) may be the result of till squeezing toward the edges of flutes when water pressure fell in cavities.

Hydraulic diffusivity, and consequently sediment texture, may play a role in flute formation, although this conclusion is based on inference and not on observed textural variations in tills of this study, which were minimal. Once flute formation is initiated, coarser-grained and more permeable tills are likely to strengthen more quickly and hence more fully in response to both loading by the glacier and water pressure decreases in nearby parts of the connected subglacial hydrologic system. Thus, coarse-grained tills, therefore, may be more likely to propagate cavities than finer-grained and less permeable tills.

6.2 Magnetic Mineralogy

The magnetic minerals that control the susceptibility signal of tills in this study are primarily pseudo-single-domain and multi-domain titanomaghemite (at Múlajökull) and magnetite (at Breiðamerkurjökull). Elongate forms of these minerals have shape anisotropic magnetic susceptibility, so that maximum susceptibility orientations align with the long axes of particles. The magnetic mineralogy of the tills measured in this study are similar to those measured by [Hooyer et al. \(2008\)](#) that developed triaxial AMS fabrics when sheared at moderate to high shear strains. [McCracken \(2015\)](#) showed that in ring-shear experiments Múlajökull tills developed essentially identical fabrics at high strains ([Table 3-2](#)). These data support the inference made in [Hooyer et al. \(2008\)](#) that

silt-sized, ferrimagnetic, shape-anisotropic, PSD and MD particles align during shear and cause AMS patterns in till that can reliably be used to infer strain orientation, type, and, to some extent, magnitude in deformed tills.

REFERENCES

- AGICO, 2009, MKF1-FA/CS4/CSL, MFK1-A/CS4/CSL, MFK1-FB, MFK1-B, User's Guide, AGICO, Andanced Geoscience Instruments Co.
- , 2011, SAFYR4W MFK1 Kappabridge Control Software for Windows: User Manual Version 4.0.3.
- Allmendinger, R. W., Cardozo, N. C., and Fisher, D., 2012, Structural Geology Algorithms: Vectors & Tensors, Cambridge, England, Cambridge University Press.
- Åmark, M., 1980, Glacial flutes at Isfallsglaciaren, Tarfala, Swedish Lapland: *Geologiska Foreningens i Stockholm Forhandlingar*, v. 102, no. 3, p. 251-259.
- Ankerstjerne, S., Iverson, N. R., and Lagroix, F., 2015, Origin of washboard moraine of the Des Moines Lobe inferred from sediment properties: *Geomorphology*, v. 248, p. 452-463.
- Anthony, J. W., Bideaux, R. A., Bladh, K. W., and Nichols, M. C., 1997, Magnetite, *in* Bladh, K. W., ed., *Handbook of Mineralogy, Volume III*: Chantilly, VA, Mineralogical Society of America, p. 333.
- ASTM, 2007, D422-63 Standard test method for particle-size analysis of soils: West Conshohocken, PA.
- Balsley, J. R., and Buddington, A. F., 1960, Magnetic susceptibility anisotropy and fabric of some Adirondack granites and orthogneisses: *American Journal of Science*, v. 285, p. 6-20.
- Banerjee, S., 1971, New grain size limites for paleomagnetic stability in hematits: *Nature Physical Science*, v. 232, p. 15-16.
- Benediktsson, I. O., Schomacker, A., Johnson, M. D., Geiger, A. J., Ingolfsson, O., and Guðmundsdóttir, E. R., 2015, Architecture and structural evolution of an early Little Ice Age terminal moraine at the surge-type glacier Múlajökull, Iceland: *Journal of Geophysical Research: Earth Surface*.
- Benn, D. I., 1994a, Fabric shape and the interpretation of sedimentary data: *Journal of Sedimentary Research*, v. A64, no. 4, p. 910-915.
- , 1994b, Fluted morain formation and till genesis below a temperate valley glacier: Slettmarbreen, Jotunheimen, southern Norway: *Sedimentology*, v. 41, p. 279-292.
- , 1995, Fabric signature of subglacial till deformation, Breiðamerkurjökull, Iceland: *Sedimentology*, v. 42, p. 735-747.
- Benn, D. I., and Evans, D. J. A., 1996, The interpretation and classification of subglacially-deformed materials: *Quaternary Science Reviews*, v. 15, p. 23-52.
- , 2010, *Glaciers and glaciation*, New York, Routledge.

- Bilardello, D., and Jackson, M., 2013, What do the Mumpsies do?, *in* Bilardello, D., ed., Volume 23: Minneapolis, MN, Institute for Rock Magnetism.
- Bingham, C., 1964, Distributions on the sphere and on the projective plane [Ph.D.: Yale University.
- , 1974, An antipodally symmetric distribution on a sphere: *Annals of Statistics*, v. 2, p. 1201 - 1225.
- Björnsson, H., 1986, Surface and bedrock topography of ice caps in Iceland, mapped by radio echo-sounding: *Annals of Glaciology*, v. 8, p. 11-18.
- , 1996, Scales and rates of glacial sediment removal: a 20 km long and 300 m deep trench created beneath Breiðamerkurjökull during the Little Ice Age: *Annals of Glaciology*, v. 22, p. 141-146.
- Björnsson, H., and Pálsson, F., 2008, Icelandic Glaciers: Jökull, v. 58, p. 365-386.
- Björnsson, H., Pálsson, F., Sigurðsson, O., and Flowers, G. E., 2003, Surges of glaciers in Iceland: *Annals of Glaciology*, v. 36, no. 1, p. 82-92.
- Borradaile, G. J., 1988, Magnetic susceptibility, petrofabrics and strain: *Tectonophysics*, v. 156, p. 1-20.
- , 2003, *Statistics of earth science data: Their distribution in time, space and orientation*, New York, Springer.
- Boulton, G. S., 1971, Till genesis and fabric in Svalbard, Spitsbergen, *Till: a symposium*: Columbus, Ohio, Ohio State University Press, p. 41-72.
- , 1976, The origin of glacially fluted surfaces - observations and theory: *Journal of Glaciology*, v. 17, no. 76, p. 287-309.
- Boulton, G. S., Dent, D. L., and Morris, E. M., 1974, Subglacial shearing and crushing, and the role of water pressures in tills from south-east Iceland: *Geografiska Annaler. Series A, Physical Geography*, v. 56, no. 3/4, p. 135-145.
- Boulton, G. S., Dobbie, K. E., and Zatsepin, S., 2001, Sediment deformation beneath glaciers and its coupling to the subglacial hydraulic system: *Quaternary International*, v. 86, p. 3-28.
- Boulton, G. S., and Hindmarsh, R. C. A., 1987, Sediment deformation beneath glaciers: rheology and geological consequences: *Journal of Geophysical Research*, v. 92, no. B9, p. 9059-9082.
- Cohen, D., Hooyer, T. S., Iverson, N. R., Thomason, J. F., and Jackson, M., 2006, Role of transient water pressure in quarrying: A subglacial experiment using acoustic emissions: *Journal of Geophysical Research*, v. 111.
- Cuffey, K. M., and Paterson, W. S. B., 2010, *The Physics of Glaciers*, Burlington, Massachusetts, Elsevier.
- Day, R., Fuller, M., and Schmidt, V. A., 1977, Hysteresis properties of titanomagnetites: Grain-size and compositional dependence: *Physics of the Earth and Planetary Interiors*, v. 13, p. 260-267.

- de Wall, H., and Worm, H. U., 2000, A cautionary note on interpreting frequency-dependence of susceptibility solely in terms of paramagnetism, *The IRM Quarterly*, Volume 10: Minneapolis, MI, Institute for Rock Magnetism.
- Dearing, J. A., Dann, R. J. L., Hay, K., Lees, J. A., Loveland, P. J., Maher, B. A., and O'Grady, K., 1996, Frequency-dependent susceptibility measurements of environmental materials: *Geophysical Journal International*, v. 124, p. 228-240.
- Dekkers, M. J., 1989, Magnetic properties of natural pyrrhotite Part I: behavior of initial susceptibility and saturation magnetization related rock magnetic parameters in a grain-size dependent framework: *Physics of the Earth and Planetary Interiors*, v. 52, p. 376-393.
- Derbyshire, E., McGown, A., and Radwan, A., 1976, 'Total' fabric of some till landforms: *Earth Surface Processes*, v. 1, no. 1, p. 17-26.
- Dowdeswell, J. A., and Sharp, M. J., 1986, Characterization of pebble fabrics in modern terrestrial glacial sediments: *Sedimentology*, v. 33, no. 5, p. 699-710.
- Dunlop, D. J., 2002, Theory and application of the Day plot (Mrs/Ms versus Hcr/Hc) 1. Theoretical curves and tests using titanomagnetite data: *Journal of Geophysical Research*, v. 107, no. B3.
- Dunlop, D. J., and Özdemir, Ö., 1997, *Rock Magnetism: Fundamentals and Frontiers*, New York, Cambridge University Press.
- Dyson, J. L., 1952, Ice-ridged moraines and their relation to glacier: *American Journal of Science*, v. 250, p. 204-211.
- Eklund, A., and Hart, J. K., 1996, Glaciotectonic deformation within a flute from the Isfallsglaciaren, Sweden: *Journal of Quaternary Science*, v. 11, no. 4, p. 299-310.
- Evans, D. J. A., and Benn, D. I., 2004, *A practical guide to the study of glacial sediments*, Routledge, 270 p.:
- Evans, D. J. A., Nelson, C. D., and Webb, C., 2010, An assessment of fluting and "till esker" formation on the foreland of Sandfellsjökull, Iceland: *Geomorphology*, v. 114, p. 453-465.
- Evans, D. J. A., and Twigg, D. R., 2000, *Breiðamerkurjökull 1998*: University of Glasgow and Loughborough University, scale 1:30 000.
- , 2002, The active temperatre glacial landsystem: a model based on Breiðamerkurjökull and Fjallsjökull, Iceland: *Quaternary Science Reviews*, v. 21, p. 2143-2177.
- Eyles, N., Boyce, J. I., and Putkinen, N., 2015, Neoglacial (<3000 years) till and flutes at Saskatchewan Glacier, Canadian Rocky Mountains, formed by subglacial deformation of a soft bed: *Sedimentology*, v. 62, no. 1, p. 182-203.
- Eyles, N., Day, T. E., and Gavican, A., 1987, Depositional controls on the magnetic characteristics of lodgement tills and other glacial diamict facies: *Canadian Journal of Earth Sciences*, v. 24, no. 12, p. 2436-2458.
- Eyre, J. K., 1997, Frequency dependence of magnetic susceptibility of populations of single-domain grains: *Geophysical Journal International*, v. 129, p. 209-211.

- Fara, H. D., and Scheidegger, A. E., 1963, An eigenvalue method for the statistical evaluation of fault plane solutions of earthquakes: *Seismological Society of America Bulletin*, v. 53, p. 811-816.
- Ferré, E. C., 2002, Theoretical models of intermediate and inverse AMS fabrics: *Geophysical Research Letters*, v. 29, no. 7, p. 31-31 - 31-34.
- Fisher, N. I., Lewis, T., and Embleton, B. J. J., 1987, *Statistical analysis of spherical data*, Cambridge.
- Fisher, R. A., 1953, Dispersion on a sphere: *Proceedings of the Royal Society*, v. A217, p. 295-305.
- Fleming, E. J., Stevenson, C. T. E., and Petronis, M. S., 2013, New insights into the deformation of a Middle Pleistocene glaciotectioned sequence in Norfolk, England through magnetic and structural analysis: *Proceedings of the Geologists' Association*, v. 124, no. 5, p. 834-854.
- Flinn, D., 1962, On folding during three-dimensional progressive deformation: *Quarterly Journal of the Geological Society*, v. 118, no. 1-4, p. 385-428.
- Flood, R. D., Kent, D. V., Shor, A. N., and Hall, F. R., 1985, The magnetic fabric of surficial deep-sea sediments in the HEBBLE area (Nova Scotian continental rise), *in* Nowell, A. R. M., and Hollister, C. D., eds., *Deep Ocean Sediment Transport - Preliminary Results of the High Energy Benthic Boundary Layer Experiment*, Volume 66, p. 146-167.
- Fuller, F. M., 1962, A magnetic fabric in till: *Geological Magazine*, v. 99, no. 03, p. 233-237.
- Gentoso, M. J., Evenson, E. B., Kodama, K. P., Iverson, N. R., Alley, R. B., Berti, C., and Kozlowski, A., 2012, Exploring till bed kinematics using AMS magnetic fabrics and pebble fabrics: the Weedsport drumlin field, New York State, USA: *Boreas*, v. 41, no. 1, p. 31-41.
- Glasser, N. F., and Hambrey, M. J., 2001, Styles of sedimentation beneath Svalbard valley glaciers under changing dynamic and thermal regimes: *Journal of the Geological Society, London*, v. 158, p. 697-707.
- Gordon, J. E., Whalley, W. B., Gellatly, A. F., and Vere, D. M., 1992, The formation of glacial flutes: assessment of models with evidence from Lyngsdalen, North Norway: *Quaternary Science Reviews*, v. 11, p. 709-731.
- Gourmelen, N., Kim, S. W., Sheperd, A., Park, J. W., Sundal, A. V., Björnsson, H., and Pálsson, F., 2011, Ice velocity determined using conventional and multiple-aperture InSAR: *Earth and Planetary Science Letters*, v. 307, p. 156-160.
- Graham, J. W., 1954, Magnetic susceptibility anisotropy, an unexploited petrofabric element: *Geological Society of America Bulletin*, v. 65, no. 12, p. 1257-1258.
- Granar, L., 1958, Magnetic measurements on Swedish varved sediments: *Arkiv för Geofysik*, v. 3, p. 1-40.

- Gravenor, C. P., 1984, Magnetic and pebble fabrics of the glaciomarine diamictos in the Champlain Sea, Ontario, Canada: *Canadian Journal of Earth Sciences*, v. 22, p. 422-434.
- Gravenor, C. P., Stupavsky, M., and Symons, D. T. A., 1973, Paleomagnetism and its relationship to till deposition: *Canadian Journal of Earth Sciences*, v. 10, no. 7, p. 1068-1078.
- Guðmundsson, S., 2014, Reconstruction of late 19th century geometry of Kotárjökull and Breiðamerkurjökull in SE-Iceland and comparison with the present [M.S.: University of Iceland, 79 p.
- Hamilton, N., and Rees, A. I., 1970, The use of magnetic fabric in palaeocurrent estimation, *in* Runcorn, S. K., ed., *Palaeogeophysics*: New York, Academic Press, Inc.
- Hannesdóttir, H., Zöhrer, A., Davids, H., Sigurgeirsdóttir, S. I., Skírnisdóttir, H., and Árnason, Þ., 2010, Vatnajökull National Park: Geology and Geodynamics.
- Harrison, R. J., and Feinberg, J. M., 2008, FORCinel: An improved algorithm for calculating first-order reversal curve distributions using locally weighted regression smoothing: *Geochemistry, Geophysics, Geosystems*, v. 9, no. 5, p. n/a-n/a.
- Hart, J. K., 1998, The deforming bed/debris-rich basal ice continuum and its implications for the formation of glacial landforms (flutes) and sediments (melt-out till): *Quaternary Science Reviews*, v. 17, p. 737-754.
- Hart, J. K., and Smith, B., 1997, Subglacial deformation associated with fast ice flow, from the Columbia Glacier, Alaska: *Sedimentary Geology*, v. 111, p. 177-197.
- Hext, G. R., 1963, The estimations of second-order tensors, with related tests and designs: *Biometrika*, v. 50, no. 3-4, p. 353-373.
- Hicock, S. R., Goff, J. R., Lian, O. B., and Little, E. C., 1996, On the interpretation of subglacial till fabric: *Journal of Sedimentary Research*, v. 66, no. 5, p. 928-934.
- Holmes, C. D., 1941, Till fabric: *Geological Society of America Bulletin*, v. 52, no. 9, p. 1299-1354.
- Hooyer, T. S., and Iverson, N. R., 2000, Clast-fabric development in a shearing granular material: Implications for subglacial till and fault gouge: *Geological Society of America Bulletin*, v. 112, no. 5, p. 683-692.
- , 2002, Flow mechanism of the Des Moines lobe of the Laurentide ice sheet: *Journal of Glaciology*, v. 48, no. 163, p. 575-586.
- Hooyer, T. S., Iverson, N. R., Lacroix, F., and Thomason, J. F., 2008, Magnetic fabric of sheared till: A strain indicator for evaluating the bed deformation model of glacier flow: *Journal of Geophysical Research*, v. 113, no. F2.
- Hopkins, N. R., Evenson, E. B., Kodama, K. P., and Kozlowski, A., 2015, An anisotropy of magnetic susceptibility (AMS) investigation of the till fabric of drumlins: support for an accretionary origin: *Boreas*.

- Hoppe, G., and Schytt, V., 1953, Some observations on fluted moraine surfaces: *Geografiska Annaler: Series A, Physical Geography*, v. 35, no. 2, p. 105-115.
- Hrouda, F., 2007, Magnetic Susceptibility, Anisotropy, *in* Gubbins, D., and Herrero-Bervaer, E., eds., *Encyclopedia of Geomagnetism and Paleomagnetism*: Dordrecht, The Netherlands, Springer.
- Hrouda, F., and Kahan, S., 1991, The magnetic fabric relationship between sedimentary and basement nappes in the High Tatra Mountains, N. Slovakia: *Journal of Structural Geology*, v. 13, no. 4, p. 431-442.
- Hubbard, T. D., and Reid, J. R., 2006, Analysis of flute forming conditions using ice sheet reconstructions and field techniques: *Geomorphology*, v. 74, no. 1-4, p. 137-151.
- Hunt, C. P., Moskowitz, B. M., and Banerjee, S. K., 1995, Magnetic properties of rocks and minerals, v. 3, p. 189-204.
- Iverson, N. R., 1991, Potential effects of subglacial water-pressure fluctuations on quarrying: *Journal of Glaciology*, v. 37, no. 125, p. 27-36.
- Iverson, N. R., 2010, Shear resistance and the continuity of subglacial till: hydrology rules: *Journal of Glaciology*, v. 56, no. 200, p. 1104-1114.
- Iverson, N. R., Hooyer, T. S., Thomason, J. F., Graesch, M., and Shumway, J. R., 2008, The experimental basis for interpreting particle and magnetic fabrics of sheared till: *Earth Surface Processes and Landforms*, v. 33, no. 4, p. 627-645.
- Iverson, N. R., and Iverson, R. M., 2001, Distributed shear of subglacier till due to Coulomb slip: *Journal of Glaciology*, v. 47, no. 158, p. 481-488.
- Jelinek, V., 1977, The statistical theory of measuring anisotropy of magnetic susceptibility in rocks and its applications: *Geofyzika*.
- , 1981, Characterization of the magnetic fabric of rocks: *Tectonophysics*, v. 79, no. 3-4, p. T63-T67.
- , 1997, Measuring anisotropy of magnetic susceptibility on a slowly spinning specimen - Basic theory.
- Jóhannesson, H., 2014, Geological map of Iceland: Icelandic Institute of Natural History, Bedrock Geology.
- Jóhannesson, T., Sigurðsson, O., Einarsson, B., and Thorsteinsson, T., 2006, Mass balance modeling of the Hofsjökull ice cap based on data from 1988-2004.: National Energy Authority OS-2006/004.
- Johnson, M. D., Schomacker, A., Benediktsson, I. O., Geiger, A. J., Ferguson, A., and Ingolfsson, O., 2010, Active drumlin field revealed at the margin of Mulajökull, Iceland: A surge-type glacier: *Geology*, v. 38, no. 10, p. 943-946.
- Jónasson, K., 2007, Silicic volcanism in Iceland: Composition and distribution within the active volcanic zones: *Journal of Geodynamics*, v. 43, no. 1, p. 101-117.

- Jónsson, S. A., Schomacker, A., Benediktsson, Í. Ö., Ingólfsson, Ó., and Johnson, M. D., 2014, The drumlin field and geomorphology of the Múlajökull surge-type glacier, central Iceland.: *Geomorphology*, v. 207, p. 213-220.
- Kąkol, Z., 1990, Magnetic and transport properties of magnetite in the vicinity of the Verwey transition: *Journal of Solid State Chemistry*, v. 88, p. 104-114.
- Kąkol, Z., and Honig, J. M., 1989, Influence of deviations from ideal stoichiometry on the anisotropy parameters of magnetite $\text{Fe}_3(1-\delta)\text{O}_4$: *Physical Review B*, v. 40, no. 13, p. 9090-9097.
- Kąkol, Z., Sabol, J., Sticker, J., Kozłowski, A., and Honig, J. M., 1994, Influence of titanium doping on the magnetocrystalline anisotropy of magnetite: *Physical Review B*, v. 49, no. 18, p. 12767 - 12772.
- Kamb, W. B., 1959, Ice petrofabric observations from Blue Glacier, Washington, in relation to theory and experiment: *Journal of Geophysical Research*, v. 64, no. 11, p. 1891-1909.
- , 1987, Glacier surge mechanism based on linked cavity configuration of the basal water conduit system: *Journal of Geophysical Research*, v. 92, no. B9, p. 9083-9100.
- Kamb, W. B., Raymond, C. F., Harrison, W. D., Engelhardt, H. F., Echelmeyer, N., Humphrey, N., Brugman, M. M., and Pfeffer, T., 1985, Glacier Surge Mechanism: 1982-1983 Surge of Variegated Glacier, Alaska: *Science*, v. 227, no. 4686, p. 469-497.
- Karlén, W., 1981, Flutes on bare bedrock: *Journal of Glaciology*, v. 27, no. 95, p. 190-192.
- Kirkbride, M. P., 2000, Ice-marginal geomorphology and Holocene expansion of debris-covered Tasman Glacier, New Zealand: *IAHS Publication*, p. 211-218.
- Kosterov, A., 2007, Magnetic properties, low-temperature, *in* Gubbins, D., and Herrero-Bervera, E., eds., *Encyclopedia of Geomagnetism and Paleomagnetism*: Dordrecht, The Netherlands, Springer.
- Krasa, D. F., K., 2007, Rock Magnetism, Hysteresis Measurements, *in* Gubbins, D., and Herrero-Bervera, E., eds., *Encyclopedia of Geomagnetism and Paleomagnetism*: Dordrecht, The Netherlands, Springer.
- Lagroix, F., and Banerjee, S. K., 2002, Paleowind directions from the magnetic fabric of loess profiles in central Alaska: *Earth and Planetary Science Letters*, v. 195, p. 99-112.
- Lambe, W. T., and Whitman, R. V., 1969, *Soil Mechanics*, John Wiley & Sons, Inc., 576 p.:
- Lawson, D. E., 1979, A comparison of the pebble orientations in ice and deposits of the Matanuska glacier, Alaska: *The Journal of Geology*, v. 87, no. 6, p. 629-645.
- Liu, Q., Banerjee, S., Jackson, M. J., Chen, F., and Pan, Y. Z., Rixiang, 2003, An integrated study of the grain-size-dependent magnetic mineralogy of the Chinese

- loess/paleosol and its environmental significance: *Journal of Geophysical Research*, v. 108, no. B9.
- Love, J. J., 2007a, *Bingham Statistics*, Encyclopedia of geomagnetism and paleomagnetism: Dordrecht, Netherlands, Springer, p. 45-47.
- , 2007b, Principal component analysis for paleomagnetism, Encyclopedia of Geomagnetism and Paleomagnetism: Dordrecht, The Netherlands, Springer, p. 845-850.
- Mark, D. M., 1973, Analysis of Axial Orientation Data, Including Till Fabrics: *Geological Society of America Bulletin*, v. 84, no. 4, p. 1369.
- , 1974, On the Interpretation of Till Fabrics: *Geology*, v. 2, no. 2, p. 101.
- McCracken, R., 2015, Physical characteristics of drumlins, with implications for their formation, as an active drumlin field, Múlajökull, Iceland [Master of Science: Iowa State University].
- McCracken, R., Iverson, N. R., Hooyer, T. S., Schomacker, A., Ives, L. R. W., Johnson, M. D., and Benediktsson, I. O., 2014, Drumlin formation at Múlajökull, Iceland. , *International Glaciology Society International Symposium on Glaciers and Ice Sheets Contribution to Sea-Level Change (Observations, Modelling and Predictions)*: Chamonix, France, .
- Menzies, J., and Maltman, A. J., 1992, Microstructures in diamictites - evidence of subglacial bed conditions: *Geomorphology*, v. 6, no. 1, p. 27-40.
- Morris, E. M., and Morland, L. W., 1976, A theoretical analysis of the formation of glacial flutes: *Journal of Glaciology*, v. 17, no. 76, p. 311 - 323.
- Moskowitz, B. M., 1991, *Classes of Magnetic Minerals*, *Hitchhiker's Guide to Magnetism*, Volume 2015, Institute for Rock Magnetism.
- Moskowitz, B. M., Jackson, M., and Kissel, C., 1998, Low-temperature magnetic behavior of titanomagnetites: *Earth and Planetary Science Letters*, v. 157, p. 141-149.
- Muxworthy, A. R., 2001, Effect of grain interactions on the frequency dependence of magnetic susceptibility: *Geophysical Journal International*, v. 144, p. 441-447.
- Muxworthy, A. R., and Roberts, A. P., 2007, First-order reversal curve (FORC) diagrams, in Gubbins, D., and Herrero-Bervera, E., eds., *Encyclopedia of Geomagnetism and Paleomagnetism*: Dordrecht, The Netherlands, Springer.
- Naylor, M. A., and Woodcock, N. H., 1977, Transition analysis of structural sequences: *Geological Society of America Bulletin*, v. 88, no. 10, p. 1488.
- Nichols, R. L., and Miller, M. M., 1952, The Moreno Glacier, Lago, Argentina, Patagonia: *Journal of Glaciology*, v. 11.
- O'Reilly, W., 1984, *Rock and mineral magnetism*, London, Blackie & Son.
- Otsuka, N., and Sato, H., 1986, Observations of the Verwey Transition in Fe₃O₄ by high-resolution electron microscopy: *Journal of Solid State Chemistry*, v. 61, p. 212-222.

- Özdemir, Ö., and Dunlop, D. J., 2010, Hallmarks of maghemitization in low-temperature remanence cycling of partially oxidized magnetite nanoparticles: *Journal of Geophysical Research*, v. 115.
- Özdemir, Ö., Dunlop, D. J., and Moskowitz, B. M., 1993, The effect of oxidation on the verwey transition in magnetite: *Geophysical Research Letters*, v. 20, no. 16, p. 1671-1674.
- Ozima, M. L., E.E., 1970, Low- and high- temperature oxidation of titanomagnetite in relation to irreversible changes in the magnetic properties of submarine basalts: *Journal of Geophysical Research*, v. 75, no. 5, p. 1003-1017.
- Paul, M. A., and Evans, H., 1974, Observations on the internal structure and origin of some flutes in glacio-fluvial sediments, Blomstrandbreen, north-west Spitsbergen: *Journal of Glaciology*, v. 13, p. 393-400.
- Petrovsky, E., 2007, Susceptibility, *in* Gubbins, D., and Herrero-Bervera, E., eds., *Encyclopedia of geomagnetism and paleomagnetism*, Springer.
- Piotrowski, J. A., Mickelson, D. M., Tulaczyk, S., Krzyszkowski, D., and Junge, F. W., 2001, Were deforming subglacial beds beneath past ice sheets really widespread?: *Quaternary International*, v. 86, p. 139-150.
- Potter, D. K., and Stephenson, A., 1988, Single-domain particles in rocks and the magnetic fabrics analysis: *Geophysical Research Letters*, v. 15, no. 10, p. 1097-1100.
- Raposo, M. I. B., 1997, Magnetic fabrics and its significance in the Florianopolis dyke swarm, southern Brazil: *Geophysical Journal International*, v. 131, no. 159-170.
- Rees, A. I., Von Rad, U., and Shepard, F. P., 1968, Magnetic fabrics of sediments from the La Jolla submarine canyon and fan, California: *Marine Geology*, v. 6, p. 145-178.
- Richter, C., and van der Pluijm, B. A., 1994, Separation of paramagnetic and ferrimagnetic susceptibilities using low temperature magnetic susceptibilities and comparison with high field methods: *Physics of the Earth and Planetary Interiors*, v. 82, p. 113-123.
- Roberson, S. A. M., Hubbard, B., Coulson, H. R., and Boomer, I. A. N., 2011, Physical Properties and Formation of Flutes at a Polythermal Valley Glacier: Midre Lovénbreen, Svalbard: *Geografiska Annaler: Series A, Physical Geography*, v. 93, no. 2, p. 71-88.
- Robin, G. d. Q., 1976, Is the basal ice of a temperate glacier at the pressure melting point: *Journal of Glaciology*, v. 16, p. 183-196.
- Rochette, P., Aubourg, C., and Perrin, M., 1999, Is this magnetic fabrics normal? A review and case studies in volcanic formations: *Tectonophysics*, v. 307, p. 219-234.
- Rochette, P., Jackson, M., and Aubourg, C., 1992, Rock magnetism and the interpretation of anisotropy of magnetic susceptibility: *Reviews of Geophysics*, v. 30, no. 3, p. 209-226.

- Rose, J., Drumlins as part of a glacier bedform continuum, *in* Proceedings Drumlin Symposium, Manchester, 1987, A.A.Balkema, p. 103 - 116.
- , 1989, Glacier stress patterns and sediment transfer associated with the formation of superimposed flutes: *Sedimentary Geology*, v. 62, p. 151-176.
- Scheidegger, A. E., 1964, The tectonic stress and tectonic motion direction in Europe and western Asia as calculated from earthquake fault plane solutions: *Seismological Society of America Bulletin*, v. 54, p. 1519-1528.
- , 1965, On the statistics of the orientation of bedding planes, grain axes, and similar sedimentological data: *U.S. Geological Survey Professional Paper*, v. 535-C, p. 164-167.
- Schomacker, A., 2010, Expansion of ice-marginal lakes at the Vatnajökull ice cap, Iceland, from 1999 to 2009: *Geomorphology*, v. 119, no. 3-4, p. 232-236.
- Schoof, C. G., and Clarke, G. K. C., 2008, A model for spiral flows in basal ice and the formation of subglacial flutes based on a Reiner-Rivlin rheology for glacial ice: *Journal of Geophysical Research*, v. 113, no. B5.
- Schytt, V., 1959, The glaciers of the Kebnekajse- Massif: *Geografiska Annaler*, v. 41, no. 4, p. 213-227.
- , 1962, Notes on the Glaciological Activities in Bebneskajse, Sweden 1962: *Geografiska Annaler*, v. 44, no. 3/4, p. 407-412.
- , 1963, Fluted moraine surfaces: *Journal of Glaciology*, v. 4, p. 825-827.
- Shumway, J. R., and Iverson, N. R., 2009, Magnetic fabrics of the Douglas Till of the Superior lobe: exploring bed-deformation kinematics: *Quaternary Science Reviews*, v. 28, no. 1-2, p. 107-119.
- Sigurðsson, O., 1998, Glacier variations in Iceland 1930-1995: From the database of the Iceland Glaciological Society: *Jökull*, v. 45, p. 3-25.
- Sigurkarlsson, M. F., 2015, Surge history of Múlajökull, Iceland, since 1945 detected with remote sensing data [B.S.: University of Iceland.
- Stevenson, J. A., McGarvie, D. W., Smellie, J. L., and Gilbert, J. S., 2006, Subglacial and ice-contact volcanism at the Öräfajökull stratovolcano, Iceland: *Bulletin of Volcanology*, v. 68, p. 737-752.
- Stewart, R. A., Bryant, D., and Sweat, M. J., 1988, Nature and origin of corrugated ground moraine of the Des Moines lobe, Story County, Iowa: *Geomorphology*, v. 1, p. 111-130.
- Stupavsky, M., Gravenor, C. P., and Symons, D. T. A., 1974a, Paleomagnetism and Magnetic Fabric of the Leaside and Sunnybrook Tills near Toronto, Ontario: *Geological Society of America Bulletin*, v. 85, no. 8, p. 1233.
- Stupavsky, M., Symons, D. T. A., and Gravenor, C. P., 1974b, Paleomagnetism of the Port Stanley Till, Ontario: *Geological Society of America Bulletin*, v. 85, no. 1, p. 141.

- Tarling, D. F., and Hrouda, F., 1993, *The Magnetic Anisotropy of Rocks*, London, Chapman and Hall, 217 p.:
- Tauxe, L., 2015, *eqarea_ell.py*, in Tauxe, L., ed., *PmagPy*.
- Tauxe, L., Banerjee, S., Butler, R. F., and Van der Voo, R., 2015, *Essentials of Paleomagnetism*, University of California Press.
- Thomason, J. F., and Iverson, N. R., 2006, Microfabric and microshear evolution in deformed till: *Quaternary Science Reviews*, v. 25, no. 9-10, p. 1027-1038.
- Thomason, J. F., and Iverson, N. R., 2009, Deformation of the Batestown till of the Lake Michigan lobe, Laurentide ice sheet: *Journal of Glaciology*, v. 55, no. 189, p. 1-17.
- Thordarson, T., and Larsen, G., 2007, Volcanism in Iceland in historical time: Volcano types, eruption styles and eruptive history: *Journal of Geodynamics*, v. 43, no. 1, p. 118-152.
- Tulaczyk, S., 1999, Ice sliding over weak, fine-grained tills: dependence of ice-till interaction on till granulometry, in Mickelson, D. M., and Attig, J. W., eds., *Glacial processes: past and present*: Boulder, Co., Geological Society of American, p. 159-177.
- Tulaczyk, S., Kamb, W. B., and Engelhardt, H. F., 2000, Basal mechanics of Ice Stream B, west Antarctica: 1. Till mechanics: *Journal of Geophysical Research*, v. 105, no. B1, p. 463.
- Van der Meer, J. J. M., 1993, Microscopic evidence of subglacial deformation: *Quaternary Science Reviews*, v. 12, no. 7, p. 553-587.
- Van der Meer, J. J. M., 1997, short-lived streamlined bedforms (annual small flutes) formed under clean ice, Turtmann Glacier, Switzerland: *Sedimentary Geology*, v. 111, p. 107-118.
- Van der Meer, J. J. M., Menzies, J., and Rose, J., 2003, Subglacial till: the deforming glacier bed: *Quaternary Science Reviews*, v. 22, p. 1659-1685.
- Van der Wateren, F. M., 1999, Structural geology and sedimentology of the Heiligenhafen till section, Northern Germany: *Quaternary Science Reviews*, v. 18, p. 1625-1639.
- Verwey, E. J. W., 1939, Electron conduction of Magnetite (Fe_3O_4) and its transition point at low temperatures: *Nature*, v. 144, p. 327-328.
- Verwey, E. J. W., and Haayman, P. W., 1941, Electronic conductivity and transition point of magnetite (Fe_3O_4): *Physica*, v. VIII, no. 9, p. 979-987.
- Vreeland, N. P., Iverson, N. R., Graesch, M., and Hooyer, T. S., 2015, Magnetic fabrics of drumlins in the Green Bay Lobe, southeastern Wisconsin: *Quaternary Science Reviews*, v. 122, p. 33-44.
- Watson, G. S., 1956, A test for randomness of directions: *Geophysical Supplements to the Monthly Notices of the Royal Astronomical Society*, v. 7, no. 4, p. 160-161.
- , 1966, The statistics of orientation data: *Geology*, v. 74, p. 786-797.

- Weertman, J., 1964, Glacier Sliding: Cold Regions Research and Engineering Lab.
- Weiler, P. D., 2007, Magnetic Anisotropy, Sedimentary Rocks and Strain Alteration, *in* Gubbins, D., and Herrero-Bervera, E., eds., *Encyclopedia of Geomagnetism and Paleomagnetism*: Dordrecht, The Netherlands, Springer.
- Williams, W., 2007, Magnetometer, Laboratory, *in* Gubbins, D., and Herrero-Bervera, E., eds., *Encyclopedia of Geomagnetism and Paleomagnetism*: Dordrecht, The Netherlands, Springer.
- Woodcock, N. H., 1977, Specification of fabric shapes using an eigenvalue method: *Geological Society of America Bulletin*, v. 88, no. 9, p. 1231.
- Worm, H.-U., 1998, On the superparamagnetic-stable single-domain transition for magnetite, and frequency dependence of susceptibility: *Geophysical Journal International*, v. 133, p. 201-206.
- Worm, H.-U., Clark, D., and Dekkers, M. J., 1993, Magnetic susceptibility of pyrrhotite: grain size, field and frequency dependence: *Geophysical Journal International*, v. 114, p. 127-137.
- Zhu, R., Liu, Q., and Jackson, M. J., 2004, Paleoenvironmental significance of the magnetic fabrics in Chinese loess-paleosols since the last interglacial (< 130 ka): *Earth and Planetary Science Letters*, v. 221, p. 55-69.

APPENDIX A. MATLAB SCRIPT FOR DETERMINING LOCATIONS OF AMS SAMPLES FROM FIELD PHOTOS

The following Matlab script was used to calculate the coordinates of AMS samples. Photographs were taken of sampling platforms once all AMS boxes were emplaced and numbered ([Fig. A-1A](#)).

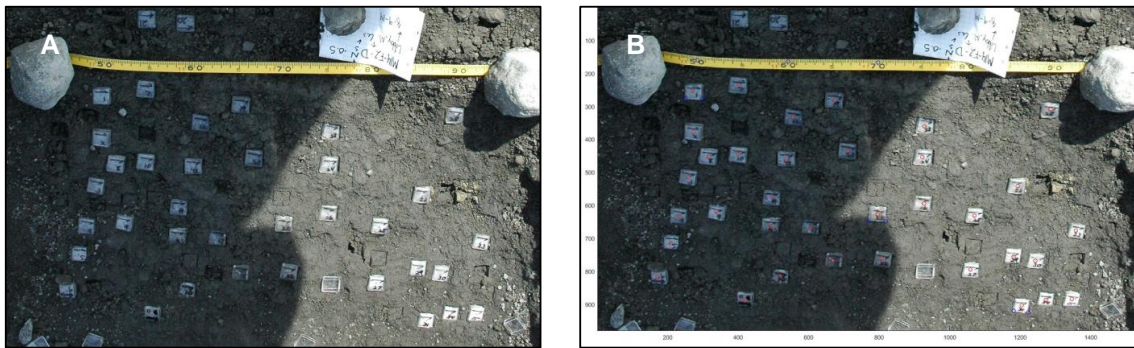


Figure A-1. (A) AMS sampling platform in a flute at Múlaþjökull. (B) The same photograph imported into the Matlab program described in this appendix, with all of the boxes marked by open, red circles.

Photographs always included a measuring tape that marked both the location of the center line ($y = 0$) and the distance from the flute's stoss-side boulder. Prior to importing the photograph into Matlab, the picture is processed so that the measuring tape is horizontal.

```
clear all
close all
%Determine real-world value of photo Origin
ulx = 3950
uly = 0

%Read in Photo
I1 = imread('b14_f2_B_0.85A.jpg');

%Bunch of Clicks
% This section by Geoff Gadd
n = 0;
```

```

p = 0;
imagesc(I1)
hold on
but = 1;
but1 = 3;
%Scaling Picture
read = 'First two blue selections are for the measuring tape'
read = 'Selections 3 - 8 are for three AMS boxes'
read = 'Selection 9 is for the origin'
while but1 == 3
    [xu,yu,but1] = ginput(1);
    p = p+1;
    dist(p,:) = [(xu);(yu)];
    plot(dist(:,1),dist(:,2),'bo')
end

while but == 1
    [xi,yi,but] = ginput(1);
    n = n+1;
    xy(n,:) = [(xi);(yi)];
    plot(xy(:,1),xy(:,2),'ro')
end

%Determine Scale of Picture

%For 10 cm measured on measuring tape
x1 = dist(1,1);
x2 = dist(2,1);
y1 = dist(1,2);
y2 = dist(2,2);

d = sqrt((x2-x1)^2 - (y2-y1)^2);
dt = d/10;

%For 1.8 cm measured on three boxes
x3 = dist(3,1);
x4 = dist(4,1);
y3 = dist(3,2);
y4 = dist(4,2);

d = sqrt((x4-x3)^2 - (y4-y3)^2);
dbi = d/1.8;

x5 = dist(5,1);
x6 = dist(6,1);
y5 = dist(5,2);
y6 = dist(6,2);

d = sqrt((x6-x5)^2 - (y6-y5)^2);
dbii = d/1.8;

x7 = dist(7,1);
x8 = dist(8,1);
y7 = dist(7,2);
y8 = dist(8,2);

```

```

d = sqrt((x8-x7)^2 - (y8-y7)^2);
dbiii = d/1.8;

%Average of Measuring Tape and Boxes

da = [dt, dbi, dbii, dbiii]
dai = mean (da)

%Assign Origin
ox = dist(9,1)/dai;
oy = dist(9,2)/dai

%Convert xy from pixel to cm scale
xym = xy/dai;

%Adjust for Origin - Right
xm = xym(:,1);
ym = xym(:,2);
x = - xm + ulx + ox;
y = ym + uly - oy;

%Adjust for Origin - Left
xm = xym(:,1);
ym = xym(:,2);
x = xm + ulx - ox;
y = -ym + uly - oy;
final = [x, y]

```

APPENDIX B. MATLAB SCRIPT FOR CALCULATING PRINCIPAL VECTORS OF AND ORIENTATION TENSOR

For a set of AMS or clast vector data with measured trends (D^* , declination) and plunges (I^* , inclination), all observations (N) are assumed to be unit vectors. Each axis is converted to its equivalent directional cosines $\mathbf{x} = (x_1, x_2, x_3)$, where \mathbf{x} represents the geographic components north, east, and down ([Fisher et al., 1987](#); [Borradaile, 2003](#); [Love, 2007b](#); [Tauxe et al., 2015](#)):

$$x_1 = \cos(D^*) \cos(I^*); x_2 = \sin(D^*) \cos(I^*); x_3 = \sin(I^*).$$

The orientation tensor is defined as:

$$\mathbf{T} = \frac{\sum_{i=1}^N \begin{bmatrix} x_1^2 & x_1 x_2 & x_1 x_3 \\ x_2 x_1 & x_2^2 & x_2 x_3 \\ x_3 x_1 & x_3 x_2 & x_3^2 \end{bmatrix}}{N}$$

and is a symmetrical, positive-definite matrix ([Scheidegger, 1965](#); [Fisher et al., 1987](#)).

For a symmetrical, positive-definite matrix there are three eigenvalues ($\lambda_i = \lambda_1, \lambda_2, \lambda_3$) that modify the orientation tensor so that all of the non-unique (“off-axis”) terms are equal to zero. This concept can be expressed as:

$$\mathbf{T}\mathbf{V} = \lambda\mathbf{V} \Leftrightarrow \det|\mathbf{T} - \lambda\mathbf{I}_n| = 0,$$

where λ are eigenvalues, \mathbf{V} are non-zero eigenvectors that satisfy an eigenvalue, and \mathbf{I}_n is a 3 x 3 identity matrix ([Fisher et al., 1987](#); [Tauxe et al., 2015](#)). For \mathbf{T} :

$$\lambda_1 \geq \lambda_2 \geq \lambda_3 \geq 0; \lambda_1 + \lambda_2 + \lambda_3 = N$$

and are normalized so:

$$S_1 = \frac{\lambda_1}{N}; S_2 = \frac{\lambda_2}{N}; S_3 = \frac{\lambda_3}{N}; S_1 + S_2 + S_3 = 1$$

Eigenvectors of an orientation tensor can be converted from Cartesian coordinates to spherical coordinates using the following equations:

$$D^* = \tan^{-1}\left(\frac{x_2}{x_1}\right); I^* = \sin^{-1}\left(\frac{x_3}{R}\right); R = \sqrt{\sum x_1^2 + \sum x_2^2 + \sum x_3^2}.$$

The script reads as follows:

```
clear all
close all

dirtx = dir ('*.txt');
L = size (dirtx,1);
v1d = [];
v1i = [];
v2d = [];
v2i = [];
v3d = [];
v3i = [];
s1 = [];
s2 = [];
s3 = [];
elo = [];
iso = [];
cgi = [];
r1 = [];
r2 = [];
ki = [];
c = [];
np = [];
dec = [];
inc = [];

for k= (1:L)
    fullname = dirtx(k).name;
    [pathstr,filename,ext]= fileparts(fullname);
    di = readtable (filename, 'ReadVariableNames', false, 'Delimiter',
'\t');
    DI = table2array(di);

    % Orientation Tensor

    % Import Declination and Inclination data
    N = size (DI,1);
    % D = DI (:,1);
    % I = DI (:,2);
    d = DI (:,1);
    i = DI (:,2);
```

```

% Convert negative declination to position declinations
dminus = d < 0;
dplus = d >= 0;
dminusnum = d (dminus);
dplusnum = d (dplus);
dminusi = i (dminus);
dplusi = i (dplus);
dminustrans = dminusnum + 360;
D = vertcat (dminustrans,dplusnum);
I = vertcat (dminusi,dplusi);

% Convert D and I to directional cosines
cosD = cosd(D);
cosI = cosd(I);
sinD = sind(D);
sinI = sind(I);
x1 = cosD.*cosI;
x2 = sinD.*cosI;
x3 = sinI;

% Calculate orientation tensor element values
T11 = sum(x1.*x1);
T12 = sum(x1.*x2);
T13 = sum(x1.*x3);
T21 = sum(x2.*x1);
T22 = sum(x2.*x2);
T23 = sum(x2.*x3);
T31 = sum(x3.*x1);
T32 = sum(x3.*x2);
T33 = sum(x3.*x3);

% Cumulative vector analysis
R = sqrt ((sum(x1)^2) +(sum(x2)^2) + (sum(x3)^2));
x1m = (sum(x1)/R);
x2m = (sum(x2)/R);
x3m = (sum(x3)/R);
Dm = atand (x2m/x1m);
Im = asind (x3m/R);

% Solve Orientation tensor
t = [T11 T12 T13; T21 T22 T23; T31 T32 T33] ;
T = t/N;
A = eye (3);
[V,e] = eig (T, 'nobalance');

% Normalized eigenvalues
S3 = e (1,1);
S2 = e (2,2);
S1 = e (3,3);

% Eigenvectors

% V3
%Retrieve directional cosines from T

```

```

V3x1 = V (1,1);
V3x1(isnan(V3x1)) = 0;
V3x2 = V (2,1);
V3x2(isnan(V3x2)) = 0;
V3x3 = V (3,1);
V3x3(isnan(V3x3)) = 0;
% Convert Directional Consines to D and I
V3R = sqrt ((V3x1^2) +(V3x2^2) + (V3x3^2));
V3D = atan2 (V3x2/V3x1);
V3D(isnan(V3D)) = 0;
V3I = asind (V3x3/V3R);
% Convert Upper Hemisphere to Lower Hemisphere
if V3D < 0
    V3D = V3D+360;
    V3I = abs(V3I);
end

% V2
%Retrieve directional cosines from T
V2x1 = V (1,2);
V2x1(isnan(V2x1)) = 0;
V2x2 = V (2,2);
V2x2(isnan(V2x2)) = 0;
V2x3 = V (3,2);
V2x3(isnan(V2x3)) = 0;
% Convert Directional Consines to D and I
V2R = sqrt ((V2x1^2) +(V2x2^2) + (V2x3^2));
V2D = atan2 (V2x2/V2x1);
V2D(isnan(V2D)) = 0;
V2I = asind (V2x3/V2R);
% Convert Upper Hemisphere to Lower Hemisphere
if V2D < 0
    V2D = V2D+360;
    V2I = abs(V2I);
end

% V1
%Retrieve directional cosines from T
V1x1 = V (1,3);
V1x1(isnan(V1x1)) = 0;
V1x2 = V (2,3);
V1x2(isnan(V1x2)) = 0;
V1x3 = V (3,3);
V1x3(isnan(V1x3)) = 0;
% Convert Directional Consines to D and I
V1R = sqrt ((V1x1^2) +(V1x2^2) + (V1x3^2));
V1D = atan2 (V1x2/V1x1);
V1D(isnan(V1D)) = 0;
V1I = asind (V1x3/V1R);
% Convert Upper Hemisphere to Lower Hemisphere
if V1D < 0
    V1D = V1D+360;
    V1I = abs(V1I);
end

```

```

% Create array with all calculated values
v1d = [v1d V1D];
v1i = [v1i V1I];
v2d = [v2d V2D];
v2i = [v2i V2I];
v3d = [v3d V2D];
v3i = [v3i V2I];
s1 = [s1 S1];
s2 = [s2 S2];
s3 = [s3 S3];

%Calculate normalized eigenvalue parameters
%Benn
E = 1- (S2/S1);
I = S3/S1;
CGI = (S1-S2)/(S1-S3);

%Woodcock
LN1 = log (S2/S3);
LN1(isnan(LN1)) = 0;
LN2 = log (S1/S2);
LN2(isnan(LN2)) = 0;
Ki = (LN2/LN1);
Ki(isnan(Ki)) = 0;
C = log (S1/S3);

elo = [elo E];
iso = [iso I];
cgi = [cgi CGI];
r1 = [r1 LN1];
r2 = [r2 LN2];
ki = [ki Ki];
c = [c C];

%Determine Distribution Type (Bingham[-1]/Watson[1]/Girdle[0])

NP = 0;
a95 = 7.81; %For three degrees of freedom
if((Ki > 1))
    %Normalized by principal axis
    x1np = x1 - V1x1;
    x2np = x2 - V1x2;
    x3np = x3 - V1x3;
    R2np = ((sum(x1np)^2) + (sum(x2np)^2) + (sum(x3np)^2));
    critp = (R2np/N);
    if critp > a95
        NP = -1;
    elseif critp <= a95
        NP = 1;
    end

elseif (CGI > 0.5)
    %Normalized by principal axis
    x1np = x1 - V1x1;
    x2np = x2 - V1x2;
    x3np = x3 - V1x3;

```

```

R2np = ((sum(x1np)^2) + (sum(x2np)^2) + (sum(x3np)^2));
critp = (R2np/N);
if critp > a95
    NP = -1;
elseif critp <= a95
    NP = 1;
end
end

np = [np NP];
dec = [dec (d')];
inc = [inc (i')];

end

```

APPENDIX C. TEST FOR SYMMETRICAL DISTRIBUTION OF ORIENTATIONS ABOUT A POLE

To determine whether a Watson or a Fisher distribution would be a more appropriate way to describe an AMS fabric, orientation data are tested for randomness using a test described by [Watson \(1956\)](#); [Fisher et al. \(1987\)](#); [Tauxe et al. \(2015\)](#). The squared resultant length ($R^2 = \sum x_1^2 + \sum x_2^2 + \sum x_3^2$), or the cumulative length of all orientation vectors in a sample set, is calculated. If the R^2 value is large enough, the hypothesis for uniformity is rejected, and the orientations have a non-random and likely symmetrical distribution. If R^2 is too small, the orientations are likely not symmetrically distributed. A set $N \geq 10$ orientations is symmetrically distributed if

$$\frac{3R^2}{N} > 7.81$$

([Fisher et al., 1987](#); [Tauxe et al., 2015](#)).

The following Matlab script was written to determine whether axes were distributed symmetrically or non-symmetrically. The data were normalized by their principal component orientation to account for apparent bimodal distributions that were common. This script is incorporated into the script discussed in [Appendix B](#).

```
%Test Fisherian Distribution
%
a95 = 7.81; %For three degrees of freedom

%Normalized by principal axis
x1np = x1 - V1x1;
x2np = x2 - V1x2;
x3np = x3 - V1x3;
R2np = ((sum(x1np)^2) + (sum(x2np)^2) + (sum(x3np)^2));
critp = (R2np/N);
if critp > a95
    %disp ('Data ARE NOT fisher distributed.')
    NP = 0;
elseif critp <= a95
    %disp (' Data ARE fisher distributed.')
```

```
        NP = 1;  
end
```

APPENDIX D. MAGNETIC MINERALOGY DISCUSSION

The magnetic mineralogy that controls the AMS signal of sediments from Múlajökull and is a mixture of primarily PSD titanomagnetite [$\text{Fe}_{(3-x)}\text{Ti}_x\text{O}_4$], with some titanomaghemite [$\text{Fe}_{(2-x)}\text{Ti}_x\text{O}_3$] and magnetite [Fe_3O_4]. The magnetic mineral controlling the susceptibility signal of diamictos from Breiðamerkurjökull is low-Ti titanomagnetite ($x \leq 0.1$), with small contributions from higher-Ti titanomagnetites. It is likely that the titanomagnetite at both Múlajökull and Breiðamerkurjökull are partially maghematized (oxidized). The magnetic susceptibility of the black sediments from B14-F1- A is probably controlled by maghemite (oxidized, cation-deficient magnetite) [Fe_2O_3].

D.1 Múlajökull

D.1.1 Mineralogy

Múlajökull tills have T_c values that include 182 °C, 485 °C, and ~550 °C ([Fig. 4-1A](#)). The 182 °C and ~550 °C Curie temperatures are reversible (present in both the high-temperature heating and cooling curve), while the 485 °C transition is not ([Fig. D-1A](#)). Although these T_c values are reasonable for titanomagnetite, the irreversibility of the 485 °C indicates the presence of titanomaghemite and correspondingly the oxidation of high-Ti titanomagnetites ([Ozima, 1970](#); [Moskowitz et al., 1998](#)). Titanomagnetites with T_c values of 182 °C and ~550 °C characterize Ti substitution values (x) of 0.6 and 0.1 and are called TM60 and TM10, respectively ([Tauxe et al., 2015](#)).

At low temperatures (< 300 K), the susceptibility of Múlajökull sediment is a smooth function of temperature, with no indication of the Verwey transition (120 K) indicative of magnetite ([Fig. 4-2A](#), [Fig. 3-19](#)). Although Ti substitution and

maghematization (oxidation) both result in the suppression of the Verwey transition, as seen in [Figure 4-2A](#), low-temperature SIRM results and frequency dependence on susceptibility, in addition to the T_c values, of the Múlajökull till, suggest titanomagnetite and not maghemite, which typically has T_c values > 560 °C. Remanence-on-cooling SIRM curves for the Múlajökull till show not only a suppression of the Verwey transition but also a depression to ~60-80 K ([Fig. 4-3](#)), which is characteristic to titanomagnetite ([Moskowitz et al., 1998](#)). The χ_{fd} value of 5.38% measured in the Múlajökull till is characteristic of MD titanomagnetites with T_c values of ~150-200 °C ([de Wall and Worm, 2000](#)). These values are consistent with T_c values measured for this till.

The SIRM curves of bulk sample M14-F2-B ([Fig. 4-3](#)) have an un-suppressed Verwey transition at 120 K, indicating that its magnetic signal is controlled by magnetite. The presence of a sample dominated by magnetite indicates that there is some variability in the magnetic mineralogy at Múlajökull.

The magnetic characteristics of the Múlajökull till are best attributed to a mixture of primarily unoxidized and oxidized TM60 with some TM10 and magnetite. This mineralogy is consistent with the lithologies observed in the forefield, and the lithology and age of the bedrock associated with Hofsjökull. Titanomagnetite is the primary magnetic carrier in mid-ocean ridge basalts, which is consistent with effusive eruptions along Iceland's central rift zone ([Tauxe et al., 2015](#)). The presence of TM60, TM10, and magnetite is also consistent with subglacial eruptions and the presence of basalt, vesicular basalt, and porphyritic basalt with glassy phenocrysts in the forefield. The TM60 in the till was likely sourced from rocks that were erupted subglacially and then rapidly cooled. The TM10 and magnetite is likely sourced from volcanic rocks that cooled more slowly.

Partial, but not complete, low-temperature (i.e. earth-surface temperature) maghematization of titanomagnetites is to be expected in young rocks (< 8,000 ka) that have experienced subglacial weathering ([Tauxe et al., 2015](#)). Finally, there was no consistent difference in magnetic mineral composition between the fine and coarse fractions of the Múlajökull till. This is evidence that both fractions have similar provenance and transport histories, which is characteristic of subglacial sediments.

Since ~96% of the magnetic susceptibility for Múlajökull till comes from its ferrimagnetic sources (TM60, TM10, and magnetite) any contribution to AMS from the paramagnetic component is likely inconsequential.

D.1.1 Magnetic grain size/domain state

First-order reversal curve analyses show that the Múlajökull sediments have dominantly PSD domain states with some MD grains ([Fig. 4-6A](#)). The hysteresis properties of the tills are consistent with this interpretation ([Fig. 4-5A](#)).

D.2 Breiðamerkurjökull till

D.2.1 Mineralogy

Breiðamerkurjökull tills have T_c values of ~320 °C, ~490 °C, and ~550 °C. The minerals with the curie temperature of 550 °C have significantly stronger remanence signals than those with a T_c value of 490 °C and 320 °C. The ~550 °C Curie temperature is reversible, whereas the 490 °C and 320 °C transitions were not ([Fig. D-1B](#)). Either pyrrhotite or greigite could account for the 320 °C T_c because both are magnetic minerals with Curie temperatures around 320°C that break down to magnetite at high temperatures ([Tauxe et al., 2015](#)). There is not enough data to identify the mineral with a ~490 °C

Curie temperature. The ~550 °C Curie temperature is only slightly less than the typical T_c value of magnetite (560 °C).

Clear Verwey transitions in both low-temperature susceptibility ([Fig. 4-2B](#)) and low-temperature remanence data ([Fig. 4-3](#)) indicate that magnetite, or very low Ti titanomagnetite, dominate the magnetic susceptibility signals in the Breiðamerkurjökull tills.

The magnetic characteristics of the Breiðamerkurjökull till are best attributed to magnetite. Because magnetite is common in most igneous rocks, this result is consistent with the wide variety of volcanic lithologies associated with the Öræfajökull volcano, which underlies western Breiðamerkurjökull ([Anthony et al., 1997](#)).

Since ~99% of the magnetic susceptibility for Múlajökull till comes from its ferrimagnetic sources, any contribution to AMS from the paramagnetic component is likely inconsequential.

D.2.2 Magnetic grain size/domain state

First-order reversal curve analyses show that the Múlajökull sediments have dominantly PSD domain states with some MD grains ([Fig. 4-6B](#), 10 and 11). The hysteresis properties of the tills are consistent with this interpretation ([Fig. 4-5B](#)). The frequency dependence on susceptibility for the Breiðamerkurjökull till sample was < 2%, which is reasonable, if slightly high, for natural MD magnetite samples ([Dearing et al., 1996](#)). The presence of pyrrhotite, titanomagnetite, and smaller (i.e. PSD) magnetic grain sizes may also increase frequency dependence on susceptibility ([Worm et al., 1993](#); [Dearing et al., 1996](#); [de Wall and Worm, 2000](#))

D.3 B14-F1, Site A Black Sand

The black sand from B14-F1, site A, has a Curie temperature of ~550 °C, which is characteristic of magnetite but can also occur in natural maghemites ([Liu et al., 2003](#); [Tauxe et al., 2015](#)). The irreversible nature of the curve more strongly suggests maghemite than magnetite ([Fig. D-1B](#)). The subdued but present Verwey transitions in SIRM curves also suggest maghemite. The difference between the fine and coarse/bulk SIRM curves indicates that the fine fraction is less oxidized.

High-field hysteresis results show that a larger percent of magnetic susceptibility comes from paramagnetic minerals in the coarse fraction (~12%) than in the fine fraction (~6%).

FORC distributions show that the black sediment's coarse fraction has both MD and SD domain states ([Fig. 4-6B](#), 8), and the fine fraction is mostly PSD with some MD ([Fig. 4-6B](#), 9). These results are consistent with hysteresis results showing that the coarse fraction had a higher coercivity than the fine fraction ([Table 4-1](#)).

The magnetic differences between the fine and coarse fraction of this sediment indicate that it is not likely a till and has been sorted. The differences in magnetic mineralogy between the coarse and fine fractions of the sediment are more likely derived from transport and weathering histories than from provenance.

The SD component of this black sediment does not seem to have drastically affected fabric orientation or shape, because it yielded nearly identical fabrics to adjacent tills ([Fig. 4-12](#)).

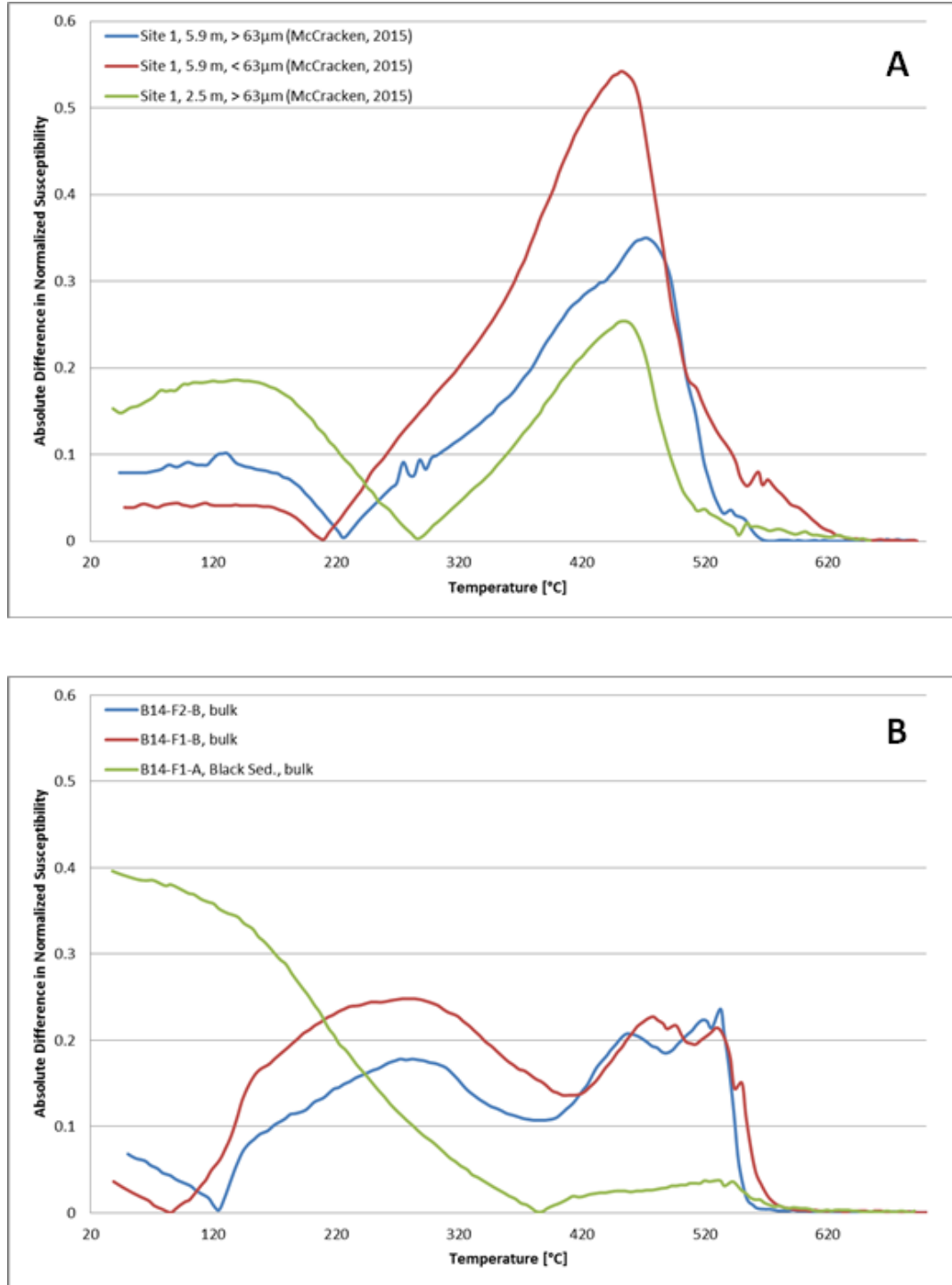


Figure D-1. Absolute difference in normalized susceptibility of heating and cooling curves vs. temperature for (A) Mulajokull till and (B) Breiðamerkurjökull sediments. Differences are large where minerals with a certain Curie temperature were altered upon heating. Only certain minerals are altered at high temperatures, including (titano)maghemite. These changes are therefore diagnostic of magnetic mineralogy.